University of Alberta

Large Scale ULF Waves and Energetic Particles in the Earth's Magnetosphere

by

Eun Ah Lee

A thesis submitted to the Faculty of Graduate Studies and Research
in partial fulfillment of the requirements for the degree of

Doctor of Philosophy

Department of Physics

Spring 2011
Edmonton, Alberta

Examining Committee

Dr. Ian R. Mann, Physics

Dr. Frances Fenrich, Physics

Dr. Moritz Heimpel, Physics

Dr. Ying Tsui, Electrical & Computer Engineering

Dr. P.T. Jayachandran, Physics, University of New Brunswick, Canada

Abstract

In this thesis we examine the generation mechanisms of Pc 5 ULF waves during geomagnetic storms. Also, we study the interaction between Pc 5 ULF waves and energetic particles in the radiation belts and the observed energetic particle flux modulation by Pc 5 ULF waves is verified using particle simulations.

Firstly, we present case studies of Pc 5 pulsations using ground-based magnetometer and satellite data during geomagnetic storm times, specifically we selecting three storm time events which show a brief increase in Dst in the main phase of the storms. By studying these events, we attempt to identify the generation mechanisms responsible for the geomagnetic pulsations. The observed pulsations exhibit the characteristic features of a Field Line Resonance, i.e., a latitudinally narrow peak in power accompanied by a 180 degree latitudinal phase shift. Our results also show evidence for the penetration of ULF wave power in the Pc 5 band to much lower L-shells than normal, suggesting significant reduction of the local Alfven eigenfrequency continuum as compared to non-storm times. This may have considerable significance for the interaction between ULF waves and MeV electrons in the outer radiation belt during storms.

Secondly, based on the hypothesis that Pc 5 ULF waves may play an important role in energetic particle dynamics in the radiation belt and ring current, we investigated the relationship between Pc 5 pulsations and energetic particle flux oscillations. We observed very strong Pc 5 oscillations during the great magnetic storm of March 24, 1991 [Lee et al., 2007] and electron flux simultaneously oscillating with the same frequencies in the time domain. We also characterize two more events and present an examination of the relationship between the electron flux modulation and Pc 5 ULF pulsations. Based on our observations, the modulation of energetic particles might be associated with a drift-resonance interaction, or the advection of an energetic particle density gradient.

Finally, we numerically calculate the trajectories and energy change of charged particles under the influence of model ULF wave electric fields. This modeling work is used to help to explain the observations and provides evidence which supports the modulation mechanisms such as advection of a flux gradient and drift resonance.

Acknowledgements

I would like to express my deep and sincere gratitude to my supervisor, Dr. Ian Mann, for his guidance, support, enthusiasm and encouragement during my doctoral study. Many thanks also to Dr. Frances Fenrich for her advise and support.

Special thanks to Dr. Louis Ozeke who has served as a mentor throughout the course of my research and has helped me with simulation model development. Thanks to Dr. Zoe Kale and Paul Loto'aniu for their assistance in data analysis. Thanks to to Andy Kale, and David Milling for all the technical support. Thanks to my officemates Adrienne Parent, Maria Usanova, Kyle Murphy, Laura Mazzino, David Miles, and Aziz Hoque and the rest of members of the space physics group for sharing joys and difficult moments during my PhD research.

Thanks to Dr. Orla Aaquist, Dr. Shelley Lorimer, Michelle Hanlon and Sharareh Karmand at the Grant MacEwan University for their help and giving me an enjoyable experience. Thanks to Cornelia Blunck at the observatory of Telus World of Science for her warm heart and encouragement for many years.

Thanks to Dr. Yu Yi, Dr. Byung-Ho Ahn, Dr. Yong-Ha Kim and Dr. Young-Deuk Park in Korea for their continuous concern and motivation.

Thanks to my old friends Caroline Lee, Hyunah Ryu, and Mira Oh for their support and friendship.

Finally, many thanks to my husband Jan Paral, my son Luca Lee Paral, and my dear parents for their endless love and support.

Table of Contents

List of Figures

List of Tables

List of Symbols

α	Local pitch angle
α_{eq}	Equatorial pitch angle
β	Plasma beta
$\mathbf{B}$	Magnetic Field
c	Speed of light
c_s	Sound speed
$\mathbf{E}$	Electric Field
e	Electron charge
ϵ_0	Permeability of free space
f	Phase space distribution function
γ_s	Ratio of specific heats
γ	The relativistic correction factor
k	Wave vector
k_B	Boltzmann constant
$\mathbf{J}$	Particle flux
$\mathbf{j}$	Current density
J	The second adiabatic invariant
$\mathbf{J}_P$	Pedersen current density
L	L-shell parameter

l	Length of box model magnetosphere
m_e	Electron mass
M	The first adiabatic invariant
M_r	Relativistic magnetic moment
μ_0	Permittivity of free space
n_i	Ion number density
n_e	Electron number density
σ_H	Hall conductivity
σ_P	Pederson conductivity
σ_0	Longitudinal conductivity
Ω_i	Ion gyrofrequency
Ω_e	Electron gyrofrequency
ω_g	Gyro frequency
p	Plasma pressure
$p_{\perp r}$	Perpendicular relativistic momentum
$p_{\perp}$	Perpendicular momentum
$p_{\parallel}$	Parallel momentum
Φ	The third adiabatic invariant
r_g	Gyroradius
R_E	Equatorial radius of Earth
ρ	Density of the fluid element
ρ^*	Charge density
σ_0	Longitudinal conductivity
σ_p	Pedersen conductivity
τ	Characteristic time scale
$\mathbf{v}$	Velocity

Chapter 1

Sun-Earth Connection

1.1 The Sun and Solar Wind

The Sun is a normal main-sequence G2 star composed of approximately 73.4% hydrogen and 25.0% helium of the mass and a rest of heavier elements such as carbon, oxygen, nitrogen, and others [e.g., *Kivelson and Russell*, 1995]. It has an equatorial radius of 696,000 km, mass 1.989×10^{30} kg and temperature 5785 K in the surface and 15,600,000 K in the core. At this temperature in the core of the Sun, nuclear fusion occurs by turning four hydrogen nuclei into one helium nucleus producing light and heat energy of about 3.8×10^{23} kW.

The energy travels from the core towards the outer regions by electromagnetic radiation and this region is called *radiative zone*. The next layer is the convective zone, so called because energy is transported primarily through the process of convection. The visible atmosphere of the sun is the *photosphere* and is one of the coolest regions of the Sun with a temperature of around 6000 K. In the *photosphere*, dark spots called *sunspots* are visible where the magnetic field is intense (up to 0.3 Tesla). The strong magnetic field inhibits the convection of hot

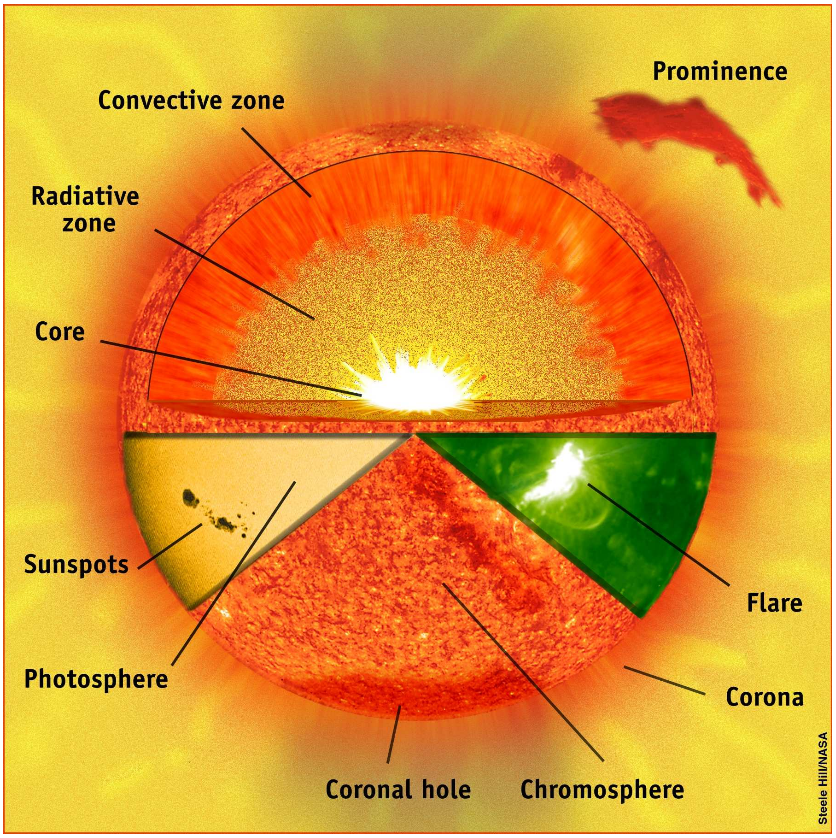

Figure 1.1: The interior of the Sun. Taken from Solar & Heliospheric Observatory, located at http://sohowww.nascom.nasa.gov/gallery/images/sunparts.html.

gas from the sun's interior, resulting in a cooler temperature. Hence, the spots appear dark compared with surrounding regions due to the lower temperature (about 4,500 K) in contrast with the surrounding surface temperature (about 6,000 K). The darkest part of a sunspot is at the center with highest magnetic field strength and is called the umbra; the surrounding less dark part is called the penumbra. Above the photosphere is the *chromosphere* which is visible during solar eclipse and its light is dominated by the deep red glow of the $H\alpha$ spectral line of hydrogen. The outer most layer of the Sun's atmosphere is the *corona* which extends millions of km and has high a temperature of several million Kelvin. *Prominences* appear as a large bright structures at the solar limb, often with a loop shape and appear as dark filaments on the disk of the sun in $H\alpha$ images due to having a cooler temperature than the surrounding corona (Figure 1.1).

The Sun and the Earth are intimately connected. The Sun can affect the Earth not only via the emission of electromagnetic radiation but also via a solar wind of high-speed charged particles which constantly buffets the Earth. The solar wind plasma is highly conducting which causes the Sun's magnetic field to be frozen into the plasma. Solar wind speed is typically 300 - 1400 km/s. The Sun's magnetic field carried into space by the solar wind is called the Interplanetary Magnetic Field (IMF). *Parker* [1958] proposed that the IMF has a spiral form because the solar rotation causes the magnetic field to become distorted.

The solar wind can affect the Earth and other planets and some of magnificent influences occur in association with *solar flares* and *coronal mass ejections (CMEs)*. A CME is a sudden and violent release of plasma and magnetic field from the solar corona. CME carry up to ten billion tons of plasma away from the Sun. Solar flares also release energetic particles into space via magnetic reconnection. The Earth's magnetosphere protects the surface of the Earth from this solar wind radiation. The details about the magnetosphere are described in the following section.

1.2 The Magnetosphere

The solar wind continuously blows from the Sun with supersonic speed and encounters the Earth's magnetic field. The *bow shock* is the boundary at which the solar wind speed abruptly drops and change the motion of particle. Beyond the bow shock the plasma is subsonic and deflects around the magnetic obstacle of the Earth's magnetosphere. Thus the Earth's magnetic field is confined

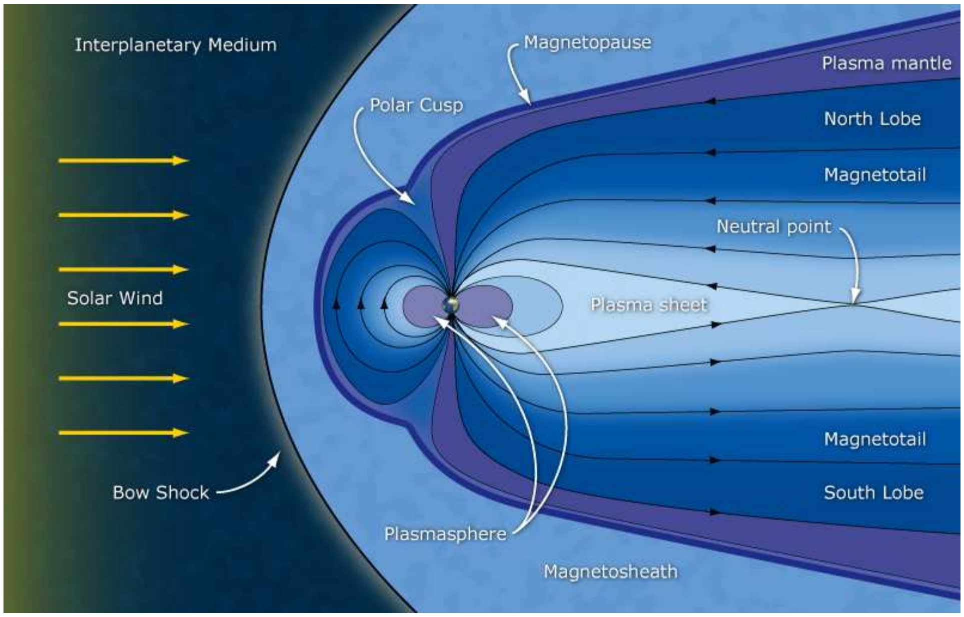

Figure 1.2: Schematic diagram of Earth's magnetosphere. Taken from ESA website, located at http://www.esa.int/esaSC/SEM6L529R9F_index_1.html.

in the magnetospheric cavity by the solar wind. The dayside magnetic field is compressed while the night side magnetic field is stretched out. Figure 1.2 shows the basic structure of the magnetosphere and the major regions are indicated.

The boundary between the shocked solar wind plasma and magnetospheric plasma is called the *magnetopause* where the dynamic ram pressure from the upstream solar wind and magnetic pressure from the Earth's magnetic field balance on both sides. The location of the magnetopause is about 10 Re (Earth radius), but varies depending on the solar wind pressure and external field direction. The shell-like region between the bow shock and the magnetopause is called the *magnetosheath* and is characterized by strongly compressed and shocked solar wind plasma.

The night side magnetic extension of the magnetosphere is called the *magnetotail* and *polar cusps* are regions which allow the solar wind particles from the magnetosheath to enter the magnetosphere and the ionosphere. In the center of the magnetotail where two oppositely directed magnetic fields meet lies a *current sheet* and a region of hot plasma (∼1 keV) is called the *plasma sheet* which separates the northern and southern magnetospheric lobes.

The origin of magnetospheric plasma is either ionospheric or from the solar wind. The *plasmasphere* in the inner magnetosphere contains cold (∼1 eV), and high density ($\sim 10 - 10^4$ cm^{-3}) plasma of ionospheric origin consists of protons, electrons and some heavy ions. While H^+ (nominally about 80 % by number) is the principal plasmaspheric ion species , $\mathrm{He}^+, \mathrm{O}^+, \mathrm{O}^{2+}, \mathrm{N}^+$ and N^{2+} ions are also observed in smaller quantities [e.g., *Kivelson and Russell*, 1995].

1.3 Ionosphere

The ionosphere is the uppermost part of the Earth's outer atmosphere and it consists of a mixture of neutral and ionized particles where the sources of ionization are solar extreme ultraviolet (EUV) radiation and x-ray photons or impact ionization by energetic particle from the magnetosphere. The ionosphere lies approximately from 70 km to 1000 km above Earth. The ionosphere can be split into different layers. The lower ionosphere D-region is weakly ionized region and mostly dominated by neutral gas. The E-region has ionization peak at about 110 km and contains mostly O_2^+ and NO^+. Typically electron density in E-region is several 10^5electrons/cm^3 during the day. F-regions has two layers, F1-layer peak is at around 200 km where electron density of about 2.5×10^5electrons/cm^3 at noon and F2-layer peak is at around 300 km height where it shows electron density of several 10^6electrons/cm^3 [*Baumjohann and Treumann*, 1997]. Overall the F layer is composed primarily of O^+. Those height and electron density are highly variable due to the day-night variability, season, solar cycle, and geomagnetic activity. The ionosphere plays an important role in the electrodynamics of space environment. The most visible manifestation of space weather is the intense auroral activity, which occurs in polar ionosphere during the magnetic storms and substorms, thus resulting in the ionospheric conductivity enhancement along the auroral oval. The ionospheric conductivities are given by

$$\sigma_0 = \frac{n_e e}{B}(\frac{\Omega_i}{\nu_i} - \frac{\Omega_e}{\nu_e}) \tag{1.1}$$

$$\sigma_P = \frac{n_e e}{B}(\frac{\Omega_i \nu_i}{\Omega_i^2 + \nu_i^2} - \frac{\Omega_e \nu_e}{\Omega_e^2 + \nu_e^2}) \tag{1.2}$$

$$\sigma_H = \frac{n_e e}{B}(\frac{\Omega_i^2}{\Omega_i^2 + \nu_i^2} - \frac{\Omega_e^2}{\Omega_e^2 + \nu_e^2}) \tag{1.3}$$

where $\sigma_0, \sigma_P, \sigma_H$ are longitudinal, Pederson, and Hall conductivity. n_e is electron density, Ω_i and Ω_e are ion and electron gyrofrequencies and ν_i and ν_e are ion-neutral collision frequency and electron-neutral collision frequencies, respectively.

1.4 The Aurora

Aurora is the spectacular visible space weather phenomena caused by energetic particles (mainly electrons) colliding with neutral atmospheric constituents (N_2, O_2, and O) in the ionosphere. The atmospheric atoms and molecules are excited by collision and emit photons of various wavelengths (from infrared to ultraviolet) in the process of returning to a lower energy state. The particular colors of the aurora depends on the type of atmospheric gas and its electrical state, and on the energy of the particle hitting the atoms and molecules. The brightest visible aurora is a green-yellow line by emission from oxygen atoms at altitudes between about 100 km and 200 km. Oxygen at higher altitude gives off red color where collisions with other atoms or molecules are rare and nitrogen molecules emits blue or purple color [e.g., *Baumjohann and Treumann*, 1997].

1.5 Geomagnetic Storms

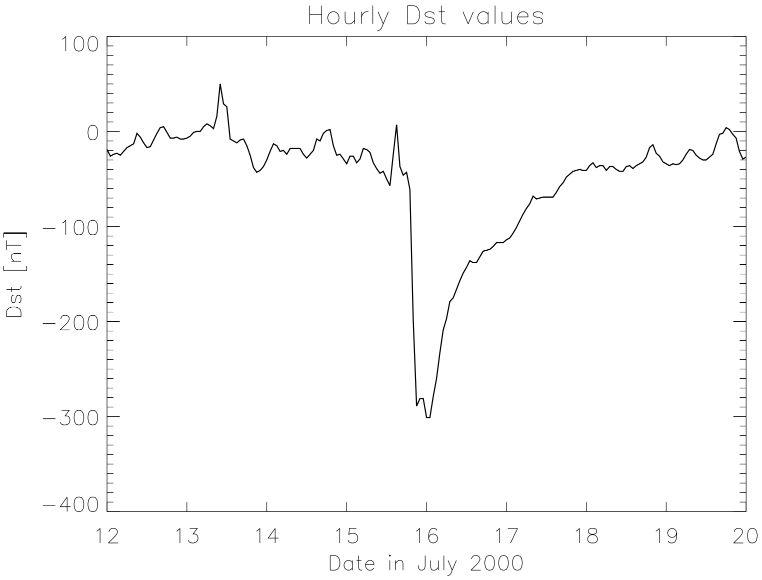

Figure 1.3: Dst values for the July 12-19, 2000 storm.

There is a population of very energetic charged particles which are stably trapped by the Earth's magnetic field and which consists mainly of protons with energies between 100 keV and several hundred MeV and electrons with energies between a few tens of keV and 10 MeV. Because these trapped positive ions and negative electrons drift in opposite directions (see Section 1.6), that motion will create a westward electric current around the Earth called the *ring current*. The global strength of the ring current can be monitored by ground-based magnetometers at middle or equatorial latitudes because of its diamagnetic effect (it decreases the intensity of the Earth's magnetic field on the Earth's surface).

Figure 1.4: Location of four low-latitude observatories, Honolulu, San Juan, Hermanus, and Kakioka. Taken from Istituto Nazionale di Geofisica e Vulcanologia website, located at http://portale.ingv.it/research-areas/sun-earth/dst-geomagnetic-index/.

When a large CME is ejected from the Sun it can couple to the Earth's magnetosphere, transfer energy from solar wind to the magnetosphere, and intensify the ring current encircling the Earth.

This enhanced ring current can be monitored with the Dst index. The hourly Dst index is the average deviation of the H-component (northward horizontal) obtained from selected magnetometer stations (Honolulu, San Juan, Hermanus and Kakioka) near the equator (see Figure 1.4). The negative Dst values indicate geomagnetic storms in progress and these geomagnetic storms can be classified into intense, moderate, or weak storms (intense storms: Dst <-100 nT, moderate storms: -100 nT < Dst < -50 nT, and weak storms: -50 nT < Dst < -30 nT) [*Gonzalez et al.*, 1994].

Large storms are usually accompanied by storm sudden commencement (SSC) which is a sharp compression of the Earth's magnetic field caused by increased solar wind dynamic pressure. Typically storms have three phases: initial, main, and recovery phases. In the initial phase, Dst increases to positive and lasts minutes to hours. Large increases of magnetospheric ring current intensity cause a rapid decrease in Dst (over several hours) in the main phase of the storm. During the recovery phase, Dst gradually returns to normal as ring current ions are gradually lost (duration about 1-5 days) (see Figure 1.3).

1.6 Adiabatic Invariant and Trapped Particle Motion

An adiabatic invariant is the property of a physical system which remains constant for slow changes of the system compared with some typical periodic particle motion. There are three types of adiabatic invariants that occur on different time scales. The first adiabatic invariant, M, is associated with the gyro-motion of a particle about a magnetic field line. The second invariant (longitudinal invariant), J, is associated with the bounce motion of a particle along the ambient field line. The third invariant, Φ , is related to the azimuthal drift of a particle about the Earth due to the gradient and curvature of the magnetic field [e.g., *Baumjohann and Treumann*, 1997].

Figure 1.5 shows how the motion of energetic charged particles trapped in an axi-symmetric magnetic field consists of three periodic components, gyro-motion, bounce motion, and drift motion.

1) Gyro-motion around the magnetic field lines

The equation which describe the motion of a non-relativistic charged particle in magnetic and electric fields can be written as

$$m\frac{d\mathbf{v}}{dt} = q(\mathbf{E} + \mathbf{v} \times \mathbf{B}) \tag{1.4}$$

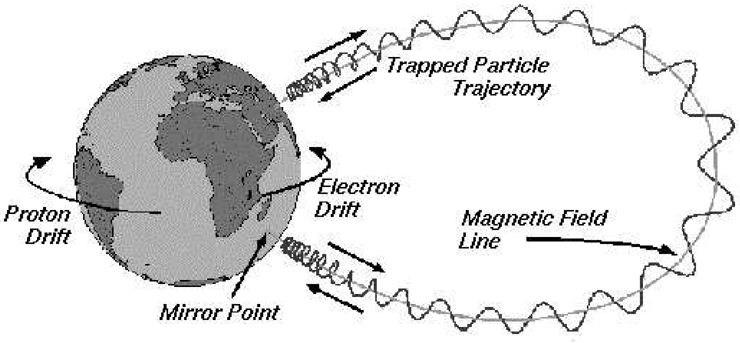

Figure 1.5: Trajectories of particles confined in closed field lines. Taken from SPENVIS, located at `http://www.spenvis.oma.be/help/background/traprad/traprad.html`

where $\mathbf{E}$ and $\mathbf{B}$ represent electric field and magnetic field, m the particle mass and $\mathbf{v}$ the particle velocity. For a non-relativistic particle in a uniform magnetic field where $\mathbf{E} = \mathbf{0}$, the solution of Equation 1.4 gives the periodic circular motion around the background magnetic field. Opposite charges circle in opposite directions; in the case of a magnetic field pointing up from the page, ions circle clockwise and electrons circle counter-clockwise with frequency ω_g (gyrofrequency) defined as

$$\omega_g = \frac{qB}{m} \tag{1.5}$$

and which carries opposite signs for electrons (negative) and ions (positive). The radius of cyclotron motion, the *gyroradius*, is defined as

$$r_g = \frac{v_\perp}{\omega_g} = \frac{mv_\perp}{|q|B} \tag{1.6}$$

The first adiabatic invariant, M is defined by the gyro-motion of the particle about a field line

$$M = \frac{mv_{\perp}^2}{2B} = \frac{p_{\perp}^2}{2m_0 B} \tag{1.7}$$

where $p_{\perp}$ is the momentum perpendicular to magnetic field B and m_0 is the rest mass of the particle. Here M is a constant of the cyclotron motion in (spatially or temporally) varying magnetic fields B, as long as the changes of the magnetic field are slow compared to the gyroperiod ($2\pi/\omega_g$) of the particle, and as long as the gyroradius (r_g) is much larger than the magnetic field line curvature radius and gradient scale.

2) Mirror motion/bounce motion

As particles circle guiding field line, the guiding center of their rotation gradually change up and down. A dipole magnetic field has a minimum field strength at the equator and stronger field strength at the polar region where field lines converge. Equation 1.7 can be rewritten in the following form

$$M = \frac{mv^2 sin^2\alpha}{2B} \tag{1.8}$$

here the magnetic moment is invariant and the only pitch angle (α) can change when the magnetic field increase or decrease along the guiding center trajectory [*Baumjohann and Treumann*, 1997]. Thus, the magnetic field strengths and pitch angles of a particle has the relation such as

$$\frac{sin^2\alpha_2}{sin^2\alpha_1} = \frac{B_2}{B_1} \tag{1.9}$$

As a particle moves into a region of stronger magnetic field, its pitch angle will increase to keep the magnetic moment constant. In Equation 1.4, taking the dot product with $\mathbf{v}$ yields the equation

$$m\frac{d\mathbf{v}}{dt} \cdot \mathbf{v} = \frac{d}{dt}(\frac{mv^2}{2}) = 0 \tag{1.10}$$

which shows that particle kinetic energy is constant. Thus, transverse energy $W_\perp$ increases at the cost of parallel energy $W_\|$. Once particle reach the *mirror point* where the pitch angle reaches $\alpha = 90°$, it will change direction and travel back along the magnetic field line toward the other hemisphere. If the particles can bounce back or mirror at both ends of the field line then ions and electrons would be trapped in the Earth's magnetosphere. The bounce period, τ_b, between mirror points can be calculated by

$$\tau_b = 4\int_0^{\lambda_m} \frac{ds}{v_\|} \tag{1.11}$$

where λ_m is the magnetic latitude of the particle's mirror point.

This can be approximated in a dipole field to give

$$\tau_b \approx \frac{LR_E}{(W/m)^{1/2}}(3.7 - 1.6sin\alpha_{eq}) \tag{1.12}$$

where W is particle energy, L is r_{eq}/R_E, and α_{eq} is equatorial pitch angle.

The second adiabatic invariant, J, is defined by the periodic bouncing motion of a particle trapped between two mirror points on a magnetic field-line and is given by

$$J = \oint p_{||}ds = 2\int mv_{||}ds \tag{1.13}$$

where $p_{||}$ is the particle momentum parallel to the magnetic field and ds is an element of distance a particle travels along the field line. J is invariant as long as the magnetic field varies on the time scale longer than the bounce time.

3) Azimuthal drift motion

The third motion is drift motion around the Earth which is an effect of the gradient and curvature of the dipole magnetic field. The ions and electrons drift in opposite directions; westward for ions and eastward for electrons and the total magnetic drift is described in the equation below :

$$v_B = v_R + v_\bigtriangledown = (v_{||}^2 + \frac{1}{2}v_\perp^2)\frac{B \times \bigtriangledown B}{\omega_g B^2} \tag{1.14}$$

where v_R is the curvature drift and $v_\bigtriangledown$ is the gradient drift [*Baumjohann and Treumann*, 1997].

The average drift period can be obtained numerically, but the approximate formula is

$$< \tau_d > \approx \frac{6L^2W}{qB_ER_E}(0.35 + 0.15 sin\alpha_{eq}). \tag{1.15}$$

The third adiabatic invariant Φ, total magnetic flux enclosed by the drift trajectory, is invariant as long as the frequency of electromagnetic field variations perturbing the particle motion is much smaller than the drift frequency ω_d. The drift motion of the particle causes interesting effects in the Earth's inner magnetosphere. Because positive ions and negative electrons drift in opposite directions, the motion will create an westward electric current called the ring current around the Earth as described in section 1.5 . Also, if the Earth's magnetic field is compressed by slowly increasing or decreasing solar wind, dynamic pressure, charged particles move radially inward or outward to conserve the magnetic flux enclosed by their drift orbit [*Walt*, 1971].

1.7 Radiation Belt

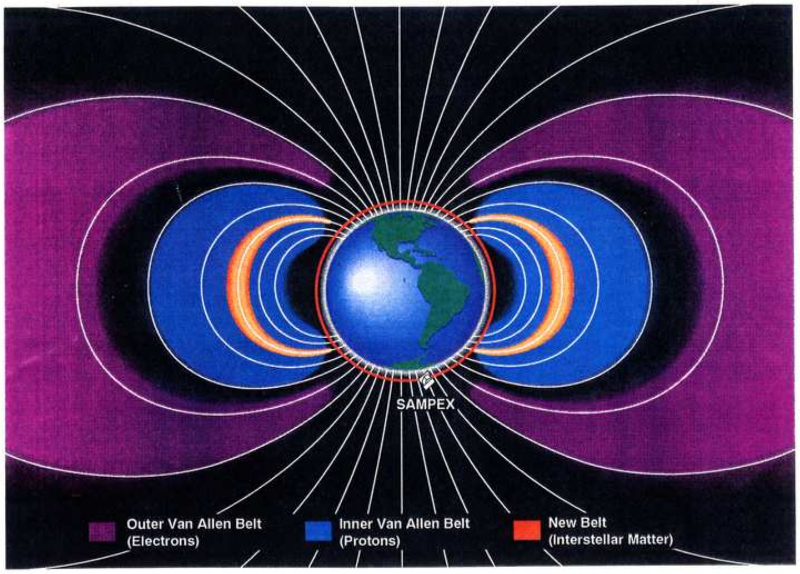

Figure 1.6: Schematic view of the Van Allen radiation belts. Trapping of energetic particles on the dipole-like field lines near the Earth results in torus-like regions, i.e., the radiation belts. Courtesy of J. Cummings. Taken from the SAMPEX Data Center website, located at `http://www.srl.caltech.edu/sampex/DataCenter/Gallery/`.

The radiation (or Van Allen) belts are composed of magnetically trapped very high-energy ions and electrons surrounding the Earth (Van Allen et al., 1958; Van Allen and Frank, 1959). The belts are separated into two radiation belts : the **inner radiation belt** (below L $\sim$ 2) and the **outer radiation belt** (above L $\sim$ 3). Between these two belts a **slot** region at $L \sim 2.5$ exists and it is believed that wave-particle interactions (electrons are scattered in pitch angle due to whistler mode hiss) cause the electron losses [*Thorne*, 1973]. However, it can be filled up during the severe magnetic storm times such as the storm of March 24, 1991 or the Halloween storms of Oct - Nov, 2003 ([e.g., *Blake et al.*, 1992; *Baker et al.*, 2004]).

The **inner radiation belt** contains primarily energetic protons (exceeding 50 MeV) confined by strong magnetic field to the inner regions of the magnetosphere. Based on data from National Space Science Data Center, protons above 100 keV show a maximum flux ($\sim 2 \times 10^8$ protons $\mathrm{cm}^{-2}\mathrm{s}^{-1}$) at about $L \sim 3.1$ and protons above 50 MeV shows the maximum flux ($\sim 2 \times 10^4$ protons cm^{-2} s^{-1}) at $L \sim 1.5$ [*Walt*, 2005]. This observational result shows that the the average energy of trapped particles increases with decreasing L values. The source of these energetic ions is mainly the decay of neutrons freed in the collision of cosmic rays with nuclei in the upper atmosphere. Other ions in the radiation belts have either solar origins or result from the direct trapping of charged energetic cosmic particles [e.g., *Mewaldt et al.*, 1994].

The **outer radiation belt** contains mainly very high energy (0.1 - 10 MeV) electrons trapped by the Earth's magnetosphere. Also, various ions mostly in the form of energetic protons and small amount of alpha particles and oxygen ions are found within this belt. Its greatest intensity is usually around $L \sim 4 - 5$ and the flux decreases rapidly with increasing energy. The outer radiation belt constantly changes with geomagnetic conditions while the inner radiation belt is quite stable. Major magnetic storms and substorms affect the configuration of trapped particles but the mechanisms are not fully understood [*Walt*, 2005].

1.8 Summary

In this thesis, we will examine the generation mechanisms of Pc 5 ULF waves during geomagnetic storms using the ground-based and satellite data. Also, the interaction between Pc 5 ULF waves and energetic particle flux in the radiation belts will be studied using the ground-based and satellite data and the numerical modeling. In Chapter 2, we will introduce a brief explanation about the ultra-low frequency (ULF) waves in the Earth's magnetosphere. In Chapter 3, instrumentation and analysis techniques used in this thesis will be presented. In Chapter 4, we will present the case studies of Pc 5 geomagnetic pulsations during geomagnetic storm and discuss the possible excitation mechanisms. In Chapter 5, we will show observational evidence of the interaction between the Pc 5 ULF waves and energetic particles in outer radiation belt for three storm time events using the ground-based and satellite data. Finally, in Chapter 6, we will show particle simulations where flux modulation occur and verify the interpretation of the observational data presented in Chapter 5.

Chapter 2

Ultra-Low Frequency Waves in the Earth's Magnetosphere

2.1 Magnetospheric Ultra-Low-Frequency Waves

Magnetospheric ULF (ultra low frequency) waves are geomagnetic pulsations in the frequency band 1 mHz to 1Hz. *Jacobs et al.* [1964] categorized the ULF pulsations into different types depending on their period and on how well-defined the pulsations wave form is, as shown in Table 2.1. ULF waves are perturbed via the interaction of the solar wind and the Earth's magnetosphere.

Continuous regular well defined wave form					
	Pc 1	Pc 2	Pc 3	Pc 4	Pc 5
Ts	0.2-5	5-10	10-45	45-150	150-600
f	0.2-5 Hz	0.1-0.2 Hz	22-100 mHz	7-22 mHz	2-7 mHz
Irregular wave form					
	Pi 1	Pi 2			
Ts	1-40	40-150			
f	0.025-1 hz	2-25 mHz			

Table 2.1: Geomagnetic pulsation classes

2.2 Magnetohydrodynamic Theory

ULF waves produced by processes in the magnetosphere and solar wind can be described by magnetohydrodynamics (MHD) because they have temporal and spatial scales longer than particle gyroperiod (τ_g) and larger than gyroradius (r_g). The equations of MHD are derived by combining both Maxwell's equations of electrodynamics and hydrodynamic fluid equations.

Maxwell's equations :

$$Gauss's\ law:\ \nabla \cdot \mathbf{E} = \frac{\rho^*}{\epsilon_0} \tag{2.1}$$

$$\nabla \cdot \mathbf{B} = 0 \tag{2.2}$$

$$Faraday's\ law\ :\ \nabla \times \mathbf{E} = -\frac{\partial \mathbf{B}}{\partial t} \tag{2.3}$$

$$Ampere's\ law\ :\ \nabla \times \mathbf{B} = \mu_0(\mathbf{j} + \epsilon_{\mathbf{0}}\frac{\partial \mathbf{E}}{\partial \mathbf{t}}) \tag{2.4}$$

where $\mathbf{E}$ and $\mathbf{B}$ are the electric field and magnetic field, $\mathbf{j}$ and $\rho^* = e(n_i - n_e)$ (assuming the ions are singularly charged) are the current and charge density, n_i and n_e are the ion and electron number densities and e is the electron charge, and ϵ_0 and μ_0 are the permeability and permittivity of free space, respectively.

We assume the typical lengthscale for plasma variation is L and the typical timescales are of order T, then typical plasma can be defined as $v \sim L/T$. The left hand side of Equation 2.4 is approximately B/L and the displacement current term in the Equation can be written as

$$\mu_0\epsilon_0\frac{\partial \mathbf{E}}{\partial t} \sim \frac{1}{c^2}\frac{E}{T} = \frac{B}{L}\frac{v^2}{c^2}$$

For an MHD plasma, the displacement current term can be neglected if $v^2 <<$

c^2 then $\nabla \times \mathbf{B} >> \mu_0 \epsilon_0 \frac{\partial \mathbf{E}}{\partial t}$ so that Ampere's law can be rewritten as

$$\nabla \times \mathbf{B} = \mu_o \mathbf{j}. \tag{2.5}$$

Also, on MHD time scales and length scales, $\rho^* \sim 0$ since the plasma is neutrally charged ([see e.g., *Allan and Poulter*, 1992] for further discussion). Thus Coulomb's law in the MHD limit can be simplified as

$$\nabla \cdot \mathbf{E} = 0 \tag{2.6}$$

In MHD theory, the hydrodynamic component of the MHD equations incorporates the following conservation principles.

Continuity Equation :

$$\frac{\partial \rho}{\partial t} + \bigtriangledown \cdot (\rho \mathbf{v}) = 0 \tag{2.7}$$

where $\mathbf{v}$ is the fluid velocity and ρ is the mass density. This expresses mass conservation.

Equation of Motion :

$$\rho(\frac{\partial \mathbf{v}}{\partial t} + \mathbf{v} \cdot \bigtriangledown \mathbf{v}) = \mathbf{j} \times \mathbf{B} - \bigtriangledown p \tag{2.8}$$

where p is the plasma pressure. This expresses momentum density conservation.

Equation of state :

$$\frac{p}{\rho^{\gamma_s}} = constant \tag{2.9}$$

where γ_s is the ratio of the two specific heats at constant pressure and constant volume. For the adiabatic case $\gamma_s = 5/3$.

In the electromagnetic component of the MHD equations, Ohm's law also needs to be considered

$$\mathbf{j} = \sigma(\mathbf{E} + \mathbf{v} \times \mathbf{B}) \tag{2.10}$$

where σ is the plasma conductivity. In ideal MHD theory it is assumed that $\sigma = \infty$ so that Ohm's law becomes

$$\mathbf{E} + \mathbf{v} \times \mathbf{B} = 0. \tag{2.11}$$

here the magnetic field lines remain "frozen-in" to the plasma [see e.g., *Baumjohann and Treumann*, 1997], such that the magnetic field threading a plasma element remains "frozen-in" to that element.

2.2.1 Magnetic Pressure and Tension

Using the equation (2.4), Lorentz force term, $\mathbf{j} \times \mathbf{B}$, can be written as

$$\mathbf{j} \times \mathbf{B} = -\frac{1}{\mu_0}\mathbf{B} \times (\nabla \times \mathbf{B}). \tag{2.12}$$

Applying the vector identity $(\nabla \times \mathbf{B}) \times \mathbf{B} = -\nabla B^2/2 + (\mathbf{B} \cdot \nabla)\mathbf{B}$, equation (2.12) can be written as

$$\mathbf{j} \times \mathbf{B} = -\nabla(\frac{B^2}{2\mu_0}) + \frac{1}{\mu_0}(\mathbf{B} \cdot \nabla)\mathbf{B} \tag{2.13}$$

The first term represents a force that acts to reduce gradients in *magnetic pressure*, $B^2/2\mu_0$. The Lorentz force also produces a force which lies in the plane of the curved magnetic field lines. The second term acts to straighten out the curved magnetic field lines which is called *magnetic tension* in the conducting plasma.

In equilibrium conditions, the equation of motion (equation (2.8)) becomes

$$\mathbf{j} \times \mathbf{B} = \nabla p \tag{2.14}$$

If we assume isotropic particle pressure and homogeneous magnetic field and using equation (2.13), we can approximate equation (2.14) by

$$\nabla\left(p + \frac{B^2}{2\mu_0}\right) = 0 \tag{2.15}$$

here, $p + B^2/2\mu_0$ is the total pressure where p is thermal pressure and $B^2/2\mu_0$ is magnetic pressure. During equilibrium conditions the total pressure is constant. The ratio of thermal and magnetic pressure is called the *plasma beta* and is defined as $\beta = 2\mu_0 p/B^2$.

When a magnetic field line is displaced from its equilibrium position both thermal and magnetic pressure forces can act as a restoring force. A plasma with a low-beta ($\beta \ll 1$) is known as a cold plasma and a high-beta plasma ($\beta \gg 1$) is generally referred to as a warm or hot plasma.

2.3 Introduction to Hydromagnetic Waves

To illustrate the basic idea of hydromagnetic wave theory, we restrict our analysis to the simplest case of a uniform straight magnetic field embedded in a uniform, infinite, fully-ionized cold plasma. Fully ionized cold plasma waves with a straight uniform background magnetic field ($\mathbf{B}_0 = B_0\hat{\mathbf{z}}$) can be considered as two cases:

Alfvén or shear waves and fast or compressional wave modes.

Cold plasma implies that fluid kinetic pressure can be neglected as it is small compare to the magnetic pressure. We may linearize the MHD equations by assuming stationary ideal homogeneous condition and small fluctuations as

$$\rho = \rho_0 + \rho_1 \tag{2.16}$$

$$\mathbf{B} = \mathbf{B}_0 + \mathbf{B}_1 \tag{2.17}$$

$$\mathbf{E} = \mathbf{E}_0 + \mathbf{E}_1 \tag{2.18}$$

$$\mathbf{j} = \mathbf{j}_0 + \mathbf{j}_1 \tag{2.19}$$

$$\mathbf{v} = \mathbf{v}_0 + \mathbf{v}_1 \tag{2.20}$$

where the subscript 0 indicate a background time independent and unperturbed quantity and 1 indicate small perturbations in plasma density, magnetic field, electric field, velocity, and current density. Here we assume that $\mathbf{E}_0 = 0$, $\mathbf{v}_0 = 0$ then in the cold plasma limit the relevant Maxwell equations (2.3), (2.4) and the equation of motion (equation (2.8)) after linearization become

$$\nabla \times \mathbf{E}_1 = -\frac{\partial \mathbf{B}_1}{\partial t} \tag{2.21}$$

$$\nabla \times \mathbf{B}_1 = \mu_0 \mathbf{j}_1 \tag{2.22}$$

$$\rho_0 \frac{\partial \mathbf{v}_1}{\partial t} = \mathbf{j}_1 \times \mathbf{B}_0 \tag{2.23}$$

Here, because we assume $\mathbf{E}_1 + \mathbf{v}_1 \times \mathbf{B}_0 = 0$, perturbed electric field $\mathbf{E}_1$ has only the perpendicular component $\mathbf{E}_1 = \mathbf{E}_{1\perp}$. Combining equations (2.21), (2.22), (2.23) and (2.11) yields the wave equation

$$\frac{\partial^2 \mathbf{E}_1}{\partial t^2} + v_A^2 \nabla \times (\nabla \times \mathbf{E}_1) = 0 \tag{2.24}$$

where $v_A = B_0/\sqrt{\mu_0\rho}$ is called the Alfvén speed [see e.g., *Allan and Poulter*, 1992].

Equation (2.24) can be written as two coupled equations for the perpendicular component E in Cartesian coordinates with uniform background magnetic field along the z direction (after *Allan and Poulter* [1992])

$$(v_A^{-2}\frac{\partial^2}{\partial t^2} - \frac{\partial^2}{\partial y^2} - \frac{\partial^2}{\partial z^2})E_{1x} = -\frac{\partial^2 E_{1y}}{\partial x \partial y} \tag{2.25}$$

$$(v_A^{-2}\frac{\partial^2}{\partial t^2} - \frac{\partial^2}{\partial x^2} - \frac{\partial^2}{\partial z^2})E_{1y} = -\frac{\partial^2 E_{1x}}{\partial x \partial y}. \tag{2.26}$$

Assuming all electric field perturbations vary in the plane-wave form $\exp[i(k_y y + k_z z - \omega t)]$ [*Allan and Poulter*, 1992] and $\partial/\partial x \equiv 0$, two dispersion relations can be derived :

$$\omega^2 = k^2 v_A^2 \tag{2.27}$$

$$\omega^2 = k_z^2 v_A^2 \tag{2.28}$$

where $k^2 = k_y^2 + k_z^2$. Equation (2.28) is referred to as the *shear Alfvén wave*. The phase speed is $\omega/k_z = v_A$, and the direction and speed which energy is propagated by the wave is given by the group velocity, $\mathbf{v}_g$, which is given by

$$\mathbf{v}_g = \pm v_A \hat{\mathbf{z}}. \tag{2.29}$$

The *shear Alfvén wave* has the property that energy flows only along $\mathbf{B_0}$ regardless of the direction of k, thus it represents simple string-like oscillations of the magnetic field lines. The shear mode has perturbation $\mathbf{B_1}$ always perpendicular to $\mathbf{B_0}$, $\mathbf{B_1}\cdot\mathbf{B_0}$=0, so this mode carries no pressure perturbation. Also, due to the fact that energy is guided along the ambient magnetic field, this mode is also called a *guided mode*. Equation (2.27) is the *fast magnetoacoustic mode* dispersion relation. This is known as the fast mode with a phase speed of v_A and group velocity of $\mathbf{v}_g = \pm v_A \hat{k}$, where $\hat{k}$ is the unit vector in the direction of the wave vector $\mathbf{k}$. The group velocity, energy propagation, is independent of the direction of $\mathbf{B}_0$. Thus it can propagate at any angle to the magnetic field. The fast mode can also transmit magnetic pressure variation since $B_z \neq 0$. The fast mode has current $\mathbf{j}$ always perpendicular to $\mathbf{B}$, $\mathbf{j} \cdot \mathbf{B} = 0$, so its field-aligned current is zero.

If the plasma is not completely cold, then the fluid kinetic pressure is not negligible. The dispersion relation of Alfvén mode (2.28) is unchanged. Now the dispersion relation (2.27) splits into two roots as given by [see e.g., *Allan and Poulter*, 1992].

$$\frac{\omega^2}{k^2} = \frac{1}{2}\Big\{c_s^2 + v_A^2 \pm [(c_s^2 + v_A^2)^2 - 4c_s^2 v_A^2 cos\theta^2]^{\frac{1}{2}}\Big\} \tag{2.30}$$

where θ is the angle between the $\mathbf{k}$ and $\mathbf{B}_0$, so that $k_y = ksin\theta$ and $k_z = kcos\theta$. Here the sound speed $c_s = (\gamma_s p_0/\rho_0)^{1/2}$, p_0 is a finite equilibrium pressure, and ρ_0 is the mass per unit volume. For the wave propagating along the ambient magnetic field $\mathbf{B}_0$, $\theta = 0$, equation (2.30) becomes

$$\omega^2 = k^2 v_A^2, \tag{2.31}$$

and

$$\omega^2 = k^2 c_s^2, \tag{2.32}$$

such that in a warm magnetized plasma a transverse fast mode (phase speed of v_A) and a compressional sound wave (phase speed of c_s) might be expected.

For the wave propagating at an angle to the ambient magnetic field, when $cos^2\theta \simeq 0$ and c_s is much smaller than v_A, equation (2.30) becomes two hybrid modes. The dispersion relations are given by

$$\omega^2 = k^2(c_s^2 + v_A^2) \tag{2.33}$$

and

$$\omega^2 = k_z^2 \frac{c_s^2 v_A^2}{(c_s^2 + v_A^2)} \tag{2.34}$$

The two solutions are referred to as the fast magnetosonic wave which propagate with phase speed $\sqrt{c_s^2 + v_A^2}$. For the case $c_s \rightarrow 0$ this mode is same as the fast mode.

The fast magnetosonic wave has magnetic and fluid pressure perturbations in phase. These waves can propagate at arbitrary angle relative to the magnetic field. On the other hand, the slow magnetoacoustic mode has magnetic and plasma pressure variations which are out of phase and the waves are confined to propagation which is closely aligned to the magnetic field lines and it does not propagate perpendicular to the magnetic field when $\theta = \pi/2$.

The dependence of the wave phase speed on the direction of propagation for the three wave modes is shown in figure 2.1. Each of these waves has unique polarization properties with the electric, magnetic, and plasma velocity fluctuations being oriented in different directions relative to the direction of wave propagation and background field. The fast mode and Alfvén mode propagate with the Alfvén speed along the field. The fast mode speed perpendicular to the field is a combination of the Alfvén and sound speeds, $c_{ms} = \sqrt{c_s^2 + v_A^2}$, and the Alfvén mode

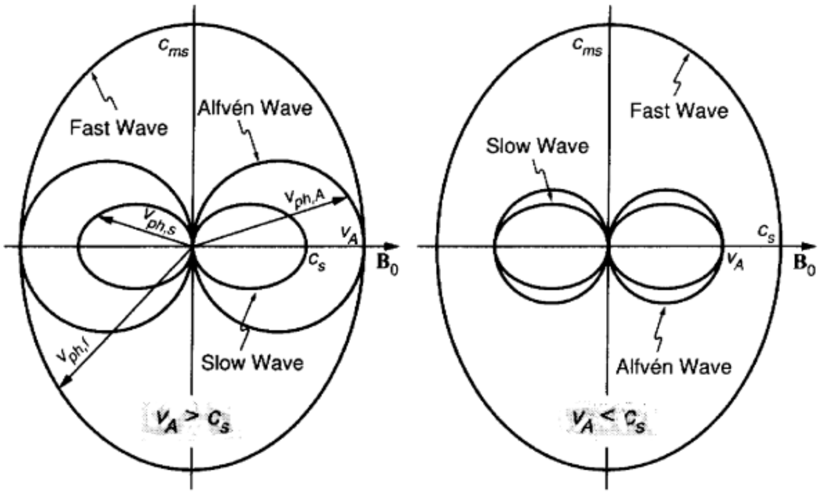

Figure 2.1: Phase velocity diagrams of fast, Alfvén, and slow waves (taken from *Baumjohann and Treumann*, 1997).

perpendicular group speed is zero which means no propagation in this direction is possible. Parallel to the field the slow mode phase speed moves at whichever speed is smallest between the sound speed, c_s, and the Alfvén speed, v_A.

The relative size of the Alfvén and sound speed in a plasma is usually expressed using the plasma beta, β, which can also be written as

$$\beta = \frac{plasma\ pressure}{magnetic\ pressure} = \frac{2c_s^2}{\gamma_s v_A^2}. \tag{2.35}$$

In a cold plasma the magnetic pressure dominates the plasma pressure, so that $v_A^2 \gg c_s^2$ and $\beta \ll 1$.

2.4 Hydromagnetic wave Coupling and Field Line Resonance

In Earth's magnetosphere, the fast and Alfvén modes may couple together. Allan and Poulter (1992) describe how fast and Alfvén modes may become coupled in a non-uniform plasma. Magnetospheric ULF waves observed on the ground with magnetometers generally originate in space as either fast mode, or shear Alfvén mode, or a combination of these.

Field line resonances are long duration ULF waves in the magnetic field of the Earth. According to ideal MHD wave theory, a cold plasma can support two basic wave types, i.e., the fast magnetosonic wave and the shear Alfvén wave (see section 2.3). In field line resonance theory, standing Alfvén waves can be excited on geomagnetic field lines, forming so called field line resonances (FLR). If the natural Alfvén frequency of the field line matches that of the fast mode wave, then a driven field line resonance will be established.

In a simple magnetospheric model, one may assume constant field-aligned Alfvén speed, straight field lines of length l with infinitely conducting ionospheres and the wavelength in the field-aligned direction is $\lambda_{||} = 2l/n$ where n is an integer. Then the local Alfvén eigenfrequency will be given by

$$\omega = v_A k_{||} = \frac{v_A 2\pi}{\lambda_{||}}. \tag{2.36}$$

If the fast mode frequency equals one of these standing resonant Alfvén eigenfrequencies, Alfvén waves may be excited on the magnetic field lines in a process called driven field line resonance. We now follow the treatment of Allan and Poulter (1992) to show how fast and Alfvén modes may become coupled in a non-uniform plasma. Following that a discussion of wave turning points and resonance will be presented. With non-uniform magnetic fields and mass density, Alfvén speed varies. We now assume that the Alfven speed varies in x-direction and the wave electric field E_x and E_y vary as

$$E_x(x,y,z,t) = E_x(x) exp[i(k_y y + k_z z - \omega t)] \tag{2.37}$$

$$E_y(x,y,z,t) = E_y(x) exp[i(k_y y + k_z z - \omega t)]. \tag{2.38}$$

Equations (2.25) and (2.26) become

$$(\frac{\omega^2}{v_A(x)} - k_y^2 - k_z^2)E_x = ik_y(\frac{dE_y}{dx}) \tag{2.39}$$

$$(\frac{\omega^2}{v_A(x)} - k_z^2)E_y = ik_y(\frac{dE_x}{dx}) - \frac{d^2E_y}{dx^2}. \tag{2.40}$$

If we now assume that $k_y = 0$, then equation (2.39) and (2.40) decouple to give

$$(K(x)^2 - k_z^2)E_x = 0 \tag{2.41}$$

$$(K(x)^2 - k_z^2)E_y = -\frac{d^2E_y}{dx^2}. \tag{2.42}$$

where $K(x)^2 = \omega^2/v_A^2(x)$ is assumed to be monotonically increasing with x.

In equation (2.42), E_y has turning point $(x = x_r)$ where $K^2 = k_z^2$. At $x = x_r$, the solutions to the equation change from oscillatory to evanescent. For $x > x_r$ a wave has oscillatory spatial structure while for $x < x_r$ wave growth or decay will occur with x.

In the case of $k_y \neq 0$, we may combine equations (2.39) and (2.40) to a single equation

$$\frac{d^2E_y}{dx^2} - C\frac{dE_y}{dx} + (K^2 - k_y^2 - k_z^2)E_y = 0 \tag{2.43}$$

where

$$C = \frac{k_y^2}{[(K^2 - k_z^2)(K^2 - k_y^2 - k_z^2)]}(\frac{dK^2}{dx}). \tag{2.44}$$

The coupled equation (2.44) has a turning point, x_r, being approximately zero at the turning point where $K^2 - k_y^2 - k_z^2 = 0$. At $x > x_r$, the fast wave will have an oscillatory structure while at $x < x_r$ the wave will be evanescent. There is also a resonance at the position $x = x_{res}$ where $K^2(x) - k_z^2 = 0$. At x_{res}, the fast mode phase velocity in the field aligned direction equals the Alfvén phase velocity. The resonance occurs in the evanescent region of the wave ($x < x_r$). Most of the energy of the fast mode wave is transferred to the standing Alfvén wave at the resonant field line causing the field line oscillation with an enhanced amplitude. This mechanism is called field line resonance (FLR) and represents a major form of energy transport into the magnetosphere.

At the location of the resonant field line an FLR will have an amplitude maximum and the polarization will switch across the latitude of the resonant field line and also across local noon (see Figure 2.2) [*Samson et al.*, 1971].

2.5 ULF waves in the Dipole Coordinate System

Dungey [1954] recognized that geomagnetic pulsations are magneto-hydromagnetic eigenmodes of approximately dipolar geomagnetic field lines. We use here a dipole coordinate system (ν, μ, ϕ) defined as

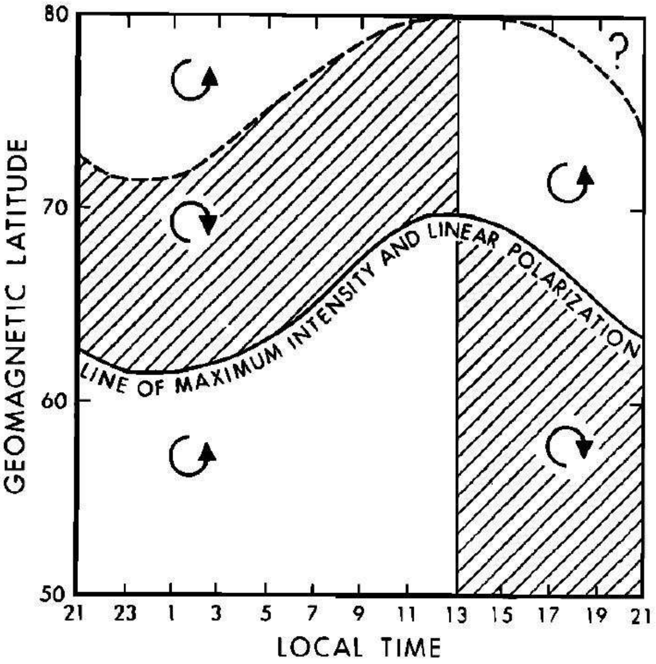

Figure 2.2: Variation of wave polarization (After *Samson et al.*, 1971).

$$\nu = \frac{\sin^2\theta}{r}, \mu = \frac{\cos\theta}{r^2} \tag{2.45}$$

where r, θ, and ϕ are the spherical polar coordinates. ν along the principle normal to a field line is constant on a given magnetic L-shell, μ is in the direction of the ambient magnetic field in a dipole magnetic field, and ϕ is in the azimuthal direction. By assuming a wave variation of the form $exp(im\phi - i\omega t)$ where m is the azimuthal mode number and ϕ is the azimuthal phase angle, *Radoski* [1967] derived the linearized wave equations in dipole coordinates as

$$h_\phi^{-2}\Big[\frac{\partial}{\partial\mu}(h_\nu^{-2}\frac{\partial\varepsilon_\nu}{\partial\mu}) + \frac{\partial}{\partial\phi}(\frac{\partial\varepsilon_\nu}{\partial\phi} - \frac{\partial\varepsilon_\phi}{\partial\nu})\Big] + k^2\varepsilon_\nu = 0 \tag{2.46}$$

$$h_\nu^{-2}\Big[\frac{\partial}{\partial\phi}(h_\phi^{-2}\frac{\partial\varepsilon_\phi}{\partial\mu}) + \frac{\partial}{\partial\nu}(\frac{\partial\varepsilon_\nu}{\partial\phi} - \frac{\partial\varepsilon_\phi}{\partial\nu})\Big] + k^2\varepsilon_\phi = 0 \tag{2.47}$$

where dipole scale factors are $h_\phi = \nu^{1/2}r^{3/2}$, $h_\nu = [\nu(1+3\cos^2\theta)]^{-1/2}r^{3/2}$ and $h_\mu = h_\nu h_\phi$. Here, $k = \omega/v_A$ where v_A is the Alfvén speed, and $\varepsilon_\nu = h_\nu E_\nu$, $\varepsilon_\phi = h_\phi E_\phi$. E_ν and E_ϕ are the electric field in the ν-direction and ϕ-direction.The azimuthal variation in the wave perturbation may be expressed as exp(imϕ) where m is know as azimuthal wavenumber.

If the wave is axisymmetric ($m = 0$), equations (2.46) and (2.47) decouple and have two independent solutions, given by equations (2.48) and (2.49) [*Radoski*, 1967]

$$h_\phi^{-2}\frac{\partial}{\partial\mu}\left[h_\nu^{-2}\frac{\partial}{\partial\mu}\varepsilon_\nu\right] + k^2\varepsilon_\nu = 0 \tag{2.48}$$

$$h_\nu^{-2}\{\frac{\partial}{\partial\nu}\left[h_\phi^{-2}\frac{\partial}{\partial\mu}\varepsilon_\phi\right] + \frac{\partial^2\varepsilon_\phi}{\partial\nu^2}\} + k^2\varepsilon_\phi = 0. \tag{2.49}$$

Standing field line oscillations in a dipole field can be described by *guided toroidal modes* and *guided poloidal modes* as suggested by *Dungey* [1954]. Equation (2.48) describes a guided toroidal mode in which the electric field is purely radial and the magnetic field and field line velocity oscillate in the azimuthal direction (see the left side of figure 2.3). Also, the guided toroidal mode can only propagate along the field. Equation (2.49) describes the compressional fast poloidal mode in which the whole magnetospheric cavity pulsates coherently [e.g., *Radoski*, 1967; *Hughes*, 1994]. For the poloidal mode, the electric field is azimuthal while the magnetic field and field line velocity perturbations are radial (see the right side of figure 2.3).

If $m \to \infty$ equation (2.46) and (2.47) can also decouple producing separate toroidal and poloidal equations. In this case the poloidal mode becomes guided along the ambient magnetic field and is given by

$$h_{\nu}^{-2}\frac{\partial}{\partial\mu}\left[h_{\phi}^{-2}\frac{\partial}{\partial\mu}\varepsilon_{\phi}\right]+k^{2}\varepsilon_{\phi}=0. \tag{2.50}$$

This equation describes a poloidal mode standing Alfvén wave ($\omega^2 = k_{||}^2 v_A^2$) but which propagate purely along the field corresponding to a guided poloidal mode (see the right side of Figure 2.3).

Figure 2.3 shows a diagram of the two lowest frequency standing toroidal and poloidal modes. Here we have assumed that the field lines are tied to the ionosphere, i.e., the ionosphere is a perfect conductor. How Alfvén and fast modes may become coupled in a non-uniform plasma was described in section 2.4. In the following section, we describe some of the excitation mechanisms of ULF waves.

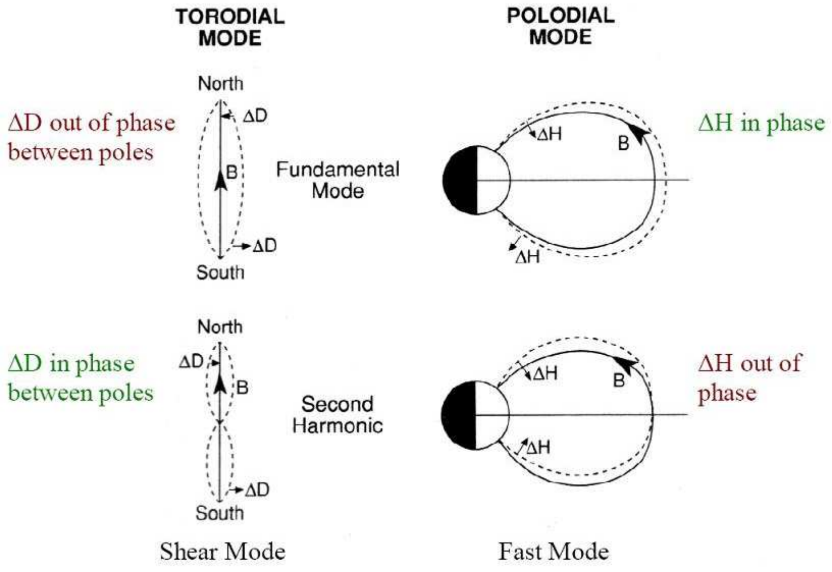

Figure 2.3: The oscillation of a field line in the two lowest frequency field-aligned standing toroidal modes (left) and standing poloidal modes (right). (After *Southwood and Hughes*, 1983).

2.6 External Excitation Mechanisms of Geomagnetic Pulsation

Geomagnetic ULF pulsations can be excited in the magnetosphere either externally by solar wind or internally by energetic particles. Externally excited waves have low azimuthal m values ($m \lesssim 10$). On the other hand, guided poloidal mode wave with high azimuthal number ($m > 10$) can be excited internally by energetic particles. The following subsections discuss how ULF waves are excited by external sources.

2.6.1 The Kelvin-Helmholtz Instability

The most popular proposed driving mechanism for observed field-line resonances has been the Kelvin-Helmholtz instability (KHI) on or near the magnetopause [e.g., *Lee et al.*, 1981]. When two different fluids flow relative to one another the velocity shear at the boundary between the two fluids can give rise the KHI. In space, a KHI may occur at the magnetopause along the flanks of the magnetosphere where the shocked solar wind is flowing fast relative to the stagnant magnetospheric plasma [e.g., *Hasegawa et al.*, 2004]. The amplitude of the KHI surface waves decays evanescently away from the boundary but can penetrate deep into the magnetosphere in the fast mode. Thus these waves may couple to toroidal oscillations in the Pc 3-Pc 5 range and also may excite field line resonances [e.g., *Walker et al.*, 1992]. If the velocity difference between the plasma flows on the two sides of the boundary exceeds a critical speed, v_c, an instability can develop, where (adopted from *Kivelson*, 2005)

$$v_c^2 = \frac{\rho_1 + \rho_2}{\mu_0 \rho_1 \rho_2}((\mathbf{B}_1 \cdot \hat{k})^2 + (\mathbf{B}_2 \cdot \hat{k})^2). \tag{2.51}$$

Here ρ and $\mathbf{B}$ are mass density and the magnetic field, $\hat{k}$ is a unit vector of the wave vector [e.g., *Kivelson*, 2005]. At the magnetopause, this instability condition with $\rho_1 \gg \rho_2$, $|\mathbf{B}_1| \ll |\mathbf{B}_2|$ can be approximated as

$$v_c^2 = \frac{((\mathbf{B}_1 \cdot \hat{k})^2 + (\mathbf{B}_2 \cdot \hat{k})^2)}{\mu_0 \rho_2} \tag{2.52}$$

where, side 1 is the magnetosheath and side 2 is the magnetosphere [e.g., *Kivelson*, 2005]. In equation (2.52), if $\hat{k} \perp \mathbf{B}_2$, the lowest possible critical speed is

$$v_c^2 = \frac{(\mathbf{B}_1 \cdot \hat{k})^2}{\mu_0 \rho_2} \tag{2.53}$$

Hence the instability threshold is determined by the magnetosheath field and magnetospheric density [e.g., *Kivelson*, 2005].

2.6.2 Cavity/Waveguide Modes

While the KHI mechanism explains many of the observed features of field line resonances, it does not account for how the field line resonances may be excited at low-latitudes and the discrete nature of the observed frequency spectra. These features could be explained by cavity mode theory [e.g., *Kivelson and Southwood*, 1985a]. If we approximate the magnetosphere as a spherical cavity then it is obvious that the region between the magnetopause and the plasmapause forms a complex, doughnut-shaped cavity. In the cavity model, fast magnetoacoustic waves can be produced by such as solar wind pressure pulses, substorm commencements, or even sporadic magnetic reconnection. If these waves are reflected from a turning point inside the magnetosphere, and also from the magnetopause, discrete frequency cavity modes may be found. The fast mode waves can also propagate around the magnetosphere in the azimuthal direction. Later modeling suggested that fast mode wave propagation is better described by a waveguide rather than a cavity, whereby the cavity is open downtail in the outer magnetosphere [e.g., *Samson et al.*, 1992; *Wright*, 1994; *Rickard and Wright*, 1994]. Many studies have shown the existence of discrete frequencies (such as 1.3, 1.9, 2.6 and 3.4 mHz) which are believed to correspond to FLRs excited by discrete frequency compressional eigenmodes of the magnetic cavity [*Ruohoniemi et al.*, 1991].

2.6.3 Directly Driven Waves

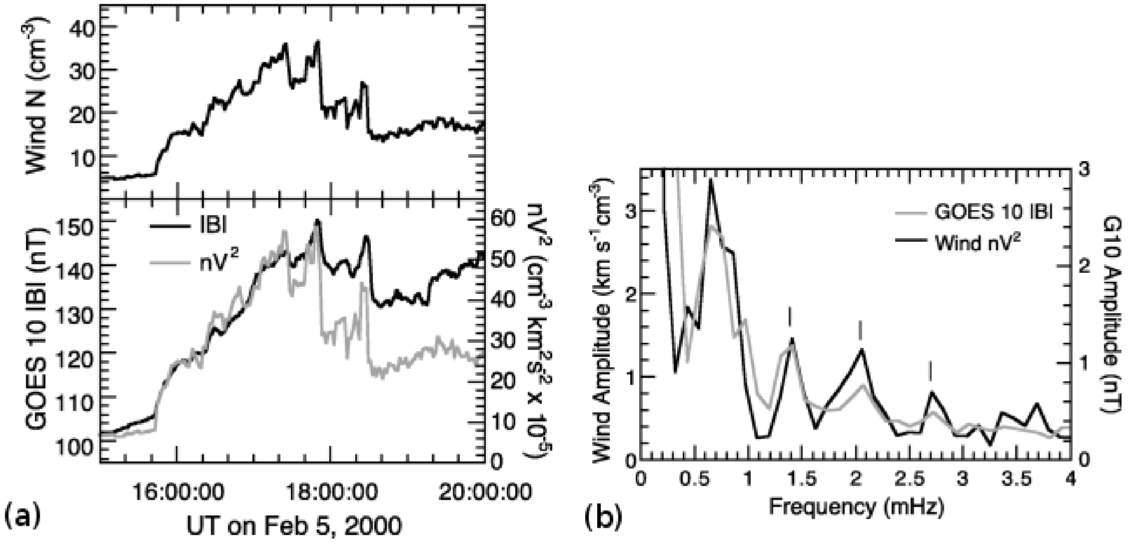

Figure 2.4: (a) Solar wind number density N measured by the Wind spacecraft (upper panel) and GOES-10 Bz measurements (black) and solar wind dynamic pressure, nV^2 (grey) from February 5, 2000. (b) Fourier transforms of the solar wind dynamic pressure (nV^2) and GOES 10 geosynchronous magnetic field perturbations (from *Kepko and Spence* [2002]).

Global cavity/waveguide mode have been offered as a possible source of discrete FLR frequencies (1.3, 1.9, 2.7, and 3.3 mHz) as suggested by *Samson et al.* [1991]. However, on the dayside with $L \leq 10$ and the Alfvén speed ≈ 1000 km/s, the lowest frequency $f(Hz) \approx 2V_A/LR_E \approx 1/3L$ is hard to make as small as $\approx$

1 mHz. Also, the characteristic frequencies do not change with magnetospheric conditions which is not consistent with cavity/waveguide resonant frequencies determined by internal properties such as size of the outer magnetosphere, mass density distribution. Thus, several authors [e.g., *Kepko and Spence*, 2002; *Takahashi and Ukhorskiy*, 2007] suggested that these pulsations might be directly driven by solar wind pressure pulses. During one interval on February 5, 2000 studied by *Kepko and Spence* [2002], the WIND spacecraft was located in the upstream solar wind, and the number density, dynamic pressure (grey) measurement are shown in Figure 2.4 (a). Also, magnetic field magnitude (black) obtained from GOES 10 is shown in the lower panel. Figure 2.4 (b) shows that the Fourier transforms of WIND solar wind dynamic pressure and GOES10 magnetic field measurements have high correlation with similar peaks in frequency. *Kepko and Spence* [2002] suggest that in some cases global ULF waves (multiple, discrete-frequency $\leq$ 3 mHz) can be driven directly by density structures in the solar wind.

2.7 ULF Wave-Particle Interactions

Charged particles experience three periodic motions as described in chapter 1 in section 1.6. While executing a drift motion around the Earth particles can respond to the magnetospheric waves. Energy can be transferred between charged particles and standing poloidal ULF waves (azimuthally propagating waves) in the magnetosphere [see e.g., *Southwood et al.*, 1969; *Kivelson and Southwood*, 1985a]. In section 2.6 we discussed some external excitation mechanisms of geomagnetic pulsations. ULF waves also can be internally generated via interaction with energetic particles. For instance, magnetospheric ULF waves can be generated by a ring current ion drift-bounce resonance. High-m guided polidal Alfvén waves are believed to be generated by unstable energetic particle distribution [see e.g., *Southwood et al.*, 1969]. Conversely radiation belt electrons can be energized by ULF waves [*Elkington et al.*, 1999; *Ozeke and Mann*, 2008].

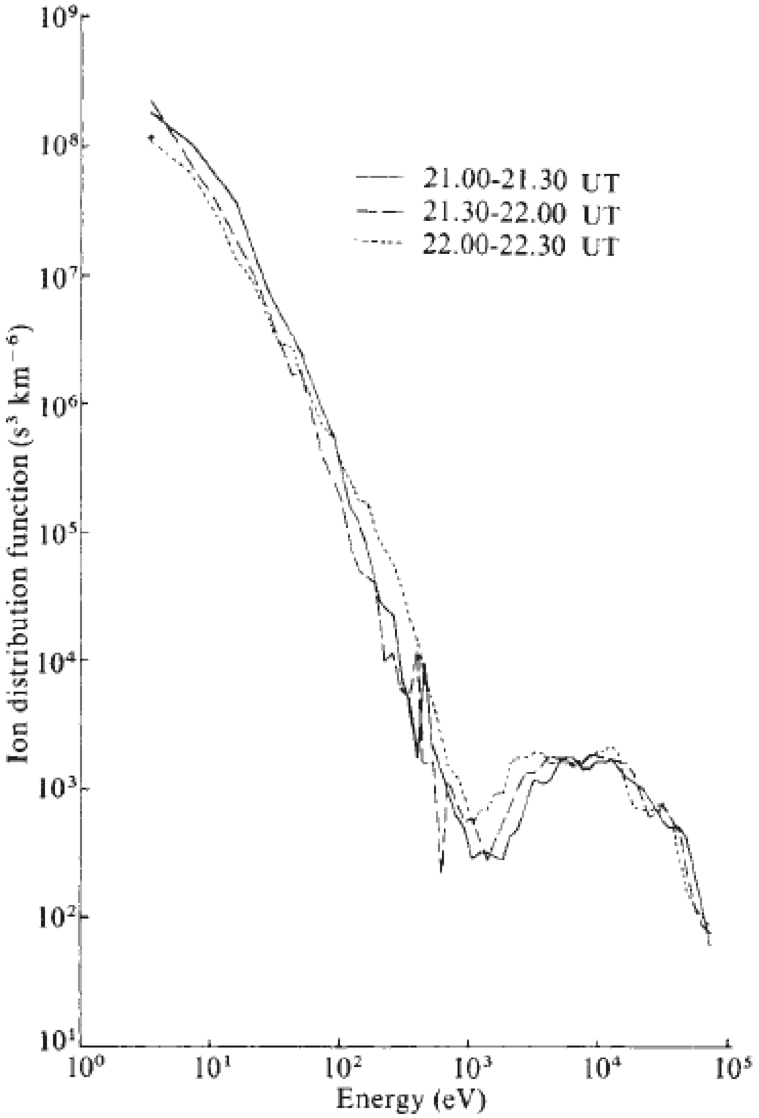

Figure 2.5: Ion distribution functions measured on ATS6 (From *Hughes and Southwood* [1978]).

2.7.1 Drift-Bounce Resonance

(a)

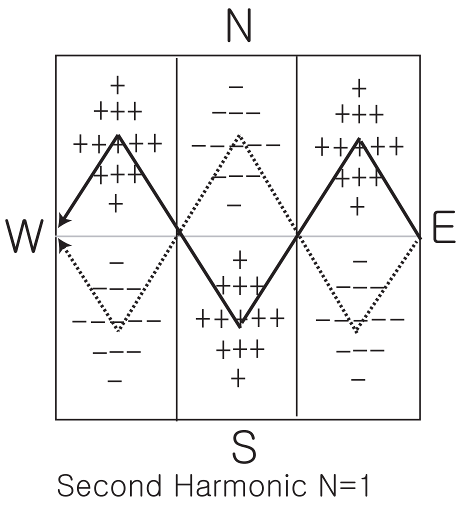

(b)

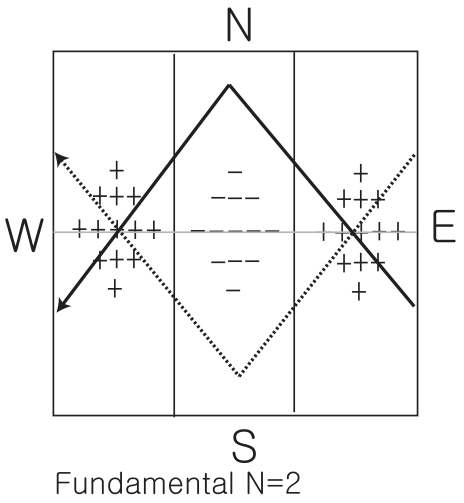

Figure 2.6: Schematic showing the resonant trajectories of protons in the stationary frame of standing guided poloidal Alfvén waves. The electric field intensity corresponds to the density of signs. The positive and negative signs represent eastward and westward directed electric field, respectively. (a) trajectory of resonant particles interacting with poloidal second harmonic mode wave via the N=1 resonance.(b) trajectory of resonant particles interacting with fundamental mode via N=2 resonance.

Drift-Bounce resonance is one of the mechanisms which can explain how energy can be transferred between energetic particles and waves. Drift-bounce resonance is a resonant interaction between the drift-bounce motion of the particles and an azimuthally propagating ULF wave. In the magnetosphere, particles bouncing back and forth between magnetic mirror points drift azimuthally around the Earth. As a particle drifts through the azimuthally propagating waves, it will see the Doppler shifted frequency $(\omega - m\omega_d)$ and drift-bounce resonance will occur if the following condition is satisfied [*Southwood et al.*, 1969]

$$\omega - m\omega_d = N\omega_b \tag{2.54}$$

where ω is the wave frequency, m is an azimuthal wave number, ω_d and ω_b are particle drift and bounce frequencies, and $N = 0, \pm 1, \pm 2, \pm 3, ...$

The particles distribution function, f can be expressed in terms of the particles kinetic energy, W, L-shell and the particles 1st adiabatic invariant, M; $f = f(M, L, W)$. If M is constant then [*Southwood et al.*, 1969]

$$\frac{df}{dW} = \frac{\partial f}{\partial W} + \frac{dL}{dW}\frac{\partial f}{\partial L}. \tag{2.55}$$

If the distribution is stable where $df/dW < 0$ more particles will be accelerated by the wave thus cause the wave amplitude to be damped [see e.g., *Southwood et al.*, 1969; *Chisham*, 1996]. At a points of a positive phase space density gradient, $df/dW > 0$, it is possible for the plasma to become unstable and particle's kinetic energy will be transferred to the wave allowing its amplitude to grow. For example, Figure 2.5 shows an ion distribution as a function of energy showing evidence of a bump-on-tail instability distribution function where $\partial f/\partial W > 0$ which may contribute to wave growth [*Hughes and Southwood*, 1978]. Where

$W \sim 1$keV minimum f exists. In collisionless plasma, diffusion may occur in energy to fill the minimum in the distribution, thus energy being transferred from the fast particles to the waves causing the wave amplitude to grow.

In general the rate of changes, $\dot{W}$, of energy for a particle with a charge, q, moving adiabatically in an electric and magnetic field is given by

$$\dot{W} = q\mathbf{E} \cdot \mathbf{v}_d + \frac{M}{\gamma}\frac{\partial B}{\partial t} \tag{2.56}$$

where $\mathbf{v}_d$ and $\mathbf{E}$ are the drift velocity of particle and the wave electric perturbations, $M_r = p_\perp^2/2m_pB$ and B is the total magnetic field. Here $p_\perp$ is the particle's relativistic momentum $(p_\perp = \gamma m_p V_\perp)$ and γ is the relativistic correction factor $(\gamma = 1/\sqrt{(1 - V^2/c^2)})$ [*Southwood*, 1973].

Figure 2.6 shows schematics of standing guided poloidal Alfvén waves viewed in the wave frame. Electric field intensity is indicated as density of signs and a negative (westward) and positive (eastward) signs represent the azimuthal direction of the wave electric field. In Figure 2.6 (a), particles moving along the solid line interact with a second field-aligned harmonic mode wave via the N=1 resonance. Now we assume that particles are positively charged. The charged particle will be accelerated in the regions marked as minus signs and be decelerated in the regions marked as plus signs. Thus dashed line resonant ion will gain energy and the wave amplitude will damp. On the other hand, an ion moving along the solid line will lose the energy over many bounces and wave amplitude will grow. In Figure 2.6 (b), an ion moving along the solid line interacts with a fundamental mode wave via the N=2 resonance. Ions moving along the solid and dashed line will both lose the energy thus wave amplitude will grow.

2.7.2 Drift-Resonance in a Dipole

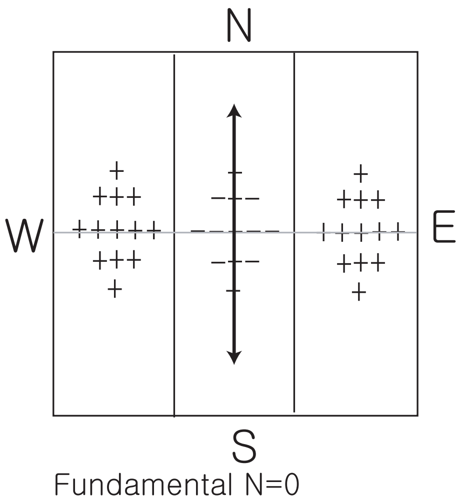

Figure 2.7: Schematic of particles interacting with fundamental mode via N=0 resonance. The field lines are shown as vertical lines extending between the northern (N) and southern (S) ionosphere.

When N=0 in equation (2.54), this leads to the drift-resonant condition in dipole

$$\omega = m\omega_d \tag{2.57}$$

It has been proposed that drift resonance may be responsible for the excitation of fundamental field-aligned guided poloidal mode waves by ring current ions [*Ozeke and Mann*, 2008]. Conversely, radiation belt electrons can be accelerated by the drift resonance with guided poloidal waves. Figure 2.7 represents schematically a drift-resonant interaction of the particles with ULF waves. Since particles azimuthally drift at the same speed as the wave ($\omega_d = \omega/m$), particle trajectories are indicated as vertical lines in the wave frame without azimuthal drift motion. If we assume that the particle is negatively charged, the charged particle will be accelerated in the region marked as minus signs and gain energy.

2.7.3 Drift-Resonance in a Compressed Dipole

As mentioned earlier, drift resonance works only for the guided poloidal waves since particles drift azimuthally. However, we often observe that ULF waves have more power in the toroidal component than the poloidal component. *Elkington et al.* [1999, 2003] suggest that global toroidal-mode waves can accelerate electrons via drift-resonance interaction in the compressed dipole. The resonance condition for drift-resonant acceleration in a compressed dipole is

$$\omega - (m \pm 1)\omega_d = 0 \tag{2.58}$$

where ω_d is the particles azimuthal drift frequency. As an example, m=2 mode wave will experience resonant acceleration where $\omega_d = \omega$ or $\omega_d = \omega/3$.

2.7.4 ULF Wave-particle Flux Modulations

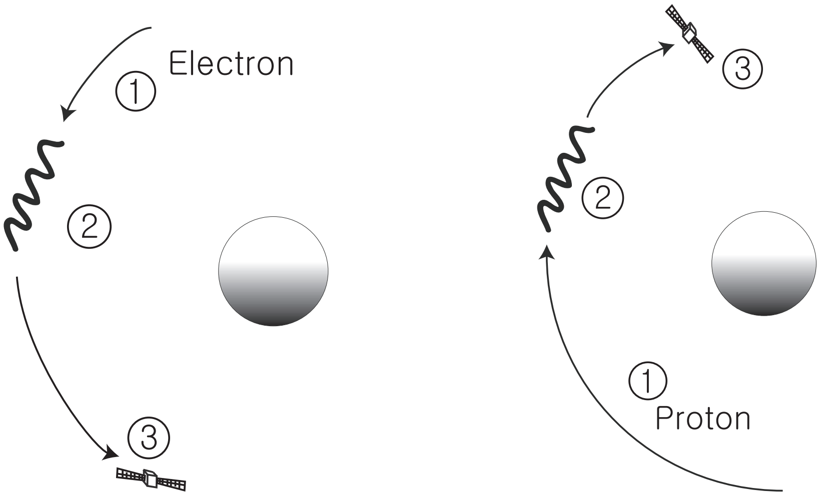

Figure 2.8: Schematic of the relative locations of the wave and a satellite needed to see the flux modulation of electron (left) and proton (right)

Figure 2.8 shows a schematic of the drift path of electrons and protons and the relative location of the waves and an example satellite. Electrons move eastward and protons move westward. Therefore, to observe flux modulation in satellite electron and proton data, the particles must pass through the wave before reaching satellite for flux modulation to be observed.

Resonance

The resonant energy for drift-bounce resonance can be calculated as follows (adapted from [*Hamlin et al.*, 1961; *Ozeke and Mann*, 2001] :

$$\omega - m\omega_d = N\omega_b. \tag{2.59}$$

where ω_d is a bounce-averaged drift frequency and ω_b is the angular bounce frequency of the particle which is given by

$$\omega_b = \frac{\pi V}{2R_E LT(\alpha_{eq})}. \tag{2.60}$$

Here $T(\alpha_{eq}) \simeq 1.30 - 0.56 sin(\alpha_{eq})$ where α_{eq} is the particle's equatorial pitch angle [*Hamlin et al.*, 1961]. The particle's rate of change of azimuthal position ϕ can be described as

$$\omega_d = -\frac{3mV^2LP(\alpha_{eq})\gamma}{qB_sR_E^2} \tag{2.61}$$

where $P(\alpha_{eq}) = 0.35 + 0.15\sin(\alpha_{\mathrm{eq}})$ [*Hamlin et al.*, 1961]. Combining equations (2.59, 2.60, 2.61) gives analytic solution for the resonant drift energies, W_{RES} for high energy radiation belt electrons including the relativistic correction factor as [*Ozeke and Mann*, 2008]

$$W_{RES} \simeq \frac{\omega}{m}\frac{qB_sR_E^2}{6P(\alpha_{eq})L} + [(\frac{\omega}{m}\frac{qB_SR_E^2}{6P(\alpha_{eq})L})^2 + m_p^2c^4]^{\frac{1}{2}} - m_pc^2. \tag{2.62}$$

Advection

The mechanism of observed flux modulations can be described by the phase space distribution function, f, and a general form of distribution function change is given by [*Southwood*, 1973; *Kivelson and Southwood*, 1985b]

$$\delta f = -\frac{Mb_{\|}}{B}\frac{\partial f}{\partial M} - \delta W\frac{\partial f}{\partial W} - \delta L\frac{\partial f}{\partial L}. \tag{2.63}$$

In Equation (2.63) the perturbation in f is a function of first adiabatic invariant M,energy W, and magnetic shell parameter L. The poloidal wave causes a change in the particles energy and L-shell, δW and δL. If M is conserved then the perturbation in f caused by the wave is given by

$$\delta f(M, W, L) = -\delta L\frac{\partial f}{\partial L} - \delta W\frac{\partial f}{\partial W} \tag{2.64}$$

Even if the particle is not in resonance with the wave a change in L or W can result in a change in f, as illustrated by Equation (2.64). In other word, if there is a gradient in density in the direction of wave perturbations and displacement, flux oscillation can result [*Southwood*, 1973; *Southwood and Kivelson*, 1981].

Figure 2.9 shows a schematic illustrating the radial advection of the distribution function (f) by a fundamental field-aligned mode Alfvén wave. The first two figures show field line oscillations in radial direction. The third figure shows the particle distribution as a function of L. Since the density gradient is in the direction of wave perturbation and displacement, the radial advection of particle flux can be observed. For example, if we assume that $\partial f/\partial W = 0$ then the f

will increase as the particles are displaced inward, as illustrated in Figure 2.9 (a). Conversely, f will decrease as the particles are displaced outward, as illustrated in Figure 2.9 (b).

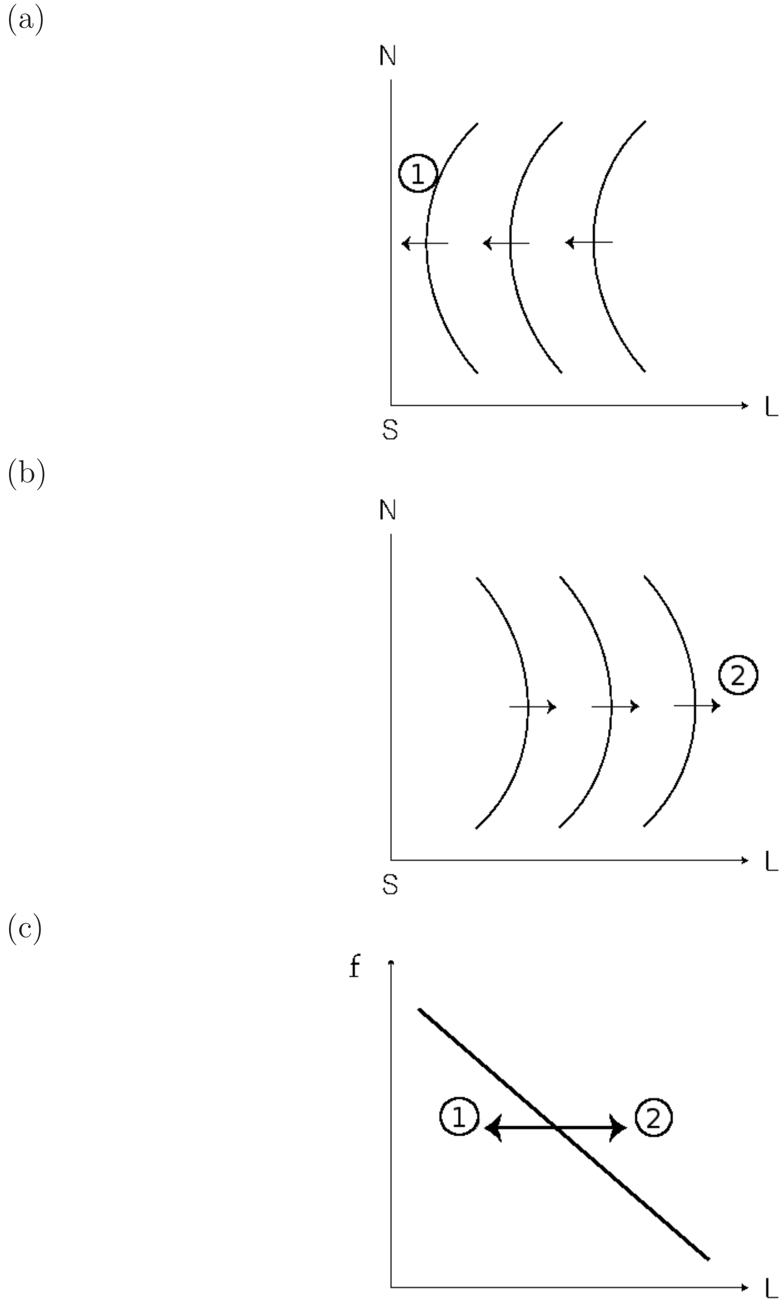

Figure 2.9: Schematic illustrating the radial advection of particle flux **J** by a fundamental mode Alfven wave.

2.8 Ionospheric Influence of ULF waves

Magnetic pulsations observed on the ground are strongly influenced by the ionosphere. The ionosphere alters the polarization of standing Alfvén waves by rotating the horizontal magnetic field signals through 90^o [*Hughes and Southwood*, 1976] and changes their amplitude, by screening small scale (high-m value) waves from the ground. Ionospheric Joule heating also damps the pulsations [*Allan and Knox*, 1979].

2.8.1 Ionospheric Reflection and Transmission of ULF Waves

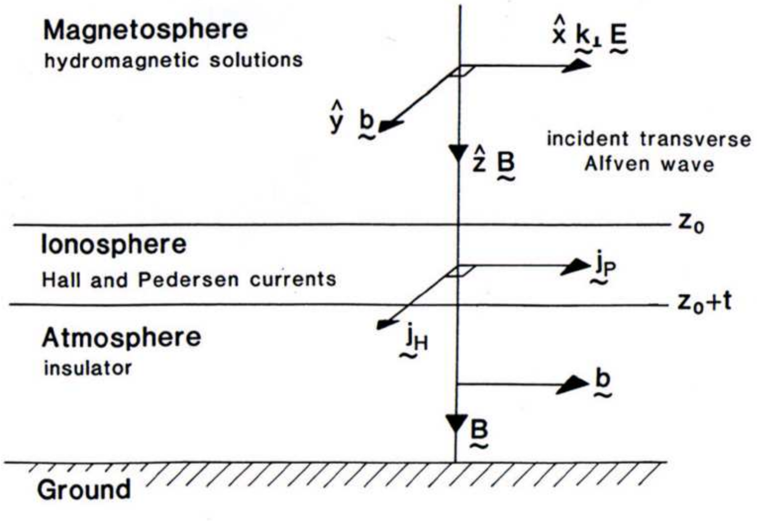

Figure 2.10: A schematic representation of a magnetospheric transverse Alfvén wave incident on a horizontally stratified ionosphere, atmosphere, and ground. (From *Hughes and Southwood*, 1976).

Transverse Alfvén waves undergo a 90° rotation as they are transmitted through a uniform ionosphere. Figure 2.10 illustrates how the polarization of the magnetic signal of a guided Alfvén wave is altered by the ionosphere as the signal is transmitted from the magnetosphere to the ground. As shown in Figure 2.10 four different regions can be identified: the magnetosphere in which the guided Alfvén wave equation holds; a thin sheet ionosphere of vertical thickness t containing the Hall (σ_H) and Pedersen (σ_P) conductivities; the neutral atmosphere which acts as an insulator allowing no field aligned currents to flow from the ionosphere to the ground; and the ground which has an isotropic conductivity.

Now we consider a hydromagnetic wave incident on the ionosphere with a horizontal variation of $exp(ik_\perp x - i\omega t)$. In this model $k_\perp \perp \mathbf{b}$ and $\mathbf{b} \perp \mathbf{B}$, so $k_\perp$ is parallel to x and $\mathbf{b} = b_y \hat{y}$. In the insulating atmosphere no currents can flow, so that

$$j_z = \frac{1}{\mu_0}(\nabla \times \mathbf{b})_z = \frac{i}{\mu_0}\mathbf{k}_\perp \times \mathbf{b}_{horizontal} = 0. \tag{2.65}$$

Accordingly the horizontal magnetic perturbation in the atmosphere must either be zero or parallel to the incident perpendicular wave number $k_\perp$, which is assumed to be in the $\hat{x}$ direction. This means that the ionosphere either acts to screen the incident magnetic perturbation or cause the rotation of magnetic perturbation by 90°. From Ampere's law we can obtain the relation

$$\frac{\partial b_y}{\partial z} = \mu_0 j_x = \mu_0 \sigma_P E_x \tag{2.66}$$

Integrating this equation over the height of the ionosphere (t) gives

$$\delta b_y = \mu_0 E_x \int_{z_0}^{z_0+t} \sigma_P dz = \mu_0 \Sigma_P E_x. \tag{2.67}$$

Here, the change in b_y component (δb_y) across the ionosphere is equal to b_y since equation (2.65) shows that $b_y = 0$ below the ionosphere. Similarly, the wave electric field, E_x, will induce a Hall current causing a magnetic perturbation in the x-direction

$$\delta b_x = \mu_0 \Sigma_H E_x. \tag{2.68}$$

In general, in the ionosphere the height integrated Hall conductivity, Σ_H, has a similar magnitude to the height integrated Pedersen conductivity, hence $\delta b_x \sim \delta b_y$. The magnetic field recorded on the ground is produced by the Hall current flowing in the ionosphere. If Σ_H were negligible, $b_{horizontal}$ would be screened from the ground.

We have mentioned that the magnetic perturbation is rotated through 90°. However *Glassmeier* [1984] shows that the assumption of 90° polarization rotation does not hold in the case of non-uniform ionospheric conductivities. Furthermore, if the incident wave is the fast mode wave, the magnetic signal will propagate through the ionosphere without rotation [*Kivelson and Southwood*, 1988; *Allan and Poulter*, 1992].

2.8.2 Ionospheric Screening and Joule Heating

The magnetic field amplitudes seen on the ground are affected by wave perpendicular scales. Waves with high azimuthal wave number (small azimuthal scale) can be screened from the ground [*Hughes and Southwood*, 1976]. As mentioned earlier, the ground magnetic signature of Alfvén waves occur as a result of the integrated effect of Hall currents flowing in the E-region of the ionosphere (of altitudes $\sim$ 120km). For waves with small perpendicular scales the ionospheric Hall current will change direction many times over a region $<$ 120km so the effects of these current elements cancel, and the ground magnetic signal will have a small amplitude.

The other source of damping of wave amplitudes is Joule heating. Energy is transferred from the magnetosphere to the ionosphere in the form of particle energy or electromagnetic energy [*Kivelson and Russell*, 1995]. In this process, the ionospheric Pedersen current results in waves dissipating energy via ionospheric Joule heating and this is the major loss mechanism for standing Alfvén waves [*Allan and Poulter*, 1992]. The height integrated Joule heating rate Q (Joule heating/unit area) is given by

$$Q = J_p \cdot E = \Sigma_P E^2 \tag{2.69}$$

where $\mathbf{J}_P$ is the Pedersen current density [*Southwood and Hughes*, 1983].

2.9 Pc 5 Pulsations

Pc 5 ULF pulsations (150-600s, 2-7 mHz frequency) are thought to play a role in mass and energy transport and magnetospheric dynamics. Pc 5 waves have attracted significant attention and been studied through theory, simulation, and observations. A number of authors have studied these to understand the global morphology and identify the generation mechanisms. To understand the generation mechanisms of ULF waves, one should consider frequency characteristics, spatial distribution, relation to solar wind parameters and correlation with geomagnetic activity. In this section, some observational studies of Pc 5 pulsations using ground-based magnetometer and satellite data are discussed. The contents of this section are divided into three sections: the poloidal and toroidal Pc 5 modes, Pc 5 pulsation external excitation mechanisms, and Pc 5 pulsations during geomagnetic storm time.

2.9.1 Guided Poloidal and Toroidal Pc 5 Modes

Hudson et al. [2004] describe the results from a statistical study of Pc 5 ULF oscillations, particulary guided toroidal and poloidal modes, using data from the Combined Release and Radiation Effects Satellite (CRRES). Two lowest frequency standing poloidal and toroidal modes are illustrated in Figure 2.3. In poloidal modes, the wave electric field oscillates in the azimuthal direction, while the wave magnetic field oscillates radially. Guided poloidal modes occur during enhanced ring current conditions, believed to be excited by such processes as drift bounce resonance of ring current ions injected into the dusk to noon sector. Typically guided poloidal mode waves are characterized by a narrow band signal in the radial and compressional components. These poloidal mode waves have high azimuthal mode number (m-number).

On the other hand, azimuthally polarized toroidal mode Pc 5 waves are low m number field line resonances [*Hudson et al.*, 2004] where the electric field is radially polarized and the magnetic field and velocity perturbations are azimuthal and each L-shell oscillates azimuthally independent of others. These are mostly excited by external sources such as solar wind dynamic pressure variation and Kelvin-Helmholtz instability (KHI). Externally driven Pc 5 pulsations are most commonly considered to be dominated by field line resonances as they are attributed to a resonant response of the magnetosphere to solar wind forcing at the magnetopause. Field-line resonance theory shows that discrete frequency fast mode waves can resonantly drive discrete frequency field line resonant Alfvén waves on closed field lines at locations where the driving fast mode frequency matches the local field line resonance (FLR) frequency [*Southwood*, 1974; *Chen and Hasegawa*, 1974].

The toroidal oscillations occur on the dawn and dusk sides of the magnetosphere at around L = 6 to 8. This higher occurrence in dawn and dusk of toroidal Pc 5 pulsations can be explained if the field line resonances were driven by magnetopause shear-flow instability. With sufficiently high magnetosheath flow speeds, the magnetopause may become unstable to shear-flow instabilities and similar shear-flow instabilities can amplify waveguide modes through the over-reflection mechanism at the magnetopause [e.g., *Mann et al.*, 1999] and hence drive large-amplitude FLRs. The flow speed would be expected to be much greater on the magnetospheric flanks than at the sub-solar point, and convectively unstable KHI waves would have greater amplitudes further from noon [e.g., *Wright et al.*, 2002]. Consquently, pulsations driven by magnetopause instabilities during intervals of high solar wind speed might occur predominantly on the flanks [*Mann et al.*, 1999; *Mathie and Mann*, 2000a].

Kivelson et al. [1984] provided an answer to the problem of how to generate a discrete frequency FLR driver by proposing magnetospheric cavity modes as a driving mechanism, and further examination of this idea was provided by a number of authors [e.g., *Kivelson and Southwood*, 1985a; *Allan et al.*, 1986; *Lee and Lysak*, 1991]. Later modelling suggested that fast mode wave propagation is better described by a waveguide rather than a cavity, whereby the cavity is open downtail in the outer magnetosphere [e.g., *Harrold and Samson*, 1992; *Wright*, 1994; *Rickard and Wright*, 1994].

For both cavity and waveguide modes, where the period of the cavity eigenmodes matches the fundamental field line eigenperiod a classic discrete frequency field line resonance is produced. Many studies have shown the existence of waves with discrete frequencies (such as 1.3, 1.9, 2.6 and 3.4 mHz) which are believed to correspond to FLRs excited by discrete frequency compressional eigenmodes of the magnetospheric cavity [*Ruohoniemi et al.*, 1991; *Samson et al.*, 1992; *Walker* *et al.*, 1992; *Ziesolleck and McDiarmid*, 1994]. A further statistical analysis during 1997-1998 confirms power enhancements at frequencies 1.1, 1.7, 2.3, 2.8 and 3.7 mHz at low latitudes [*Francia et al.*, 2001].

Ziesolleck and McDiarmid [1995] and *Mathie et al.* [1999a] have discussed how discrete frequency waveguide modes might have frequencies which vary with the dimensions and physical conditions of the magnetospheric cavity. *Mann et al.* [1999] showed that under conditions of sufficiently fast magnetosheath flow speed, discrete frequency magnetospheric waveguide modes can be driven by magnetopause shear-flow instabilities. However, the stability of the frequencies and the dayside condition that would make frequency remains controversial. Recently, some magnetospheric excitation appears to be directly driven by preferred periodic fluctuations in the solar wind dynamic pressure [e.g., *Kepko and Spence*, 2002]. In the following sections, we will review some observational studies of Pc 5 ULF pulsations associated with cavity/waveguide modes and solar wind dynamic pressure.

2.9.2 Pc 5 Pulsations during Geomagnetic Storms

Geomagnetic Pc 5 pulsations are typically observed at auroral zone latitudes [e.g., *Ziesolleck and McDiarmid*, 1994]. However, these waves are also observed at low latitudes during storm time. Global Pc 5 geomagnetic pulsations occurred during March 24, 1991 [*Lee et al.*, 2007] and 29-31 October, 2003 [*Loto'aniu et al.*, 2006] magnetic storms show similar characteristics of large amplitude well-defined Pc 5 pulsations. During these storm times, the Pc 5 pulsations are observed to have amplitudes which peak at lower latitudes than normal in the mid-latitude region and extend across a wide latitudinal and longitudinal range. *Ziesolleck and McDiarmid* [1994] discussed how the properties of geomagnetic pulsations might change due to structural changes of the magnetosphere during strong magnetic storms. Their study suggested that global compressional modes may play an important role in the generation of ULF waves in the low latitude plasmasphere. Some studies have also suggested that global cavity modes coupling to field line resonances (FLRs) may be responsible for magnetic pulsations, even at very low latitudes [e.g., *Lin et al.*, 1991; *Feng et al.*, 1995].

Unusual global monochromatic geomagnetic pulsations are observed during the great storm March 24,1991. *Fujitani et al.* [1993], *Reddy et al.* [1994] and *Schott et al.* [1998] interpreted the pulsations observed on this day in terms of compressional cavity/waveguide modes [cf. *Kivelson and Southwood*, 1986; *Samson et al.*, 1992; *Walker et al.*, 1992]. The global appearance of a wave event with a latitudinally and longitudinally invariant period supports the cavity/waveguide mode hypothesis. A very monochromatic large amplitude Pc 5 pulsation appeared during this storm time. Also, during the storm time from October 28 to November 1, 2000, *Loto'aniu et al.* [2006] observed the Pc 5 pulsations with large amplitude of about 500 - 600 nT on the ground. During this storm time, Pc 5 pulsations appeared unusually during the initial phase of the storm. In a later chapter (Chapter 4), we will show results from case studies of Pc 5 pulsations during geomagnetic storm times and discuss their possible excitation mechanisms in detail.

2.9.3 Summary

Pc 5 pulsations (frequency - 1.7 to 6.7 mHz) can provide information about the processes which couple solar wind energy across the magnetopause and into the inner magnetosphere. Pc 5 pulsations have been studied through theory, simulation, and observations for many years. However, many things still remain a puzzle and are subject of active debate, for example, the generation mechanisms and the source of wave energy. As an external source, KHI on the magnetopause has been proposed as a driving mechanism for field line resonances. Some FLR features however couldn't be explained by the KHI mechanism, which led *Kivelson and Southwood* [1985a] to propose cavity model. Later, *Samson et al.* [1992] suggested that fast mode wave propagation is better described by a waveguide rather than a cavity. Recently, some magnetospheric pulsation excitation appears to be directly driven by preferred periodic fluctuations in the solar wind dynamic pressure [e.g., *Kepko and Spence*, 2002; *Stephenson and Walker*, 2002]. In Chapter 4, we will examine the excitation mechanisms for Pc 5 ULF waves during geomagnetic storms. Since our study is based on observations from ground-based magnetometers and satellites, we will describe briefly the instrumentation and analysis techniques in Chapter 3.

Chapter 3

Instrumentation and Analysis Techniques

3.1 Magnetic Sensors

There are many ways to sense magnetic fields, and most of them are based on the intimate connection between magnetic and electric phenomena. The most commonly used magnetic sensor technologies in space physics are the search-coil magnetometer and fluxgate magnetometer. In this study, we used data from fluxgate magnetometers whose principle of operation is based on the saturation of magnetic materials.

The fluxgate magnetometer consists of a ferromagnetic material wound with two coils, a driver current winding per ring and a single secondary coil used to detect the output. Figure 3.1 shows one such device which is a toroidal-core with the energizing coil wound closely around the core and the sense coil wound around the outside and which does not pass through the central hole at all. When a sinusoidal current is applied to one of the coils, the current magnetizes the core, causing it to reach its saturation magnetization once each half-cycle while a second coil senses the resulting electromagnetic field. Under normal conditions, the sense coil will not detect the field that is generated by the toroid because it will be in balance. However, an additional external magnetic field can cause an imbalance in the toroid's hysteresis which results in a net field that is detected by the sense coil. The sensitivity to the external field is sensitive to the orientation of the sense coil with respect to the field. For minimum power consumption, the core material should have low coercivity and saturation values [*Lenz et al.*, 1990] and the sensitivity range is typically from 10^{-6}G to 100G.

The major advantage of flux-gate magnetometers is their ability to precisely measure DC magnetic fields. In the ground-based fluxgates, three mutually orthogonal sensors are used to collect information about the vector geomagnetic field, usually in the geographic north-south (X) and east-west (Y) directions, and the vertical (Z) direction. The direction and strength of the magnetic field are usually given in one of two ways: three orthogonal components, X, Y and Z or one horizontal component (H) plus two direction angles (D, I). Here declination, D, is the angle between the magnetic field vector projected into the horizontal plane and geographic north and D is positive eastward and inclination, I, is the angle between the field vector and the local horizontal.

3.2 Ground-based Magnetometers

We present brief descriptions of the arrays of ground-based magnetometers (IMAGE, SAMNET, Greenland, CANOPUS/CARISMA, WDC, 210 MM, INTERMAGNET) which we used in this thesis. The locations of each magnetometer are shown in Figure 3.2 and 3.3. See also Appendix A for station location informa-

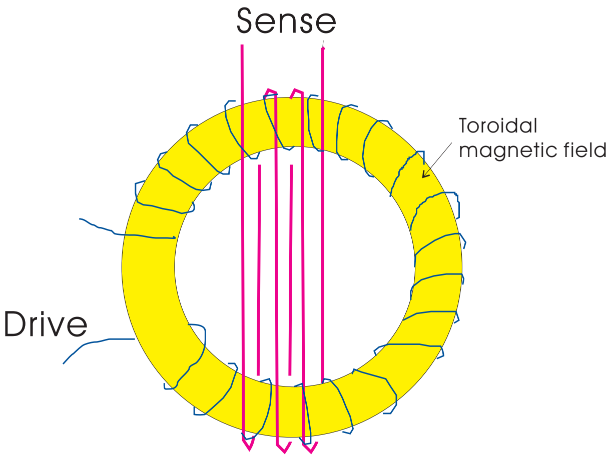

Figure 3.1: Flux-gate magnetometer.

tion. Appendix A contains station information for epoch 1991 (Table A1 and A2) and epoch 2001 (Table A3 and A4) which we used in the event studies in Chapter 4 and Chapter 5. Ground-based magnetometers are relatively inexpensive instruments which can be used to remote-sense the magnetosphere.

The International Monitor for Auroral Geomagnetic Effects (IMAGE) magnetometer network [Viljanen and Hakkinen, 1997] ranges from 55^0 to 75^o in magnetic latitude (L $\sim$ 3.3 to 15.5) and from 90^o to 115^o in magnetic longitude. IMAGE consist of 29 magnetometer stations maintained by 10 institutes from Estonia, Finland, Germany, Norway, Poland, Russia and Sweden. Each magnetometer measures magnetic field strength at a temporal resolution of ten seconds with an accuracy of 1 nT (0.1 nT at permanent stations), and the baselines of the instruments are continually checked for any obvious errors. The data are collected in X, Y, Z geographic coordinates and for the analysis in this thesis are then rotated into a magnetic H, D, Z coordinate system, where H and D point in the local magnetic north-south and east-west directions, respectively, with Z remaining in the direction of the local vertical. Geographic components (X, Y) and Geomagnetic components (H, D) are related by a rotation about the Z-axis

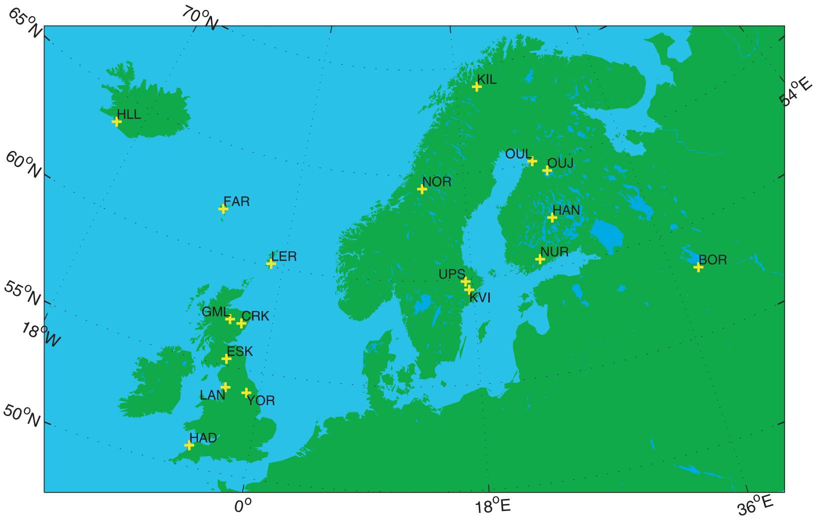

A) SAMNET

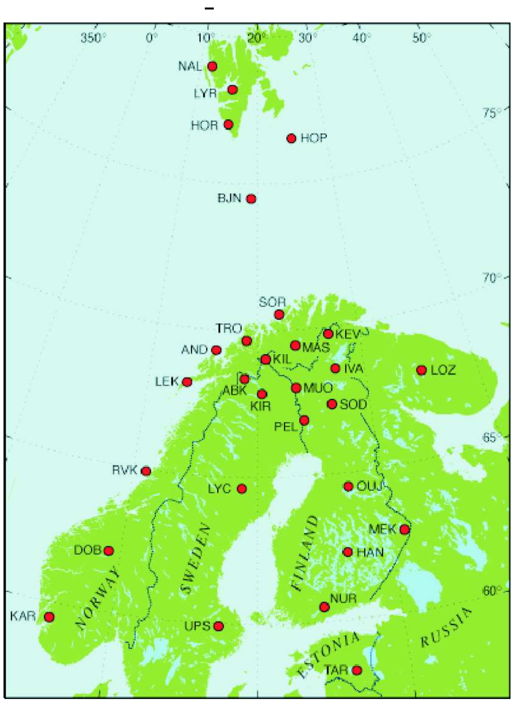

B)IMAGE

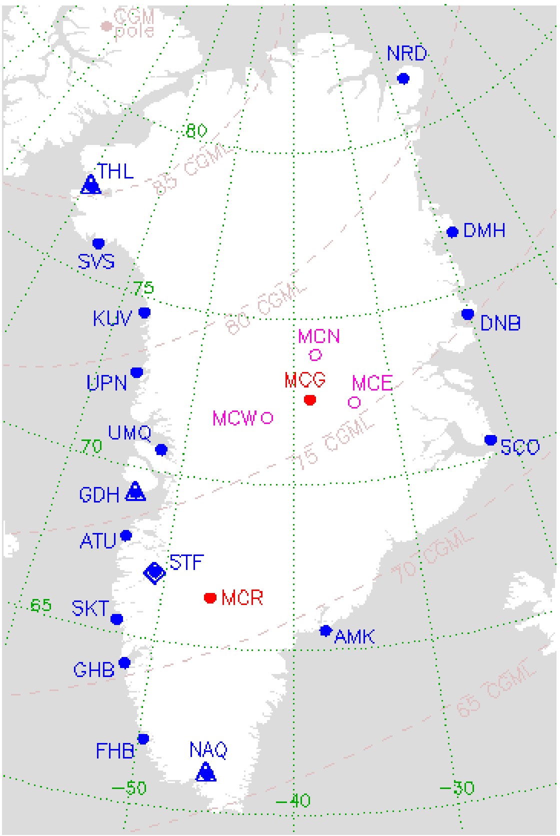

C) GREENLAND

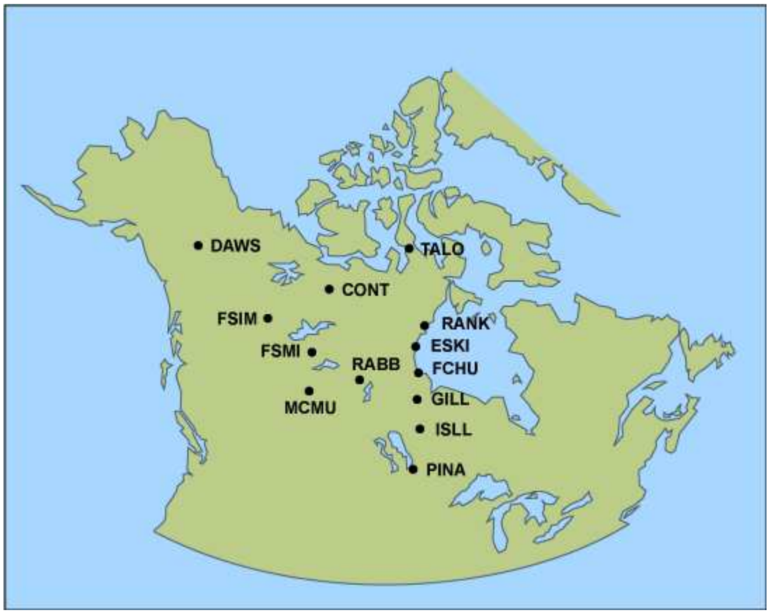

A) CANOPUS/CARISMA

Figure 3.2: SAMNET, IMAGE, GREENLAND, CARISMA magnetometer sites.

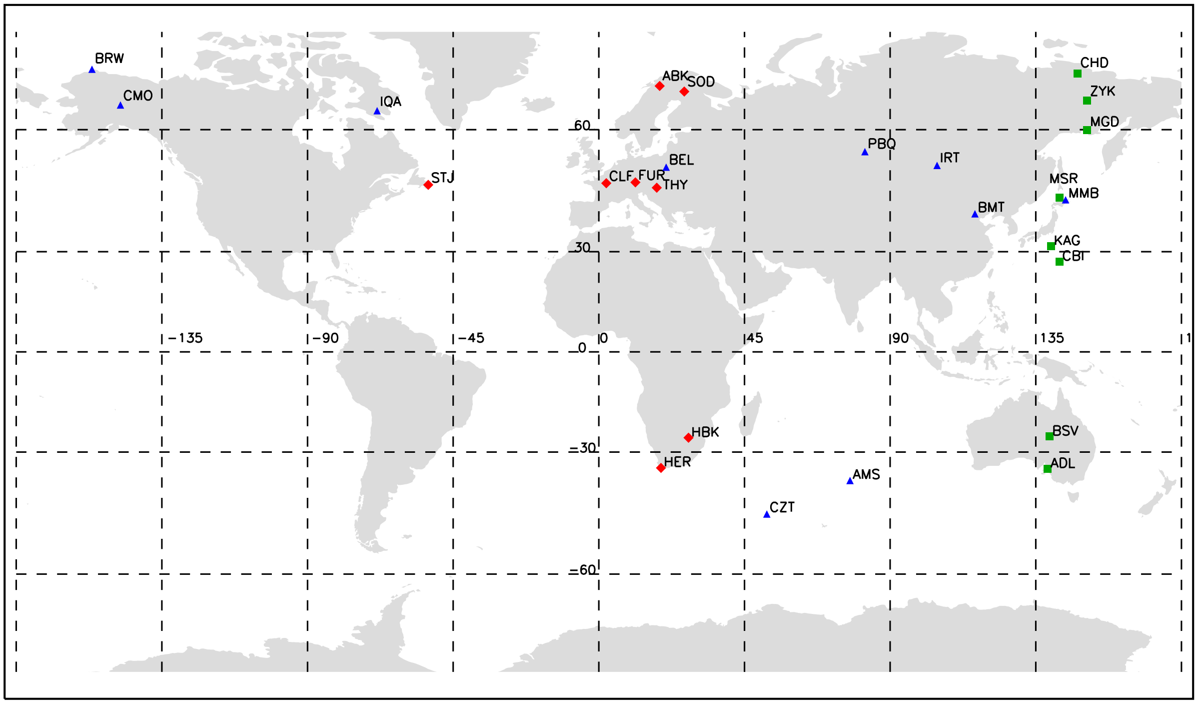

Figure 3.3: WDC (red diamond), 210 MM (green square), INTERMAGNET (blue triangle) ground-based magnetometer stations which we used in this thesis.

such that

$$H = X\cos\theta + \mathrm{Ysin}\theta \tag{3.1}$$

$$D = Y\cos\theta - \mathrm{Xsin}\theta \tag{3.2}$$

where θ is the declination, the angle between geomagnetic north and geographic north.

The Sub-Auroral Magnetometer Network (SAMNET) is one of the UK National Facilities for Solar Terrestrial Physics (STP). Until March 31, 2003, the SAMNET magnetometers were operated by York University and are currently operated by Lancaster University, UK. SAMNET also provides access to data from three magnetometers operated in the UK by the British Geological Survey (`http://www.dcs.lancs.ac.uk/iono/samnet/`). Currently 5 stations are operated equipped with fluxgate magnetometers which continuously record natural variations in the Earth's magnetic field. Also, they archive 1 second resolution data from the 5 IMAGE magnetometers (standard IMAGE resolution is 10s) and also data from the 3 British Geological Survey magnetometers. The magnetometer data contains information about the complex interactions within the coupled Solar Wind-Magnetosphere-Ionosphere system. SAMNET began taking data on the 1st October, 1987. Each station records the magnetic field in three orthogonal components: H, D and Z, these being horizontal magnetic northwards, horizontal magnetic eastwards and vertically downwards.

Danish Meteorological Institute (DMI) has acquired Greenland coastal magnetometer data in digital form since 1981. In 1986 DMI began to gradually modify the acquisition systems in order to record with 20-s sampling rate. Modification was completed by 1991, and since then all stations run at 20-s sampling rate. The rms-noise is approximately 0.1 nT in the 1 mHz - 1 Hz band. During setup the sensor axes are oriented along local magnetic north (H), local magnetic east (E) and vertical down (Z). Sensors at some stations are equipped with a gimbal system which guarantees vertical alignment within a certain tilt angle range of the sensor base.

The ground-based CARISMA (formerly CANOPUS) magnetometer array consists of 13 fluxgate magnetometers sampling at 5s. Data from the expanded 28 site CARISMA Magnetometer Array (CMA) has been upgraded to provide a standard 1s resolution data product, with raw fluxgate sampled data at 8Hz also being stored. Collectively, the expanded CARISMA array provides a unique capability for monitoring the magnetic signatures of geomagnetic activity on a continental scale. The CANOPUS project officially ended on the March 31, 2005 and now it's operating as the CARISMA (Canadian Array for Realtime Investigations of Magnetic Activity ; `http://www.carisma.ca`; [*Mann et al.*, 2008]) array with an upgraded site infrastructure and data transmission system.

World Data Center (WDC) for Geomagnetism, Kyoto (`http://wdc.kugi.kyoto-u.ac.jp/index.html`) provide geomagnetic data as well as indices of geomagnetic activity supplied from a worldwide network of magnetic observatories.

The 210 magnetic meridian (MM) observations are being conducted by Kyushu University and the database and archives are being maintained by STEL, Nagoya University [*Yumoto et al.*, 1992; *Yumoto and 210° MM Magnetic Observation Group*, 1996].

International Real-time Magnetic Observatory Network (INTERMAGNET) (`http://www.intermagnet.org/`) is a global network of observatories, monitoring the Earth's magnetic field. One minute magnetic field values are measured by a vector magnetometer, and an optional scalar magnetometer all with a resolution of 0.1 nT.

3.3 Satellites

Satellites allow us to make direct in-situ measurements of plasma characteristics in the Earth's magnetosphere or solar wind. We present brief description about WIND, ACE, GOES, LANL and SAMPEX satellites which we used in this thesis.

In this study, we used WIND [*Ogilvie et al.*, 1995] and ACE [*McComas et al.*, 1998] for magnetic fields and plasma data in the solar wind. Wind was launched on November 1, 1994 and is the first of NASA's Global Geospace Science (GGS) program. The main purpose of the Wind spacecraft is to measure the incoming solar wind, magnetic fields and particles, although early on it also observed the Earth's foreshock region. Wind, together with Geotail, Polar, SOHO, and Cluster projects, constitute a cooperative scientific satellite project designated the International Solar Terrestrial Physics (ISTP) program which aims at gaining improved understanding of the physics of solar terrestrial relations.

The Advanced Composition Explorer (ACE) orbits the L1 libration point at a distance of 1.5 million km from Earth and 148.5 million km from the Sun. ACE has a prime view of the solar wind, interplanetary magnetic field and higher energy particles. The ACE magnetometer (MAG) instrument [*Smith et al.*, 1998] consists of twin triaxial fluxgate magnetometers. The Solar Wind Electron, Proton, and Alpha Monitor (SWEPAM) [*McComas et al.*, 1998] instrument sensors measure solar wind electrons at 1.6 eV-1.35 keV energy and ions at 0.26-35 keV.

For our study of ULF waves, we used Geostationary Operational Environmental Satellites (GOES) magnetic field data. GOES circle the Earth in a geosynchronous orbit over the equator. The GOES satellites carry onboard a Space Environment Monitor subsystem that measures X-rays, Energetic Particles and the Magnetic Field at the spacecraft. Three orthogonal flux-gate magnetometer element, (spinning twin fluxgate magnetometer prior to GOES-8) provide magnetic field measurements in three mutually perpendicular components: Hp, He and Hn. Hp is perpendicular to the satellite's orbital plane. He lies parallel to the satellite-Earth center line and points earthward. Hn is perpendicular to both Hp and He, and points westward for GOES-4 and earlier satellites, and eastward for later spacecraft.

For study of radiation belt particle dynamics, we used Los Alamos National Laboratory (LANL) satellites and the Solar Anomalous and Magnetospheric Particle Explorer (SAMPEX). The satellites which carry the Los Alamos energetic particle instruments are named by their international satellite designator numbers (ISDN). These satellites are in geosynchronous orbit which has a nominal altitude of 6.7 Re (around 42,000 km), geographic latitude of 0 degrees, and a fixed (but arbitrary) longitude. The actual latitude, longitude, and altitude can vary somewhat. The spin period is about 10.24 seconds. The spin axis is actively controlled to point toward the center of the Earth. The CPA detector measures electrons in two sets of channels, LoE and HiE which range from 30 keV to 2 MeV. It also measures positive ions (nominally protons) in two sets of energy channels LoP and HiP which range from approximately 75 keV to approximately 200 MeV. The nominal energy channels for electrons are the same for all CPA instruments. However, the nominal proton energy channels are different for each satellite. The SOPA detector measures electrons from 50 keV to greater than 1.5 MeV, ions from 50 keV to 50 MeV, and heavier ions in various channels with energies in the MeV range [*Belian et al.*, 1992]. The nominal energy levels for electrons, protons, and heavy ions are the same for all satellites carrying the SOPA detectors.

SAMPEX Proton/Electron Telescope (PET) instrument [*Baker et al.*, 1993] measures both trapped and precipitating energetic particles in different parts of the low Earth orbit of SAMPEX. The PET detector responds to electrons $>$ 400keV and protons $>\sim$ 2MeV from 5 July 1992.

3.4 Fast Fourier Transforms

The waveforms of magnetic field components observed during each event were subjected to an FFT analysis in order to identify Pc5 pulsations. Here, we describe details of the FFT analysis and windowing scheme which have been used in this study. The Fast Fourier Transform (FFT) is an algorithm for efficiently calculating the Discrete Fourier Transform (DFT). In the Fourier Transform, the total time for computation of the transform is proportional to N^2 for N-point samples. However, it is possible to optimize the algorithm down to NlogN which for a large N makes a huge difference. This optimized algorithm is called the Fast Fourier Transform. We usually use the Fourier transform in the analysis of data from the time domain to the frequency domain, and vice versa. A periodic signal can be decomposed into the sum of properly chosen cosine and sine waves, such that

$$H(f) = \int_{-\infty}^{\infty} h(t) exp(-i2\pi f t) dt \tag{3.3}$$

$$h(t) = \int_{-\infty}^{\infty} H(f) exp(i2\pi f t) df \tag{3.4}$$

The best result is when we integrate from negative infinite to positive infinite limits. However, in nature, we can get only finite time and discrete data. The following is the approximation of the integral by discrete sum:

$$H(k) = \sum_{n=0}^{N-1} h(n) exp(-2\pi i k n/N) \tag{3.5}$$

$$h(n) = \frac{1}{N} \sum_{n=0}^{N-1} H(k) exp(2\pi i k n/N) \tag{3.6}$$

Here, H(k) is the DFT frequency output at the kth spectral point, where k ranges from 0 to N-1. The output of DFT is a complex number. The following is DFT output, magnitude and phase, and Power:

$$H(k) = Re[H(k)] + iIm[H(k)] \tag{3.7}$$

$$|H(k)| = \sqrt{Re[H(k)]^2 + Im[H(k)]^2} \tag{3.8}$$

$$\phi = tan^{-1}\frac{Im[H(k)]}{Re[H(k)]} \tag{3.9}$$

$$P(k) = 2|H(k)|^2 \tag{3.10}$$

Power spectral density (PSD) is similar to power in that it quantifies the frequency content of a real value signal. In this thesis, we used time-integral squared amplitude and it is defined by

$$PSD_k = \frac{P(k)}{\Delta f} \tag{3.11}$$

[*Press et al.*, 1992].

Understanding the properties of discrete FFT analysis will help us to improve the results of our signal analysis. We state some properties of such discrete FFT analysis below.

3.4.1 Effects of Discrete Signal

- Sampling Theorem

When we analyze ULF waves, we sample discrete data at regular intervals in time. This interval is called the sampling interval ($\triangle t = t_{smpl}$) and the sampling frequency is $f_{smpl} = \frac{1}{t_{smpl}}$. In discrete sampling, the signal should be within the limited bandwidth. A half of the sampling frequency is the highest frequency which can be resolved, and this is called the Nyquist: $fc = f_{smpl}/2$. Thus there is no information above this frequency. If frequencies are bigger than Nyquist frequency, then an aliasing effect will occur. To increase the frequency resolution without changing the sampling rate can be done by increasing N by acquiring more data ($f_k = k/Nt_{smpl}$).

- Aliasing

Aliasing is connected with the sampling rate. Aliasing can cause a misinterpretation of power in a given frequency, for example, power at a frequency which is bigger than Nyquist frequency can be transposed down inside of the bandwidth below the Nyquist frequency. As a result, power at a higher frequency than Nyquist frequency can came into the bandwidth and interpreted as additional power at a lower frequency.

3.4.2 Effects of Finite Time Sampling

- Spectral Resolution

Finite observation time limits spectral resolution. Spectral resolution is defined as a inverse function of total observation time ($f_k = 1/T$: T is the total observation time). Thus, the longer observation time, the better spectral resolution.

- Spectral Leakage

FFT assumes that the signal is periodic in the time domain, however we can only measure signals for a finite time and with discretely sampled data. This truncation process and discretization causes leakage and it can change the calculated amplitude and position of a spectral estimate. In fact, leakage is not a universal problem. When the signal has an integer period, leakage will not happen. However, it's difficult to obtain exactly an integer number of cycles in a sampling window, thus leakage is inevitable.

Window	Best for these signal types	Frequency resolution	Spectral leakage	Amplitude accuracy
Rectangular	Transient and Synchronous	Best	Poor	Poor
Hanning	Random	Good	Good	Fair
Barlett	Random	Good	Fair	Fair
Hamming	Random	Good	Fair	Fair
Blackman	Random or mixed	Poor	Best	Good

Table 3.1: Some common windows and their features (from application note of the LDS Test and Measurement LLC).

To reduce the effect of leakage, we should remove the jump discontinuites by making the data begin and end at the same level. Windows which are frequency weighting functions applied to the time domain data can reduce discontinuities at the window edges. Many kinds of windows has been developed to make better results. Some features of these windows are shown in Table 3.1.

Some windows are more effective for specific types of signal. To get the best result, we should understand the effects of leakage and know the advantage or disadvantage of each windowing function and choose the most appropriate window. Among these windows, the Hanning window is the most commonly used window function for random signals because it provides good frequency resolution and spectral leakage and fair amplitude accuracy. In our study, we used a Hanning window ($W(n) = 0.5 - 0.5[\cos(2\pi \mathrm{n}/(\mathrm{NP}-1))], 0 \leq \mathrm{n} < \mathrm{NP}$).

3.5 Complex Demodulation

In ULF wave studies spectral analysis techniques based on the Fast Fourier Transform are widely used. As we mentioned previously, these techniques must be applied with caution to data sets as they assume the time-series analyzed is stationary. In time-series analysis, a stationary series has statistical properties which do not depend on time t, for example, a constant mean, variance, and autocorrelation through time. However, geomagnetic data is generally non-stationary.

Bingham et al. [1967] suggested that complex demodulation might be useful in the study of a non-stationary time series. Complex demodulation allows instantaneous values of ULF wave amplitude, phase and polarization to be examined for a particular frequency band, while also providing an accurate estimate of the central period. The mathematical description of complex demodulation involves two stages. To compute the demodulates the most efficient way is by the use of an FFT. For a given time series ($x(t)$), the first operation is to shift the frequency band of interest to zero frequency by multiplying by the complex function $\exp(-i\omega' t)$, where ω' is the central frequency of the shifted band.

$$X(\omega', t) = x(t)exp(-i\omega' t) \tag{3.12}$$

Then the new frequency shifted series is low-pass filtered using a set of weights a_k (k= -m,...,m).

$$X_d(\omega', t) = \sum_{k=-m}^{m} a_k X(\omega', t) \tag{3.13}$$

If we consider time series with period ω_0 and phase shift ϕ given by

$$x(t) = Acos(\omega_0 t) \tag{3.14}$$

multiplying this time series by complex function $exp(-i\omega' t)$ where $\omega' = \omega_0 + \delta\omega$

then the frequency shifted time series is given by

$$X_d(\omega', t) = \frac{A}{2}[exp \ -i(\delta\omega t - \phi) + exp \ i((2\omega_0 + \delta\omega)t + \phi)] \tag{3.15}$$

If we use low pass filter to remove high frequency and set central frequency of the band-pass filter such that $\omega' = \omega_0$ then we may write

$$X_d(\omega', t) = (A/2)exp(i\phi) \tag{3.16}$$

This gives the instantaneous values, at time t, of the wave amplitude and phase in the frequency band centered on ω_0. The size of the filter defines the new Nyquist frequency and is chosen so that there is no aliasing. For more discussions of complex demodulation and its use in analyzing geomagnetic time series, see *Banks* [1975] or *Myers and Orr* [1995]. CXD allows the accurate determination of the central period of the event and the temporal characteristics of the wave in ULF wave analysis and we used CXD for ULF wave analysis in this thesis.

Chapter 4

Pc 5 geomagnetic pulsations during geomagnetic storm main phase

4.1 Introduction

It has been studied for many years to identify the excitation source mechanisms of Pc 5 ULF waves. There are several Pc5 pulsation excitation mechanisms which have been suggested such as FLRs (field line resonances) excited by magnetopause Kelvin-Helmholtz instability (KHI), or through the excitation of cavity/waveguide modes, or directly driven by solar wind pressure pulses [e.g., *Sibeck*, 1989] (see section 2.9 for a more extensive discussion).

To understand the generation mechanisms of ULF waves, we should consider their frequency characteristics, spatial distribution, relationship to solar wind parameters and their correlation with geomagnetic activity. In this chapter, we present observational studies of Pc5 pulsations using ground-based magnetome-

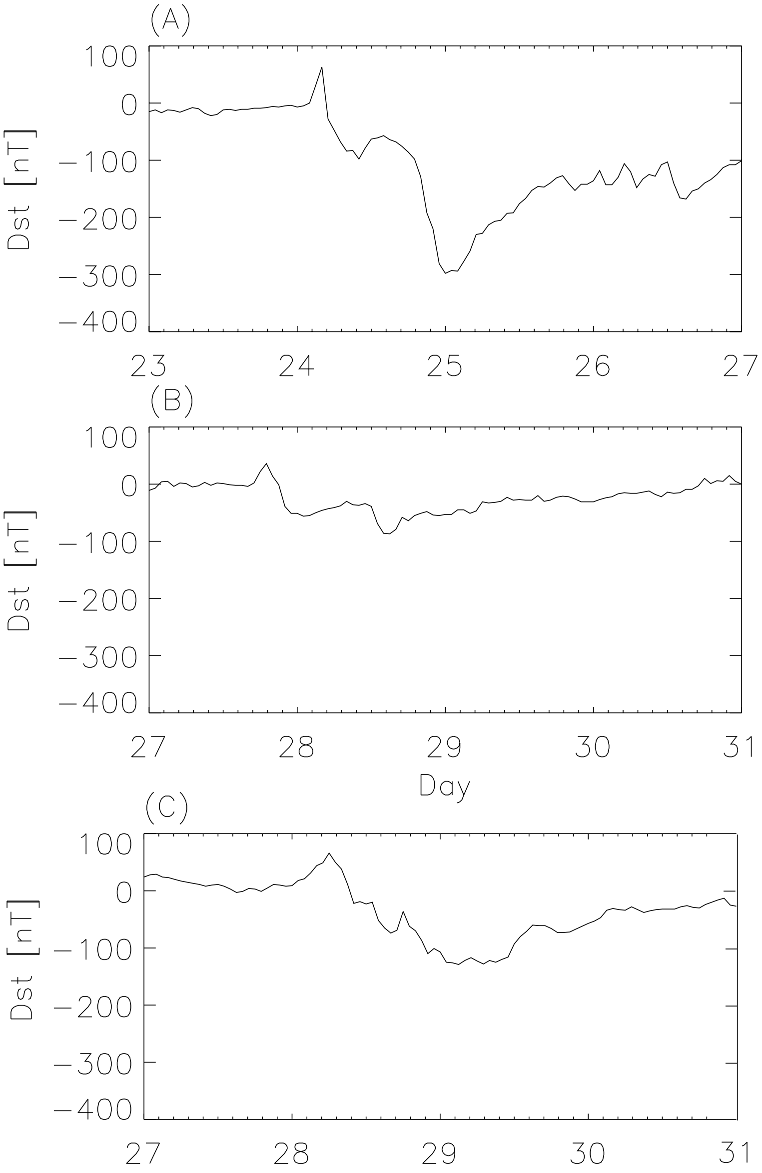

Figure 4.1: Dst indices (A) March 23 - 27, 1991, (B) March 27 - 31, 2001, and (C) July 27 - 31, 1990.

ter and satellite data. Especially, we focus on the Pc5 ULF waves excited during geomagnetic storm times. We present case studies and specifically selected three storm time events which show a brief increase in Dst in the main phase of storms. Each event has a Dst increase in the preliminary phase due to solar wind compression, and then a Dst reduction in the main phase. Figure 4.1 shows the Dst index during these selected storm times, (A) March 23 - 27, 1991, (B) March 27 - 31, 2001, (C) July 27 - 31, 1990. We studied Pc 5 pulsations observed during this three selected storm times.

In section 4.2, we study the March 24, 1991 event which showed global Pc5 pulsations in the main phase of this storm at unusually low-L. We examine the large amplitude Pc5 pulsations which were observed across a wide latitudinal and longitudinal extent. We also discuss the mechanisms by which wave energy might be excited and coupled into FLRs and examine how this might be related to the observed dawn/dusk asymmetry in Pc5 pulsation occurrence.

In section 4.3, we study Pc 5 pulsations observed from March 27 to 29, 2001. During this storm time interval, we observed high-speed solar wind, high solar wind proton density, and high solar wind dynamic pressure. We invest the relationship between the Pc 5 ULF waves and solar wind parameters.

In section 4.4, we study the July 28, 1990 storm event which shows local pulsations near noon due to periodic changes of solar wind dynamic pressure. Geosynchronous satellite magnetopause crossings and solar wind dynamic pressure pulses are often observed in the dayside magnetosphere. If the external dynamic pressure changes periodically, it is possible for magnetospheric field line oscillations to be excited by the periodic magnetopause motions. By studying these three events, we attempt to identify the energy source and the excitation mechanisms responsible for the magnetospheric pulsations.

4.2 Global Pc 5 Pulsations Observed at Unusually low-L During the Great Magnetic Storm of March 24, 1991 [1]

4.2.1 Introduction

In this subsection we examine the characteristics of discrete frequency Pc5 waves using global coverage from arrays of ground-based magnetometers during the onset day of the great geomagnetic storm of 24th March, 1991. A number of discrete spectral peaks are observed, each being observed to couple to a FLR. We observed multiple discrete spectral peaks, with a dominant peak at 2.8 mHz in the 0815-0915 UT interval, a peak at 1.9 mHz in the 1010-1110 UT interval, and a very monochromatic wave of 1.7 mHz frequency in the 1200-1340 UT interval. On this day, long period (periods $\sim$ 10 minutes, frequency $\sim$ 1.67 mHz) geomagnetic pulsations at 1200-1400 UT were reported previously by *Fujitani et al.* [1993], *Reddy et al.* [1994] and *Trivedi et al.* [1997]. Also more broad-band Pc5 pulsations (2.5-3.2 mHz) occurring in the 0600-1000 UT time interval, in the initial phase of the magnetic storm, were reported by *Schott et al.* [1998]. These authors interpreted their observations in terms of a cavity mode resonance in the inner magnetosphere, however, neither the local-time and latitudinal characteristics nor a comparison to field line resonance theory were completed.

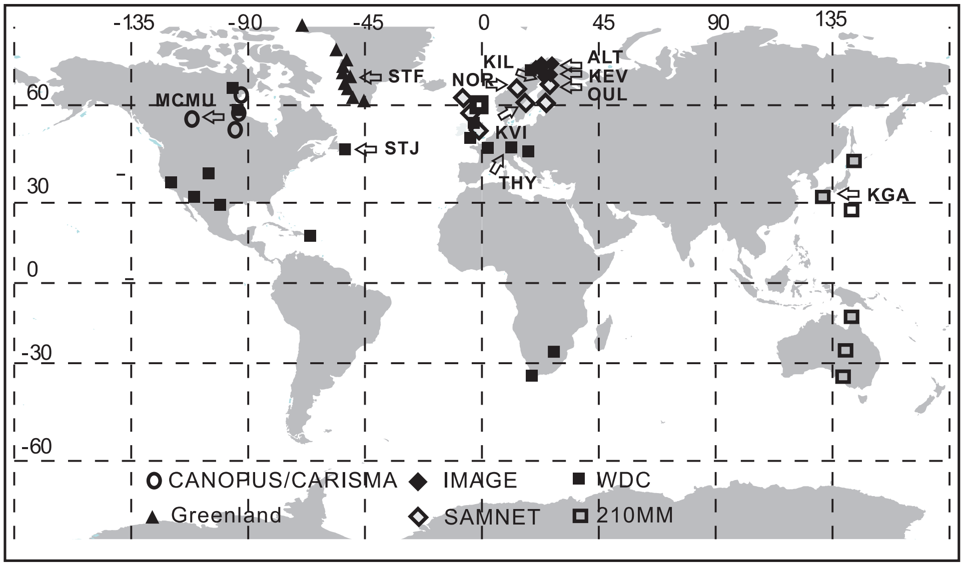

Figure 4.2: Magnetometer array station locations used in the study. Stations directed by arrows were used in the stack plots in Figures 4.3 - 4.4 and additional stations were used in Figure 4.8.

4.2.2 Data and Observations

We analyzed ground-based magnetometer array data for the onset day of the great geomagnetic storm of 24th March 1991. Our investigation is based on data from a wide range of magnetometer arrays around the world. Figure 4.2 shows the magnetometer array station locations used in this study. Time-series magnetograms from the CANOPUS/CARISMA magnetometer array, the Greenland coastal chain, SAMNET, IMAGE, the 210 MM chain in the western Pacific, and WDC were surveyed for this study (see Section 3.2). Together the stations cover between latitudes from about -46° to 86° and longitudes from about 30° to 330° in Corrected Geomagnetic Coordinates (CGM). The CGM coordinates (latitudes, longitudes) and L-values of the stations used in this study are given in Table A.1 and A.2 of Appendix A. A great geomagnetic sudden storm commencement

---

[1] This section is based on E. A. Lee et al.,Global Pc 5 pulsations observed at unusually low L during the great magnetic storm of 24 March 1991, J. Geophys., volume 122, 2007, doi:10.1029/2006JA011872.

(SSC) occurred around 0341 UT almost simultaneously at each station [*Araki et al.*, 1997] and led to the development of a great geomagnetic storm.

4.2.3 Global Pulsation Characteristics

Geomagnetic pulsations and wave power enhancements in the Pc 5 range were observed simultaneously in all stations as is clearly shown for selected stations in Figure 4.3. From the top, the panels in Figure 4.3 show time-series for the H-component (magnetic north-south) for the stations STF (Greenland chain), ALT, KIL (IMAGE), MCMU (CANOPUS), MUO (IMAGE), OUL, NOR, KVI (SAMNET), STJ, THY (WDC), and KAG (210 MM). These stacked magnetograms, from different longitudes, are plotted in order of decreasing latitude. Despite the existence of pulsations throughout the day we analyzed three intervals with clear pulsation wavepackets (see Figure 4.4). Here we chose 0815-0915 UT, 1010-1110 UT and 1200-1340 UT (hereafter referred to as events A, B, and C, respectively) to see the characteristics of waves in these wavepackets; each interval satisfies the criteria that the wave appears simultaneously in most of the stations and has at least one common spectral peak.

Waves during event A correspond to near local postmidnight (0009-0246 MLT) at CANOPUS, local morning (0526-0712 MLT) at Greenland stations, local prenoon (0904-1210 MLT) at SAMNET stations, local noon (1103-1224 MLT) at IMAGE stations, and dusk (1639-1854 MLT) at the 210 MM chain. Waves during event C correspond to near local morning (0354-0711 MLT) at CANOPUS, local prenoon (0911-1137 MLT) at Greenland stations, local postnoon (1249-1635 MLT) at SAMNET stations, local postnoon (1448-1649 MLT) at IMAGE stations, and nightside (2024-2319 MLT) at 210 MM chain. Event B lies between these two extrema in local time. For signal analysis, we used a Fast

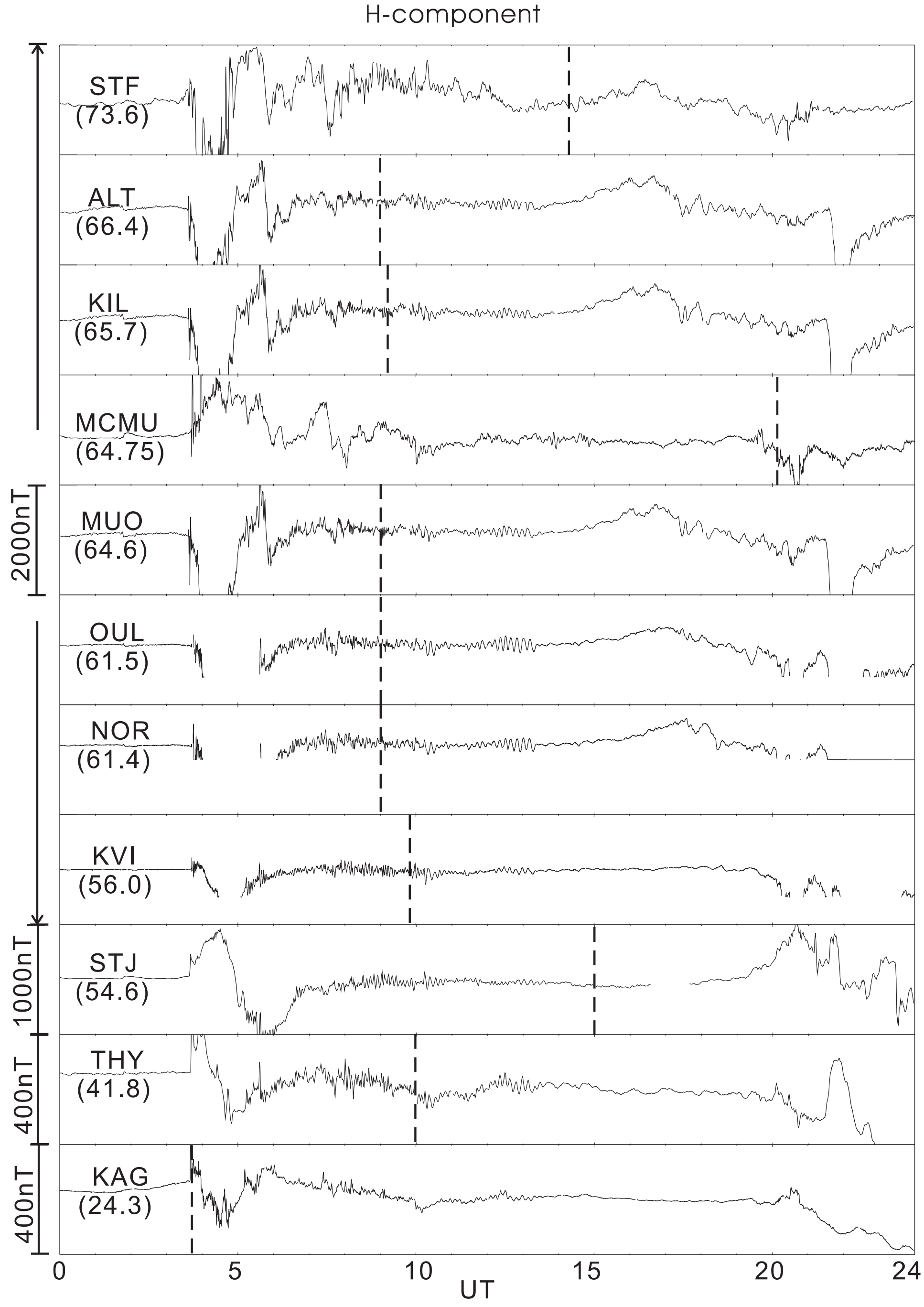

Figure 4.3: Unfiltered H-component magnetograms on March 24, 1991. The vertical dotted lines indicate local noon at each station, the number in brackets is the station CGM latitude and the nT scale for each panel is indicated in the annotation on the left. (For example, the top panel shows the H-component at STF (CGM 73.6°) station with the y-axis spanning 2000 nT in this panel.)

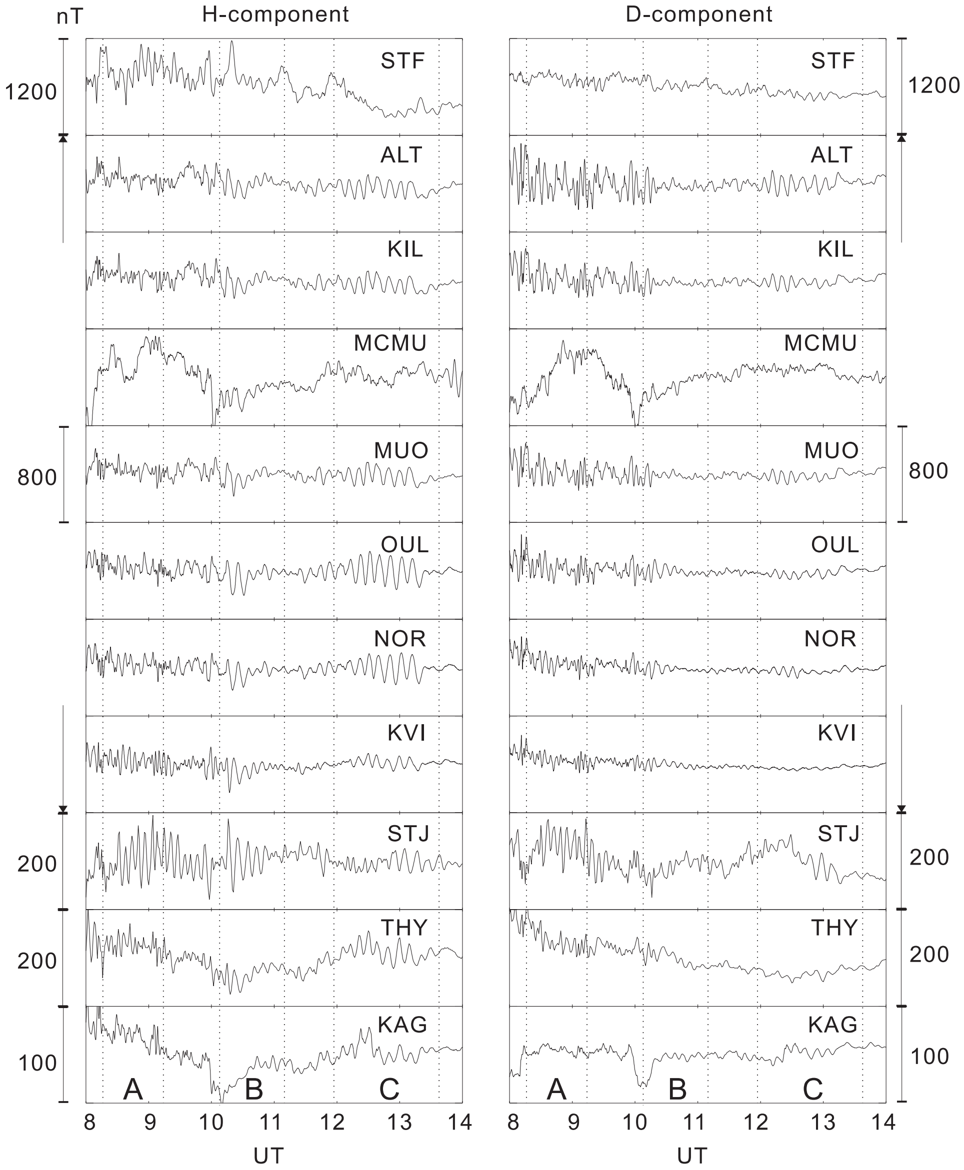

Figure 4.4: Unfiltered magnetograms for selected stations for the interval of 0800-1400UT on March 24, 1991. Magnetograms are plotted in order of decreasing latitude for the selected stations highlighted by arrows in Figure 4.2. Here we chose three wave packets (*A*) 0815-0915 UT, (*B*) 1010-1110 UT , and (*C*) 1200-1340 UT to analyze the wave characteristics in detail.

Fourier Transform (FFT) with a Hanning window. The background magnetic field is removed using a 1 mHz cut-off high-pass filter.

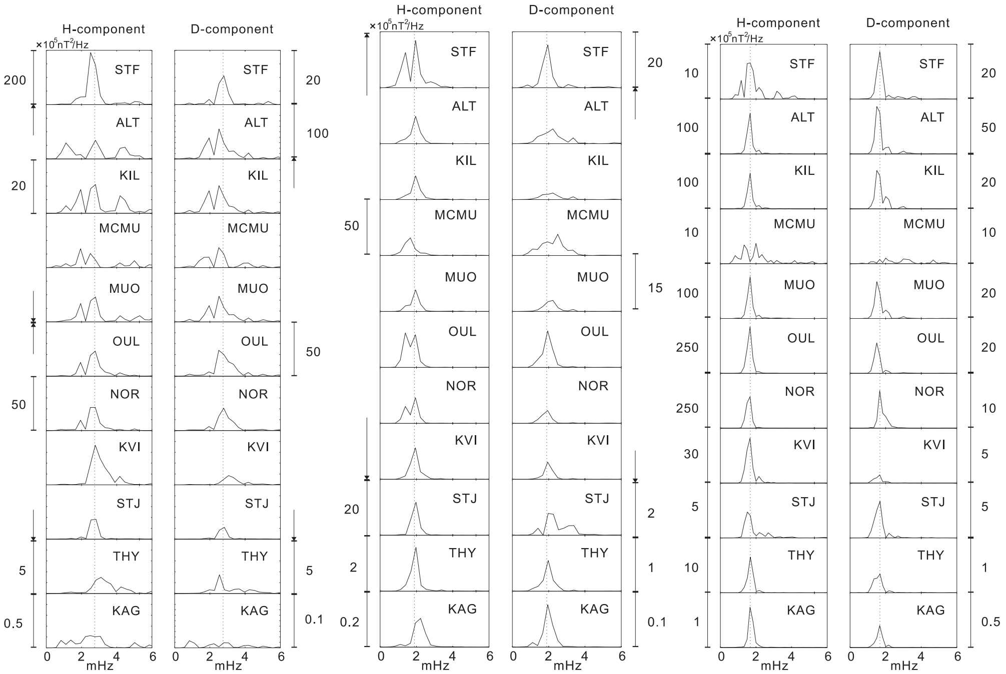

Figure 4.5: H- (left) and D-component (right) spectra of selected magnetometers for the 0815-0915 UT interval (Left: event *A*), 1010-1110 UT interval (Middle: event *B*), and 1200-1340 UT interval (Right: event *C*) on March 24, 1991. Dotted lines indicate the 2.8 mHz, 1.9 mHz, and 1.7 mHz frequency used for field line resonance analysis in Figure 4.6.

Event *A* is characterized by more broad-band oscillations, whilst the latter two intervals are seen to be characterized by very monochromatic pulsations above 1 mHz. Figure 4.4 shows the magnetograms for the H- and D-components for the interval of 0800-1400 UT and Figure 4.5 shows their power spectra during the three selected wavepacket intervals in order of UT, respectively. During event *A*, multiple discrete spectral peaks are shown at each station with a global and latitude independent peak at 2.8 mHz which dominates most of the European stations. Larger amplitudes are seen in the Greenland stations, for example at STF (Greenland), which was located in the local morning during this time.

This points to a local time amplitude variation with larger amplitudes occurring on the dawn flank. During event B, monochromatic waves (1.9 mHz) are seen in the European and Greenland stations. During event C, very monochromatic oscillations (1.7 mHz) are clearly shown in every station simultaneously. The wave amplitude is clearly dependent on latitude and the H-component is dominant than the D-component during event C.

4.2.4 Field Line Resonance Characteristics

To complete a phase and amplitude analysis of the waves we used complex demodulation [e.g., *Beamish et al.*, 1979] which provides instantaneous values of pulsation amplitude, phase, and polarization at a specific frequency through comparison to a reference signal. See *Myers and Orr* [1995] for more details about complex demodulation techniques for ULF wave analysis. Figure 4.6 panels (a), (b) and (c) illustrate the amplitude and phase as a function of latitude during events A, B, and C, respectively. We chose to analyze the 2.8 mHz frequency (360s period) waves which were dominant for event A, the 1.9 mHz (520s period) waves for event B interval, and the 1.7 mHz (600s period) waves for event C. All these pulsations have the characteristic features of FLRs, with a latitudinally narrow peak in power, accompanied by an 180° latitudinal phase shift [e.g., *Walker et al.*, 1979].

Figure 4.6(a) shows the H- and D-component amplitude and phase of the 2.8 mHz pulsation during event A which is seen clearly in the European and Greenland sectors. Different symbols indicate data from stations in different longitudinal ranges. The H-component amplitude peaks near 58° (L $\sim$ 3.6) and shows an approximately 180° latitudinal phase shift in both the 95-110° and 75-95° CGM longitude ranges. Wave amplitude from stations in the longitude range

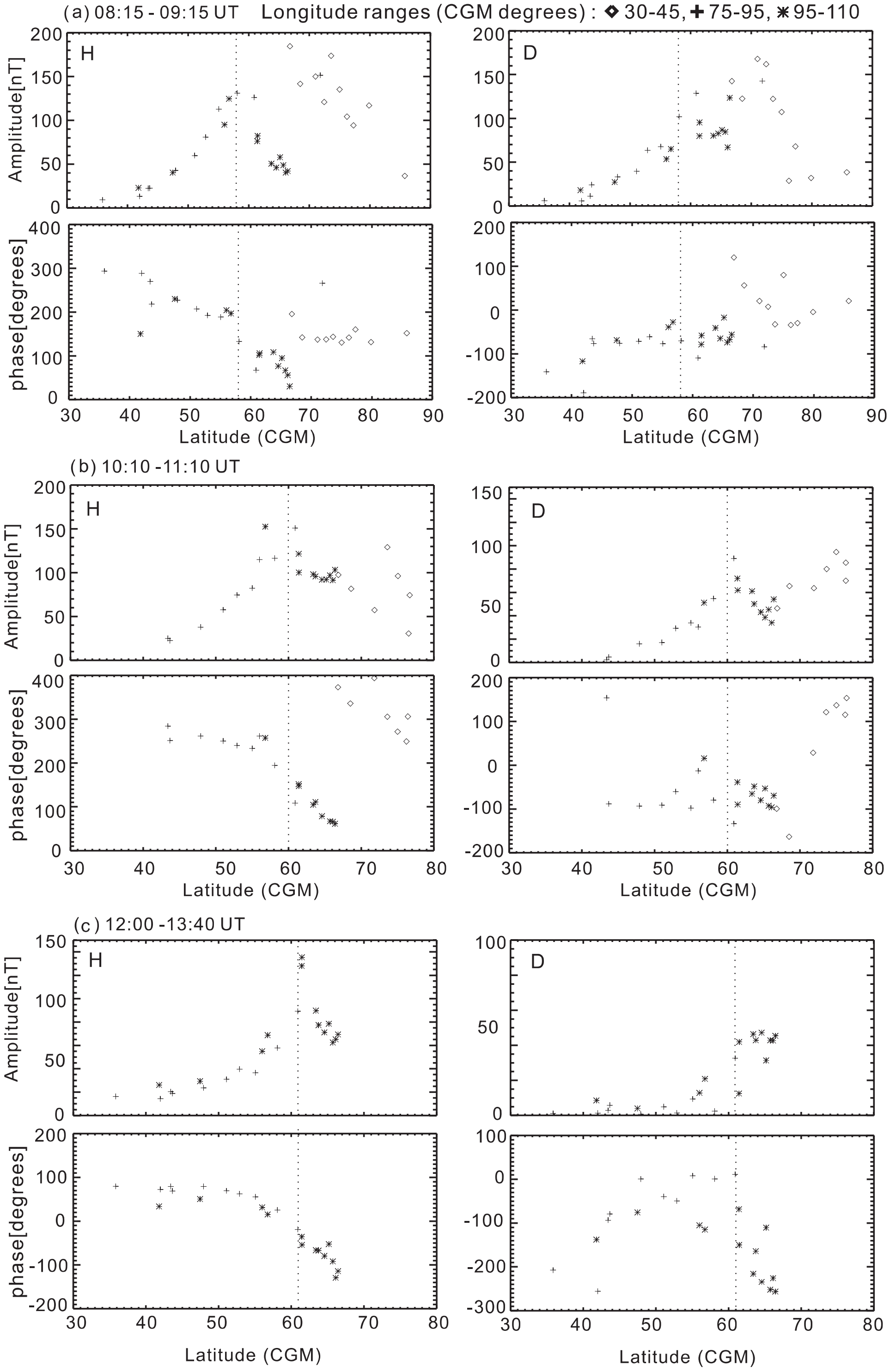

Figure 4.6: H- and D-component amplitude and phase in the interval (a) 0815-0915 UT (event *A*), (b) 1010-1110 UT (event *B*), and (c) 1200-1340 UT (event *C*) on March 24, 1991. The complex demodulation technique was applied in order to calculate the instantaneous amplitude and phase of each FLR frequency as a function of time. Dotted lines indicate the locations of the resonant field line based on H-component amplitude peak.

30°-45°, which are located in the local morning (Greenland stations) are much larger than the others which implies a local time dependence of Pc5 pulsation wave power which increases towards the dawn flank, especially if a similar latitudinally peaked amplitude profile is assumed in this CGM longitude sector. The D-component also shows an amplitude peak around L $\sim$ 4 but the FLR phase change is not as clear. Figure 4.6(b) shows similar features for the 1.9 mHz waves during event B with the H-component amplitude peak seen near 60° CGM latitude (L $\sim$ 4) and a 180° phase shift seen in each of the 95-110° and 75-95° CGM longitude sectors. Also, the wave amplitude in the 30-45° CGM longitude sector shows evidence of an amplitude peak near 74° CGM latitude (L $\sim$ 13) with a corresponding large phase change in the H-component. It is possible that a waveguide mode might drive field line resonances at two locations, inside and outside of the plasmapause, and that the higher latitude peak represents a second higher latitude FLR. The 1.7 mHz pulsations shown in Figure 4.6(c) for event C displays the clearest H-component amplitude peak among these three wavepackets, peaking near 61° CGM latitude (L $\sim$ 4.3) and again having a well-defined latitudinal 180° phase shift. Unlike the two previous intervals, the 1.7 mHz pulsations only appeared clearly in the European stations (75-95° and 95-110° CGM longitude) which were located in the local postnoon. The wave was not seen clearly in the high latitude Greenland (30-45° CGM longitude) sector which is in the local morning at this time.

4.2.5 Discussion

We have investigated pulsations occurring in three intervals during the March 24, 1991 super storm. *Fujitani et al.* [1993], *Reddy et al.* [1994] and *Schott et al.* [1998] interpreted the pulsations observed on this day in terms of compressional

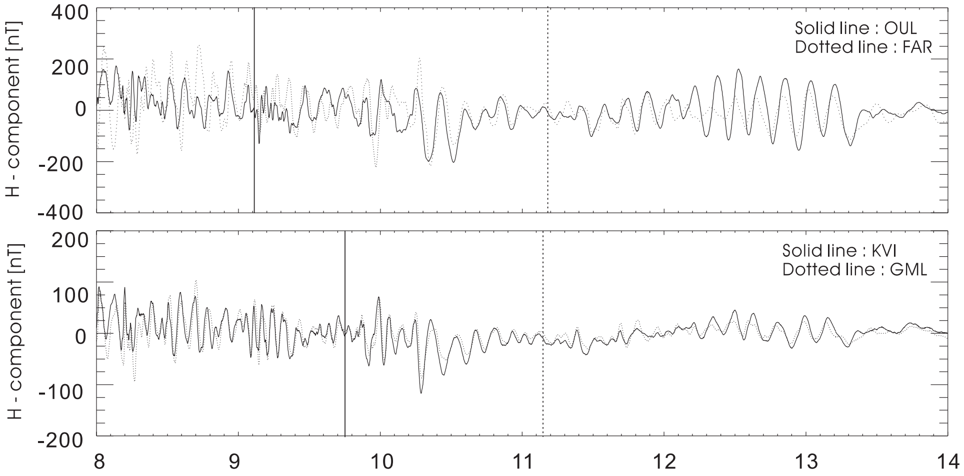

Figure 4.7: Unfiltered H-component magnetograms in the 0800-1400 UT time interval from the stations OUL [61.4, 106.1] and FAR [60.9, 78.4] (top panel), and KVI [55.99, 96.55] and GML [55.0, 78.4] (bottom panel), where the numbers in brackets represent station CGM latitude and longitude, respectively. Solid lines indicate local noon at OUL (top) and KVI (bottom) and dotted lies indicate local noon at FAR (top) and GML (bottom)

cavity/waveguide modes [cf. *Kivelson and Southwood*, 1986; *Samson et al.*, 1992; *Walker et al.*, 1992]. The global appearance of a wave event with a latitudinally and longitudinally invariant period supports the cavity/waveguide mode hypothesis. Our dominant frequencies (2.8 mHz, 1.9 mHz and 1.7 mHz) are also consistent with some of the discrete peaks observed by *Samson et al.* [1992] and *Ziesolleck and McDiarmid* [1994].

Figure 4.7 shows the azimuthal phase propagation of the H-component of the waves in the time interval 0800-1400 UT. Four European stations were chosen to examine the azimuthal propagation of the waves. This figure shows a clear phase delay in the H-component between stations which were located at different longitudes but at similar latitudes. OUL and FAR stations (top panel) are located at similar latitudes (61.4° and 60.9° CGM, respectively) but are each located at different CGM longitudes (106.1° for OUL and 78.4° for FAR). Waves at the OUL station lead in the local morning and waves in the FAR station start to lead in the local afternoon. So, the phase of these waves propagates from local noon towards the morning side, and then later from local noon towards the evening side of the magnetosphere, as seen by OUL and FAR. Bottom panel (KVI and GML) shows the same characteristics using a station pair with a slightly lower common CGM latitude. This is consistent with the results of *Schott et al.* [1998] which also showed propagation away from noon in the southern Indian Ocean at subauroral and mid-latitudes. Our observations support the conclusion that these ULF pulsations have a common source associated with anti-sunward propagating disturbances, perhaps on the magnetopause, with a source definitively associated with the solar wind. The observed anti-sunwards propagation of the waves also supports the applicability of the waveguide mode rather than the cavity mode theory. According to *Samson et al.* [1992]; *Walker et al.* [1992]; and *Wright* [1994]; compressional wave energy can propagate and disperse down the waveguide, supporting azimuthal wave propagation down both flanks.

From the phase and amplitude analysis we found that the amplitude peak of these discrete frequency Pc5 waves occurred at much lower L-values than normal (see Figure 4.6). For the 2.8 mHz pulsation (A), the 1.9 mHz pulsation (B), and the 1.7 mHz pulsation (C), the H-component amplitude peaked near 58° (L $\sim$ 3.6), 60° (L $\sim$ 4) and 61° CGM (L $\sim$ 4.3), respectively. For comparison, *Mathie et al.* [1999b] estimated a resonant latitude of 74.3° CGM (L $\sim$ 13.9) for a 1.8 mHz signal and 71.5° CGM (L $\sim$ 10.1) for 3.0 mHz FLR during a non-storm time. For event B there might be a second FLR at high latitude around L $\sim$ 13.

The cross-phase analysis were performed by Zoe Kale to examine the temporal variation of the mid-latitude eigenfrequencies in the continuum through the course of the onset day of this geomagnetic superstorm [e.g., *Menk et al.*, 1994]. We obtained some results from the station pair NUR-OUL from the SAMNET

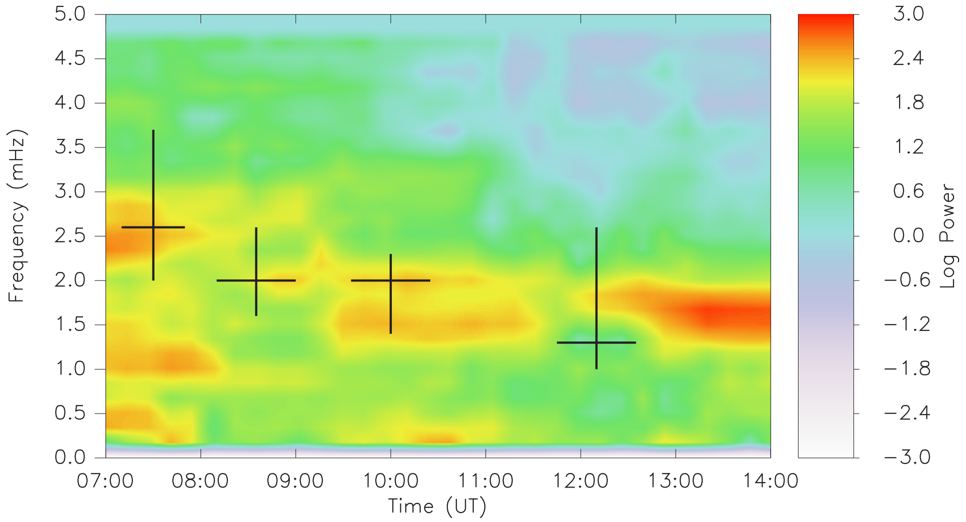

Figure 4.8: Cross-phase derived resonant frequency at L ∼ 3.87 the mid-point of the NUR-OUL stations (crosses). Also plotted is the H-component dynamic power spectrum above 0.5 mHz from NOR station (L = 4.45, the closest SAMNET station to the NUR-OUL mid-point) on March 24, 1991. The vertical and horizontal lines in the crosses indicate the estimated error range in frequency in the cross-phase peak and the length of the time windows used for the cross-phase analysis, respectively.

array, with a mid-point of 59.1° CGM (L ∼ 3.87) for four windows between 0700 UT and 1400 UT (crosses in figure 4.8). The vertical line in the first cross indicates the error estimated from the range of frequencies (2.0-3.7 mHz) spanned by the cross-phase peak with resonant frequency 2.6 mHz and the horizontal line indicates the time window (0710-0750 UT) used for the cross-phase analysis. Other crosses are determined in the same way. The cross-phase determined resonant frequency at the mid-point (L ∼ 3.87) was ∼ 2.6 mHz at around 0730 UT and reduced to ∼ 1.3 mHz at around 1200 UT. The cross-phase determined eigenfrequency of the field line at this latitude is hence also lower than under more typical magnetospheric conditions and decreases with time throughout the 0700-1400 UT interval during the storm main-phase. For comparison, at the mid-point of the NUR-OUL stations (L ∼ 3.87) the resonant frequency was observed to be

10.7 mHz on Oct 16, 1990 during a non-storm time (maximum Kp = 4+ and minimum Dst = -38nT on that day) [e.g., *Menk et al.*, 1999].

The crosses in Figure 4.8 show that the local NUR-OUL cross-phase determined resonant frequency at L ∼ 3.87 decreases with time. Similarly, the dominant power in the Pc5 ULF band can be seen to decrease in frequency with time. The dynamic power spectra from NOR in Figure 4.8 shows broadband power with a strong discrete power peak at ∼ 2.5 mHz at 0700-0800 UT, a discrete power peak at ∼ 2 mHz at 1000-1100 UT, and finally a very clear single discrete peak at ∼ 1.7 mHz at 1300-1400 UT (the third FLR interval analyzed earlier). The correspondence of the latter discrete peak in the dynamic power spectra in Figure 4.8 with the time-series in Figure 4.5 (event C) is obvious. Figure 4.8 shows strong evidence that not only the Alfvén continuum, and hence the local L-value at which a given frequency resonates, decreases with time but also that the dominant power in the ULF band also moves to lower frequencies with time on this day.

Figure 4.8 shows, together with Figures 4.5, that discrete spectral peaks dominated the Pc5 ULF wave activity during this period. The driver for the discrete frequency waves might come directly from solar wind sources such as solar wind dynamic pressure pulses but we couldn't check this hypothesis because there was no suitable upstream solar wind data available during this time interval. Another possibility is that the spectral structure comes from the natural frequencies of the magnetospheric cavity/waveguide. *Allan et al.* [1986] suggested that a m-value close to m = 3 gives the most efficient coupling of global cavity mode to drive FLRs. We calculated the m-values for A, B, and C and they were similar for each of the three time intervals being ∼ 2-4, supporting the waveguide mode hypothesis. Temporal variations in the dimensions and physical conditions within the waveguide might change the natural frequency of the waveguide modes and hence change the frequency of the driven FLRs with time [e.g., *Ziesolleck and McDiarmid*, 1995; *Mathie et al.*, 1999a; 1999b].

The resonant frequency of a field line is determined by magnetic field line length, the magnetic field intensity and plasma density distribution along the field line. *Pathan et al.* [1999] suggested that the development of strong magnetic storms can lead to significant large-scale structural changes of the magnetosphere, and thus the properties of geomagnetic pulsations observed on the ground might be expected to change significantly. Longer field lines or reduced magnetic field intensity would both cause a decrease in eigenfrequency. However, the Pc5 FLRs observed in this study resonated around L $\sim$ 4. Dayside field lines at $L \sim 4$ are not expected to be significantly affected by solar wind conditions. In any case, during a severe geomagnetic storm compressed dayside field lines would cause an increase in eigenfrequency. *Waters et al.* [1995] show the temporal variation of the continuum frequency near local noon increasing monochromatically to 7 mHz at 65°(L=6.1). Thus, a more plausible reason for the reduction of field line eigenfrequency could be increased equatorial plasma mass density during this storm event. An obvious candidate would be an increase in heavy ion (O^+) content, driven into the magnetosphere from the ionosphere. During the great storm in March 1991, the increase of the O^+ abundance was observed by other authors to be overwhelming [*Daglis and Thorne*, 1999]. Similarly, an O^+ torus has been observed to form near the plasmapause [e.g., *Roberts et al.*, 1987]. Also, *Fraser et al.* [2005] shows how an increase in O^+ density can contribute to a decrease in ULF wave frequency.

Such heavy ion mass loading could decrease the eigenfrequencies in the manner we have observed. This could allow Pc5 ULF power to penetrate to low-L, and

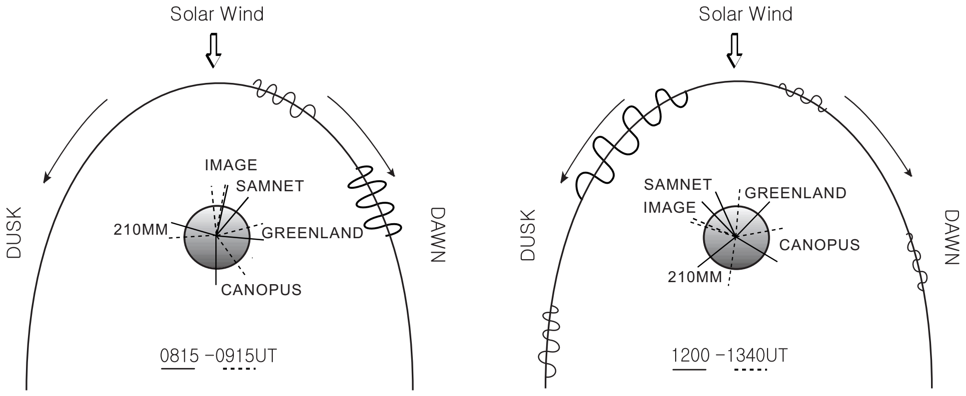

Figure 4.9: Schematic of the equatorial propagation and amplitude of Pc5 pulsations in the time intervals 0815-0915UT (event *A*) and 1200-1340 UT (event *C*) on March 24, 1991.

resonate with local FLRs at low-L, perhaps around L ∼ 4 during strong storms such as this one. Given that ULF wave power at low-L could energize radiation belt electrons through ULF wave enhanced drift-resonance [e.g., *Elkington et al.*, 2003], this suggests that thermal plasma and especially heavy ions might play a role in radiation belt dynamics through the intermediary of ULF wave penetration to L-shells in the heart of the outer radiation belt, and perhaps even beyond into the slot [e.g., *Loto'aniu et al.*, 2006].

In order to explain the dawn/dusk asymmetry in the Pc5 power observed by the ground-based magnetometers, we discuss here the possible sources which could result in the observed local time dependence of Pc5 power suggested by our study. There are a number of different possible sources for pulsation energy including solar wind pressure pulses near the magnetospheric nose [e.g., *Rostoker and Sullivan*, 1969; *Chisham and Orr*, 1997; *Mathie et al.*, 1999a] or magnetopause shear flow instability on the flanks [e.g., *Mann et al.*, 1999]. Distinguishing between different possible energy sources may also provide an explanation for the long observed dawn-dusk asymmetry in the occurrence of FLRs [e.g., *Nosé et al.*, 1995; *Mathie and Mann*, 2000a].

Figure 4.9 shows a schematic diagram of the equatorial propagation direction and amplitude of the waves as a function of local time during events A and C. During event A, the wave amplitude increases toward the dawn terminator. This local time dependence of Pc5 pulsation wave power can be explained if the field line resonances were driven by magnetopause shear-flow instability. With sufficiently high magnetosheath flow speeds, the magnetopause may become unstable to shear-flow instabilities and these instabilities can amplify the waveguide modes through the over-reflection mechanism [e.g., *Mann et al.*, 1999] and hence drive large-amplitude FLRs. As the flow speed would be expected to be much greater on the magnetospheric flanks than at the sub-solar point, and convectively unstable waves would have greater amplitudes further from noon [e.g., *Wright et al.*, 2002], pulsations driven by magnetopause instabilities during intervals of high solar wind speed might occur predominantly on the flanks [*Mann et al.*, 1999; *Mathie and Mann*, 2000a]. Such a mechanism might also act preferentially on the dawn flank if the shear flow instability is more unstable in the dawn sector than at dusk due, for example, to the stabilizing action of magnetic field line tension [e.g., *Lee et al.*, 1981].

During event C, pulsations appear across a wide range of latitude and longitude but have the largest amplitudes in the postnoon sector. As mentioned by *Fujitani et al.* [1993], the driver in this case might be identified as compressional waves caused by solar wind dynamic pressure pulses. Specifically, events with an early afternoon peak in power might be interpreted in terms of solar wind pressure pulses connected with features in solar wind hitting postnoon side of the magnetopause more frequently [*Rostoker and Sullivan*, 1969; *Chisham and Orr*, 1997; *Mathie et al.*, 1999a]. *Shea and Smart* [1993] inferred a solar wind speed of around 1400 km/s on March 24, 1991. Also, *Le et al.* [2003] determined that the

CME hit the magnetosphere slightly earlier than 1020 UT. High speed solar wind and CME impacts, perhaps including internal density structures, could provide strong dynamic pressure impulses for ULF wave excitation. Strong solar wind pressure pulses can also generate global oscillations, as mentioned by *Walker et al.* [1992] and *Lepidi et al.* [1999]. Certainly waves with discrete spectral peaks identical to those seen on the dayside by the European sector (SAMNET and IMAGE) magnetometer arrays were seen globally in the magnetosphere (e.g., Figure 4.5 (event C)). Stations such as KAK in the 210 MM array on the nightside observed spectral peaks identical to those seen on the dayside. Similarly, stations on the flanks also saw waves during event C. In contrast to event A the amplitudes clearly peaked near noon or just postnoon during event C rather than at the dawn flanks.

During event B, pulsations appeared in the European and Greenland magnetometer arrays which were located in the noon and morning sector, respectively. This interval shows more monochromatic waves than the waves during event A and appears globally around the world. The waveforms during event B suggest they are perhaps an earlier manifestation of the monochromatic waves which appeared during event C.

4.2.6 Summary

We observed intense Pc5 pulsations at unusually low sub-auroral latitudes during the great magnetic storm of March 24, 1991.We observed large amplitude discrete frequency waves in the morning and local noon, and afternoon hours, different wavepackets having power which peaked at different dayside local times. The waves were also often seen globally at small amplitude throughout the magnetosphere. We suggest that these pulsations might have been driven by different solar wind Pc5 wave sources at different times, such as magnetopause shear-flow instabilities and solar wind pressure pulses. Large amplitude waves appeared in dawn flank during event A can be explained as FLR driven by KHI instability. On the other hand, the waves observed during event C show largest amplitude in postnoon sector and they might be driven due to the solar wind dynamic pressure pulses. We observed that FLRs were excited at L $\sim$ 3.6, L $\sim$ 4 and L $\sim$ 4.3 for 2.8 mHz, 1.9 mHz and 1.7 mHz pulsations, respectively, each FLR occurring at different times. In each case the FLR latitude was unusually much lower than normal. This suggests a reduction of the local Alfvén eigenfrequency continuum as compared to non-storm times which could be due to increases in plasma mass density or to field line stretching. We suggest that the Alfvén eigenfrequency reduction is most likely due to an increase in thermal O^+ which is injected along the field-lines from the ionosphere.

Interestingly, a reduction in the local Alfvén continuum allows the penetration of Pc5 wave power, and the excitation of Pc5 FLRs, at much lower L-values than normal. In the case presented here, Pc5 waves with ground amplitudes reaching $\sim$ 400 nT p-p were resonant around L $\sim$ 4 in the heart of the outer radiation belt. This suggests the potential importance of thermal energy ions, especially heavy ions such as O^+, in radiation belt electron dynamics via the intermediary of ULF waves. This could have considerable significance for the interaction between ULF waves and MeV electrons [e.g., *Elkington et al.*, 2003] in the outer radiation belt during storms.

4.3 Direct solar wind excitation of Pc 5 pulsations on 27 - 29 March, 2001

4.3.1 Introduction

Recent works present some events showing correlations of solar wind pressure fluctuations and magnetospheric ULF waves. *Kepko and Spence* [2002] presented some events that showed ULF pulsations and solar wind dynamic pressure to contain the same discrete frequencies in the dayside magnetosphere. It was suggested that solar wind dynamic pressure fluctuations were responsible for discrete frequency oscillations of the magnetospheric field. *Kessel* [2008] also suggested the significance of solar wind pressure fluctuations as a source of ULF waves by showing the compressional Pc 5 power increased in direct proportion to the power of the solar wind dynamic pressure fluctuations.

To examine these relationships, we also suggest density or dynamic pressure has higher correlations than solar wind speed during this time. We studied a 3-day interval from 27 - 29 March, 2001, using data from ground-based magnetometers and satellites (Figure 4.10), examining the periods marked as (A), (B), and (C) in Figure 4.11. The order of the work is as follows: Section 4.3.2 describes the data, section 4.3.3 provides observations, and sections 4.3.4, 4.3.5, and 4.3.6 provide observational studies of intervals (A) - (C). Section 4.3.7 presents the summary of these studies.

4.3.2 Data

We examine ground-based magnetometer array and satellite data during the time interval from March 27 to March 29, 2001. The solar wind data were measured

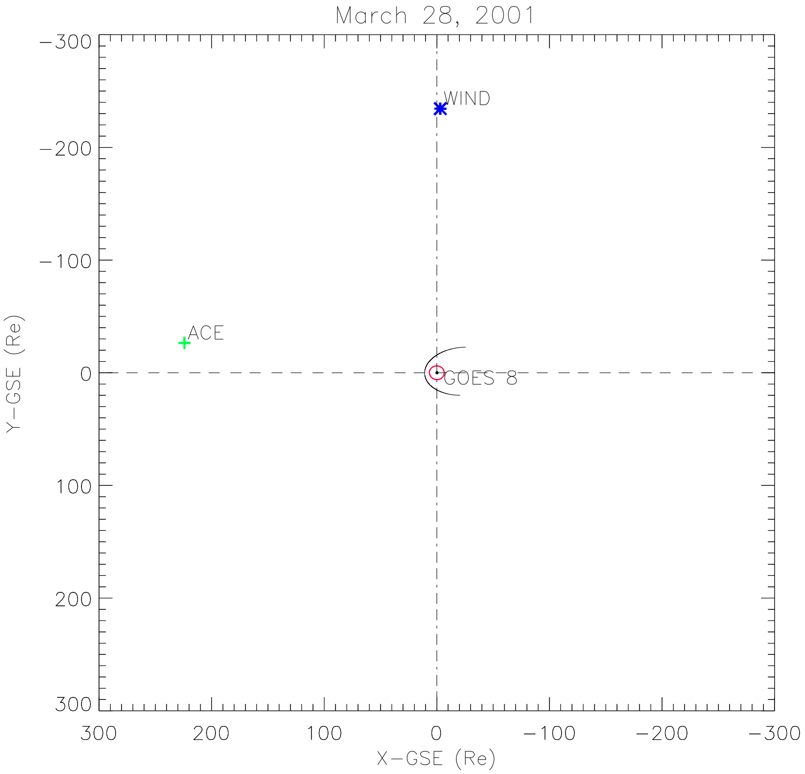

Figure 4.10: Locations of spacecrafts ACE, Wind, and GOES satellites on March 28, 2001 in GSE coordinate. The curved line shows the magnetopause.

from Wind and ACE. We used data from the SWE and SWEPAM on Wind (16 s time resolution) and ACE (64 s time resolution), respectively. On ACE, we also used interplanetary magnetic field data from the Magnetic Field Experiment (MAG) [*Smith et al.*, 1998].

Magnetic field variations were observed from GOES 8 and GOES 10 (60 s time resolution) and ground-based stations, from INTERMAGNET (60 s), IMAGE (10 s) and CARISMA (5 s) magnetometer arrays. The CGM coordinates (latitudes, longitudes) and L-values of the stations used in this study are given in Table A.3 and A.4 of Appendix A. The Dst values obtained from the World Data Center for Geomagnetism, Kyoto, Japan (see Section 3.2).

Figure 4.10 shows the locations of spacecrafts ACE, WIND and GOES8 on

March 28, 2001 in GSE coordinates. ACE moves around the Lagrange point (L1) where the gravity of the sun balances with that of the Earth. ACE moved from GSE (X, Y, Z) = (224.2,-26.9,-9.5) R_E to (223.89,-25.55,-10.38) R_E and WIND moved from GSE (X, Y, Z) = (-3.43, -233.40, 4.20) R_E to (-2.33, -236.68, 3.87) R_E during the period 1600 UT on March 27 to 2100 UT on March 28, 2001.

4.3.3 Observations

We observed high-speed solar wind, high solar wind density and high solar wind dynamic pressure during March 27 - 29 in 2001. Figure 4.11 presents the solar wind conditions, the interplanetary magnetic field (IMF) B_z, total B, and Dst index. The eight panels illustrate the solar wind speed, solar wind proton number density, dynamic pressure ($m_p N_{sw} V_{sw}^2$) observed from WIND and ACE, as well as IMF Bz and Dst index. Here, m_p is the proton mass, N_{sw} is proton density, and V_{sw} is solar wind speed. The IMF shows a switching in direction from northward to southward especially during the period of the density or dynamic pressure enhancement.

Two intervals of a steplike increase of solar wind speed (V_{sw}) were observed at 0110 UT and 1715 UT on March 27 from ACE, and proton number density (N_{sw}), dynamic pressure (P_{sw}) increases were observed simultaneously. WIND also measured increased solar wind speed, proton number density and pressure at 0203UT and 1808 UT with 52 minutes time delay. The Dst index recorded a moderate storm with Dst minimum -87 nT. We selected three intervals marked (A) - (C) in Figure 4.11 and detailed observational studies of these intervals are presented in the following subsections.

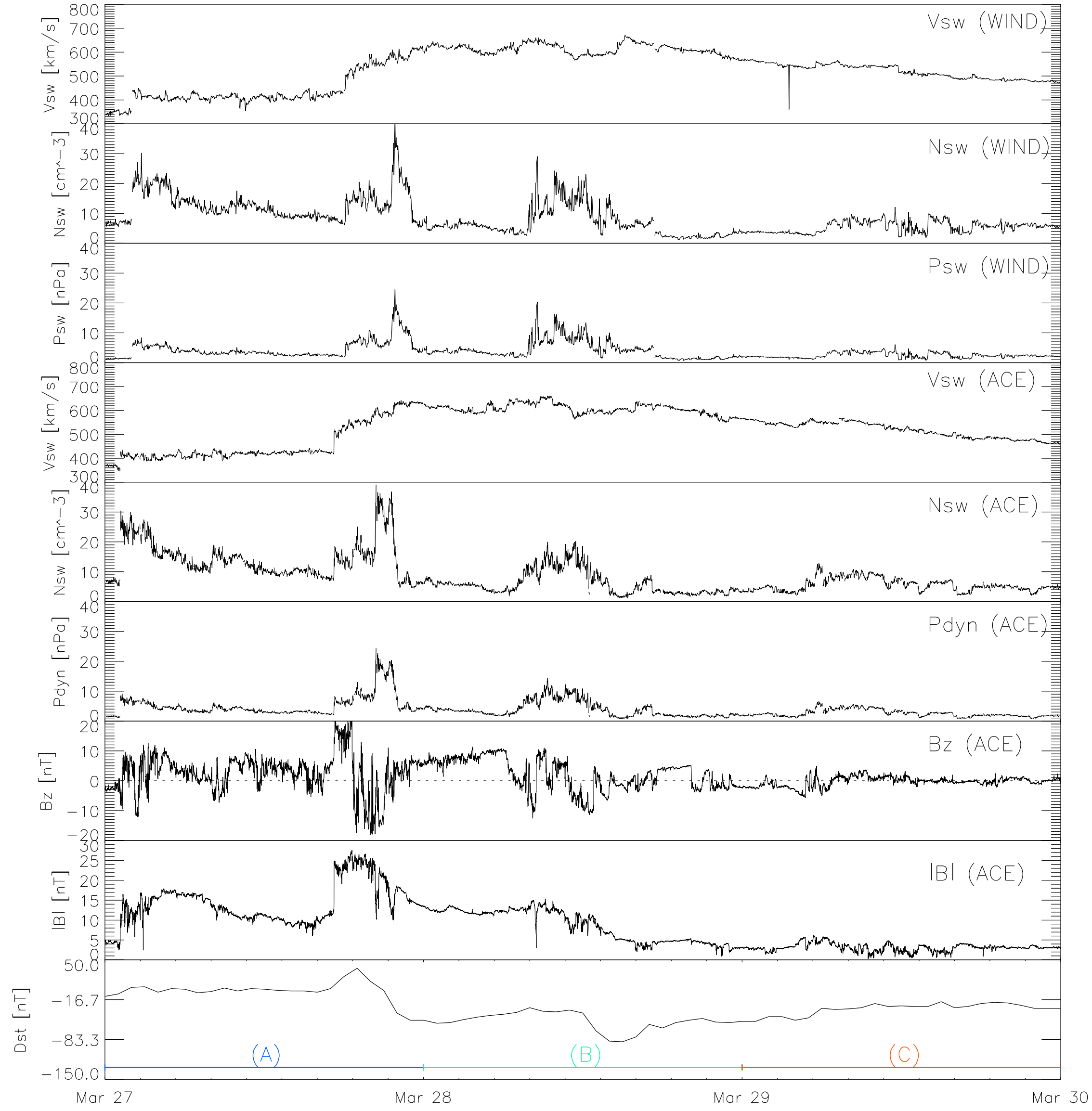

Figure 4.11: Solar wind velocity (V_{sw}), density (N_{sw}), dynamic pressure (P_{sw}) observed from WIND and ACE, IMF B_z and total $|B|$ from ACE, and Dst index from March 27 to April 04, 2001.

4.3.4 Interval A : March 27, 2001

Figure 4.12 demonstrates the correlation between the solar wind conditions and magnetospheric pulsations on March 27, 2001. From the top to bottom, the first panels show the solar wind speed (V_{sw}), proton number density (N_{sw}), dynamic pressure (P_{sw}) observed from ACE (blue) and WIND (black). The next panels show the geosynchronous magnetic field Bx in FAC, Bx in GSM, By in FAC, By in GSM, Bz in FAC, Bz and total B in GSM observed from GOES 8 (green) and GOES 10 (red), and finally the bottom panels show the magnetic field H-components from selected ground-stations (DAWS, PBQ, KEV). Here, GSM stands for the Geocentric Solar Magnetospheric System. In GSM coordinate, the x-axis is defined along the line connecting from the Earth toward the sun and the y-axis is defined as the cross product of the x-axis and the Earth's magnetic dipole. The z-axis completes the triad and points in the same sense as the northern magnetic dipole. Magnetic fields observed from GOES 8 and GOES 10 in GSM coordinate were transformed to a field aligned coordinate (FAC) system. In this FAC system, the z -axis is parallel to the direction of the running average magnetic field, the y-axis is parallel to the direction of the cross product of the running average B and the outward vector from the Earth to the spacecraft. The x-axis forms a right-handed set being usually in the outward direction. Triangles indicate local midnight and diamonds indicate local noon. GOES 10 shows magnetopause crossing near local noon as shown in Bz (GSM) of Figure 4.12. The observations (Figure 4.12) illustrate the sudden increase of the solar wind speed, proton number density and dynamic pressure and IMF Bz corresponding to the sudden storm commencements (SSC) at around 1800 UT on March 27. The sudden increases in solar wind speed, and density were detected by both ACE and Wind spacecraft at around 1715 UT and 1807 UT, respectively. Simultaneously,

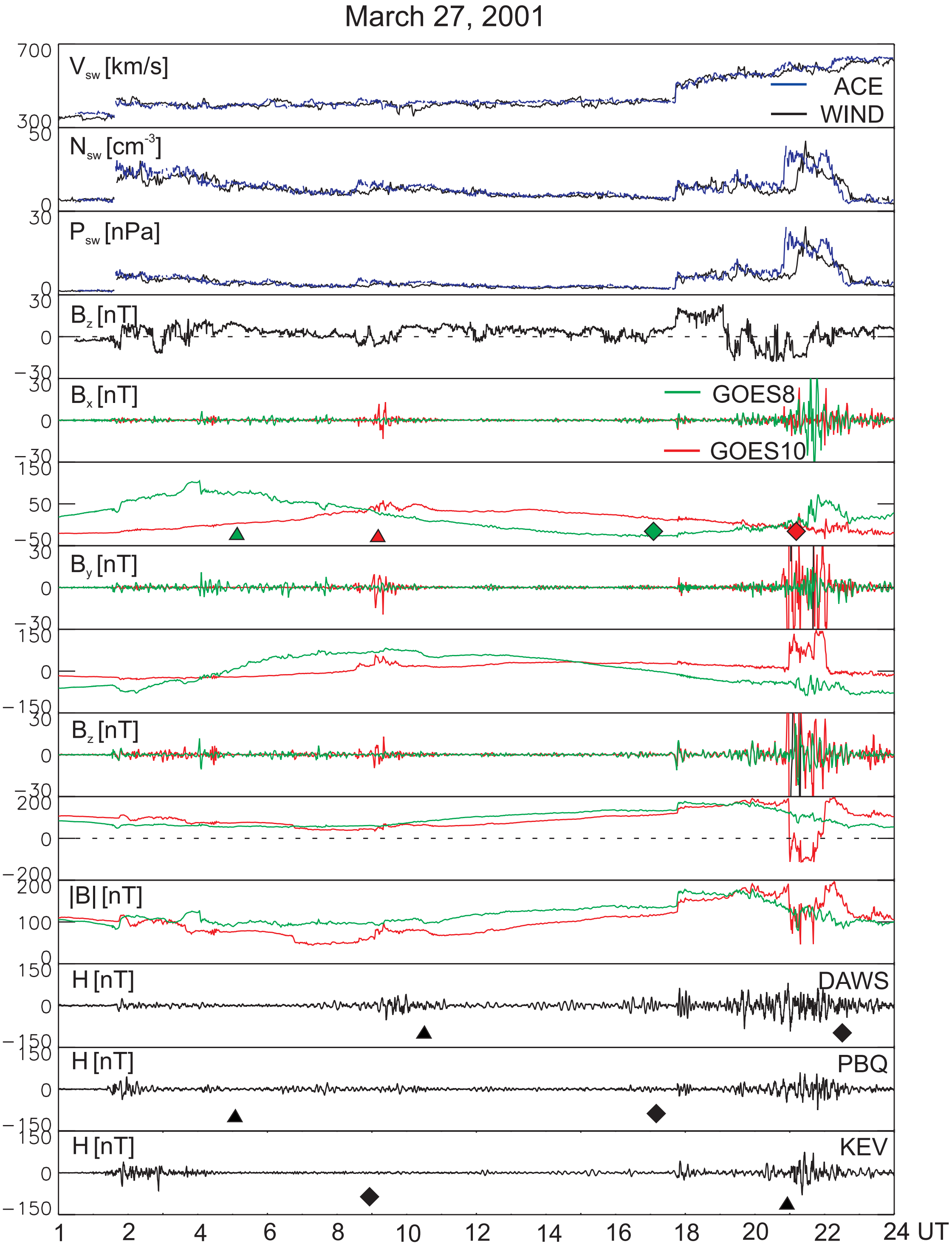

Figure 4.12: Solar Wind speed (V_{sw}), proton number density (N_{sw}), dynamic pressure(P_{sw}), magnetic field Bx in FAC, Bx in GSM, By in FAC, By in GSM, Bz in FAC, Bz in GSM and total B from GOES 8 and GOES 10, and filtered magnetic field H-components from selected ground-stations (DAWS, PBQ, KEV). The triangles indicates local midnight and the diamonds indicate local noon.

GOES 8 and GOES 10 observed a sudden increase of magnetic field at around 1748 UT. Thus, Wind and ACE data were shifted to align with the magnetic field changes observed at GOES 8 and GOES 10. ACE data were shifted 28 minutes later and Wind data were shifted 24 minutes earlier in Figure 4.12. The propagation time of the solar wind discontinuity from ACE to WIND is about 52 minutes.

Following the sudden increases in solar wind parameters, magnetic field variations in the magnetosphere increased both in space and on the ground responded concurrently. Particularly, the magnetic field variation shows enhanced amplitudes when the solar wind density and pressure show enhanced fluctuations during the period while solar wind speed is gradually increasing. Therefore, the correlation of solar wind density and pressure with magnetic field pulsation amplitudes at this time is larger than with solar wind speed, which is consistent with the result of *Takahashi and Ukhorskiy* [2007]. These authors found that solar wind dynamic pressure (or dynamic pressure variance) have the highest correlation with the Pc 5 magnetic pulsations.

Figure 4.13 shows magnetic field pulsations observed on the ground and from GOES 8 and GOES 10 from 1700 to 2400 UT in response to solar wind driving (same format as Figure 4.12). Bottom panel shows ground-based magnetic field variations from 1700 to 2400 UT. Magnetic field variations observed by GOES 8 and GOES 10 show a strong response during the period of enhanced solar wind dynamic pressure (P_{sw}). The compressional wave component, GSM Bz, is dominant during this event at geosynchronous orbit. GOES 10 crosses the magnetopause at around 2100 UT. Except, during the period of magnetopause crossing, GOES 8 and GOES 10 show compressional (Bz) coherent waves in phase. Large amplitude pulsations in both ground and space were turned on simultaneously

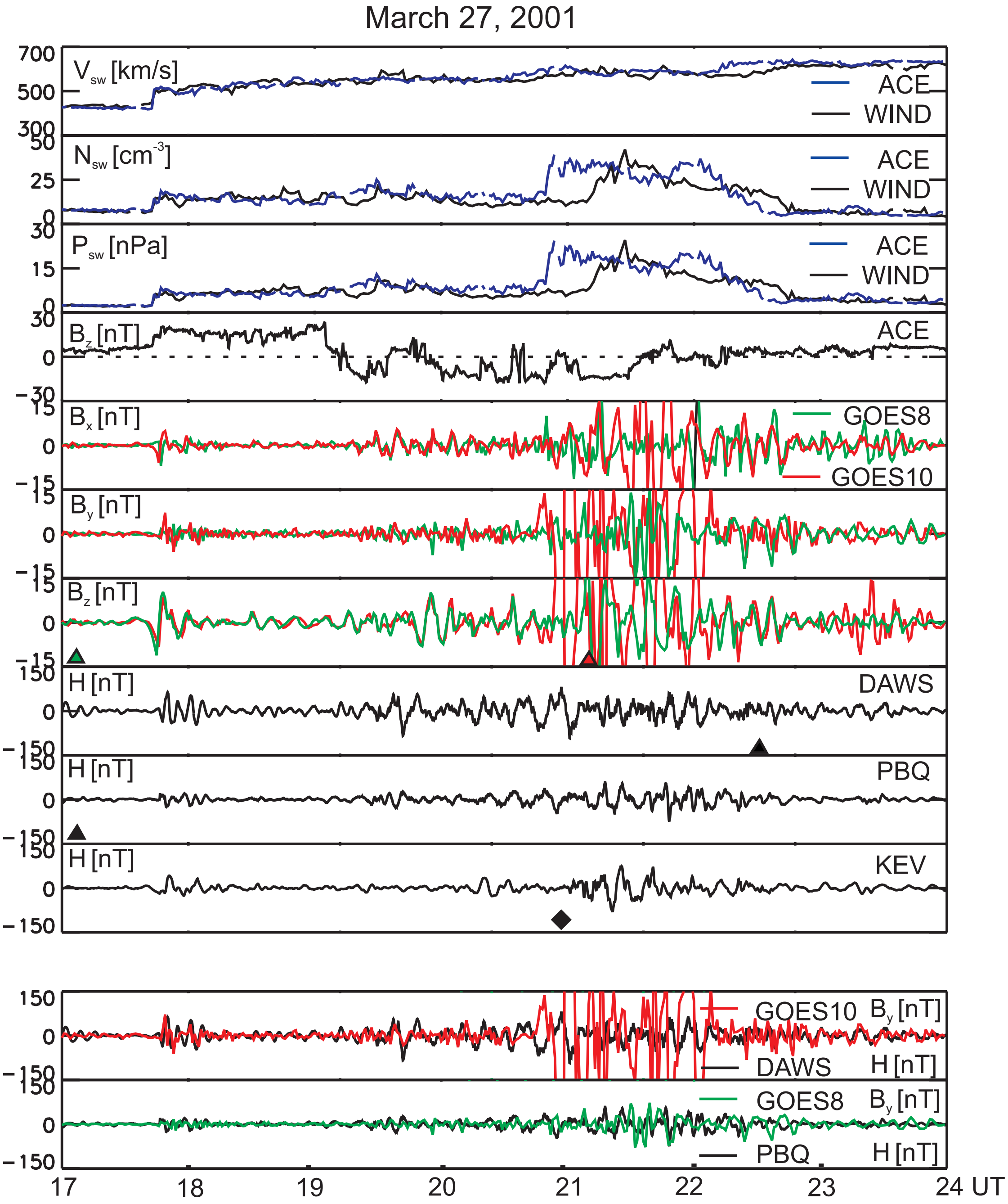

Figure 4.13: Magnetic fields observed from GOES 8, GOES 10, magnetic field H-component observed in the ground-based magnetometers. DAWS and PBQ are close stations to GOES 10 and GOES 8 respectively on March 27, 2001. (A) 1100 - 1700 UT (B) 1700 - 2400 UT. The triangles indicates local midnight and the diamonds indicate local noon.

as the solar wind speed and dynamic pressure (or density) increased during this interval. In the interval 2000 - 2200 UT in Figure 4.13, the density (N_{sw}) and dynamic pressure (P_{sw}) appear to be a more strong controlling factor of the wave activity on the ground and space than solar wind speed (magnetic field pulsation amplitudes clearly increase as the proton number density increases). These compressional magnetic pulsations might be directly driven by impulsive disturbances such as solar wind dynamic pressure variation.

4.3.5 Interval B : March 28, 2001

Figure 4.14 shows the relationship between the solar wind conditions and magnetospheric pulsations on March 28, 2001 (same format as Figure 4.12). From the top to bottom, solar wind speed (V_{sw}), proton number density (N_{sw}), dynamic pressure (P_{sw}), magnetic field Bx in FAC, Bx in GSM, By in FAC, By in GSM, Bz in FAC, Bz in GSM from GOES 8 and GOES 10, magnetic field X-components from selected ground-stations (DAWS, PBQ, KEV). In the same manner as Figure 4.12, ACE and WIND data were forwarded about 52 minutes and the triangles indicate local midnight, and diamonds indicate local noon.

The increased fluctuation of magnetic fields in space and on the ground again shows a high correlation with increased proton density and dynamic pressure. While there was a steady solar wind speed of around 600 km/s during this interval, the density and dynamic pressure increased from 0800 UT and returned to the previous level at around 1830 UT. During the same time interval, large amplitude fluctuations in the Pc 5 wave band at the GOES satellites and at the ground-based magnetometer stations appeared simultaneously.

Figure 4.15 shows ion dynamic pressure observed from ACE and Wind satellites, and toroidal magnetic field pulsations observed from GOES 8 (By) and

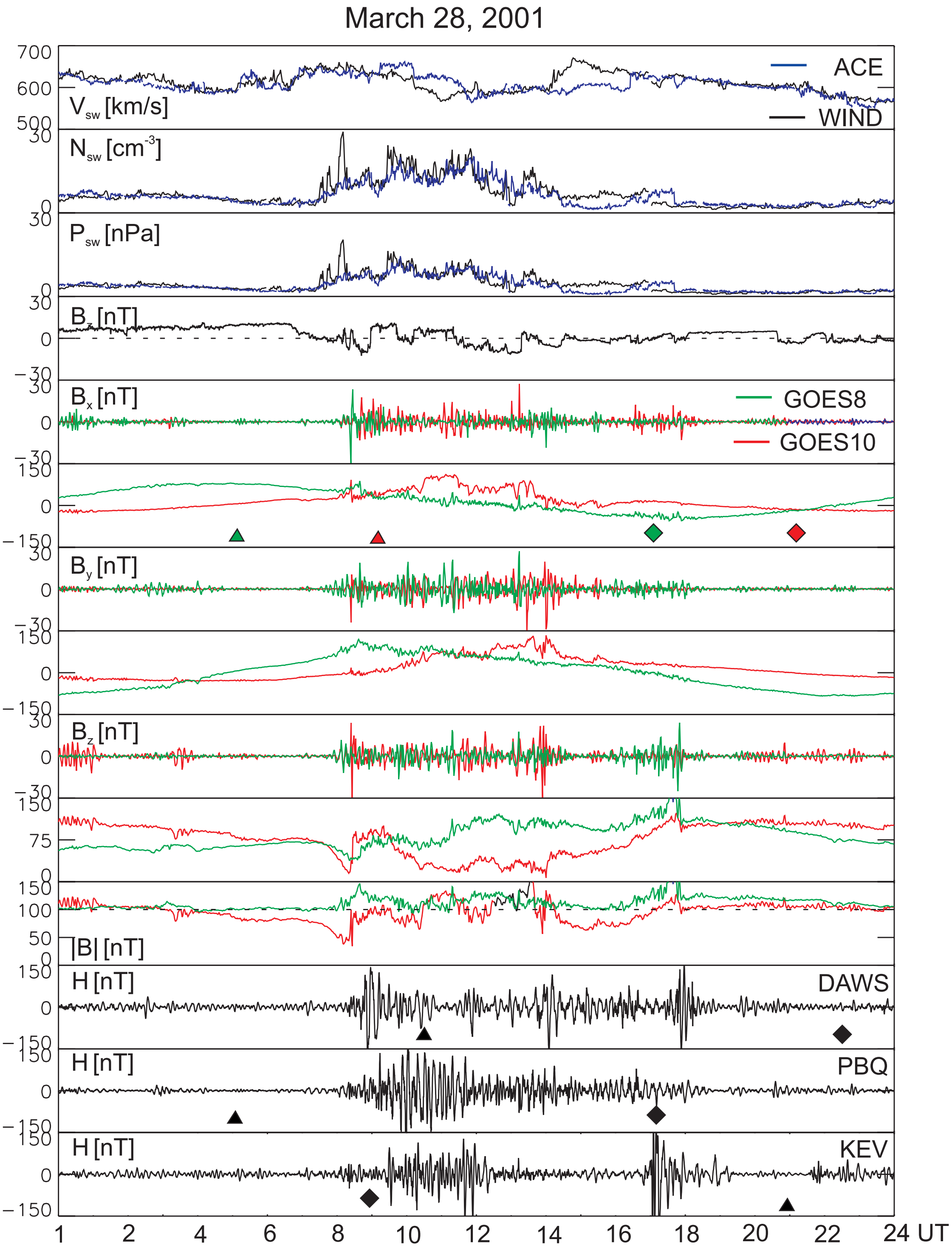

Figure 4.14: Solar wind parameters from ACE and Wind and magnetic fields observed from GOES 8, GOES 10, and magnetic field H-components observed from selected ground-based magnetometers on March 28, 2001. The triangles indicates local midnight and diamonds indicates local noon.

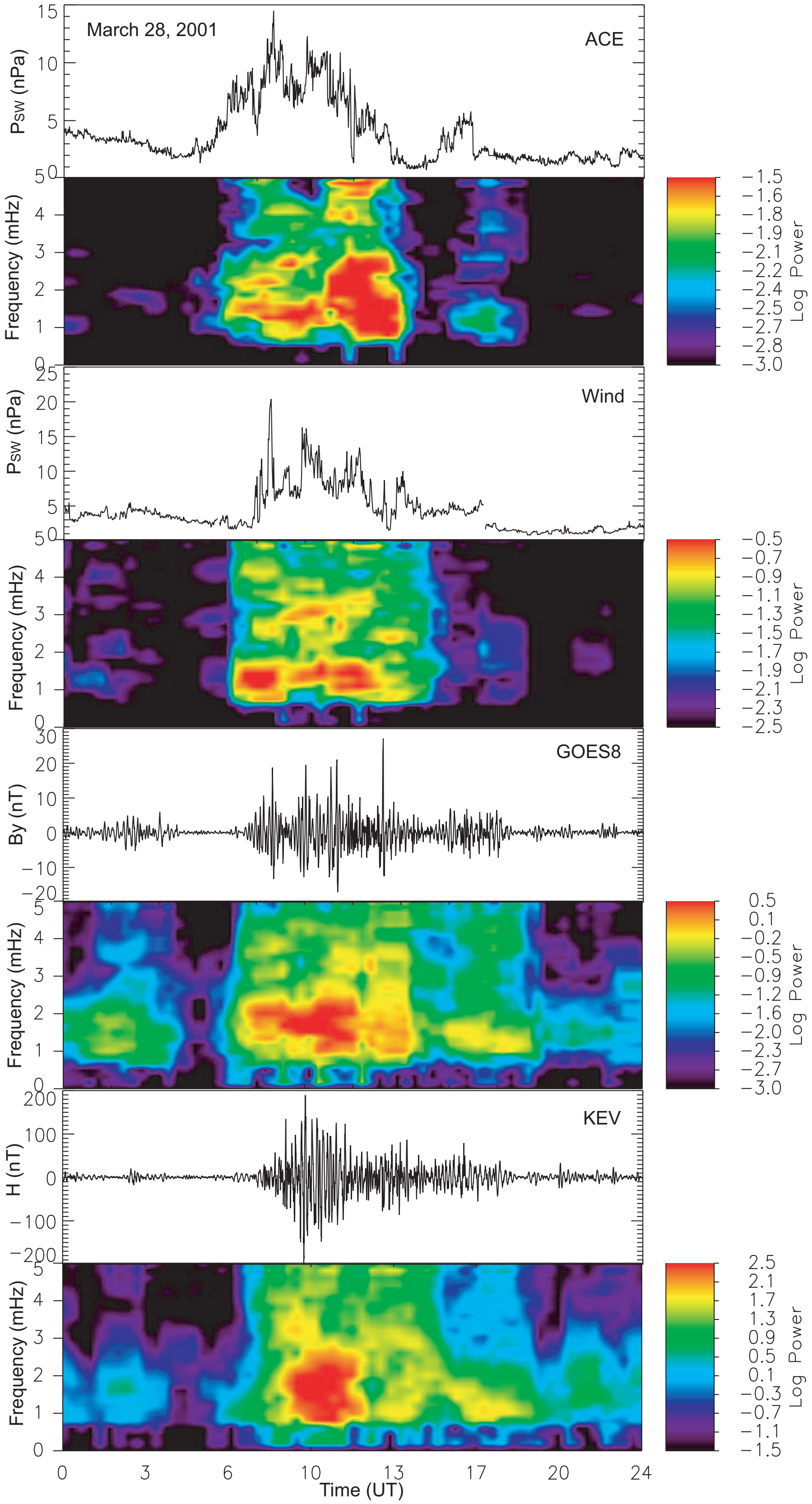

Figure 4.15: Time-series and dynamic power spectra from ACE, Wind, GOES 8, and KEV on March 28, 2001. A low-pass filter was used to filter low-frequency (less than 1 mHz) signals.

PBQ (H) on March 28, 2001. Dynamic spectra corresponding each pulsation time series are plotted below each time-series panel. Note that the ACE and Wind data time series was not shifted in time in this Figure. At about 0800 UT, spectral power increased in all observations in the 1 - 3 mHz frequency ranges and suddenly decreased at around 1830 UT concurrently. The solar wind pressure fluctuations excite a nearly global response as seen in Figure 4.14, i.e., magnetospheric wave power increased in direct response to the power of solar wind pressure fluctuations. Our result agree with the result of *Takahashi and Ukhorskiy* [2007] showing the highest relationship between solar wind dynamic pressure (and dynamic pressure variance) with the Pc5 pulsation power seen in the magnetopause at this time.

Figure 4.16 shows the magnetic field variation in H-component observed from selected station from the IMAGE magnetometer array during 0700-1300 UT on March 28, 2001. Dotted vertical red lines indicate local noon. Long duration Pc 5 ULF oscillations are observed in the pre-noon sector with increasing amplitude as the stations approach noon and beyond into the afternoon. Even though multiple frequency oscillations exist, resonance properties were well recognized as shown in Figure 4.17.

Figure 4.17 panels illustrate the amplitude and phase as a function of latitude during 1050 - 1220 UT. We chose to analyze the 2.7 mHz frequency for this event. This pulsation has the characteristic features of a FLR, with a latitudinally narrow peak in power, accompanied by an 180° latitudinal phase shift [e.g., *Walker et al.*, 1979]. Different symbols indicate data from stations in different longitudinal ranges. The 2.7 mHz pulsations appeared clearly in the European stations (SAMNET and IMAGE stations) which were located near local postnoon which implies a local time dependence of Pc5 pulsation wave power. The H-component

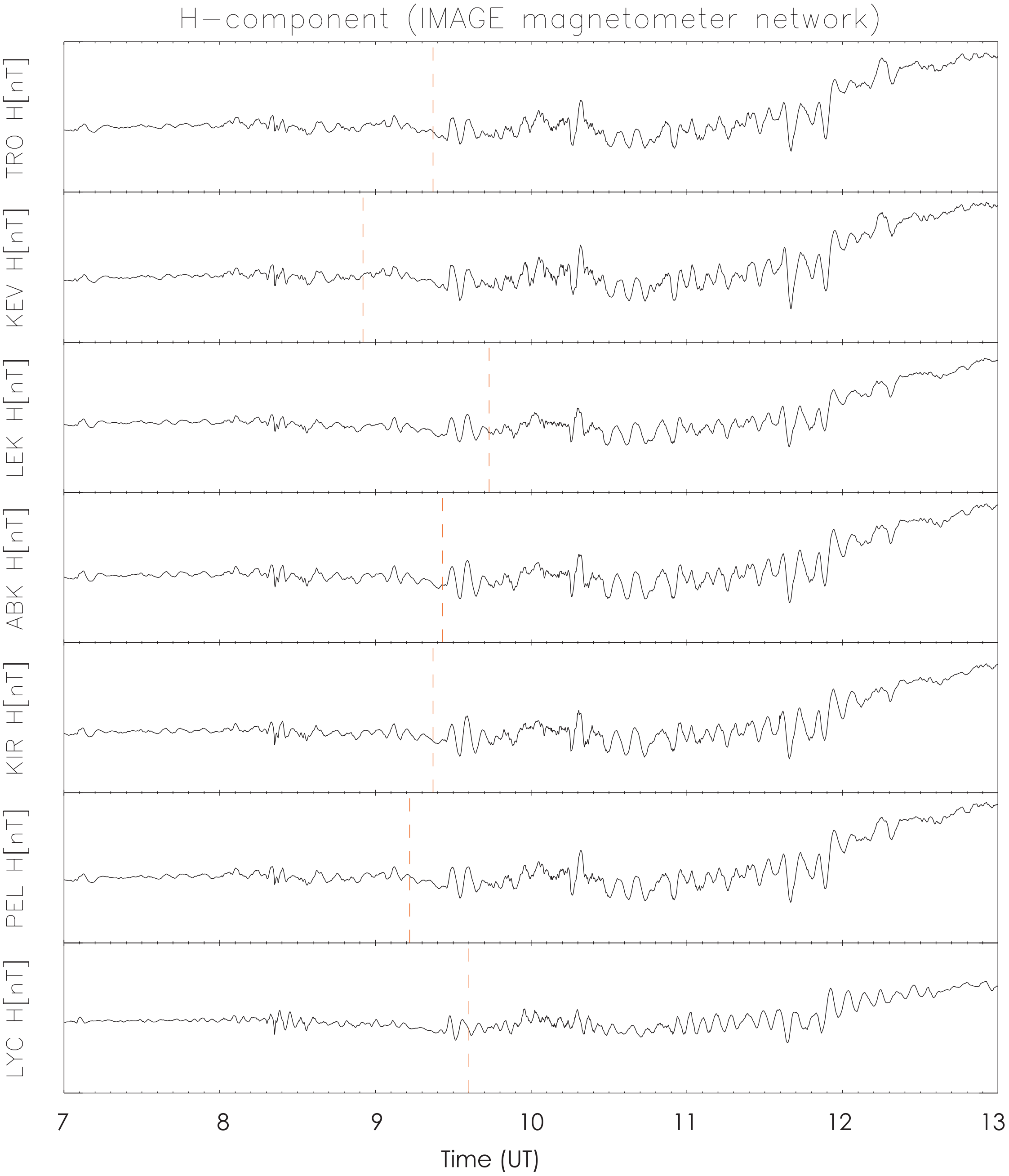

Figure 4.16: Magnetic field H-component during 0700-1300 UT from selected station from the IMAGE magnetometer array on March 28, 2001. Dashed red line shows local noon at each station.

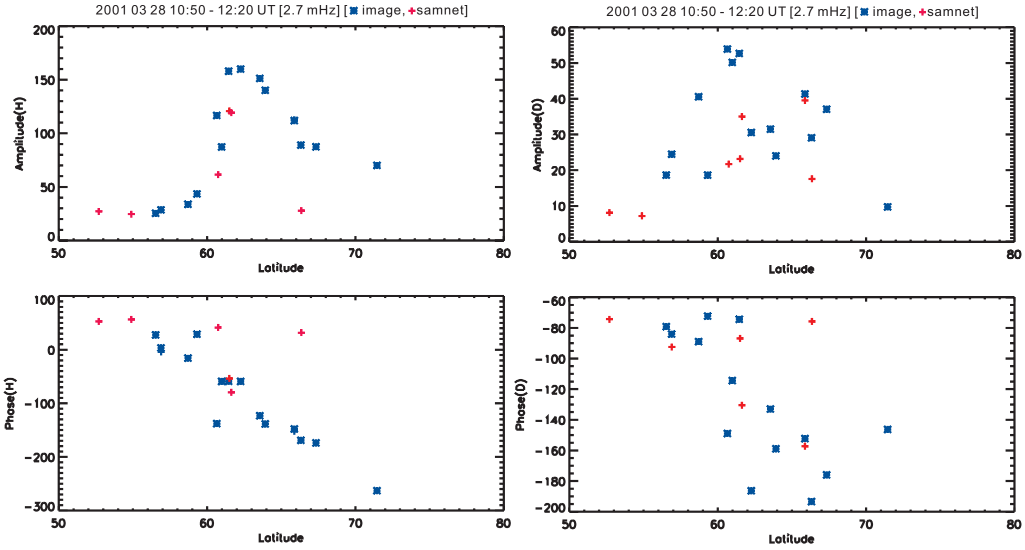

Figure 4.17: H- (left) and D-component (right) amplitude and phase as a function of latitude for the 1050-1220 UT interval on March 28, 2001.

amplitude peaks near 63° (L $\sim$ 4.9) and shows an approximately 180° latitudinal phase shift in the European stations. Similar to the March 24, 1991 event, the amplitude peak of this 2.7 mHz frequency wave occurred at much lower L-value than normal. On the other hand, D-component amplitude peak is less clear but show similar features as H-component.

Likely the explanation has the same reason as for the March 1991 event, that is an increased heavy ion content decreased the the eigenfrequencies in the same manner. Given that ULF wave power at low-L could energize radiation belt electrons through ULF wave enhanced drift-resonance [e.g., *Elkington et al.*, 2003], and we have seen similar behavior in both March 1991 and March 2001 storms, this suggests that thermal plasma and especially heavy ions might play a role in radiation belt dynamics through the intermediary of ULF wave penetration to L-shells in the heart of the outer radiation belt, and perhaps even beyond into the slot.

4.3.6 Interval C : March 29, 2001

Figure 4.18 illustrates the relationship between solar wind conditions and magnetospheric pulsations on March 29, 2001 (same format as Figure 4.12). During this interval the solar wind speed is gradually decreasing but intervals of solar wind density and dynamic pressure variations are present. No clear relationship between solar wind dynamic pressure and geomagnetic pulsations appeared. On the other hand, localized monochromatic waves were observed by GOES 8 and PBQ station located in the local morning.

Figure 4.19 shows solar wind conditions, magnetic field variation observed from GOES 8 and GOES 10 (top panel) and H-component perturbation observed from the ground-based magnetometers DAWS, PBQ, and KEV from 0800 to 1600 UT. GOES 8 shows toroidal (By) Pc5 oscillations at frequency 3.1 mHz in the local morning while GOES 10 located near midnight is quiet. PBQ (magnetically conjugate station to GOES 8) shows toroidal Pc5 oscillations simultaneously and in phase with GOES 8. The over-plotted green solid line in the bottom panel shows GOES 8 By component to compare with toroidal pulsation from PBQ station. These two wave forms show high coherency especially between 1100 and 1500 UT, indicating that the satellite and ground-based magnetometer are observing the same wave. These are spatially localized waves which show maximum amplitude in the morning and might be driven by Kelvin-Helmholtz instability.

4.3.7 Summary

Our observations show the concurrence of increases in ULF power in the solar wind dynamic pressure and in magnetic field fluctuations. During interval A, we

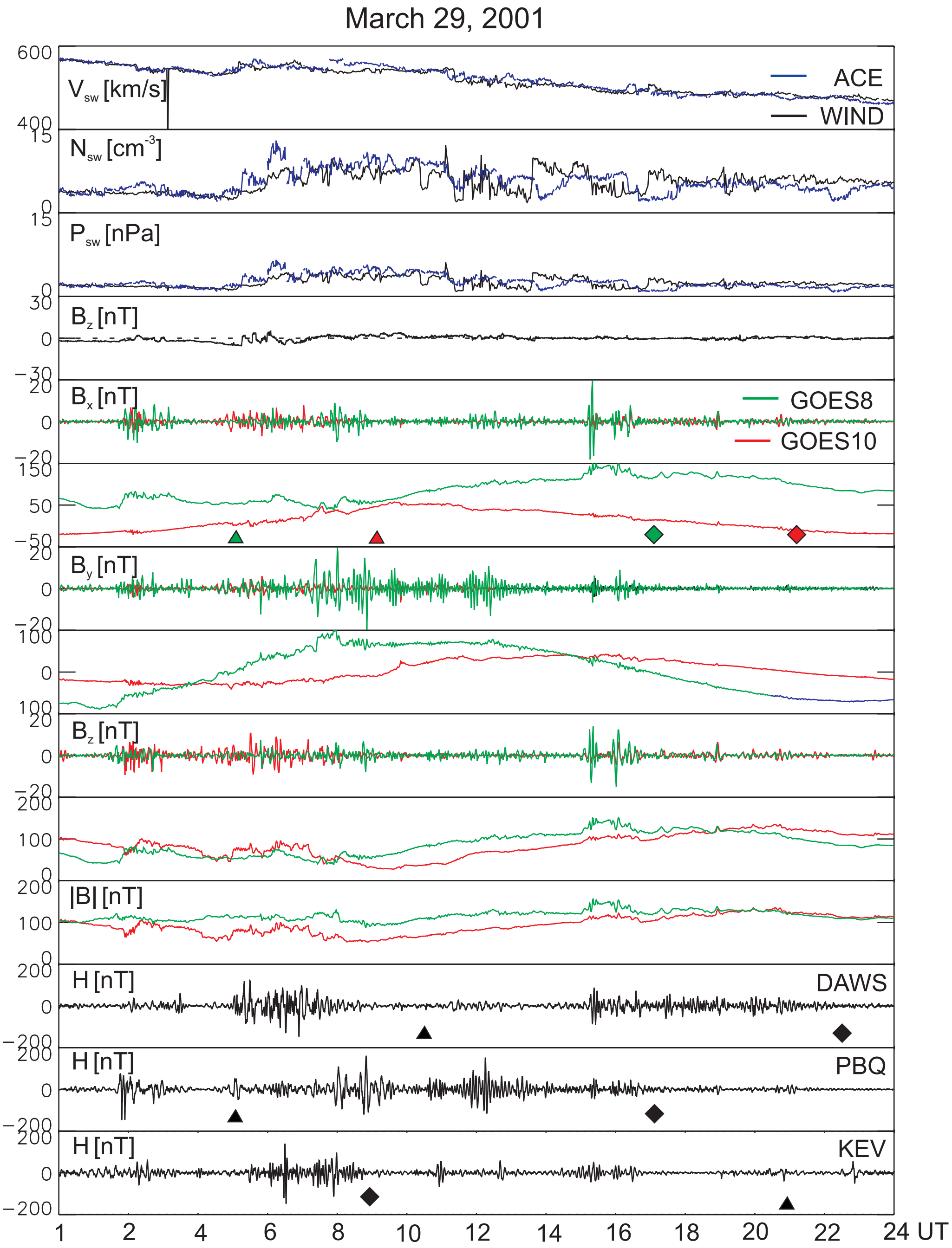

Figure 4.18: Solar wind parameters from ACE and WIND and magnetic fields observed from GOES 8, GOES 10, magnetic field H -component observed in the ground-based magnetometers at DAWS, PBQ and KEV. The triangles indicates local midnight and the diamonds indicate local noon.

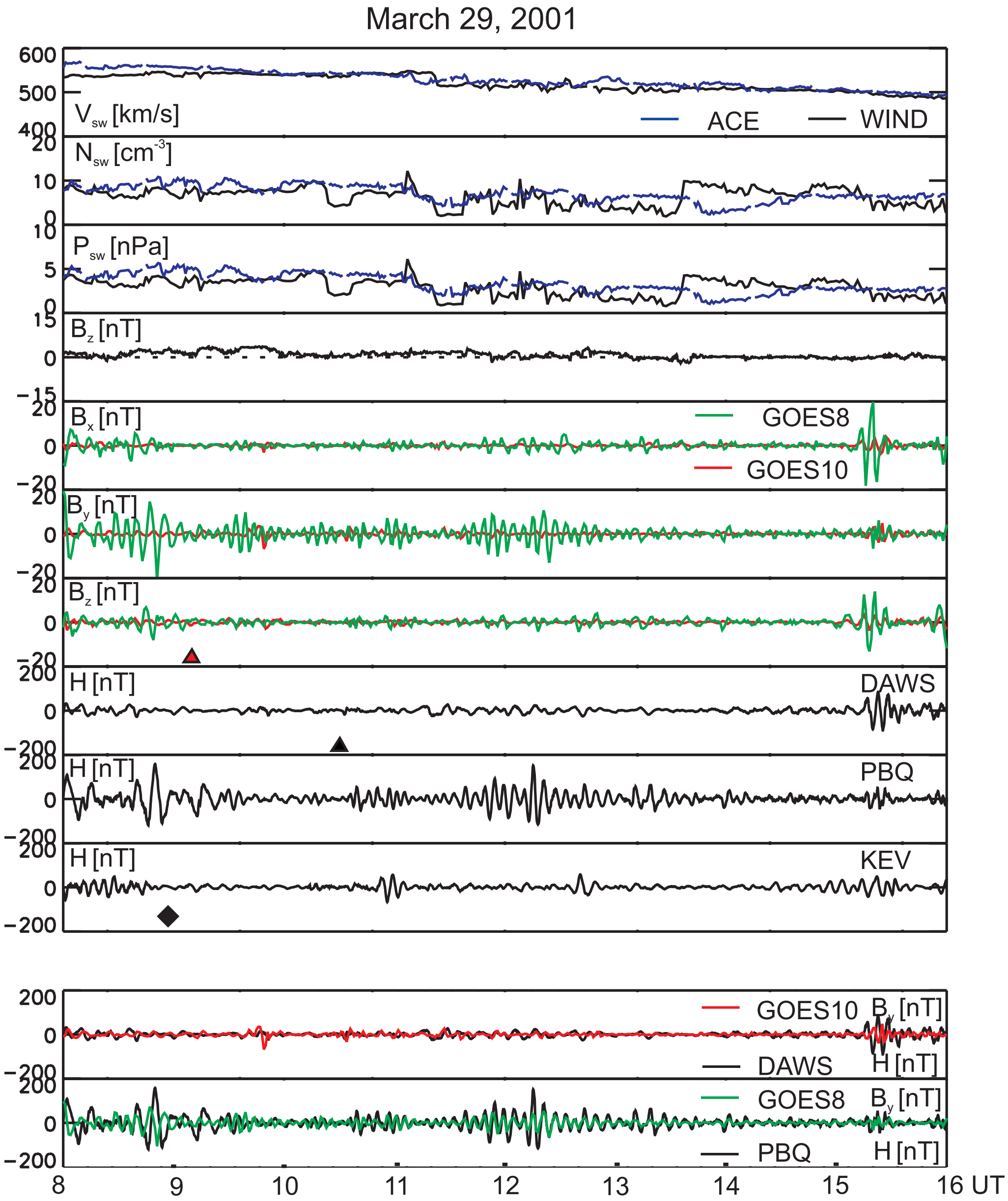

Figure 4.19: Magnetic fields observed from GOES 8, GOES 10, and magnetic field H-component observed at the ground-based magnetometers at DAWS, PBQ and KEV on March 29, 2001. DAWS and PBQ are closely magnetically conjugate stations to GOES 10 and GOES 8, respectively. The triangles indicates local midnight and the diamonds indicate local noon.

observed compressional waves in the dayside between 1700 and 2400 UT during the period of enhanced solar wind dynamic pressure. Also, during interval B on 28th March 2001, we observed magnetospheric wave power increased in direct response to the power of solar wind pressure fluctuations. Between 0800 UT and 1900 UT, both space- and ground-based observations show large amplitude waves across a broad range of frequencies. Large amplitude irregular compressional waves observed near local noon might be directly driven by density/dynamic pressure oscillations present in the ambient solar wind. Also, solar wind dynamic pressure show strong correlation with magnetic pulsations while solar wind speed is less correlated. These observations suggest that the solar wind dynamic pressure variation can be a direct source of geomagnetic pulsations. On the other hand, during interval C on 29th March 2001, we observed localized waves near morning in GOES 8 satellite and PBQ station which is magnetically conjugate to GOES8. The waves observed in these two stations show strong coherency and these waves might be driven by KHI instability.

4.4 Pc5 waves and magnetopause motion on July 28, 1990

4.4.1 Introduction

Many geosynchronous satellite observations show large inward motions of Earth's magnetopause near local noon [e.g., *Cumming and Coleman*, 1968; *Russell*, 1976; *Cahill and Winckler*, 1974]. Magnetopause crossing of satelllites in geostationary orbit have been observed and studied by [e.g., *Cahill and Winckler*, 1974]. Boundary magnetopause motions at geostationary orbit are usually associated with geomagnetic storms when the magnetopause location can move inwards of 6.6 Re, as compared to a equilibrium position at ∼ 10 Re during quite time. We observed magnotopause crossings at the GOES 6 and GOES 7 geostationary satellites during storm time on July 28, 1990. The GOES 6 and GOES 7 satellites were located near noon when a boundary magnetopause crossing was observed. We also observed very large amplitude Pc5 waves (2.7 mHz) on the ground at the same time interval during which we observed the GOES 6 and GOES 7 satellites magnetopause crossings. The focus of this study is an examination of the possibility that dayside Pc5 ULF wave excitation might be caused by magnetopause oscillation.

4.4.2 Data and Observations

We analyze ground-based magnetometer array and GOES 6 and GOES 7 satellite data during the onset day of the geomagnetic storm of 28th July 1990. Time-series magnetograms from the CARISMA magnetometer array, IMAGE and GOES 6 and GOES 7 were surveyed for this study (see Section 3.2). The time resolutions

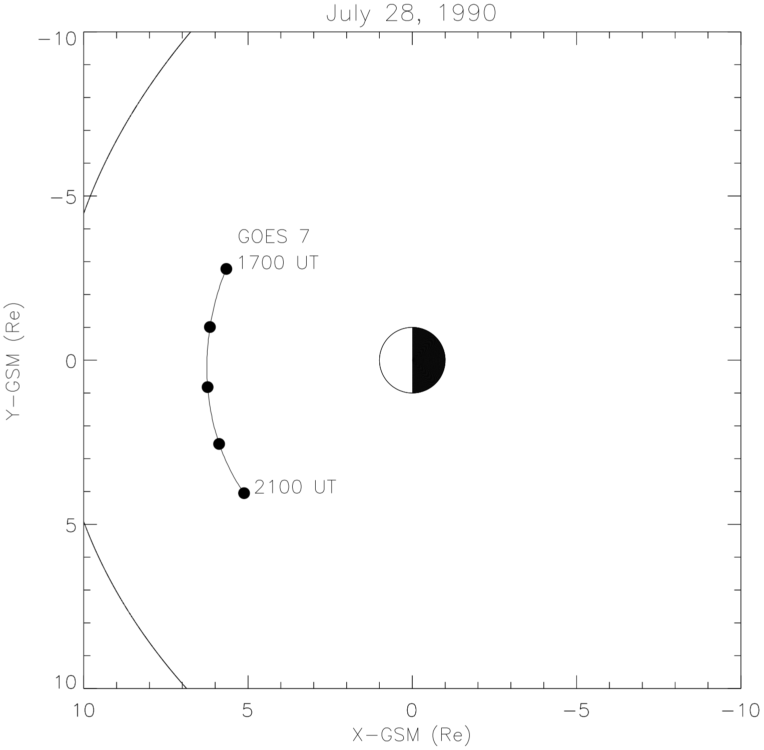

Figure 4.20: GOES 7 orbit trajectories in the time interval 1700 - 2100 UT on July 28, 1990.

for CARISMA, IMAGE, and GOES data are 5 s, 20 s and 3 s, respectively (see Appendix A. Table A3 and A3 for station information). Figure 4.20 shows the location of GOES 7 in the time interval 1700 - 2100 UT on July 28, 1990. The satellite location information was obtained from satellite situation center (SSCWeb) at http://sscweb.gsfc.nasa.gov/. The location of GOES 6 was not available during this time interval.

4.4.3 Magnetopause oscillations

Figure 4.21 shows the magnetic field H-component (north-south) observed from the CARISMA array. Very large amplitude pulsations appeared near local noon in all station (blue and yellow vertical lines indicate local morning and noon,

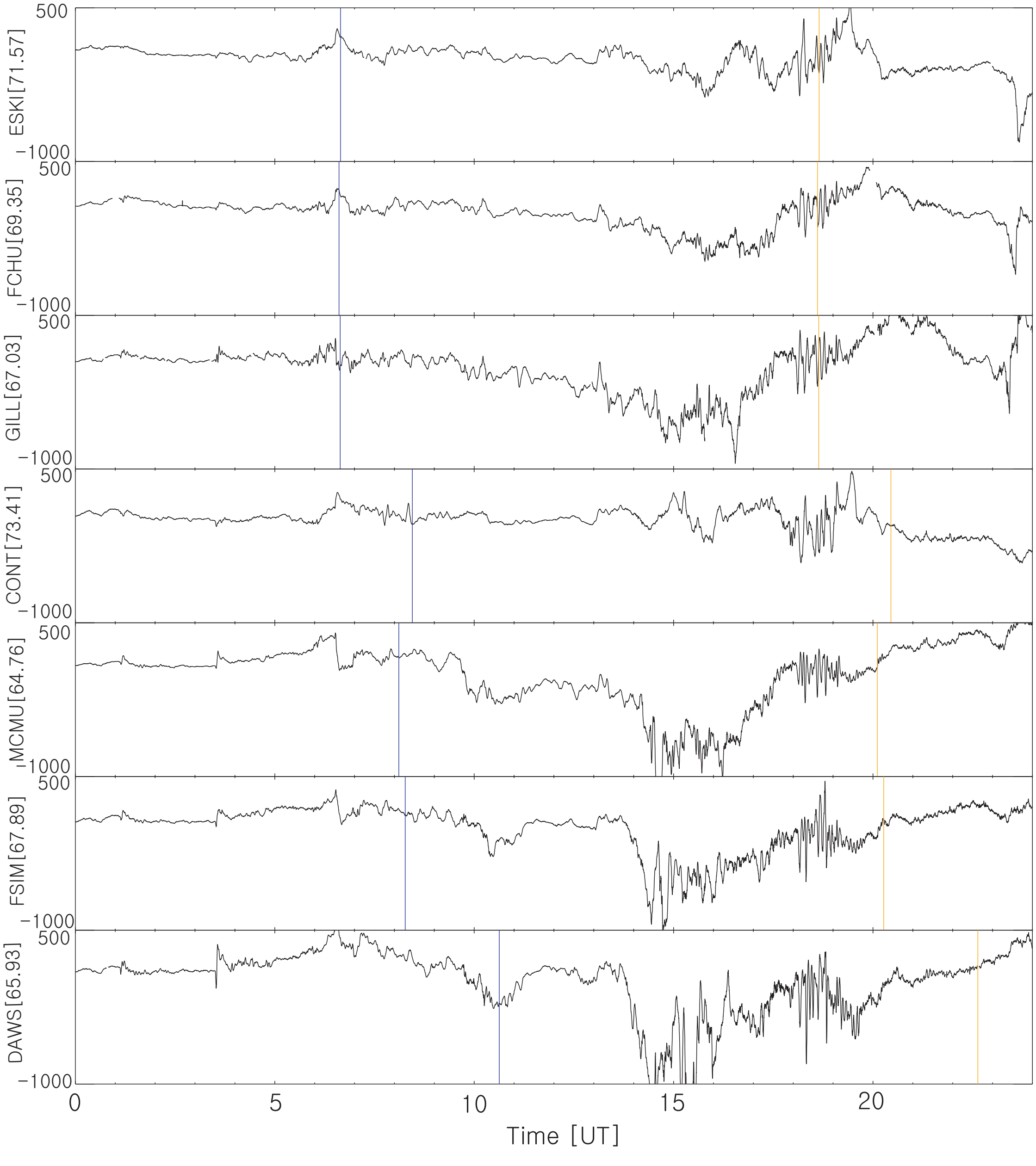

Figure 4.21: Magnetic field H-component observed in CARISMA magnetometer array on July 28, 1990

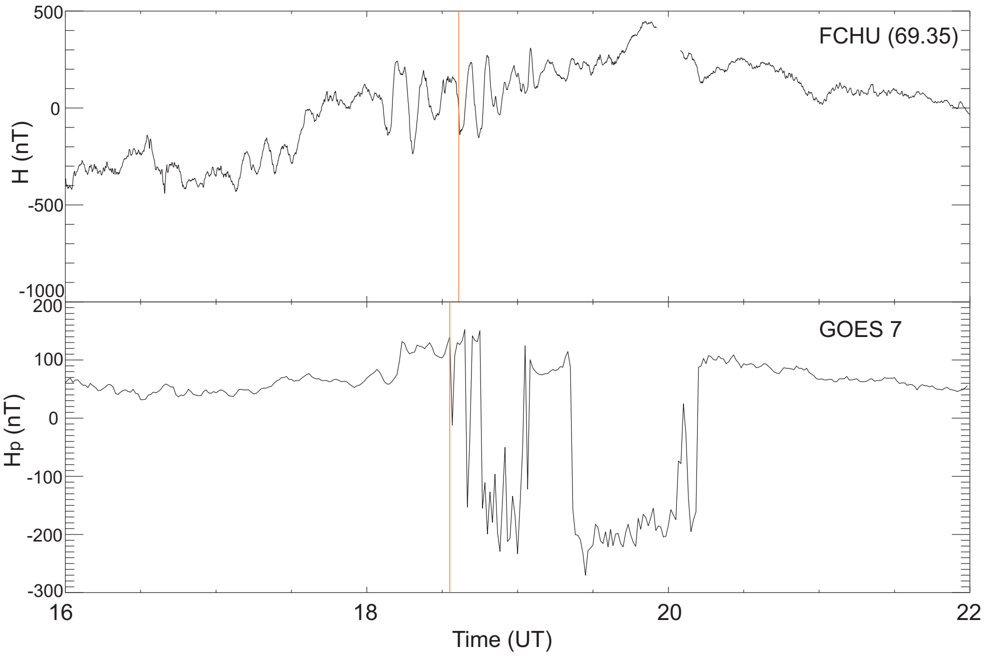

Figure 4.22: Magnetic field H-component from FCHU station and H_p component from GOES7 on July 28, 1990. Yellow vertical lines indicate local noon.

respectively). The 2.7 mHz frequency (375s period) pulsations appeared simultaneously and continued for around one hour. These waves were observed locally only near local noon in the period of the brief increase in Dst (see Figure 4.1 (c)). During this event, we observed geosynchronous satellite magnetopause crossings simultaneously with this increase in Pc 5 wave power. Perhaps repetitive variations in the solar wind dynamic pressure drove transient compression of the dayside magnetosphere observed by GOES 6 and GOES 7. Magnetopause crossing of geostationary satellites usually occurs during magnetic storms, due to a compression caused by an increase of solar wind dynamic pressure or by erosion of the magnetosphere by reconnection and transport of magnetic flux to the magnetotail[e.g., *Cahill and Winckler*, 1974]. The brief increase in Dst during the main phase implies compression of the magnetosphere may have been the cause of the magnetopause crossing in this case.

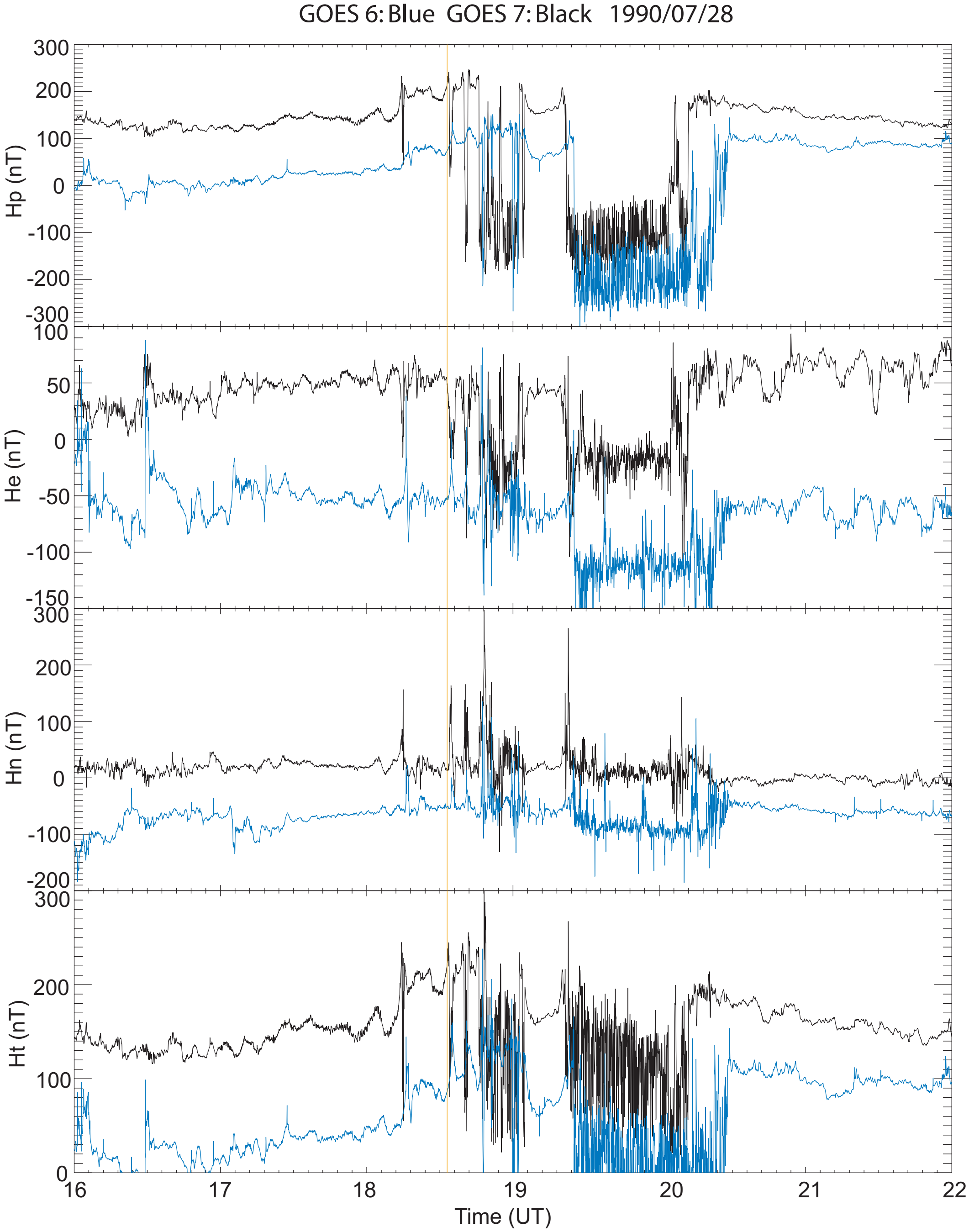

Figure 4.23: Magnetic field components from GOES 6 and GOES 7 on July 28, 1990. The data are shown in local spacecraft coordinates, such that H_p represents parallel component to spacecraft spin axis, H_e represents the earthward component, and H_n represents the eastward component. Yellow vertical lines indicate local noon.

Figure 4.22 shows geomagnetic pulsation (top panel) observed by the ground-based magnetometer at FCHU station of the CARISMA array and magnetic field H_p component observed at the GOES 7 satellite. Yellow vertical lines indicate local noon.

In this study we used three perpendicular magnetic field components from the GOES satellites to relate magnetopause motion to Pc5 pulsation activity. Figure 4.23 shows the magnetic field components, H_p, parallel to spacecraft spin axis, H_e, the earthward component, and H_n, the eastward component observed from geosynchronous satellites GOES 6 and GOES 7 (Blue: GOES 6, Black: GOES 7). At around 1830 UT, inward magnetopause motion at GOES 7 occurred and a magnetopause crossing occurred at GOES 6 a few minutes later. When the satellites cross the magnetosphere boundary into the magnetosheath, the H_p component changes dramatically. The H_p components in Figure 4.23 shows large changes within a few minutes which implies a magnetopause crossing. *Cahill and Winckler* [1974] investigated when the magnetopause crossings took place during storms. They found that main-phase magnetopause crossing events could take place during relatively brief increases in Dst during the main phase. These increases in Dst were due to the effects of brief compression of the magnetosphere, superimposed on a background decrease in Dst decreasing due to enhancement in the ring current. The magnetopause crossing observed on July 28 1990 also took place during an increase in Dst during the main phase probably due to a brief compression of the magnetosphere. In addition, the frequency of magnetic field fluctuations observed from GOES7 at the magnetopause was 2.7 mHz which is consistent with the frequency observed in the ground magnetometers (Figure 4.25). This supports the hypothesis that the possible energy source for this pulsation was periodic variation in solar wind dynamic pressure and hence periodic

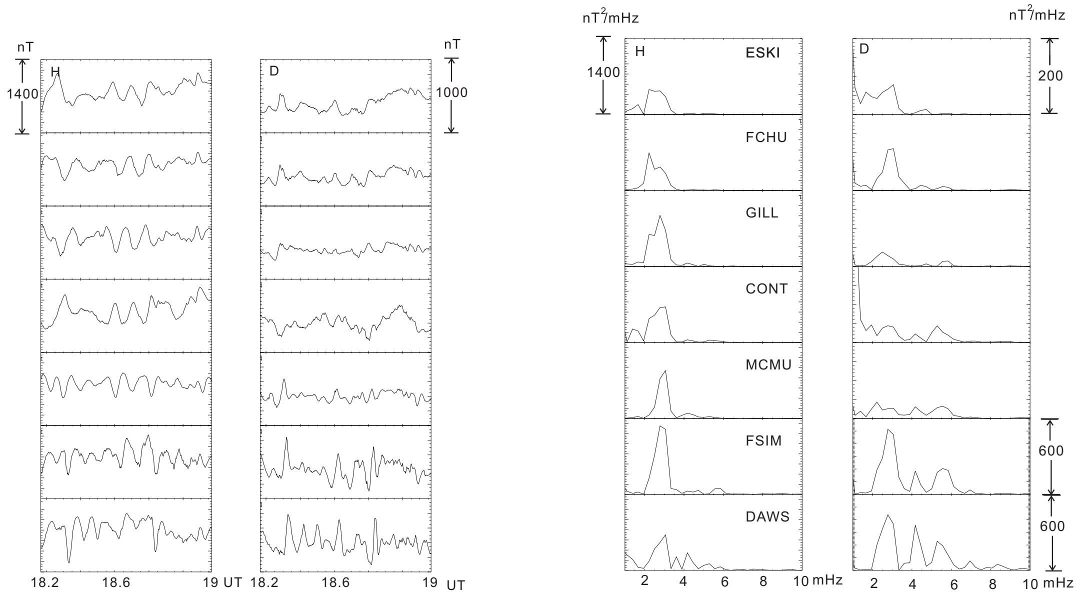

Figure 4.24: Magnetic field H- and D-component (left) and corresponding spectra (right) from CARISMA magnetometer array on July 28, 1990.

motion of the magnetopause and periodic compression of the magnetosphere.

Figure 4.24 shows magnetic field H- and D-components observed by the CANOPUS/CARISMA magnetometer array and their corresponding spectra. Very large amplitude 2.7 mHz pulsations appeared simultaneously at all latitudes. The wave amplitude is clearly dependent on latitude and the H-component is more dominant than the D-component during the time interval 1810-1910 UT. Similarly, Figure 4.25 shows magnetic field components and their spectra observed from GOES 6 and GOES 7 from the interval 1810 to 1920 UT and shows clear pulsations at 2.7 mHz as well, and which is especially clear in H_p and H_t as expected.

To complete a phase and amplitude analysis of the waves, we used complex demodulation [e.g., *Beamish et al.*, 1979] which provides instaneous values of pulsation amplitude, phase and polarization at a specific frequency through comparison to a reference signal. Figure 4.26 shows the amplitudes and phases as a function of latitude of 2.7 mHz pulsation in the time interval 1810-1910 UT.

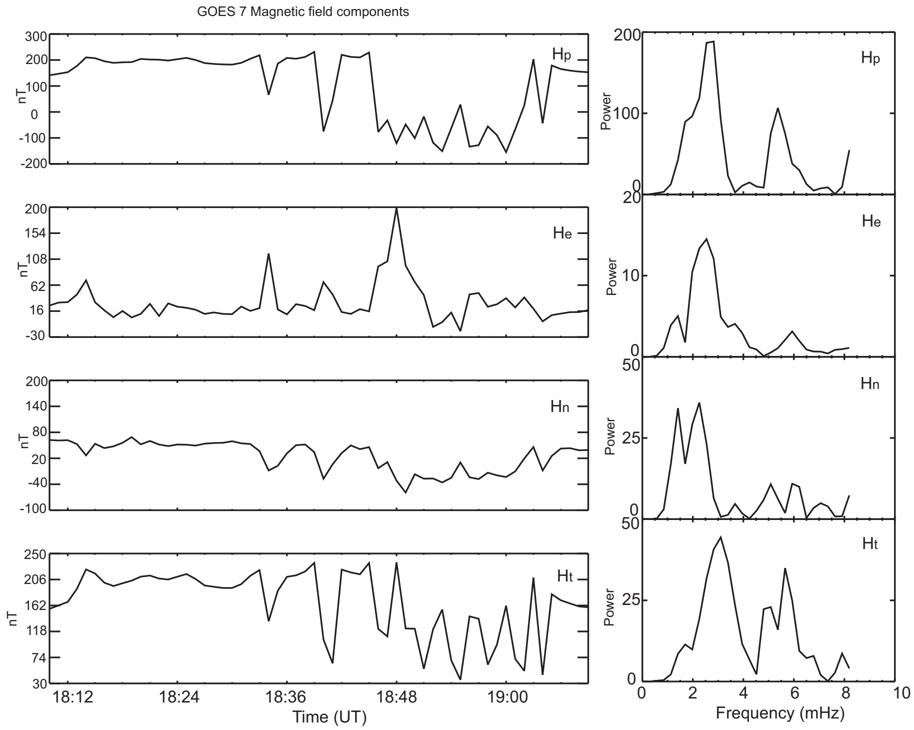

Figure 4.25: Magnetic field components (left), H_p, H_e, H_n, H_t and their power spectra (right) observed from GOES 7 on July 28, 1990.

These pulsations all have the characteristic features of FLRs, with a latitudinally narrow peak in power, accompanied by an 180^o latitudinal phase shift [e.g., *Walker et al.*, 1979]. The resonant latitude for the H-component is around 70^o in CGM coordinates.

4.4.4 Summary

We observed very large amplitude geomagnetic pulsations near local noon on the CARISMA array. On the basis of H_p (geomagnetic field northward component) observed from GOES 6 and GOES 7, we observed magnetopause boundary crossing events in the same time interval that we observed large geomagnetic perturbations on the ground. This supports the hypothesis that the possible energy source for this pulsation was periodic variation in solar wind dynamic

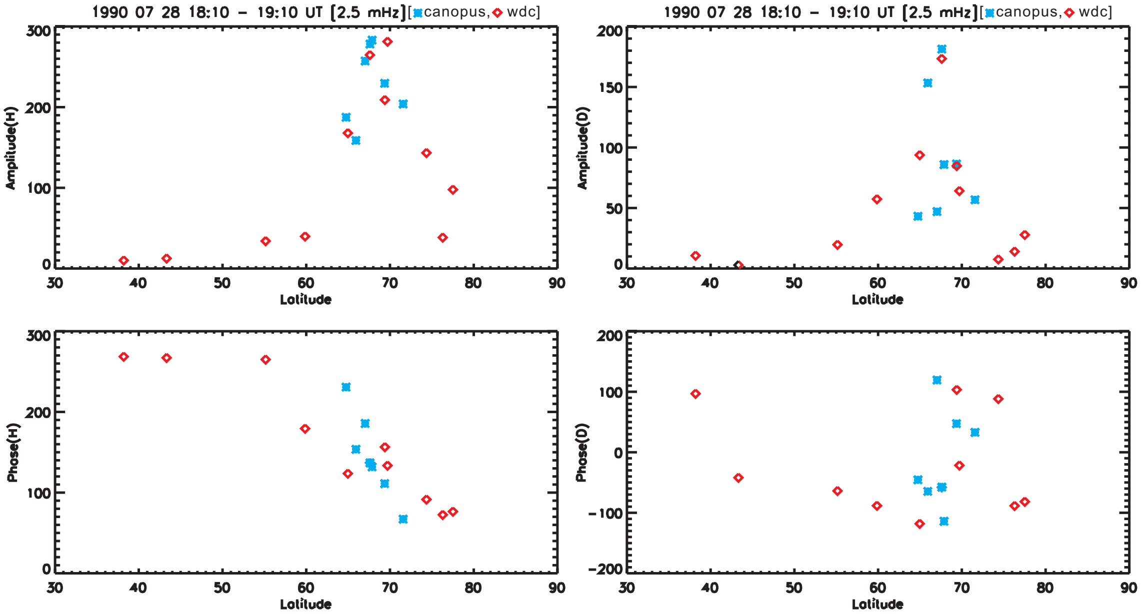

Figure 4.26: H- and D-component amplitude (left) and phase (right) in the interval 1810-1910 UT on July 28, 1990.

pressure, causing a periodic motion of the magnetopause and a injection of ULF wave compressional energy into the magnetosphere. This is the first time that magnetopause oscillations have been identified as the direct drive of Pc 5 ULF waves of the same frequency, to our knowledge.

4.5 Conclusions

In this Chapter, we presented observational studies of Pc 5 pulsations using ground-based magnetometer and satellite data during geomagnetic storm times. To identify the excitation source mechanisms of magnetospheric pulsations we observed three storm time events, (A) March 24, 1991, (B) March 27-29, 2001, and (C) July 28, 1990 were selected for detailed analysis. Each showed a brief increase in Dst in the main phase of the storm due to the compression of the magnetosphere during the development of the ring current in the main phase.

We suggest two major excitation mechanisms observed during these three storm time, cavity/waveguide modes driven by (1) the periodic variations in solar wind dynamic pressure and (2) Kelvin-Helmholtz instability. Pc 5 ULF waves driven by solar wind dynamic pressure appeared during the period of a brief increase in Dst in the main phase (see Figure 4.1). Global oscillation of 1.7 mHz on March 24, 1991, 1 - 3 mHz frequency range oscillations on March 28, 2001 and 2.7 mHz oscillations observed on July 28, 1990 might be driven by solar wind dynamic pressure pulses. During March 24, 1991 and July 28, 1990, there is no solar wind data to confirm the relationship between Pc 5 geomagnetic pulsations and the solar wind dynamic pressure variations. However, during March 28, 2001, we have solar wind data observed from ACE and WIND. Geomagnetic field variations observed on the ground and on geosynchronous satellites and solar wind dynamic pressure variations showed a strong correlation. These observations suggest that solar wind dynamic pressure variations are the direct source of the geomagnetic pulsations. On the other hand, we also observed Pc 5 pulsations in the local morning sector. The 2.8 mHz pulsations on March 24, 1991 show largest amplitude in dawn flank. Also, Pc 5 pulsations observed on 29th of March 2001 show localized monochromatic waves in dawn flank from the GOES satellites data and ground-based magnetometer data. This local time dependence of Pc 5 pulsation wave power is consistent with the magnetopause shear-flow instability which is greater on the magnetospheric flanks than at the sub-solar point. Table 4.1 summarize Pc 5 pulsations observed during three storm time intervals and their excitation mechanisms.

The observed pulsations during these three events (A), (B), and (C) showed typical features of FLRs such as an amplitude peak and phase change across the resonant L-shell. For example, during 24th of March 1991 event, we observed that

FLRs were excited at L $\sim$ 4.3 for 1.7 mHz pulsations. This FLR latitude was unusually much lower than normal. The cross-phase determined eigenfrequency of the field line at this latitude is hence also lower than under more typical magnetospheric conditions. The possible reasons for the reduction of the local Alfvén eigenfrequency continuum as compared to non-storm times might be due to the heavy ions such as O^+. The injected O^+ along the field-lines from the ionosphere could contribute to the radiation belt dynamics via the intermediary of Pc 5 ULF waves. This hypothesis lead us to study Pc 5 ULF wave-particle interaction and the study of Pc 5 ULF wave-particle interactions will be presented in Chapter 5.

Interval	ULF Waves	Frequency	MLT Amplitude Peak	Low-L FLR	Dst	Wave Source
0815 - 0915 UT on March 24, 1991	monochromatic discrete frequency, global	2.8 mHz	local morning	Yes	decrease	cavity/waveguide, KHI
1200 - 1340 UT on March 24, 1991	monochromatic discrete frequency, global	1.7 mHz	local post-noon	Yes	increase	cavity/waveguide, solar wind dynamic pressure pulses
1700 - 2400 UT on March 27, 2001	multiple packets of discrete frequency, local	1-5 mHz	local noon	No	increase	increase in solar wind dynamic pressure (P_{sw})/ P_{sw} pulsations
0800 - 1830 UT on March 28, 2001	multiple packets of discrete frequency, global	1-3 mHz	all LTs	No	increase	broad band solar wind dynamic pressure pulses with same frequency
1050 - 1220 UT on March 28, 2001	monochromatic discrete frequency, local	2.7 mHz	local post-noon	Yes	increase	cavity/waveguide, solar wind dynamic pressure pulses
0800 - 1600 UT on March 29, 2001	monochromatic discrete frequency, local	3.1 mHz	local morning	No	decrease	cavity/waveguide mode, KHI
1810 - 1920 UT on July 28, 1990	monochromatic discrete frequency, local	2.7 mHz	local prenoon	No	increase	cavity/waveguide, solar wind dynamic pressure pulses

Table 4.1: Summary of Pc 5 Pulsations observed during three case studies and their excitation mechanisms

Chapter 5

Pc 5 ULF Wave-Particle Interactions

5.1 Introduction

The Van Allen radiation belts contain a population of energetic charged particles which are extremely variable, the flux being variable in space and energy increase over more than two orders of magnitude over intervals less than one day [e.g., *Blake et al.*, 1992] (The composition of particles, and their energy ranges in the radiation belts are discussed in Section 1.7). There has been increased interest in relativistic electron dynamics in the inner magnetosphere mainly due to the correlation between the occurrence of enhanced relativistic electron flux [e.g., *Hudson et al.*, 1995] and spacecraft operational anomalies or even failures [e.g., *Baker et al.*, 1994].

Relativistic electron events are often observed during great storms associated with ULF waves. For example, a large build up of relativistic electrons was observed during the great storm of March 24, 1991 [e.g., *Li et al.*, 1993; *Hudson* *et al.*, 1995] and during the Hollowe'en storms period from October 29 to November 4, 2003 [e.g., *Baker et al.*, 2004; *Horne et al.*, 2005]. However, the dominant processes which accelerate magnetospheric electrons to MeV energies are not well-understood. Many recent observations have suggested that enhancements in the flux of energetic electrons are closely associated with ULF waves in Pc 4 (7-22 mHz) or Pc 5 (1-7 mHz) frequency ranges [e.g., *Rostoker et al.*, 1998; *Mathie and Mann*, 2000b]. Furthermore, the observation of the modulation of energetic electron and proton fluxes in the Pc 5 range implies that energetic particles and Pc 5 ULF waves are closely related [e.g., *Southwood and Kivelson*, 1981; *Higbie et al.*, 1982; *Takahashi et al.*, 1985]. *Elkington et al.* [1999, 2003] also suggested that relativistic electrons can be accelerated via drift resonance with Pc 5 ULF waves.

In this chapter we examine the relationship between Pc 5 ULF waves and energetic particle flux in the radiation belts during geomagnetic storms. Specifically, we examine the Pc 5 ULF wave interaction with energetic particles in the outer radiation belt in a series of case studies. The case studies are presented investigating simultaneous observations of ULF waves with ground- and space-based magnetometers as well as their effect on energetic particles using in-situ particle detectors. All three events were observed in the main or recovery phase of geomagnetic storms.

In section 5.2, we discuss global Pc 5 pulsations in the main phase of the March 24, 1991 storm at unusually low-L (see also Chapter 4, Section 4.2). In section 5.3, we study the electron and proton flux modulations in the recovery phase of the geomagnetic storm of July 16, 2000. Finally, in section 5.4 we report the modulation of electron and proton flux near local noon during the recovery phase of the geomagnetic storm on June 09, 2000.

Figure 5.1 shows magnetic field line traces using the Tsyganenko 04 magnetic field model [*Tsyganenko and Sitnov*, 2005] (a) during a quiet time on March 16, 2000 and (b) during a geomagnetic storm time on March 31, 2001. During a quiet time, magnetic field lines reach up to L = 10 in the dayside. On the other hand, during a geomagnetic storm time, the magnetopause can be compressed to near L $\sim$ 7 and magnetic field in the tail can become highly stretched. Figure 5.2 shows the contours of constant magnetic field using the Tysganenko 04 magnetic field model [*Tsyganenko and Sitnov*, 2005] (a) during a quiet time on March 16, 2001 and (b) during a geomagnetic storm time on March 31, 2001. Particles drift along contours of constant magnetic field magnitude. Thus, particles will drift in a circular trajectory during a quiet time while particles will drift in a compressed dipole trajectory during a storm time as shown in Figure 5.2 (b). In the following sections, we study energetic particle behavior during geomagnetic storm times. Thus, we will assume that magnetic field lines are more compressed in the dayside and stretched in the nightside than at quiet times. In the absence of any applied external electric field, the drift period for MeV electrons is $\sim 1-10$ minutes which is also in the frequency range of Pc 5 ULF waves. Thus, Pc 5 (1-10 minutes) period waves can potentially resonantly interact with electrons drifting in the radiation belt.

Our goal is to examine the mechanisms of energetic particle interactions with Pc 5 ULF waves during magnetic storm times. Previous studies have reported flux modulations by adiabatic acceleration, convection of density gradients, and the mirror effect [e.g., *Southwood and Kivelson*, 1981; *Takahashi et al.*, 1985] (see Chapter 2). However, the importance of this modulation as related to MeV electrons has not been widely discussed. We suggest in this Chapter that particle flux can be modulated via drift-resonance, or through the advection of a density gradient. As shown in Figure 2.8 in Chapter 2, the relative locations of the waves and the satellite are also important in determining whether a flux modulation will be observed by any given satellite platform.

(a)

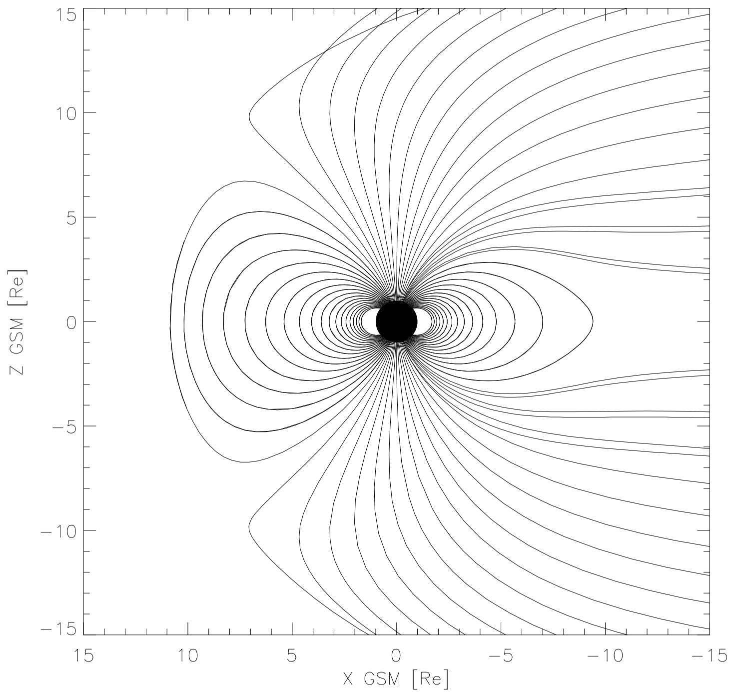

(b)

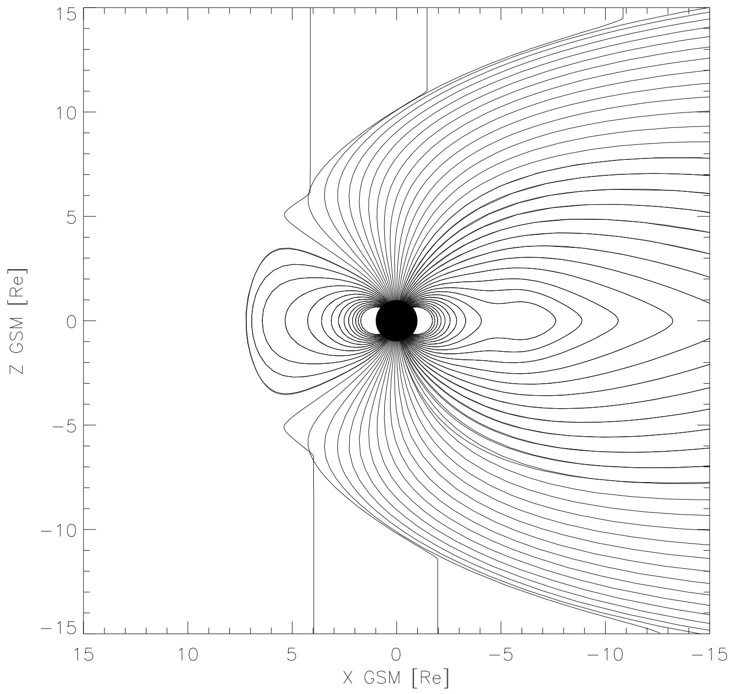

Figure 5.1: Magnetic field line traces using a Tsyganenko 04 magnetic field model [*Tsyganenko and Sitnov*, 2005] (a) during a quiet time (March 16, 2001) and (b) during a geomagnetic storm time (March 31, 2001).

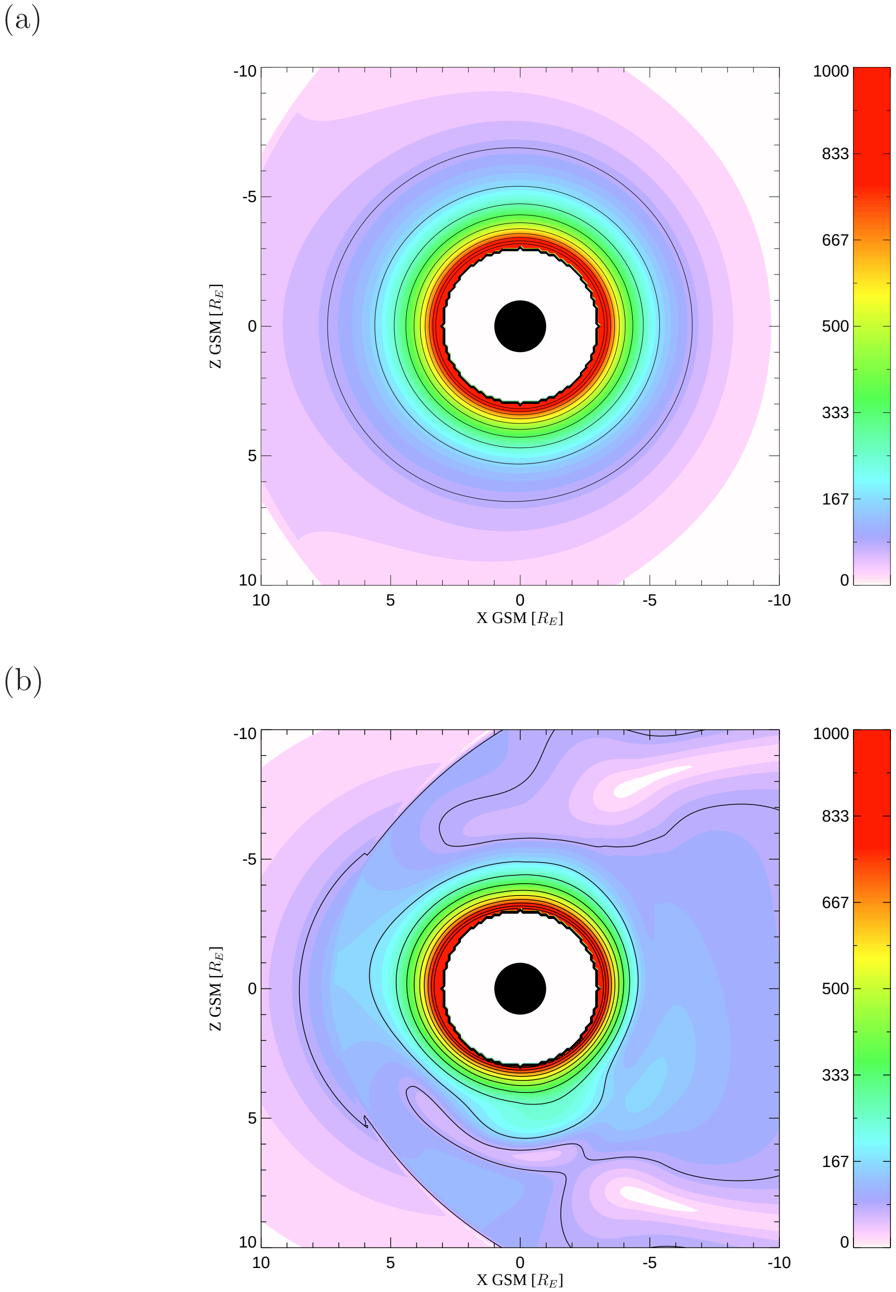

Figure 5.2: Contours of constant magnetic field strength using a Tsyganenko 04 magnetic field model $|\mathbf{B}|$ [*Tsyganenko and Sitnov*, 2005] (a) during a quiet time (March 16, 2001) and (b) during a geomagnetic storm time (March 31, 2001).

5.2 Case Study 1 : March 24, 1991

In section 4.2 we reported Pc 5 FLRs on this day at the unusually low L-shell of L $\sim$ 4 which suggests a significant reduction in the local Alfven eigenfrequency continuum as compared to non-storm times. This could have considerable significance for the interaction between ULF waves and MeV electrons in the outer radiation belt. Several authors have reported the enhancement of relativistic electrons during the March 24, 1991 storm [*Li et al.*, 1993; *Hudson et al.*, 1995]. During the great geomagnetic storm event of March 24, 1991 storm, the CRRES satellite observed that a new electron radiation belt formed around L $\sim$ 2.6 in a less than one minute [*Li and Temerin*, 2001]. Also, *Blake et al.* [1992] observed an injection of greater than 13 MeV electrons from the CRRES satellite. One of the sources of electron acceleration could be an interaction between particles and ULF waves, in addition to the shock acceleration which is also known to have occurred during this time [*Li et al.*, 1993]. We examine the relationship between energetic particles and ULF waves and discuss the possible mechanisms which may be responsible.

5.2.1 Instrumentation

We used magnetic field data from the IMAGE magnetometer array, and particle data from the MEA spectrometer of the CRRES satellite and the SOPA particle detectors on board the LANL geostationary satellites (specifically LANL 1989-046 and 1990A-095). Figure 5.3 shows the location of the LANL 1990A-095, LANL 1989-046 and CRRES spacecraft between 1000 and 1300 UT on 24 March 1991. All three satellites were located in the nightside. Both LANL satellites are in geosynchronous orbit at L = 6.67 but CRRES is approaching the Earth during

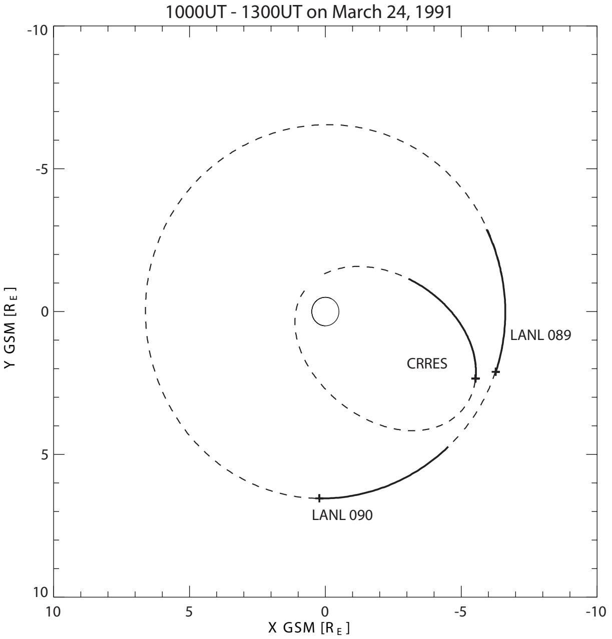

Figure 5.3: Trajectory of LANL90, LANL89, and CRRES satellites during the time interval 1000-1300 UT on March 24, 1991. Crosses show the beginning of each orbital element.

this time on L-shell changing from 6.8 to 3.9.

5.2.2 Variation of Energetic Particle Flux and Magnetic Field

Figure 5.4 shows the Dst index, the flux of 1.1 - 1.5 MeV electrons and the flux of > 7.7 MeV protons observed from LANL 1989-046. On March 24, 1991 a great geomagnetic sudden storm commencement (SSC) occurred around 0341 UT almost simultaneously at each station [*Araki et al.*, 1997] and led to the development of a great geomagnetic storm. A brief increase in Dst in the main phase of the storm implies compression of magnetosphere, superimposed on the decrease due to the ring current. During the recovery phase, the electron flux is enhanced at $L \sim 6.67$, while the proton flux was enhanced in the main phase

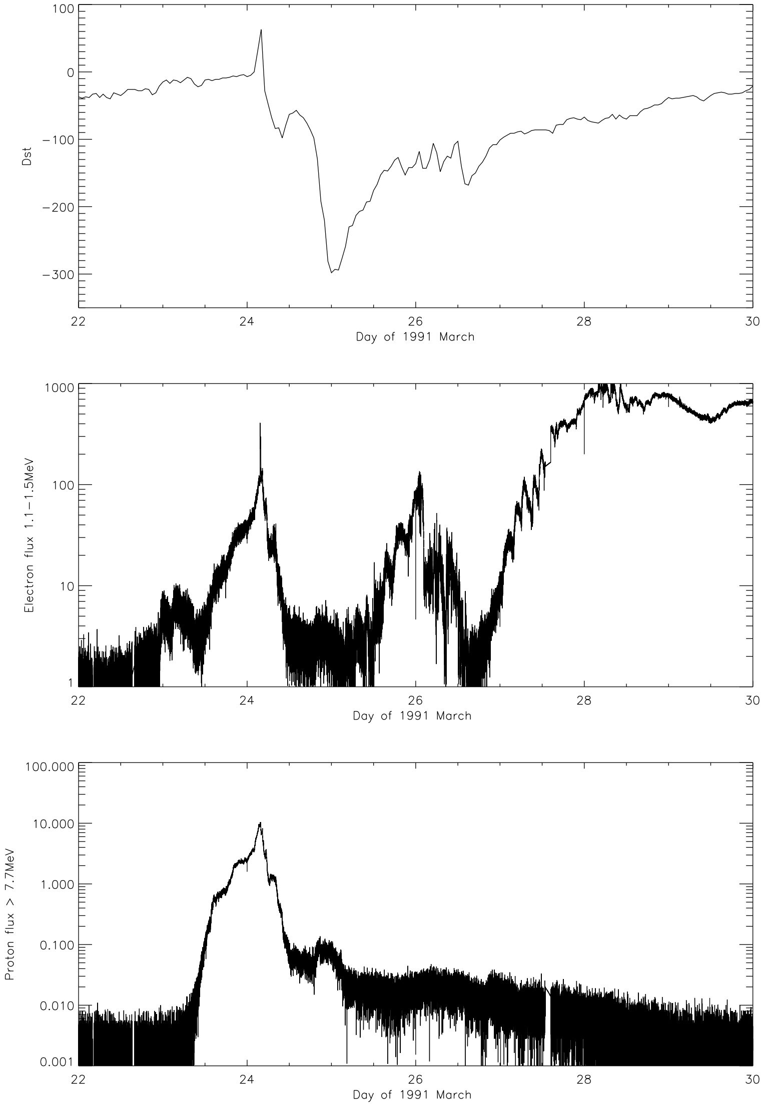

Figure 5.4: From the top : Dst index, electron flux (1.1-1.5 MeV) and proton flux ($>$ 7.7 MeV) from LANL 1989-046.

of the storm. Typically, high-energy electron flux drops during the main phase of the storm until the Dst index reaches a minimum value. Subsequently, the electron flux can increase to a larger value than before the storm during the recovery phase.

In the main phase of this storm, we have observed global Pc 5 ULF waves in the ground magnetometer arrays (see Chapter 4 Section 4.2). Figure 5.5 (a)

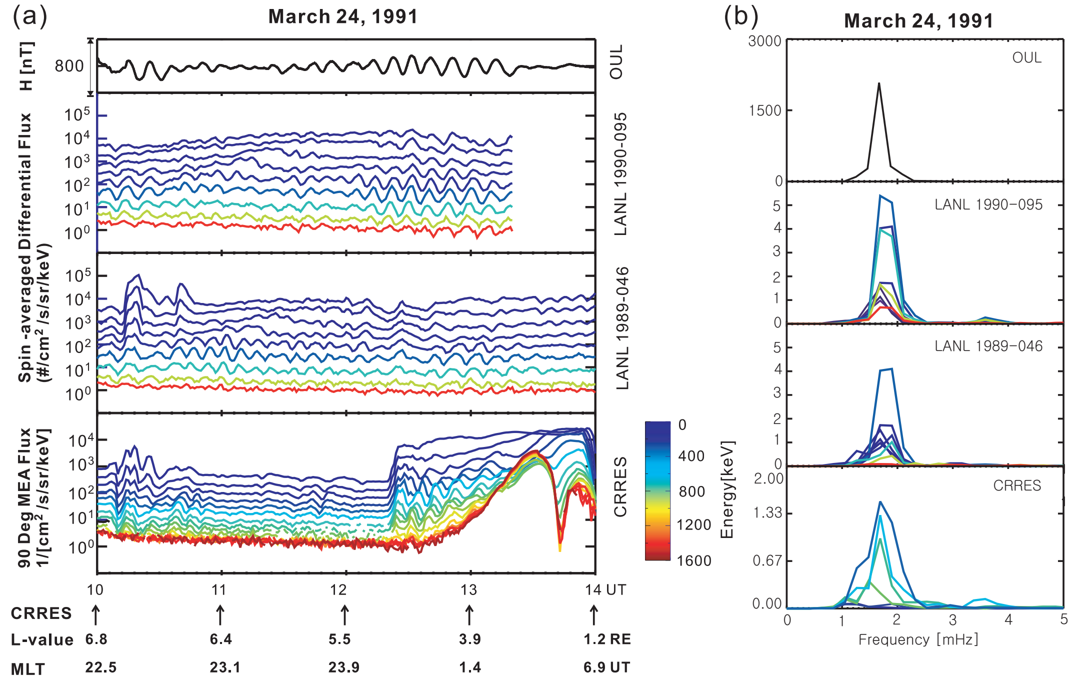

Figure 5.5: (a) H-component of magnetic field observed in the OUL station, omnidirectional differential flux of energetic electrons observed by the SOPA instrument on board the 1990-095 and 1989046 at geosynchronous orbit, and differential electron flux at 90° picth angle measured on CRRES (panels from top to bottom). L-value and MLT of CRRES are marked in x-axis. (b) Corresponding spectra on March 24, 1991 for 1200-1330 UT.

shows, from top to bottom, the magnetic field H-component from the ground-based magnetometer at Oulu station from the SAMNET magnetometer array, the omni-directional differential electron flux amplitude from LANL 1990-085 and LANL 1989-046, and the differential electron flux at 90° pitch angle from CRRES during the interval 1000 - 1400 UT. Figure 5.5 (b) shows the corresponding spectra of Figure 5.5 (a) during the time interval 12:00 -13:30 UT. Different colors in Figure 5.5 (a) indicate different energies. In the case of LANL 1990-085 and LANL 1989-046 the energy ranges are 50-75 keV, 75-105 keV, 105-150 keV, 150-225 keV, 225-315 keV, 315-500 keV, 500-750 keV, 0.75-1.1 MeV, and 1.1-1.5 MeV from the top to bottom. In the case of CRRES the energies vary as 214

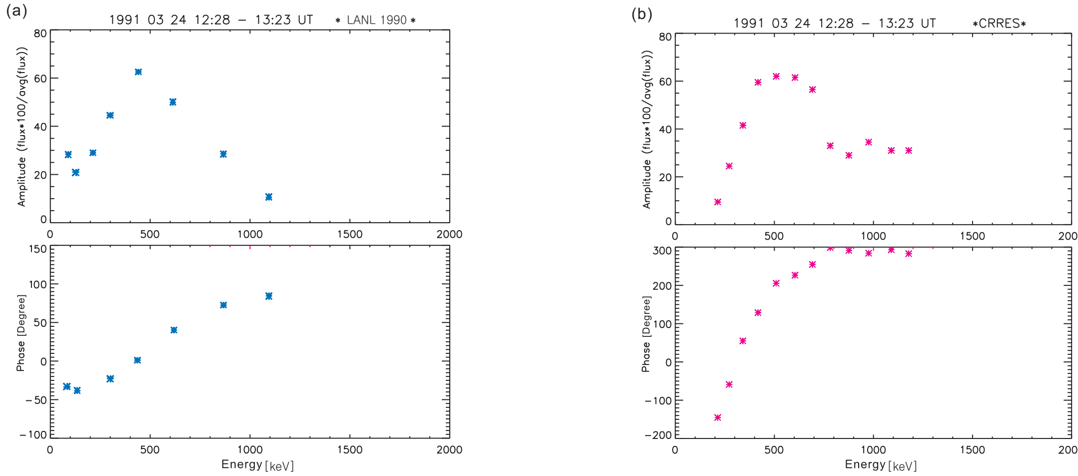

Figure 5.6: Differential electron flux amplitude and phase of 600s period fluctuations as a function of energy at LANL 1990-085 (a) and CRRES (b) for 1228 - 1323 UT on March 24, 1991.

keV, 272 keV, 341 keV, 417 keV, 509 keV, 604 keV, 692 keV, 782 keV, 876 keV, 976 keV, 1090 keV, 1178 keV, 1288 keV, 1368 keV, 1472 keV, 1581 keV from the top to bottom.

In Figure 5.5 (b), both magnetic field and electron flux show monochromatic pulsations with a spectral peak at the same frequency ($\sim$ 1.7 mHz). The strong relationship between particle flux and magnetic field before the enhancement of energetic electrons implies that the mechanism which enhances the MeV electron flux might be related to the interaction between energetic electrons and ULF waves. LANL 1990-095 and 1989-046 stay in geosynchronous orbit at L = 6.67 and the electron flux oscillates with a phase change across the different energy channels. On the other hand, CRRES moves in L-value from 6.8 to 1.2 R_E and after 1220 UT the electron flux oscillation starts with a large phase changes across the different energy channels. Also, from the power spectra (Figure 5.5 (b)), we notice that the amplitude of the electron flux oscillations depends on energy.

Using complex demodulation we plot the amplitude and phase of the dominant frequency (1.7 mHz) response of the electrons as a function of energy channel for (a) LANL 1990-085 and (b) CRRES in Figure 5.6. There is an amplitude peak at an energy of 315-500keV and ~ 130 ° phase change with energy across the peak in the case of LANL 1990-085, while a $\sim 450°$ phase change was observed across the peak at an energy of ~ 509 keV in the case of CRRES. As mentioned in Chapter 2, a drift resonant flux modulation might be expected to show the characteristic of a resonance such as an amplitude peak and phase change across the resonant energy. The reason that the phase change observed by CRRES is more than three times that observed by LANL may be due to the fact that CRRES moved in L from ~ 6.8 to ~ 1.2 while the LANL spacecraft remained located at L ~ 6.67.

5.2.3 Discussion

We showed a strong correlation between toroidal mode Pc 5 pulsations and electron flux oscillations with the characteristics expected from resonant behavior. For an electron moving eastward around the Earth, electrons could be modulated by poloidal mode ULF waves which have azimuthal electric field components. However in a compressed dipole (see Figure 5.2), the toroidal mode can also accelerate electrons via drift-resonance interaction [*Elkington et al.*, 1999, 2003]. The resonance condition for drift-resonant acceleration in a compressed dipole is

$$\omega - (m \pm 1)\omega_d = 0 \tag{5.1}$$

where ω, ω_d and m represent wave frequency, drift frequency and azimuthal wave number, respectively.

Figure 5.7 shows the resonant energy as a function of m-value calculated by solving equation (5.1). We solved this equation for $\omega - (m + 1)\omega_d = 0$ and

$\omega - (m-1)\omega_d = 0$ with wave frequency 1.7 mHz for the case of equatorial pitch angle 45° and 90°. LANL 1990-095 and CRRES show the resonant energy about 315-500 keV and 417-692 keV, respectively (see Figure 5.6). Figure 5.7 (a) shows the resonant energy vs azimuthal wave number for L = 6.67 at the position of LANL 1990-095. The azimuthal wave number which resonates with electrons with energies at 315-500 keV is m ∼ 1 or m ∼3 as shown in Figure 5.7 (a). Similarly, Figure 5.7 (b) shows the resonant energy as a function of azimuthal wave number but at L = 4.25 which was the location of the CRRES satellite at 1245 UT. The azimuthal wave number which resonate with electrons with energies at 417-692 keV is also m ∼ 1 or m ∼ 3 as shown in Figure 5.7 (b). We suggest the explanation for the flux modulation is a drift-resonant interaction with toroidal-mode Pc 5 waves with azimuthal wave number $m \sim 1$ or $m \sim 3$. This is consistent with the observational result that the azimuthal wave number is 2-4 during this interval as stated in Chapter 4 Section 4.2. The reason why resonant energy is slightly higher for CRRES than LANL might be because CRRES moves to lower L-shell up to about $L \sim 4$ and the resonant energy is higher for lower L.

5.2.4 Summary

During this storm, we observed very strong Pc 5 oscillations of 1.7 mHz frequency between 1200 and 1340 UT and electron flux modulations with same frequencies simultaneously. The observed electron flux modulations show phase and amplitude changes across the peak amplitude at resonant energy. In this event, the amplitude of observed D-component waves is much smaller compared to the H-component waves, i.e., toroidal mode waves are dominant. For a toroidal mode to be modulated, the dipole needed to be compressed to interact with a toroidal mode wave. During this March 24 1991 storm, high solar wind speed around

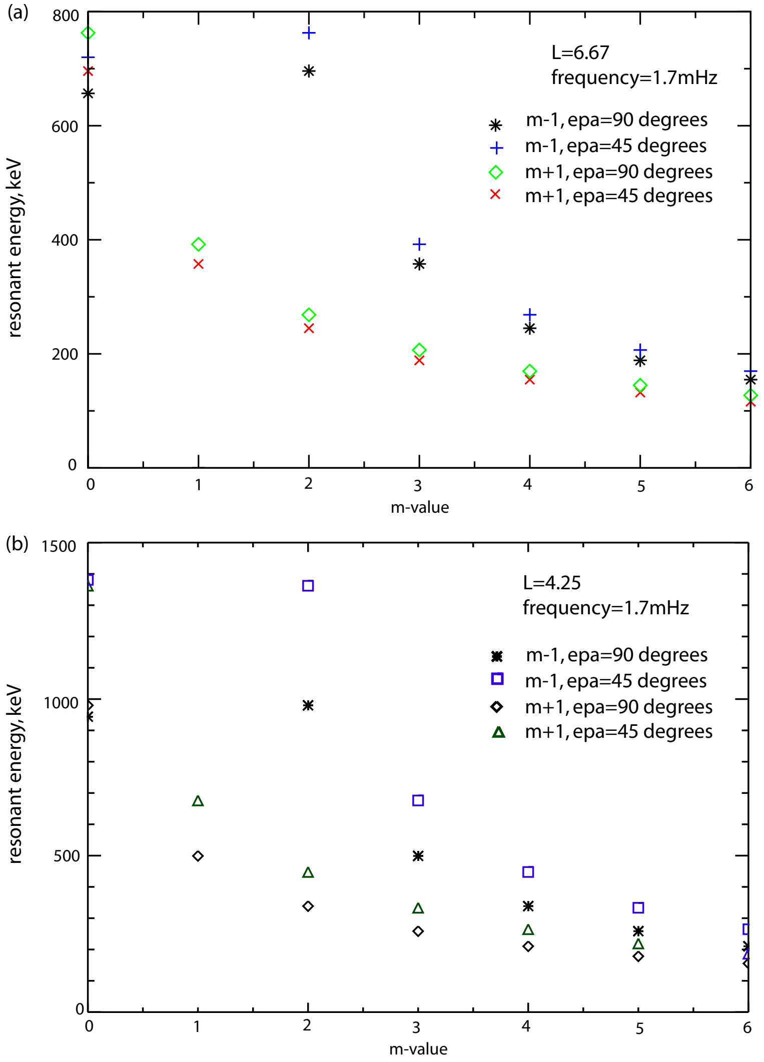

Figure 5.7: Drift-resonance energy in a compressed dipole as a function of azimuthal m-value at (a) L = 6.67 and (b) L = 4.25.

1400 km/s and CME impact suggest that dipole might be highly compressed as Figure 5.1 (b). We suggest that during this storm time, in a compressed dipole, toroidal mode Pc 5 ULF waves may have accelerated electrons via drift-resonance interaction.

5.3 Case Study 2 : Bastille Day Storm July 15-16, 2000

We present observations of Pc 5 ULF waves in the recovery phase of the Bastille day storm of July 16, 2000 and electron flux simultaneously oscillating with the same frequencies in the time-domain. Compared to the March 24, 1991 event however, the relation between energetic particle flux and ULF waves is more complicated for the Bastille Day storm of July 16, 2000. The mechanism for the observed electron flux modulations are examined using ground-based and satellite observations. During this storm time, multiple packets of discrete frequency Pc 5 ULF waves appeared associated with energetic particle flux oscillations.

We model the drift paths of electrons and protons to determine if the particles drift through the ULF wave to understand why some particle fluxes are modulated by the ULF waves and others are not. We also analyze the flux oscillations of electrons and protons as a function of energy to determine if the particle modulations are caused by a ULF wave drift resonance or advection of a particle density gradient.

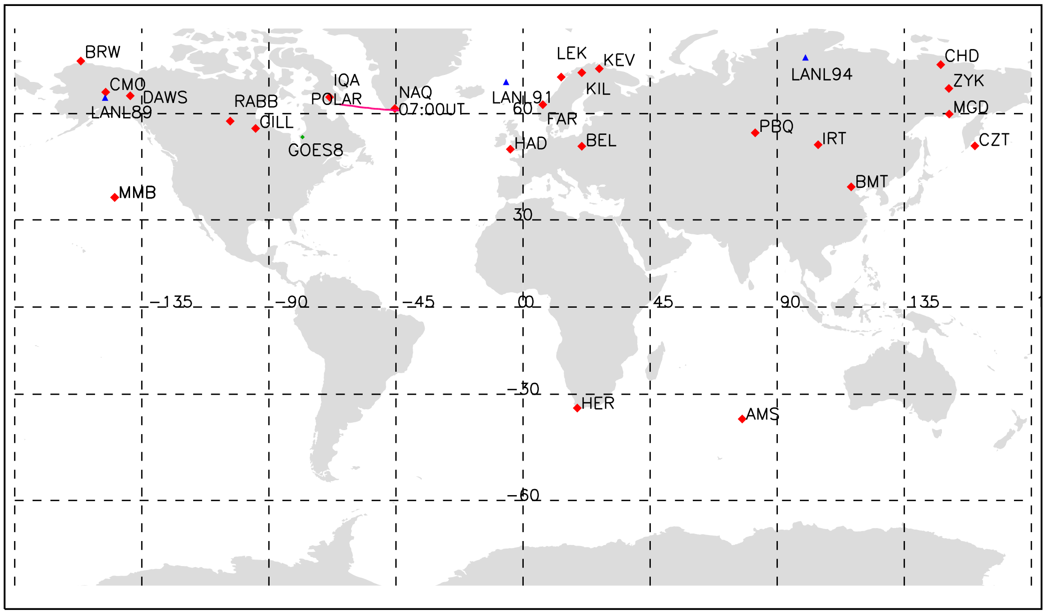

Figure 5.8: Locations of ground-based magnetometers used in this study and north B Traces of LANL89, LANL91, LANL94, GOES8, and Polar (0700-0900 UT) with geographic latitude and longitudes.

5.3.1 Instrumentation

We analyze ground-based magnetometer array and satellite data during the recovery phase of the geomagnetic storm of 16th July 2000. We examine magnetic field data using the following ground-based magnetometer arrays: IMAGE, SAMNET, the 210 magnetic meridian (MM) chain in the western Pacific, the CARISMA magnetometer array and INTERMAGNET (See Table A.3 and A.4 in Appendix A for the location information). Figure 5.8 shows the locations of the ground-based magnetometers and the north B trace of LANL89, LANL91, LANL94, and GOES8 (see Chapter 3 Section 3.3 for detail information of ground-based magnetometers and satellites). For the solar wind and interplanetary magnetic field (IMF) measurements, we used 64 s and 16 s averages, respectively, observed by the ACE spacecraft near the L1 Lagrangian point. We also surveyed GOES 8 magnetic field data for this study. Particle flux data for this study was obtained from the SOPA instrument on board the LANL geostationary satellites and SAMPEX (see Chapter 3 Section 3.3).

5.3.2 Solar Wind Observations

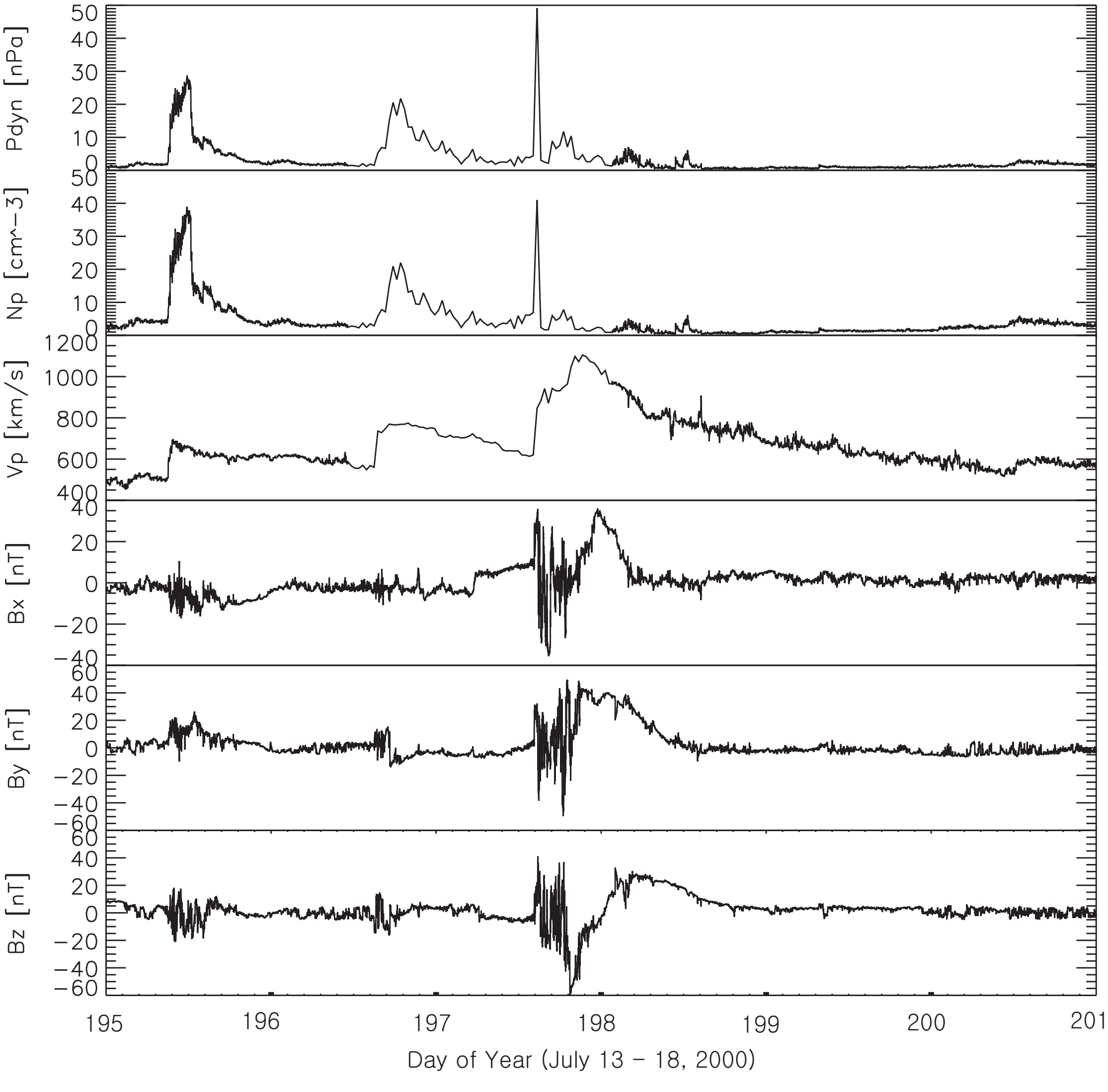

Figure 5.9: From the top, proton dynamic pressure (nPa), proton density (cm$^-$3), solar wind speed (km/s) and magnetic field components Bx (nT), By (nT), Bz (nT) in GSM coordinates from ACE.

Figure 5.9 shows interplanetary solar wind parameters observed by ACE (position at GSE (X, Y, Z) = (247.10, 18.34, 15.82) R_E). The panels from the top to bottom illustrate the dynamic pressure, plasma proton density, solar wind bulk speed, and interplanetary magnetic field (IMF) in geocentric solar magnetospheric (GSM) coordinates. The great geomagnetic storm was caused by an interplanetary coronal mass ejection (ICME) driving interplanetary shocks and impacting the magnetosphere (see e.g., *Smith et al.* [2001]). ACE observed three times when there were discontinuities in solar wind dynamic pressure, density and solar wind speed through 13 - 18 July. Dynamic pressure enhancements just behind each shock are mainly due to density variations. The solar wind velocity was very high, and slowly decreased from $\sim$ 1030 km/s to $\sim$ 670 km/s throughout the course of the day on July 16, 2000 (DOY 198). IMF Bz fluctuated from south to north at the the end of July 15th (DOY 197). A period of southward IMF lasted from 1835 UT on July 15 to 0022 UT on July 16 for around 6 hours with a minimum of $B_z = -58$nT before changing to northward IMF.

5.3.3 Observations : Overview of Energetic Particles in the Van Allen Radiation Belts

In Figure 5.10, the top two panels show the electron and proton flux from the SOPA instrument on board the geosynchronous LANL 1994-084 satellite during the period of 13 - 20 July 2000. Three times of dispersionless injections are observed in the main phase of the storm, and several packets of electron and proton flux oscillations appeared in the recovery phase of the storm during July 16, 2000. The bottom panel shows log flux of 2 - 6 MeV electrons measured by the low Earth orbiting SAMPEX satellite and Dst index. Before the storm, the outer radiation belt was centered near L = 3.5 - 4 during the period of 8 - 15 July 2000 and enhanced electron flux appeared near L = 2.7 in the recovery phase of the storm during the period of 16 - 17 July 2000 and back to L=3.5 after 1-2 days. The hourly Dst index (Figure 5.10) data taken from the World Data Center for Geomagnetism, Kyoto (http://wdc.kugi.kyoto-u.ac.jp/index.html) shows minimum Dst = -301 nT at 0100 UT on 16 July 2000. The red section of the curve indicates the period of 13 - 20 July 2000. Radial transport of 2-6 MeV electrons in SAMPEX might be due to a drift-resonant interaction with Pc 5 ULF waves. To prove this hypothesis, we investigate the evidence of particle and wave interactions. In the following sections, we will study Pc 5 ULF waves observed on the ground and in space, and energetic particle flux observed by the LANL satellites on July 16, 2000.

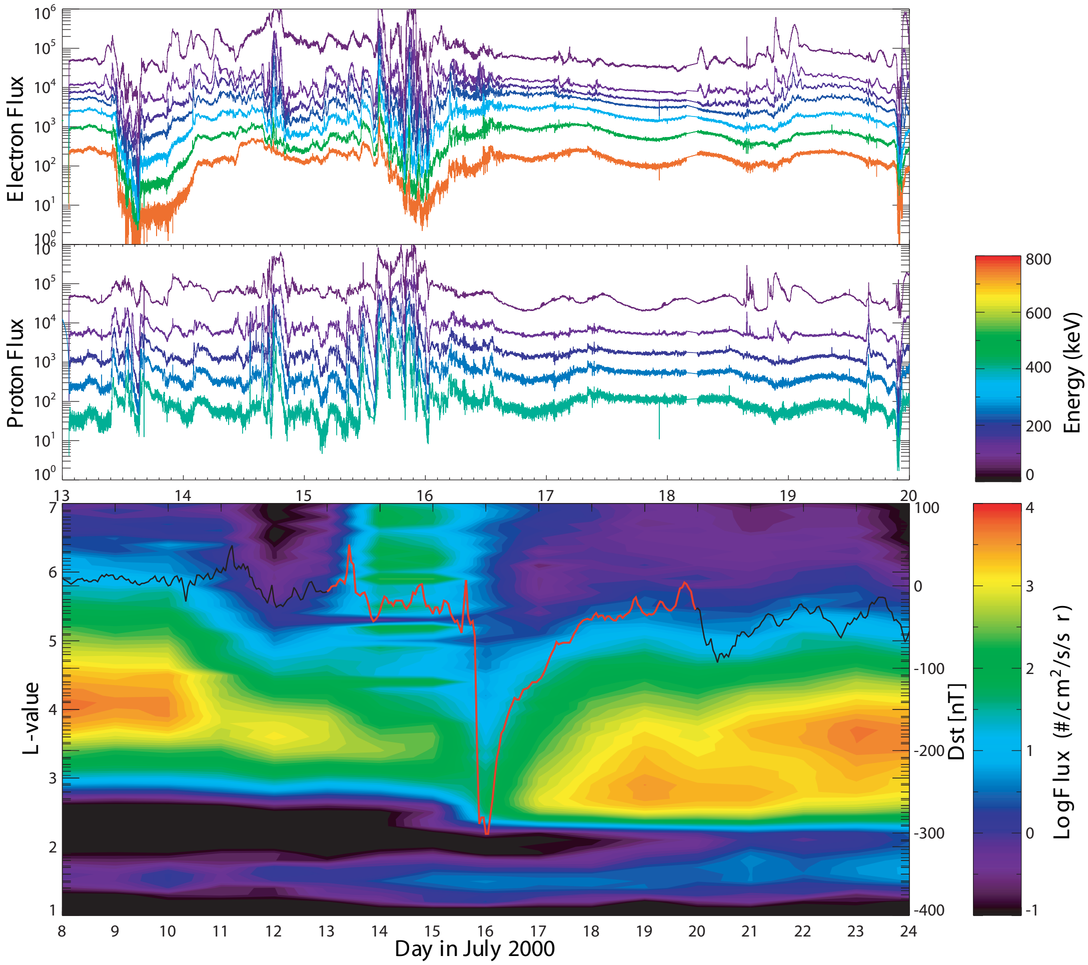

Figure 5.10: From the top to bottom: Electron and proton flux respectively, from LANL 1994-084 satellite on 13-20 July 2000; SAMPEX electron energetic particle flux (2.0-6.0 MeV) as a function of L and Dst index on 8 - 24 July 2000. For the LANL 1994-084 particle fluxes, from the top to bottom, the ranges of electron energies are 50-75 keV, 75-105 keV, 105-150 keV, 150-225 keV, 225-315 keV, 315-500 keV, and 500-750 keV and proton energies are 50-75 keV, 75-113 keV, 113-170 keV, 170-250 keV, and 250-400 keV.

5.3.4 Observations : Pc 5 ULF waves

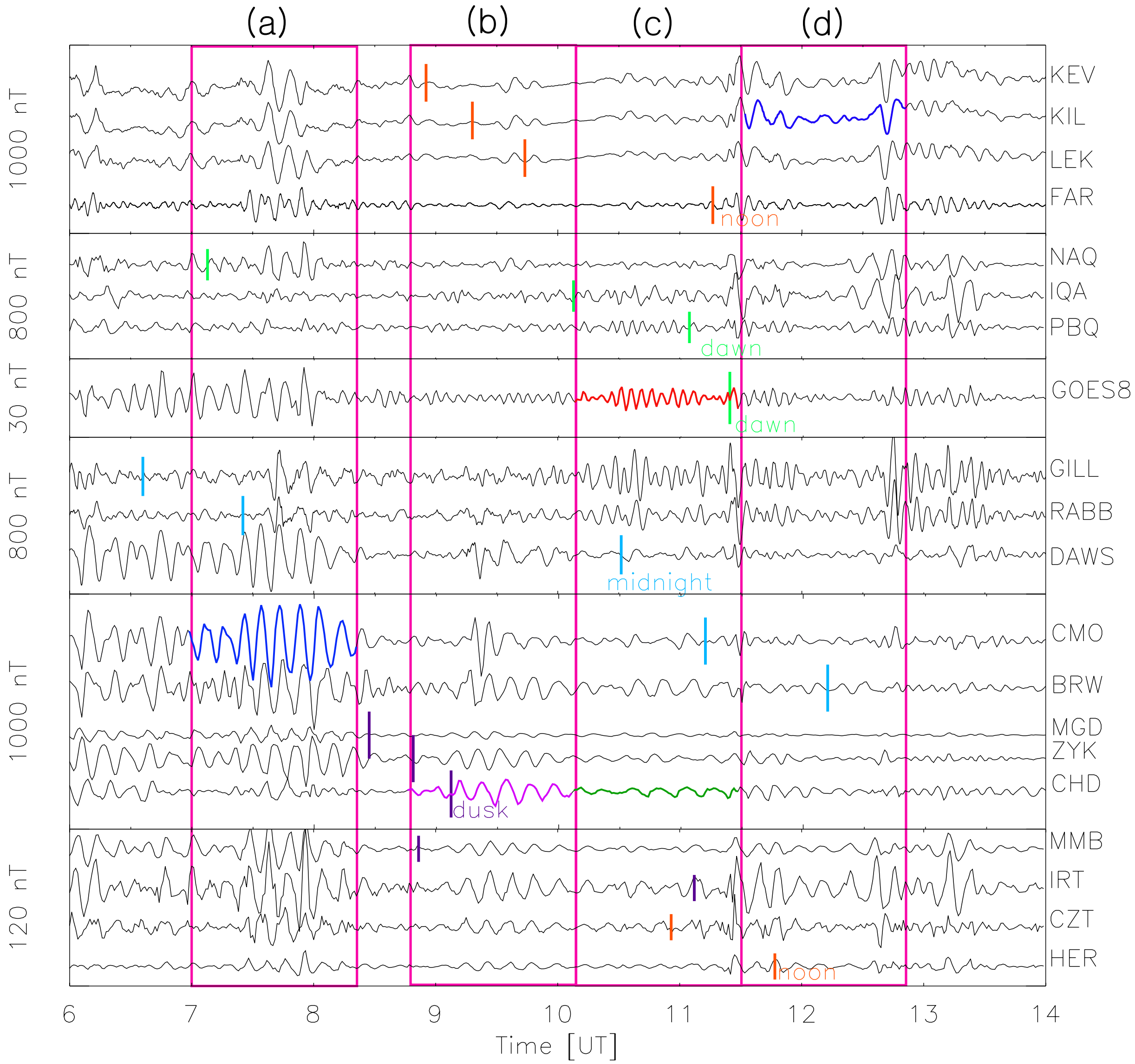

Figure 5.11: Magnetic field H-components observed by selected ground-based magnetometer stations and the GSM Y-component from GOES 8 on July 16, 2000. In each panel, the size of the y-axis spanning the entire panel is indicated in nT. Time intervals are divided such as (a) 0700 - 0820 UT (b) 0850 - 1010 UT (c) 1010 - 1130 UT and 1130 - 1250 UT

Figure 5.11 shows the magnetic field H-component observed by selected ground-based magnetometers around the world. Table A.1 in Appendix A shows the

CGM latitude, longitude, L-value of the magnetometers plotted in Figure 5.11. The stations shown in this plot are organized such that stations were longitudinally ordered from noon to dawn, midnight, and dusk.

Due to the complexity of the observed waves, we divided our analysis to concentrate on four intervals to interpret the modulation of the flux of energetic particles. From left to right; (a) 0700-0820 UT, (b) 0850 - 1010 UT, (c) 1010 - 1130 UT and (d) 1120-1250 UT. Colored oscillations in Figure 5.11 indicate the Pc 5 ULF waves we observed during each time interval.

Interval (a) 0700 - 0820 UT

The first time interval (0700-0820 UT) shows strong evidence of a global oscillation with frequency of 1.7 mHz (600 s) in the ground-based magnetometer stations except stations located near midnight such as IQA, PBQ, and RABB. Pc 5 ULF waves with a frequency of 1.7 mHz appeared even at very low latitudes such as the MMB stations located at L $\sim$ 1.6. The Faroes (FAR) station located near the dawn flank showed multiple discrete frequency waves with periods of 300 s (3.3 mHz) and 600 s (1.7 mHz). The largest amplitude toroidal waves with a frequency of 1.7 mHz, assuming a 90° ionospheric rotation into the the H-component on the ground, appear near the dusk flank (DAWS, CMO, BRW) while no clear oscillation appears near midnight.

Interval (b) 0850 - 1010 UT

The second time interval (0850-1010 UT) shows a spectral peak at 1.4 mHz (690 s) in BRW, ZKY and CHD stations located near dusk. These longer period waves appear in the dayside of the magnetosphere during this time interval, and the largest amplitude still appears at the dusk flank. However, GOES 8 which was located close to the dawn flank shows evidence of higher frequency (3.3 mHz) waves.

Interval (c) 1010 - 1130 UT

The third time interval (1010-1130 UT) shows that waves have the largest amplitude near dusk (BRW, ZYK, and CHD) with frequency of 1.2 mHz (810 s). Waves with frequency of 3.3 mHz (300s) still appear in the dawn flank.

Interval (d) 1130 - 1250 UT

During the fourth time interval (1130-1250 UT), 1.7 mHz (600 s) waves were observed in the afternoon local time sector with largest amplitude near dusk. Again, 3.3 mHz waves are still observed in the dawn flank (such as PBQ, GOES 8, GILL, and RABB stations).

In summary, multiple packets of discrete frequency Pc 5 ULF waves appeared globally as well as with a more limited local time extent during the great geomagnetic storm of July 16, 2000. Global Pc 5 pulsations with a frequency of 1.7 mHz appeared in the dayside of the magnetosphere simultaneously, with the largest amplitude near dusk and pre-midnight. Also, waves with frequencies of 1.4 mHz (690s) and 1.2 mHz (810s) appeared localized from post-noon to pre-midnight with largest amplitude near dusk. However, 3.3 mHz (300s) waves appeared locally in the morning sector with largest amplitude at the dawn flank.

Previous case studies have shown a relationship between energetic electrons and ULF waves (see Section 5.2). Particle flux measurements obtained from the SOPA instrument on board the LANL geosynchronous satellites show evidence of an energetic particle and ULF wave interaction during the July 16 storm and this will be studied in the following section.

5.3.5 Observations: Energetic electron and proton fluxes

Figure 5.12 shows the magnetic field H-components observed from ground-based stations (KIL, FAR, CMO and ZYK), magnetic field Y-component observed from GOES 8 and the electron and proton fluxes observed by LANL 1994-084, LANL 1989-046 and LANL 1991-080, respectively. The ground-based stations were located at different local times to enable a comparison between the magnetic waves dependence on local time and the observed energetic particle flux modulations. The bottom six panels show spin-averaged differential flux for LANL satellites in different energy ranges. From the top to bottom, the ranges of the electron energy channels are 50-75 keV, 75-105 keV, 105-150 keV, 150-225 keV, 225-315 keV, 315-500 keV, and 500-750 keV and the proton energy channels are 50-75 keV, 75-113 keV, 113-170 keV, 170-250 keV and 250-400 keV. Blue colors represent lower energy channels and red colors represent higher energy channels.

Figure 5.13 shows the power spectra for the four time intervals (a) - (d) for the same panels as Figure 5.12. From left to right, the columns show (a) 0700-0820 UT, (b) 0850 - 1010 UT, (c) 1010 - 1130 UT and (d) 1130-1250 UT. Multiple discrete spectral peaks were observed in the energetic particle flux similar to the magnetic waves observed by the ground-based magnetometers. A 600 s (1.7 mHz) period oscillation of electron and proton flux appeared between 0700-0820 UT during interval (a) and longer period waves of 690 s (1.4 mHz) and 810 s (1.2 mHz) appeared during the intervals (b) and (c), respectively. During the interval (d) we again observed 600 s (1.7 mHz) period waves. Also, 300s (3.3 mHz) small amplitude oscillations were observed in LANL 1991-080 in the local morning during all intervals (a) - (d).

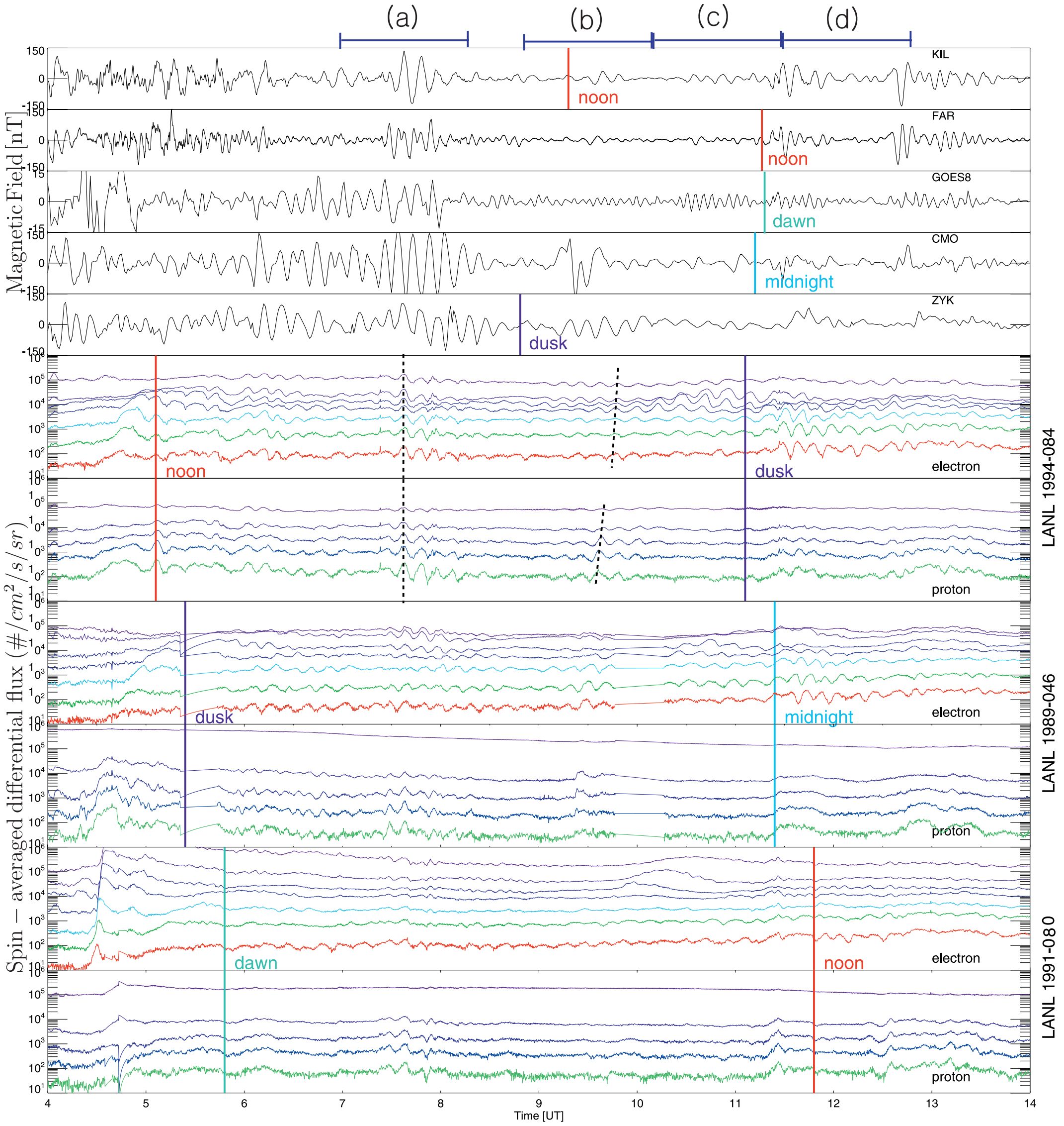

Figure 5.12: Stack plot of magnetic field H-components of the selected ground-based stations (KIL, FAR, CMO, ZYK), magnetic field Y-component from GOES8 and electron and proton spin-averaged differential flux observed from SOPA on board LANL satellites between 0400 - 1400 UT on July 16, 2000. The ranges of electron energy channels are 50-75 keV, 75-105 keV, 105-150 keV, 150-225 keV, 225-315 keV, 315-500 keV and 500-750 keV, and proton energy channels are 50-75 keV, 75-113 keV, 113-170 keV, 170-250 keV and 250-400 keV. The black vertical dotted lines show no phase changes and phase change in flux modulations, respectively.

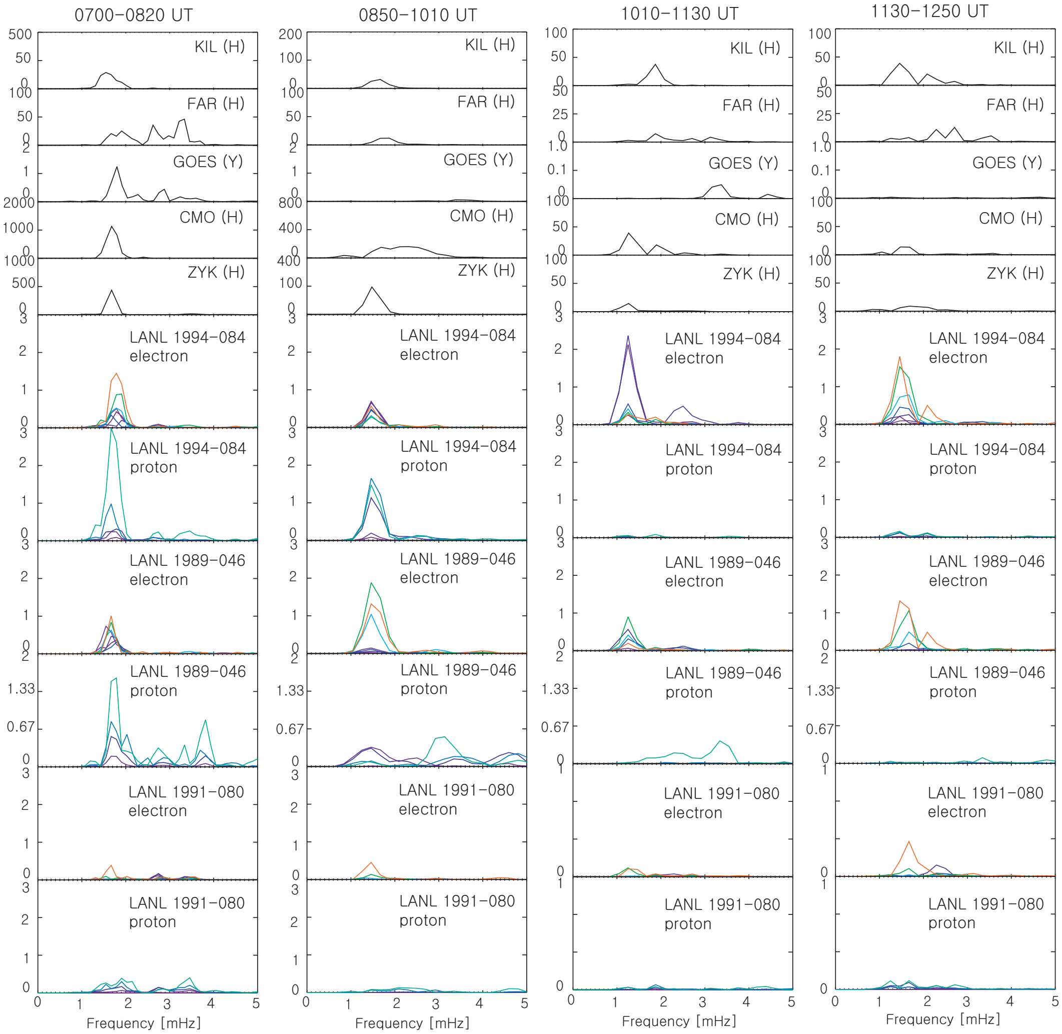

Figure 5.13: Stack plot of power spectra of magnetic fields H-components on ground-based magnetometers and Y-component on GOES8 and electron and proton fluxes for 80 minute intervals (a), (b), (c), and (d) corresponding to Figure 5.12 on July 16, 2000.

Interval (a) 0700 - 0820 UT

The first time interval (0700-0820 UT) is characterized as a global oscillation of 1.7 mHz frequency Pc 5 waves in the ground-based magnetometer data and 3.3 mHz frequency Pc 5 waves in the morning sector (see Figure 5.13 (a)). We observed at LANL 1994 and LANL 1989 that the proton and electron flux oscillate with same frequency 1.7 mHz and that all energy channels of both electrons and protons oscillated in phase. In Figure 5.12, a dotted vertical line in LANL 1994-084 during interval (a) is drawn to indicate that there was no phase change between electrons and ions and between different energies. On the other hand, LANL 1991-080 shows 600 s (1.7 mHz) period flux modulation in the energy channels between 500 and 750 keV for electrons, and a 300 s (3.3 mHz) period modulation appears in the lower energy channels with a smaller amplitude. Proton flux oscillations at 1.7 mHz appear at most energies but with small amplitudes.

The particle flux modulations seem to be related with magnetospheric Pc 5 waves observed on the ground and in space. Both particle flux and geomagnetic field oscillations at 1.7 mHz show the largest amplitude in the afternoon. For example, CMO ($L = 5.72$, MLT = 19:49 - 21:09) shows the largest amplitude pulsations on the dusk flank and electron flux and proton flux oscillate simultaneously with very large amplitude at LANL 1994-084 ($L = 6.8$, MLT = 13:42 - 14:58) and LANL 1989-046 ($L = 6.6$, MLT = 19:46 - 21:02). In the same manner, 3.3 mHz frequency waves appeared in the morning for both magnetic field from FAR station ($L = 4.3$, MLT = 06:44 - 08:04) and electron flux from LANL 1991-080 ($L = 6.6$, MLT = 07:21 - 08:37). Coherent observations of Pc 5 pulsations and particle flux oscillations with same frequency at the same time interval strongly suggest that there was a interaction between Pc 5 ULF waves and energetic particles.

Interval (b) 0850 - 1010 UT

The second time interval (0850-1010 UT) (Figure 5.13 (b)) shows magnetic pulsations with a peak amplitude at 1.4 mHz at ZKY (L = 4.04, MLT = 16:11 - 17:31) located near dusk. Clear phase and amplitude change across the energy channels appear in the observed electron and proton flux modulations (see the dotted lines during interval (b) on LANL 1994-084 flux data in Figure 5.12 for a clear example). Both proton and electron flux modulation appeared at LANL 1994-084 (L = 6.8, MLT = 15:26 - 16:43), but only electron modulation appeared in LANL 1989-046 (L = 6.6, MLT = 21:31 - 22:48). LANL 1991-080 (L = 6.6, MLT = 0906 - 10:23) also shows only electron oscillation at 1.4 mHz with small amplitude in the energy channels between 315 and 750 keV. The species and MLT dependence of modulation can be explained by the drift path of electron and proton as well as the location of satellites (see section 2.7.4). A detailed explanation of the observed modulation will be presented in the discussion section.

Interval (c) 1010 - 1130 UT

The third time interval (1010-1130 UT) is characterized by magnetic Pc 5 waves with power spectra with a discrete peak at 1.2 mHz, e.g., ZYK (L = 4.04, MLT = 17:31 - 18:51) and CMO (L = 5.72, MLT = 22:59 - 00:19). Phase and amplitude changes across energy channels are clear in electron flux. Large amplitude electron flux modulation with 1.2 mHz frequency appeared in LANL 1994-084 (L = 6.8, MLT = 16:43 - 18:01) and LANL 1989-046 (L = 6.6, MLT = 22:48 - 00:06) while proton flux modulation didn't appear at either satellite (see Figure 5.13). On the other hand, LANL 1991-080 which was located in the morning sector observed 1.2 mHz frequency electron flux oscillation at higher energy channels between 315 and 750 keV and 3.3 mHz electron flux oscillation at lower energy channels.

Interval (d) 1130 - 1250 UT

The fourth time interval (1130-1250 UT) shows magnetic power spectra with a spectral peak at 1.7 mHz in KIL (L = 6.09, MLT = 08:48 - 10:08) station located in the post-noon sector. Electron flux modulation appeared in both LANL 1994-084 (L=6.8, MLT = 18:01 - 19:22) and LANL 1989-046 (L = 6.6, MLT = 00:06 - 01:27) with the largest amplitude in the energy channel at around 500 - 750 keV. On the other hand, proton flux modulations appeared only in LANL 1994-084 with small amplitudes. Similar to the previous interval, LANL 1991 - 080 still observe 1.7 mHz electron flux oscillations at higher energy channels and 3.3 mHz oscillations at lower energy channels.

Table 5.1 summarizes observed magnetic Pc 5 oscillation frequencies and the energetic particles flux modulation frequencies seen for the four intervals (a) - (d).

5.3.6 Modeling energetic particle drift paths

Frequently, energetic particle flux modulations are not observed simultaneously at geosynchronous satellites at different local times (see Figure 5.12, 5.13). The reason might be related to the relative location of the ULF waves, their sources and the drift path of the electrons and protons. The bounce-averaged guiding center trajectories of charged particles in a dipole model of magnetosphere, including the effects of convection and co-rotation electric fields, can be written as

$$\dot{\phi} = -\frac{3m_p V^2 L P(\alpha_{eq})\gamma}{qB_S R_E^2} + \frac{2\psi_0 L^3 \mathrm{sin}\phi}{B_S R_E^2} + \Omega_E \tag{5.2}$$

Ground magnetic field

time (UT)	dusk (mHz)	dawn (mHz)	noon (mHz)	midnight (mHz)
(a)0700-0820	*1.7	1.7, *3.3	1.7	NONE
(b)0850-1010	*1.4	*3.3	1.4	NONE
(c)1010-1130	*1.2	*3.3	1.2	NONE
(d)1130-1250	*1.7	*3.3	1.7	NONE

electrons

time (UT)	LANL1994 (mHz)	LANL1989 (mHz)	LANL1991 (mHz)	energy of spectral peak (keV)
(a)0700-0820	1.7	1.7	1.7, 3.3	NONE
(b)0850-1010	1.4	*1.4	1.4, 3.3	315-500
(c)1010-1130	*1.2	1.2	1.2, 3.3	105-225
(d)1130-1250	*1.7	1.7	1.7, 3.3	500-750

protons

time (UT)	LANL1994 (mHz)	LANL1989 (mHz)	LANL1991 (mHz)	energy of spectral peak (keV)
(a)0700-0820	1.7	1.7	1.7	NONE
(b)0850-1010	*1.4	NONE	NONE	175-250
(c)1010-1130	NONE	NONE	NONE	NONE
(d)1130-1250	1.7	NONE	NONE	250-400

Table 5.1: Summary of magnetic Pc 5 oscillation frequencies and the energetic particle flux modulation frequencies. * indicate dominant frequency in each interval and their energy of spectral peak with lagest amplitude is indicated in the column of energy of spectral peak.

$$\dot{L} = -\frac{\psi_0 L^4 \cos\phi}{B_S R_E^2} \tag{5.3}$$

where $\dot{\phi}$ and $\dot{L}$ are the particle's rate of change of azimuthal position (ϕ) and L with respect to time and $P(\alpha_{eq}) \simeq 0.35 + 0.15\sin\alpha$ [*Hamlin et al.*, 1961; *Chisham*, 1996].

The total electric potential is composed of the convection and the corotation electric potential, $\Phi = \Phi_{con} + \Phi_{cor}$, and can be written as

$$\Phi = \psi_0 L^2 \sin\phi - \frac{\Omega_E B_S R_E^2}{L}. \tag{5.4}$$

Here the first term of equation (5.4) is the electric potential from convection, and the second term is the electric potential from corotation. ϕ is the azimuthal angle measured eastwards as positive at midnight (0°) and ψ_0 can be expressed empirically as a function of Kp [*Hamlin et al.*, 1961; *Chisham*, 1996].

$$\psi_0 = 45(1 - 0.159K_p + 0.0093K_p^2)^{-3}. \tag{5.5}$$

We used these equation of guiding center motion to examine the energetic particle drift paths relative to the location of observed ULF waves. In our simulations we used Kp=8 and equatorial pitch angles of 90^o. The effect of ULF wave interactions are excluded such that only unperturbed drift paths are shown. In the discussion section below, we used this model to explain the relationship between the observed ULF waves and enhanced particle flux modulations.

5.3.7 Discussion

Interval (a) 0700-0820 UT

The top row of Figure 5.15 shows the electron and proton drift paths calculated using the model described in section 5.3.6. This figure shows the drift paths of energetic electrons and protons with different initial energy at 0800 UT (top) on 16th July 2000. Particles are launched with initial energies of 100 keV, 200 keV, 300 keV, and 400 keV at L = 6.6 and in the afternoon sector at 1800 LT and drift around a static dipole magnetic field model. In Figure 5.15 top panel, the electrons drift on closed orbits but protons drift on open trajectories for the lower energies (100 and 200 keV). The location of the LANL geosynchronous satellites and the approximate MLT extent of the observed ULF waves are also shown. LANL 1994-094 was located around 1630 MLT and LANL 1989-046 was located near 2230 MLT at this time. 1.7 mHz ULF waves (blue solid oscillation) were observed globally and 3.3 mHz waves (red solid oscillation) were observed in the dawn flank. The arrows indicate the drift directions of electrons (eastward) and protons (westward). During 0700-0820 UT, the ground-based magnetometers showed global waves of 1.7 mHz and modulations of energetic electron and proton flux were also observed in all three LANL satellites at the same frequency. A possible explanation for this observed flux modulation might be the advection of an energetic particle density gradient across the satellites (see Chapter 2 section 2.7.4). If there is a gradient in density in the direction of wave perturbations and displacement, flux oscillation can result [e.g., *Southwood*, 1973; *Southwood and Kivelson*, 1981]. In the case of advection, as indicated by the dotted line in Figure 5.12, both energetic electron and proton flux oscillated in phase for different energy channels.

In the morning sector, the ground-based magnetometers observed a 3.3 mHz frequency oscillation as well as a 1.7 mHz frequency oscillation (see FAR station in Figure 5.12). LANL 1991-080, located in the morning sector, observed 1.7 mHz electron flux pulsations at higher energy channels and 3.3 mHz electron flux oscillations at lower energy channels. On the other hand, the proton flux only oscillated at 1.7 mHz. One possible explanation for this is that a westward traveling proton would be detected at the LANL 1991-080 satellite before the proton interacted with the 3.3 mHz wave oscillations further to the west (see Figure 5.15 top panel). As mentioned in Chapter 2 Section 2.7.4, to observe the flux modulation at the satellite, the energetic particles must pass through the wave before they reach the satellite.

Interval (b) 0850-1010 UT

During 0850-1010 UT, 1.4 mHz ULF waves were observed on the ground near noon and in the afternoon sector from the ground-based magnetometers. Large amplitude waves were observed near dusk (cf. ZYK and CHD stations). At the same time, proton and electron modulations clearly appeared at LANL 1994-084 at 15:26 - 16:43 MLT while only electron flux modulation appeared at LANL 1989-046 at 21:31 - 22:48 MLT (see Figure 5.12). During this second interval, typical resonance characteristics appear in the flux observations such as a phase change and amplitude peak across the resonant energy (315-500 keV for electrons and 175-250 keV for protons) (see Figure 5.12). Thus, we suggest that both electrons and protons were modulated by a resonant interaction with Pc 5 ULF waves. From the observations, the 1.4 mHz proton oscillation shows largest amplitude at energies of 175 - 250 keV at $L = 6.6$. By solving equation 5.1, we can find out that the resonant azimuthal wave number (m) for this wave is around -3 or -5 for proton modulation. Electron flux modulation also has its largest amplitude near energies of 315 - 500 keV at $L = 6.6$ which gives a resonant azimuthal wave number around 3 or 1. If the ULF waves are standing in the azimuthal direction, these could have both positive and negative signs of azimuthal wave number (m) at the same time. If this is the case, then both electrons and protons could be resonant with the ULF waves at the same time.

Thus, satellites can observe proton modulation arising from their interaction with westward traveling ULF waves and electron flux can be modulated by eastward traveling ULF waves. This means there should be waves propagating in both directions. We can find evidence of azimuthal standing waves, with components traveling both westward and eastward, in the magnetic field data observed by the ground-based magnetometers. Figure 5.14 shows H-component magnetic fields observed at different local times with similar latitude. From top to bottom, the panels in this plot show magnetic field H-component variations from BEL (CGM latitude 47.52, CGM longitude 96.19) and HAD (47.69, 74.86), HER (-42.05, 82.6) and AMS (-49.06, 138.84), and BMT (34.48, 188.71) and MMB (37.05, 215.35) in CGM coordinates. No clear phase delay appears between the stations located at different longitudes but at similar latitudes. Hence, we infer that there was both westward and eastward traveling waves creating an azimuthal standing wave as shown in Figure 5.14. Under the condition of both westward and eastward traveling waves, creating an azimuthally standing mode structure, we suggest that the modulation of electrons and protons can both be observed simultaneously as seen here.

The absence of proton modulation in LANL 1989-046 can be explained due to the relative location of the satellite with respect to the drift path of protons. Since the LANL 1989-046 satellite is located on the eastern side of the ULF waves, the modulated protons will be observed after protons circle all around the Earth on their drift orbit. However, lower energy protons will drift on open trajectories as shown in the right panel of Figure 5.15 (bottom panel), such that proton modulation at these energies will not be detected since the protons do not return to the satellite location. Also, since the drift paths are not symmetric and reach different distances from the Earth especially between dawn and dusk, there are chances protons modulated by waves will not be detected at satellites at fixed geosynchronous altitudes and which are located far from the source.

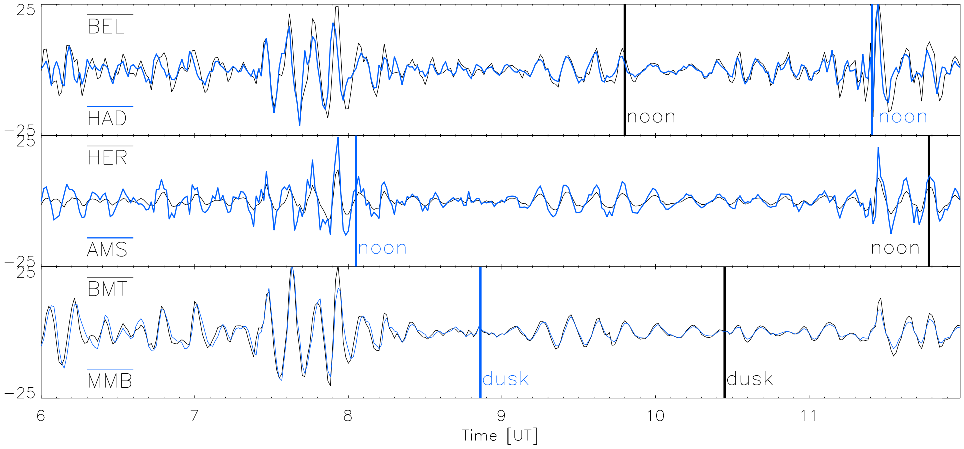

Figure 5.14: Magnetic field H-component magnetic fields observed from BEL (CGM latitude 47.52, CGM longitude 96.19) and HAD (47.69, 74.86), HER (-42.05, 82.6) and AMS(-49.06, 138.84), and BMT (34.48, 188.71), and MMB(37.05, 215.35) in CGM coordinates.

Interval (c) 1010-1130 UT

During 1010 - 1130 UT, ULF waves with 1.2 mHz frequency were observed in the afternoon sector with largest amplitude near the dusk flank (see Figure 5.16 top panel). The locations of LANL 1994-084, LANL 1989-046 and LANL 1991-080 are 1720 MLT, 2330 MLT, and 1100 MLT at 1030 UT, respectively. Energetic electron flux modulation at the frequency of 1.2 mHz was seen in LANL 1994-084 and LANL 1989-046 very clearly, but no proton flux modulations were observed at either of these satellites. The reasons for the absence of proton modulations may be related to the wave propagation direction. ULF waves propagating eastward interact only with electrons not with protons in drift resonance. Also, the proton's open drift trajectory may obstruct the return of modulated protons to the satellite location. Electron flux modulation observed at LANL 1994-084 is much larger in amplitude than at LANL 1989-046. This might be due to a particle injection in the low energy channel being superposed on top of flux modulations for LANL 1994-084 satellites detector. Drift-resonant behavior was observed during this interval in the electron enhanced flux oscillation of 1.2 mHz with a frequency and maximum amplitude at energies of 105 - 225 keV at L = 6.6, such a wave would resonate with the electrons if m=2 or m= 4 waves. Thus, we suggest that the electron flux modulation is due to a drift resonance with the Pc 5 ULF waves.

Interval (d) 1130-1250 UT

During 1130 - 1250 UT, magnetic field perturbations of 1.7 mHz frequency were observed in the afternoon sector. The location of LANL 1994-084 and LANL 1989-046 were 1820 MLT and 0030 MLT at 1130UT, respectively (see Figure 5.16 bottom panel). Electron flux modulations were also observed at both satellites but more of larger amplitude at LANL 1994-084 which was located closer to the wave source. Similar to the second interval (Interval (b)), a proton flux modulation was detected only at LANL 1994-084. LANL 1994-084 may have observed a proton flux modulation as a result of the satellite being located in the center of the region of wave activity. In this case, the flux modulation can be explained using the same reasoning as discussed for the absence of proton modulation in the interval (b).

Table 5.2 summarizes the Pc 5 ULF wave and particle flux modulations observed during the storm of July 16, 2000.

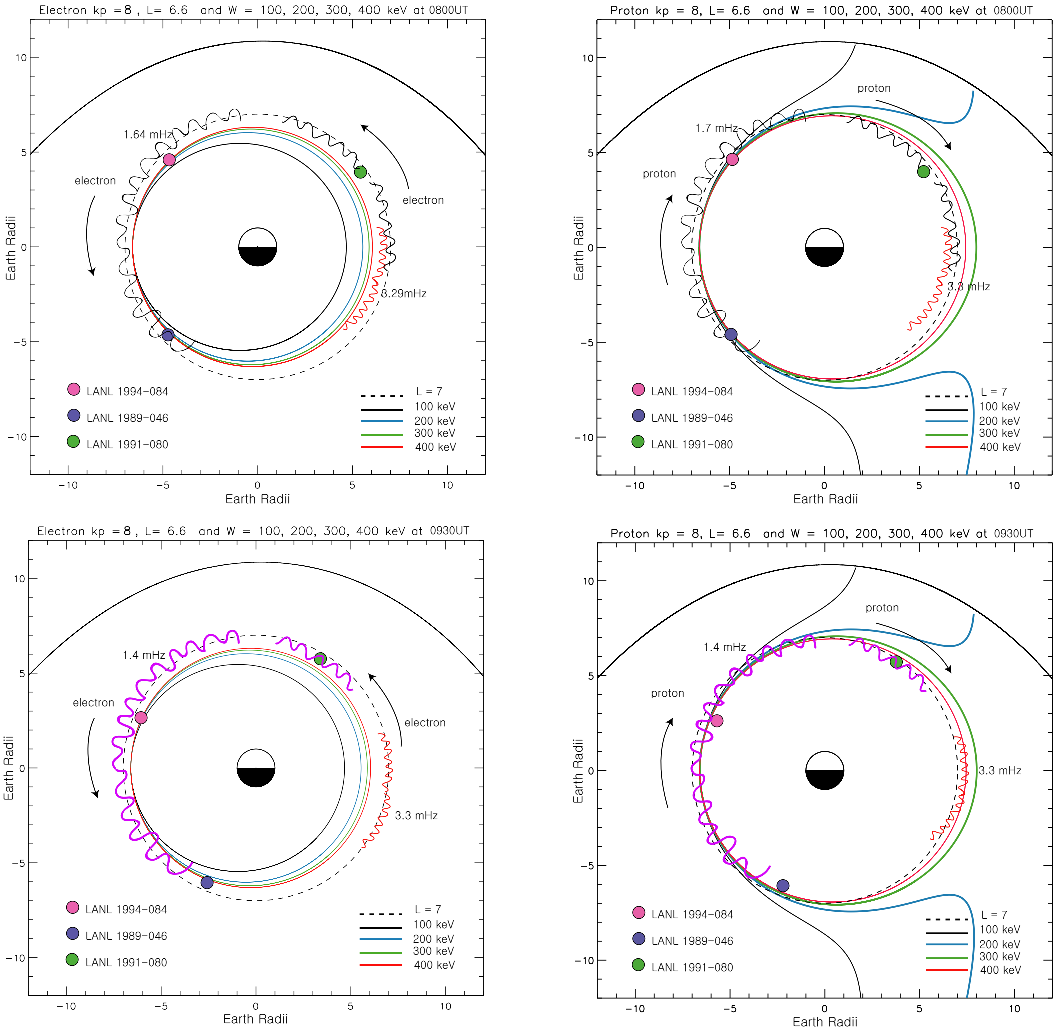

Figure 5.15: Pc 5 ULF wave (blue solid oscillation : 1.7 mHz ULF waves and red solid oscillations : 3.3 mHz ULF waves observed in the ground-based magnetometers and GOES 8), electron (left) and proton (right) drift path and LANL satellites locations at 0800 UT (top) during the interval (a) and 0930 UT (bottom) during the interval (b) on July 16, 2000.

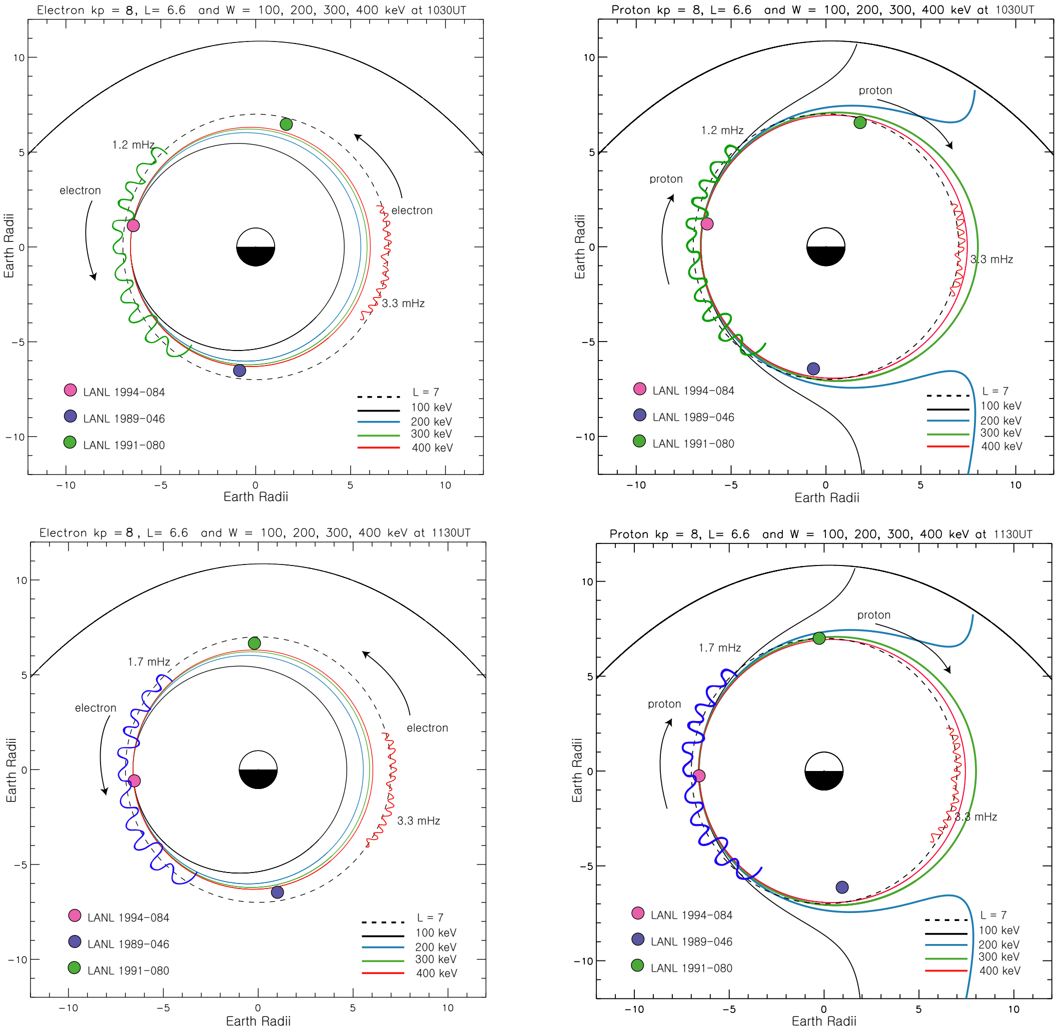

Figure 5.16: Pc 5 ULF wave (blue solid oscillation : 1.7 mHz ULF waves and red solid oscillations : 3.3 mHz ULF waves observed in the ground-based magnetometers and GOES 8), electron (left) and proton (right) drift path and LANL satellites locations at 1030 UT (top) during the interval (c) and 1130 UT (bottom) during the interval (d) on July 16, 2000.

Interval	ULF Waves	Particle Flux	Flux Modulation
(a)	✓ 1.7 mHz ULF waves - Global, largest amplitude at dusk ✓ 3.3 mHz - Local morning	✓1.7 mHz electron flux oscillations -All three LANL satellites ✓ 1.7 mHz proton flux oscillations - All three LANL satellites	Advection (both) -No phase change
(b)	✓ 1.4 mHz ULF waves - Noon-dusk, largest amplitude at dusk ✓ 3.3 mHz ULF waves - Local morning	✓ 1.4 mHz electron flux oscillations -All three satellites ✓ 1.4 mHz proton flux oscillations - LANL 1994-084	electron drift-resonance at 315 - 500 keV proton drift-resonance at 175 - 250 keV
(c)	✓ 1.2 mHz ULF waves - Noon-dusk, largest amplitude at dusk ✓ 3.3 mHz ULF waves - Local Morning	✓ 1.2 mHz electron flux oscillations -All three LANL satellites ✓ no proton flux oscillations	electron drift-resonance at 105 - 225 keV
(d)	✓ 1.7 mHz ULF waves - Postoon-dusk, Largest amplitude at dusk ✓ 3.3 mHz ULF waves - Local morning	✓ 1.7 mHz electron flux oscillations - All three LANL satellites ✓ 1.7 mHz proton flux oscillations - LANL 1994-084	electron drift-resonance at 500 - 750 keV proton drift-resonance at 250 - 400 keV

Table 5.2: Summary of Pc 5 ULF waves and particle flux modulations observed on July 16, 2000.

5.3.8 Summary

We have shown that electron and proton flux oscillations were clearly associated with Pc 5 ULF waves observed on the ground on July 16, 2000. Based on our observations, two explanations for the observed flux modulations are suggested: (1) Advection of an energetic particle density gradient (proton and electron show no change in phase with energy and similar amplitudes); (2) Energetic electron drift resonance (clear flux oscillations with amplitude and phase change across different energy channels). The absence of proton flux modulations appeared to be likely due to the wave propagation direction and the open drift paths of protons.

5.4 Case Study 3: June 08-09, 2000

Compressional Pc 5 magnetic pulsations were observed near local noon at GOES 10 on June 08, 2000. In addition, energetic particle flux oscillations of the same period (360s) were also observed near local noon by the geosynchronous satellites LANL 1994-084 and LANL 1997A-046. Compared to the previous two storm time events, both ULF waves and particle flux modulation occurred at local noon and the size of storm was much smaller (minimum Dst = -90 at 2000 UT on June 08, 2000). Statistically, compressional Pc 5 waves are observed in the afternoon sector [*Takahashi et al.*, 1985] with large azimuthal wave number ($|m| \sim$ 30-100). In this section, we show the observation of compressional waves and energetic particle flux modulations observed on June 08-09, 2000 and discuss the possible modulation mechanisms.

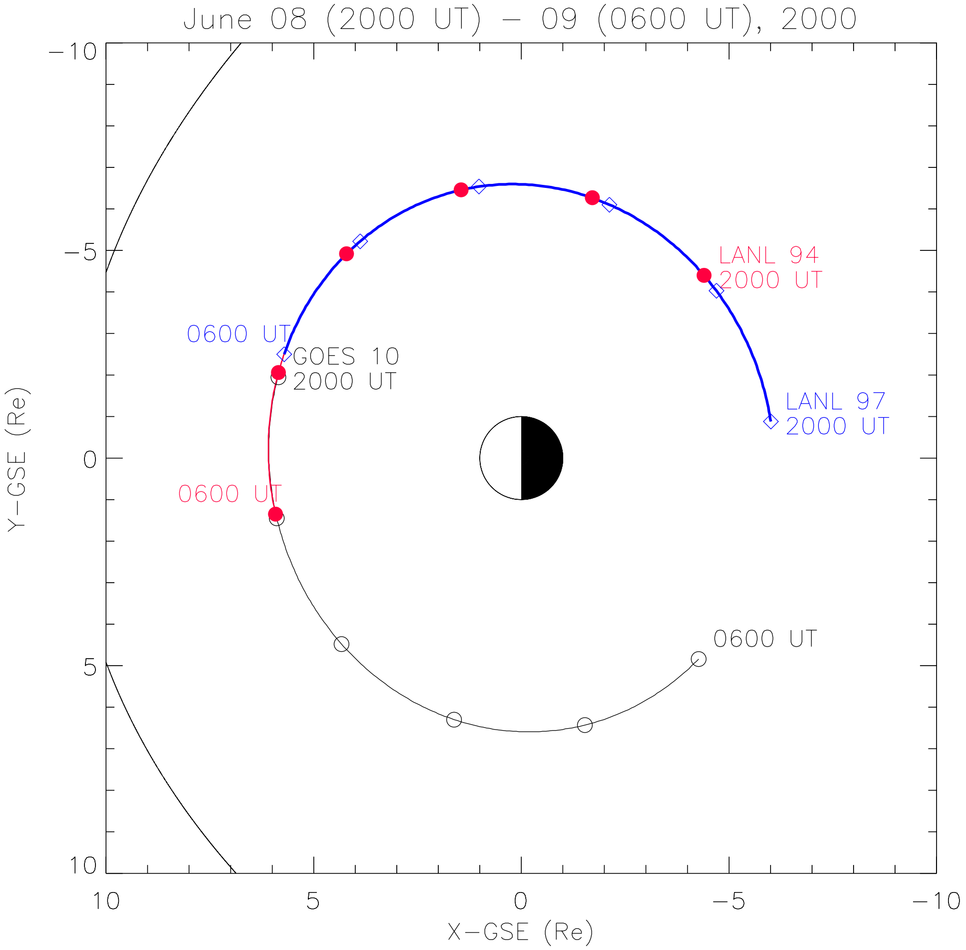

Figure 5.17: GOES 10, LANL 97 and LANL 94 trajectories in the GSE equatorial plane in the time interval from 2000 UT on June 08, 2000 to 0600 UT on June 09, 2000.

5.4.1 Instrumentation

In this study, we used magnetic field data from the IMAGE magnetometer array [*Viljanen and Hakkinen*, 1997], and the GOES 10 satellite, and particle data from the Los Alamos SOPA particle detectors on board geostationary satellites LANL 1994-084 and 1997A-046 were used in this study [e.g., *Belian et al.*, 1992]. The orbit of the GOES 10, LANL 97, and LANL 94 satellites are plotted during the time interval between 2000 UT on June 08 and 0600 UT on June 09, 2000 in Figure 5.17.

5.4.2 Solar Wind Observations

Figure 5.18 shows Dst index and interplanetary solar wind parameters observed by ACE from June 08 to June 09, 2000. The panels from the top to bottom illustrate the Dst index, solar wind proton density, solar wind bulk speed and interplanetary magnetic field (IMF) in geocentric solar magnetospheric (GSM) coordinates. The hourly Dst index shows minimum Dst = -90 nT at 2000 UT on June 08, 2000. Solar wind proton density and solar wind speed show discontinuities and stay high in the initial phase of storm and decrease during the recovery phase of storm. IMF B_z was fluctuating from south to north in the initial phase of storm.

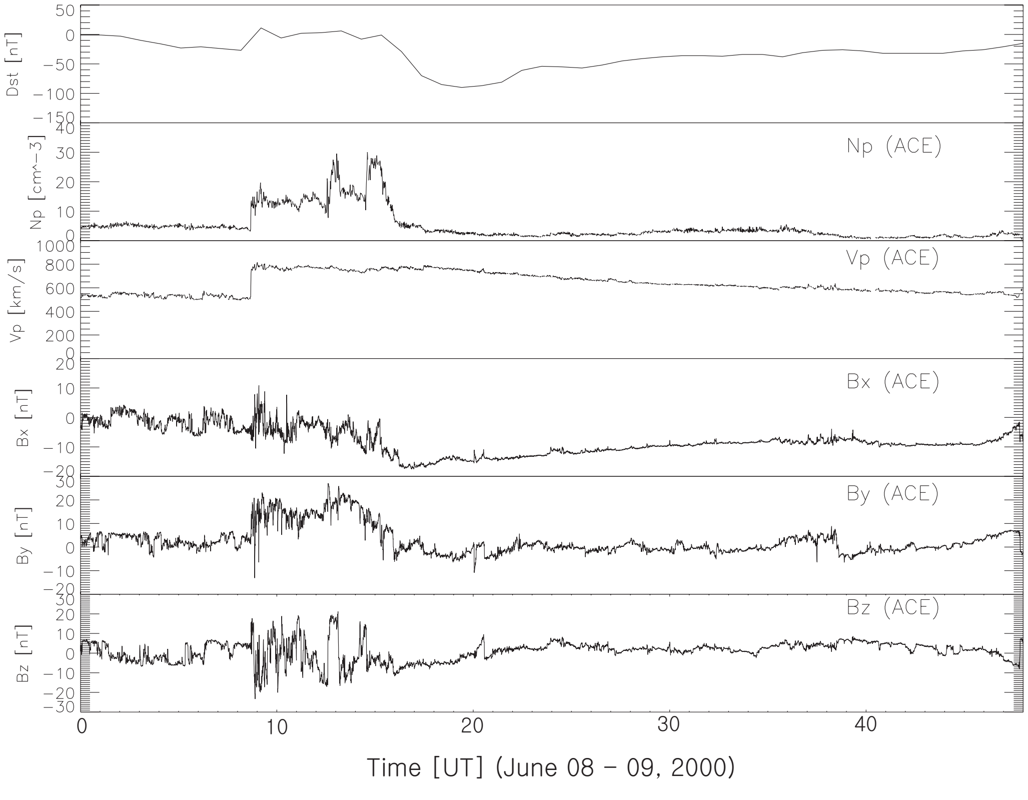

Figure 5.18: From the top, Dst index (nT), solar wind proton density (cm^-3), solar wind speed (km/s) and magnetic field components Bx (nT), By (nT), Bz (nT) in GSM coordinates from ACE from June 08, 2000 to June 09, 2000.

5.4.3 Particle flux modulations at local noon

Long duration large amplitude oscillations of electron and proton flux are illustrated in Figure 5.19. The particle flux pulsations observed from 1994-084 and 1997A-046 appeared at the same local time (near local noon) in both satellites rather than same universal time. Electrons and protons oscillate in-phase with each other and also oscillate in-phase across different energy channels. Also, the protons were modulated more strongly than the electrons for both satellites. *Kokubun et al.* [1977] show that proton modulations are usually larger in the morning and electron modulations are larger in the afternoon for drift-bounce resonance with the westward and the eastward traveling waves, respectively. However, our observation shows larger proton modulation in the noon sector with no phase change across different energies which means it is not likely explained by drift or drift-bounce resonant behavior.

Figure 5.20 shows magnetic field variations observed from GOES 10 and KIL station, and proton flux variations observed from LANL 1994-084 and LANL 1997A-046. These four panels were centered in the local noon. Thus UT in X-axis is different in each panel. ULF waves in the compressional component (Hp) of geomagnetic field are observed at GOES 10 near local noon but not in the ground station (KIL). A compressional mode with high azimuthal wave number (small azimuthal scale size) are unlikely to be observed in the ground due to the screening in the ionosphere [*Hughes and Southwood*, 1976] (see also section 2.8 in Chapter 2). The coherent wave and particle flux oscillations are similar to the behavior of advection of density gradient.

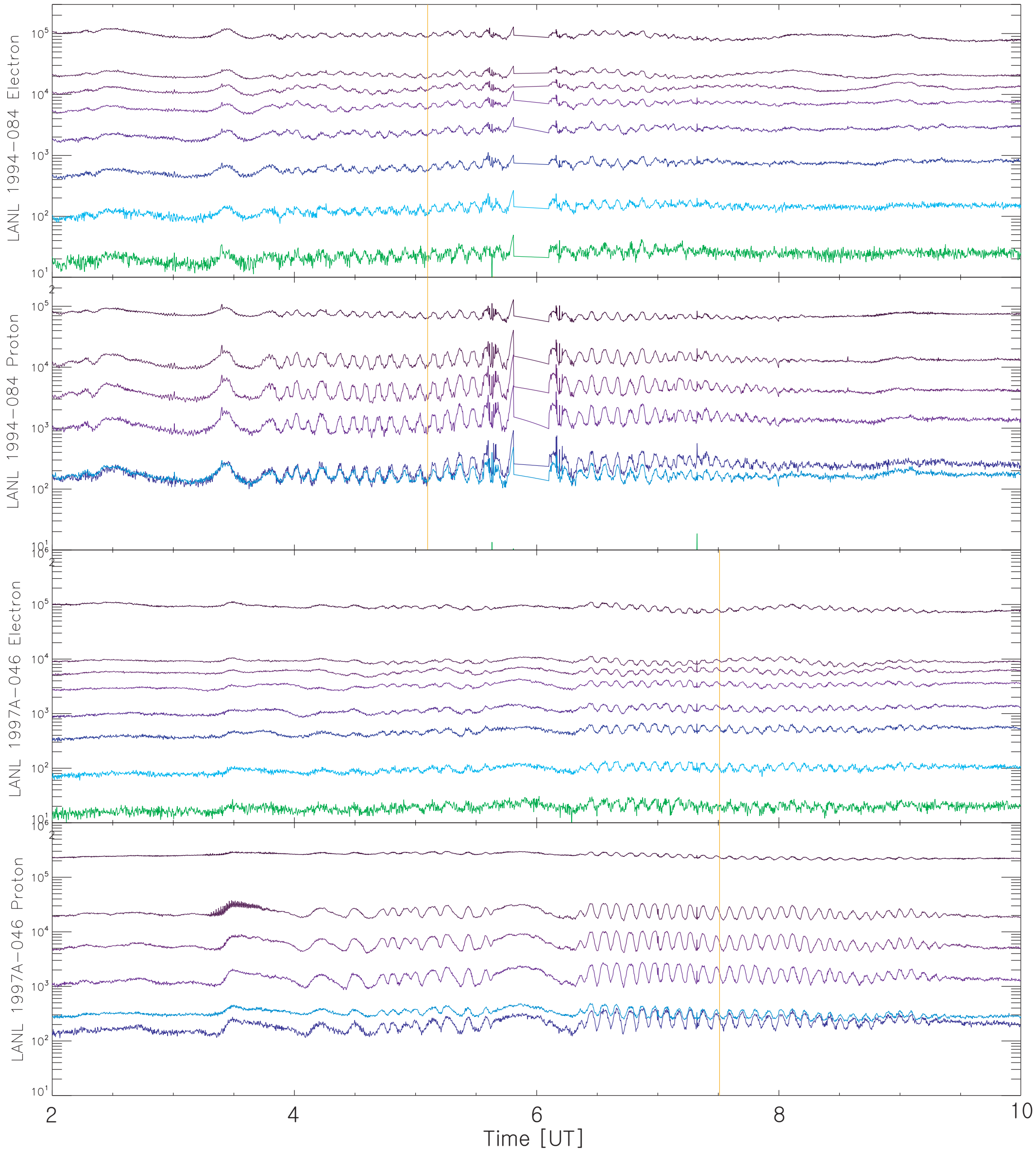

Figure 5.19: Particle flux pulsations observed on LANL in the 0200-1000 UT interval on June 09, 2000. From the top to bottom the ranges of electron energy channels are 50-75 keV, 75-105 keV, 105-150 keV, 150-225 keV, 225-315 keV, 315-500 keV, 500-750 keV,and 750-1100 keV and proton energy channels are 50-75 keV, 75-113 keV, 113-170 keV, 170-250 keV, 250-400 keV, and 400-670 keV. The yellow vertical lines indicate the local noon.

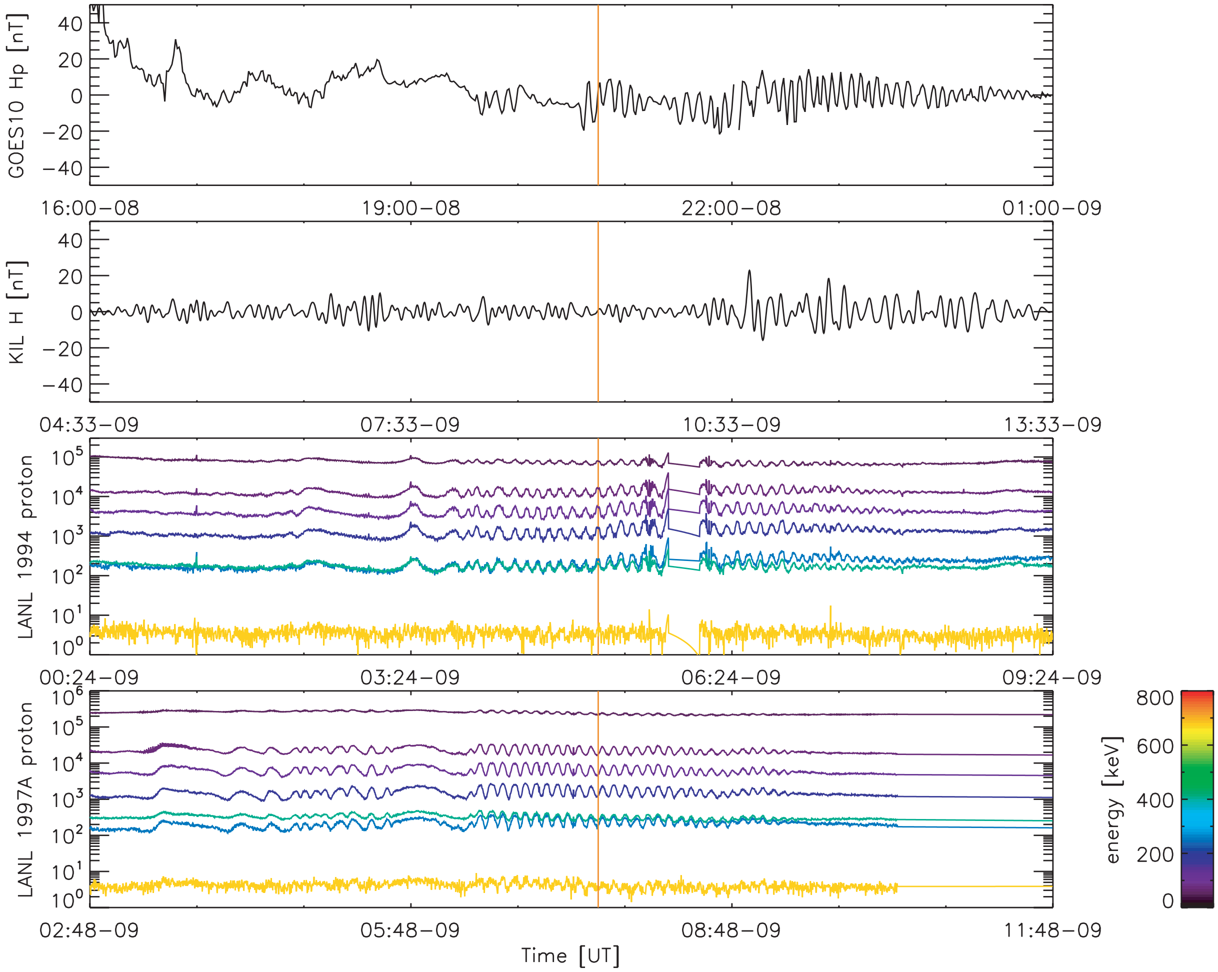

Figure 5.20: H-component magnetic field and proton flux on June 09, 2000. Red vertical lines indicate local noon. The magnetic field and proton flux data were plotted with different UT ranges to align in the local magnetic noon.

5.4.4 Summary

In this section, we observed compressional Pc 5 pulsations near local noon at GOES 10 and energetic particle flux oscillations near local noon at LANL 1994-084 and LANL 1997A-046 during the recovery phase of geomagnetic storm. As shown in Figure 5.19, both electron and protons flux modulations showed no phase changes across different energies. We suggest that a possible mechanism explaining this flux modulation is the advection of a particle density gradient which were discussed in 16th July 2000 event (see also Chapter 2 section 2.7.4).

5.5 Conclusions

In this chapter, we examined the interaction between Pc 5 ULF waves and energetic particles in outer radiation belt for the three storm time events. *Loto'aniu et al.* [2006] showed radial transport of relativistic electrons from L = 3 - 4 down to L $\sim$ 2 due to drift-resonance with Pc 5 ULF waves on 29 October 2003. Our observations also show an enhancement in the flux of 2-6 MeV electrons (see Figure 5.10), and we propose that this enhancement may also be due to ULF wave driven radial diffusion. *Horne et al.* [2005] observed 2-6 MeV electron flux depletion at L $>$ 3.5 and reformation near L = 2.5 during Halloween storm. They explained this result in terms of electrons being accelerated by the interaction with a few kilohertz waves. However, we observed milihertz geomagnetic pulsations (1- 10 mHz) in the recovery phase of the storms. Thus, we suggest that the observed relativistic electrons may have been accelerated by interaction with Pc 5 ULF waves. The observational results show that particle flux can be modulated by advection of a particle density gradient or through a drift-resonant interaction with Pc 5 waves. We showed three case studies of ULF wave interactions with energetic particles.

First, during the great storm of March 24, 1991, we observed large amplitude Pc 5 ULF waves in the ground-based magnetometer arrays located all around the world. Similarly, during the same time interval, we observed electron flux pulsations at the same frequencies from CRRES and LANL satellites. The clear phase changes of electron flux pulsations across the resonant energy suggest that the source of the electron modulation is the drift-resonant interaction (see Chapter

2 Section 2.7.2).

Second, We have observed geomagnetic Pc 5 pulsations and energetic particle flux oscillations simultaneously using ground-based and satellite instruments on 16 July 2000. Compare to the March 24, 1991 storm, multiple frequencies of Pc 5 ULF waves were observed in the ground-based magnetometers and satellites. Some particle modulations show no phase change with energy with similar amplitudes. We suggest that the possible explanation for this observed particle modulation is advection of energetic particle density gradient (see Chapter 2 Section 2.7.4. If there is a gradient in density in the direction of wave perturbations and displacement, flux oscillation can result [*Southwood*, 1973; *Southwood and Kivelson*, 1981]. The clear flux oscillations with phase changes across the resonant energy due to the drift resonance are also observed during this storm time.

Finally, we have observed energetic particle flux oscillation at local noon during the storm of June 09, 2000. This event shows a comparatively larger amplitude proton flux modulation, while the other two events showed stronger electron flux modulations. Also, very localized pulsations at noon are observed in contrast to the more global pulsations seen in the previous two events.

In summary, we find evidence that particles can be modulated through either a drift-resonant interaction with Pc 5 waves or by advection of a particle density gradient. Clear resonant behavior between the particle flux oscillations and Pc 5 pulsations suggests that Pc 5 ULF waves may play an important role in electron acceleration in the radiation belt.

Chapter 6

Modeling the Interaction Between Pc5 ULF Waves and Energetic particles [1]

6.1 Introduction

We have shown observational evidence for the interaction between Pc5 ULF waves and energetic particles in the form of flux modulation in Chapter 5. For example, the drift resonance mechanism is one possible way in which particle-flux may be modulated. The drift-resonant condition in an axisymmetric magnetic dipole is $\omega - m\omega_d = 0$, as described in section 2.7.2, and particles can be accelerated by this drift resonance with guided poloidal waves. *Elkington et al.* [1999, 2003] suggested that particles can be accelerated via the drift-resonance interaction with toroidal mode waves in a compressed dipole, where $\omega - (m \pm 1)\omega_d = 0$ (see section 2.7.3).

---

[1] We acknowledge Dr. Louis Ozeke for assistance with simulation model development used in this chapter.

Based on the observations presented in Chapter 5, we proposed that a particle flux modulation mechanisms such as advection of particle density gradient and drift resonance might be operating. In this Chapter we numerically calculate the trajectories and energy change of charged particles under the influence of model ULF wave electric fields. This modeling work is used to help to explain the observations in Chapter 5 and support our hypothesis that the active modulation mechanisms were advection of a flux gradient and drift resonance.

6.2 The Model

6.2.1 Non relativistic Charged Particle Motion

The equation of motion of a charged particle is

$$m\ddot{\mathbf{r}} = q\dot{\mathbf{r}} \times \mathbf{B}(\mathbf{r}, t) + q\mathbf{E}(\mathbf{r}, t) \tag{6.1}$$

where q is the charge and $\mathbf{r}$ is the particle position. After a little algebra, we can obtain the equation for the guiding center motion perpendicular and parallel to B [*Northrop*, 1963]. The equations for the motion of charged particles perpendicular to $\mathbf{B}$, i.e., the guiding center drift for non-relativistic charged particle can be written as

$$\dot{\mathbf{R}}_{\perp} = \frac{\hat{\mathbf{e}}_1}{B} \times (-\mathbf{E} + \frac{M}{q}\nabla B + \frac{m}{q}v_{\parallel}^2\frac{\partial\hat{\mathbf{e}}_1}{\partial s}) \tag{6.2}$$

where $M = mv_{\perp}^2/2B$ is magnetic moment, $v_{\parallel}$ is $\dot{\mathbf{R}} \cdot \hat{\mathbf{e}}_1(\mathbf{R})$ where $\mathbf{R}$ is the position of guiding center, s is the distance along the line of force and unit vector $\hat{\mathbf{e}}_1$ equal $\mathbf{B}/B$. In this equation, the first term is the usual "$\mathbf{E} \times \mathbf{B}$" drift, the second term is the "gradient B drift" and the third term is the "line curvature drift".

Also, the equation for the guiding center motion parallel to **B** is

$$\frac{dv_{\parallel}}{dt} = \frac{q}{m} E_{\parallel} - \frac{M}{m} \frac{\partial B}{\partial s} \tag{6.3}$$

Here $-(M/m)(\partial B/\partial s)$ is the mirror effect that produces reflection of particles *Northrop* [1963].

6.2.2 Relativistic Charged Particle Motion

In our study, Equations of relativistic particle motion from *Northrop* [1963] are simulated to track a guiding center drift path in the magnetosphere. The guiding center equation of motion of a relativistic charged particle has been solved using the Runge-Kutta method. We assumed that the Earth's magnetic field is dipole. The equation of motion for the relativistic charged particle of mass $m_0\gamma$ can be replaced by

$$m_0 \gamma \ddot{\mathbf{r}} = q\dot{\mathbf{r}} \times \mathbf{B}(r,t) + q\mathbf{E}(r,t) \tag{6.4}$$

where $\gamma = 1/\sqrt{1 - v^2/c^2}$ is the relativistic correction factor and m_0 is the rest mass. If the electric field is sufficiently small ($E_{\parallel}, E_{\perp}$ and $\partial/\partial t$ are order of ϵ, where $\epsilon = m/q$ is smallness parameter), the relativistic drift velocity become

$$\dot{\mathbf{R}}_{\perp} = \frac{\hat{\mathbf{e}}_1}{B} \times [-\mathbf{E} + \frac{M_r}{\gamma q} \nabla B + \frac{1}{\gamma q} \frac{p_{\parallel}^2}{m_0} \frac{\partial \hat{\mathbf{e}}_1}{\partial s}] \tag{6.5}$$

and the parallel force is

$$\frac{dp_{\parallel}}{dt} = qE_{\parallel} - \frac{M_r}{\gamma} \frac{\partial B}{\partial s} \tag{6.6}$$

Here the first adiabatic invariant $M_r = p_{\perp}^2/2m_o B$ is conserved where $p_{\perp} =$

$m_0 v_\perp \gamma$ (Here we used same notification with *Northrop* [1963]).

The mean rate of change of a particle's energy (dW/dt), for a particle with a charge, q, drifting adiabatically through the electric and magnetic field of a ULF wave is given by

$$\frac{dW}{dt} = q\mathbf{E} \cdot \mathbf{v}_d + \frac{M_r}{\gamma}\frac{\partial B}{\partial t}. \tag{6.7}$$

Here, $\mathbf{v}_d = \hat{\mathbf{e}}_1 v_\parallel + \dot{\mathbf{R}}_\perp$ is total guiding center velocity of particles and the electric field, $\mathbf{E}$, is the electric field of the wave. For the fundamental standing field-aligned guided toroidal and guided poloidal modes, the magnetic perturbation has a node at the equator, and we neglect compressional waves. In this study we are only considering the motion of particles in the equatorial plane, consequently the second term on the right hand side of equation (6.7) can be neglected. In addition since the motion of the high energy particles considered here is dominated by the gradient drift we have neglected the convection and co-rotation fields.

6.2.3 ULF Wave in a Dipole Field

We used a dipole coordinate system (ν, μ, ϕ) defined in Chapter 2. The electric and magnetic fields are related by Faraday's law as,

$$\nabla \times \mathbf{E} = -\frac{\partial \mathbf{b}}{\partial t} \tag{6.8}$$

In the radiation belt, high energy electrons and protons drift eastward and westward respectively. Thus, poloidal mode waves which have azimuthal electric fields (E_ϕ) will interact most strongly with these particles. For a guided poloidal mode wave the compressional magnetic component $b_\mu = 0$. Therefore,

$$\nabla \times \mathbf{E}|_\mu = 0 \tag{6.9}$$

and hence

$$\frac{\partial h_\nu E_\nu}{\partial \phi} - \frac{\partial h_\phi E_\phi}{\partial \nu} = 0 \tag{6.10}$$

In the case where we only have poloidal modes, $E_\nu = 0$ and hence

$$\frac{\partial h_\phi E_\phi}{\partial \nu} = 0 \tag{6.11}$$

where $\nu = 1/LR_E$ and $h_\phi = LR_E \sin^3\theta$. Consequently $h_\phi E_\phi \neq f(L)$ and since $h_\phi \propto L$ therefore

$$E_\phi \propto 1/L \tag{6.12}$$

Here we assume that the wave angular frequency ω_0 is constant and that the wave oscillates in azimuth as $\exp(\mathrm{i}m\phi)$, so that E_ϕ can be expressed as

$$E_\phi = A(\frac{L_r}{L})\sin(\mathrm{m}\phi - \omega_0 \mathrm{t}) \tag{6.13}$$

where L_r is the L-shell of the resonant field line in our simulations, L is assigned to be L = 6.7, the angular frequency $\omega_0 = 0.00942$ rads^{-1}, the azimuthal wave number $m = 2$ for electrons and $m = -2$ for protons, and A is assumed to be 3.0 mV/m.

6.2.4 Flux modulation

Kivelson and Southwood [1985b]; *Takahashi et al.* [1985] classified particle flux modulations depending on pulsation characteristics such as radial, azimuthal, and compressional magnetic perturbations. The reason for the modulation was explained as either due to the mirror effect, to adiabatic resonant acceleration or to convection of a particle density gradient. However, there was no study of how these are related with relativistic electrons observed in the radiation belt. In Chapter 5, we observed energetic particle flux oscillations together with magnetospheric pulsations in the Pc 5 range. We classified the flux modulation with magnetospheric Pc 5 waves into two categories: non-resonant (advection) and resonant response (drift-resonance) as mentioned in section 2.7.4. Here, we discuss the differences between advection and drift-resonance and a possible mechanism which can accelerate keV electrons up to MeV energies, using a simulation of the ULF wave-particle interaction.

6.2.5 Advection of Particle Gradient: Non-resonance

In Chapter 5, the first interval on July 16, 2000 and the event on June 09, 2000 show flux perturbations of keV electrons and protons in phase with similar amplitude. We concluded in Chapter 5 that this flux modulation arose due to the advection of a particle density gradient by the wave across the spacecraft. In this section we present results from detailed modeling which show the expected characteristics arising from the advection of a particle density gradient when the particle energy is far from the resonant energy.

As described in equation (2.64), the expected perturbation in f (phase space distribution function) is a function of energy W , first adiabatic invariant M, and magnetic shell parameter L.

If $\partial f/\partial L \neq 0$, a change in L or W can result in a change in f for the non-resonant case. In other words, if there is a gradient in density in the direction

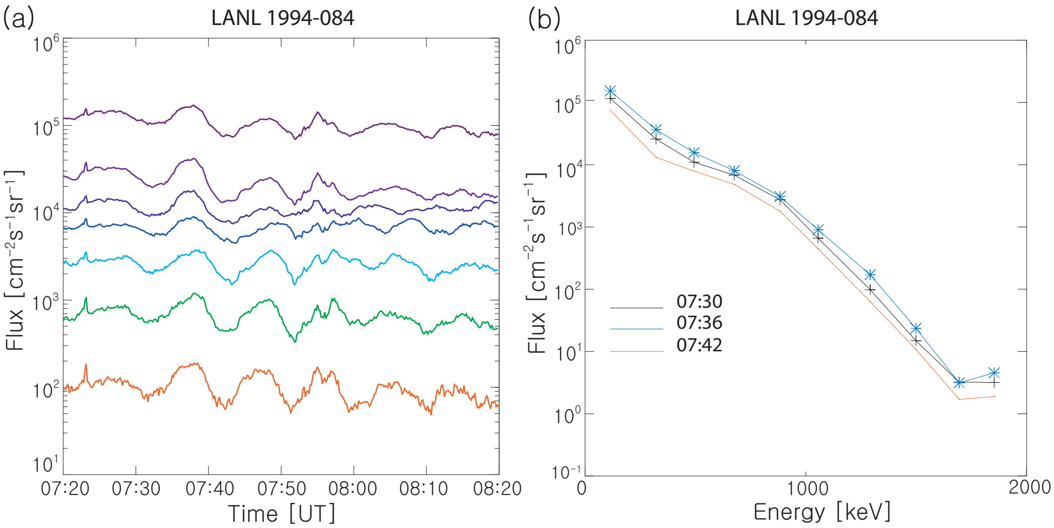

Figure 6.1: (a) Electron flux oscillation and (b) Change in energy and flux in time observed by the LANL 1994-084 on July 16, 2000.

.

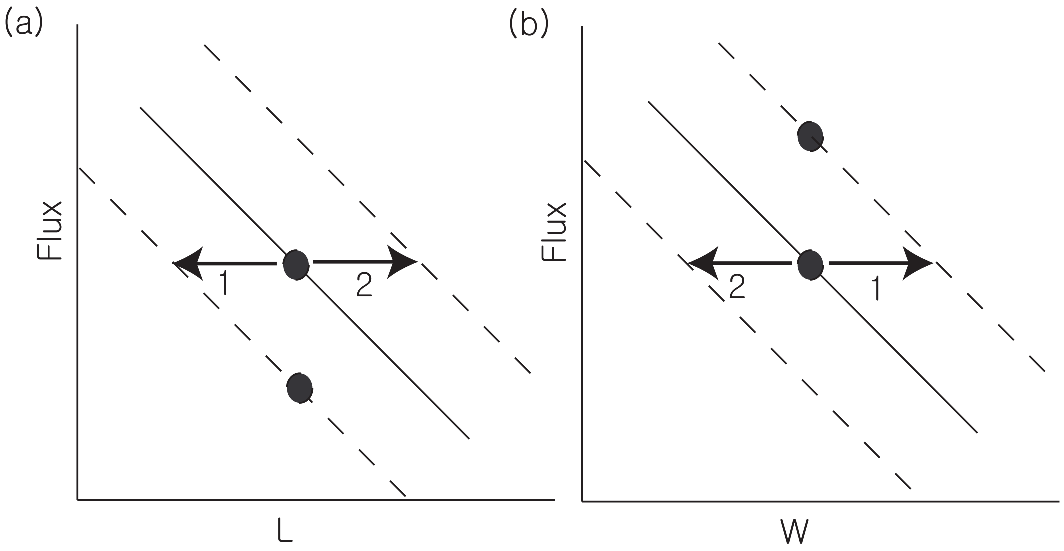

Figure 6.2: How adiabatic advection of the particle differential flux by a ULF wave changes (a) the flux as a function of L-shell, (b) the flux as a function of energy.

of the field line displacement, these can result in flux oscillations [*Southwood*, 1973; *Southwood and Kivelson*, 1981]. Here, to be consistent with observations we use particle differential flux (J) instead of a distribution function (f). The particle differential flux $J_\alpha(E;\mathbf{r})$ can be expressed using a distribution function $f(p_\parallel, p_\perp; \mathbf{r})$ as:

$$J_\alpha(E;\mathbf{r}) = p^2 f(p_\parallel, p_\perp; \mathbf{r}). \tag{6.14}$$

Here $p_\parallel = p\text{cos}\alpha$ and $p_\perp = p\text{sin}\alpha$ are the parallel and perpendicular momentum where α is the local pitch angle. For a particle with $\alpha = \pi/2$, equation (6.14) can be written as

$$J_\alpha(E;\mathbf{r}) = 2m_0 M B f(0, p_\perp; \mathbf{r}) \tag{6.15}$$

[*Schulz and Lanzerotti*, 1974]. Figures 6.1 and 6.2 show how particle flux varies with time in response to a ULF wave. Figure 6.1 (a) shows the electron flux oscillation observed by LANL 1994-084 at 0720 - 0820 UT on July 16, 2000. Figure 6.1 (b) illustrates the flux change for different energy channels in time. Different colors indicate different times. In all energy channels the flux varies in phase with the same logarithmic amplitude with time. Figure 6.2 is a schematic showing how the flux variations can occur due to advection by a ULF wave. The flux distribution has a negative gradient with L-shell and energy (W). Thus a change in L-shell (L) or energy (W) can result in a change in flux. For an adiabatic particle as it moves inward onto lower L-shells it's energy, W, will increase and vice versa. Consider a ULF wave which moves the particle flux inward as illustrated in Figure 6.2 by arrows labeled 1. As the particles move inward their energy will increase. If $\partial f/\partial W < 0$, an increase in energy will produce an increase in flux. On the contrary, if $\partial f/\partial L < 0$, the decrease in L-shell will produce decrease in flux. Thus the total change in flux depends on both the change in flux due to the advection of the $\partial f/\partial W$ and $\partial f/\partial L$ terms.

For example, if $\partial f/\partial L = 0$, flux change will depend only on $\partial f/\partial W$.

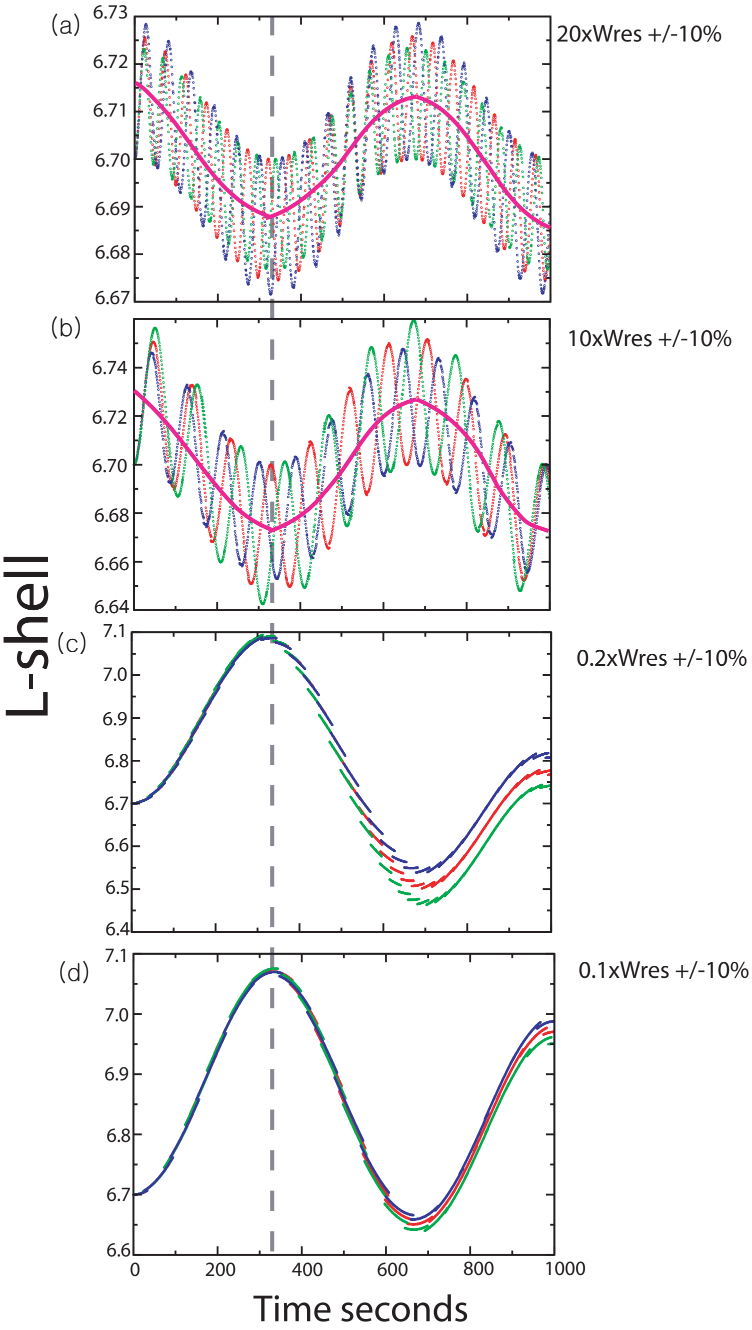

Figure 6.3: Electron flux oscillations under the influence of guided poloidal mode waves with initial energy 20 times, 10 times, 0.2 times, and 0.1 times the resonance energy. To simulate real satellite detector, we plotted error ranges (±10%(blue and green)).

Figure 6.3 illustrates the result from our simulation showing the non-resonant behavior of charged particles. The trajectories of equatorial electrons were calculated in a dipole magnetic field in the electric field of a ULF wave with frequency 1.50 mHz. The ULF electric field model used is discussed in section 6.2.3. Initially the 200 electrons were equally distributed in space at L = 6.7. The L-shell of the electrons as they pass through the morning sector, $89^\circ < \Phi < 91^\circ$, where Φ is azimuthal angle is displayed in the panels. Figure 6.3 (a) illustrates the change in L-shell of the particles which have energies 20 times the drift resonant energy ±10%. The ±10% simulates the typical energy range of a spacecraft particle detector. From the top to bottom panels in Figure 6.3, the initial energy ranges varies from much higher energy than resonance energy to much lower energy than resonance energy (from $20 \times Wres$ to $0.1 \times Wres$ where Wres is a resonant energy 370 keV). We used magnetic pulsations with 667s period, azimuthal wave number m=2, and resonant energy Wres= 370 keV.

When the initial energy is much higher than the resonant energy, the flux detected by satellite is 180^o out of phase with the wave oscillation (panels (a) and (b)). On the other hand, when the energy is much lower than the resonant energy the flux detected by satellite is in phase with the wave oscillation (panels (c) and (d). Smaller period oscillations appear at higher energies ((a) and (b) panels). This smaller period oscillation might be related with the drift period of high energy electrons. However, depends on the integration time the satellite detector may not be able to detect these high frequencies, only recording the average flux (indicated by the pink curves).

The first implication of this simulation result is that particle flux will change due to the advection of a spatial gradient back and forth by the wave when the energy is far from the resonant energy. Second, the results show a 180^o phase change across the resonance energy. Third, the simulation results show that the flux oscillation is in phase in the non-resonant case of advection of a particle gradient ((a) and (b) panels are in phase and (c) and (d) panels are in phase in Figure 6.3).

Flux modulation observed on July 16, 2000 and on June 09, 2000 showed flux oscillation in phase for particles with different energies. This observation is consistent with our modeling results. Thus we suggest that bulk velocity oscillations induced by Pc5 waves caused the advection of particle density gradient when the particle energy is far from the resonant energy as shown in Figure 6.3.

6.2.6 Drift-Resonance

Flux modulation can be caused by not only advection but also wave drift-bounce resonance or drift resonance. Electron flux modulations observed in Chapter 5 have energy ranges between 50 keV and 750 keV. To calculate resonant energy in these energy range, we used equation (2.62). The resonant energy of N=2 drift-bounce resonant electrons is either much higher or much lower than the 50 keV to 750 keV energy range observed here. However, the energy of drift resonant electrons falls within this range. Thus, we suggest that 10 - 100's keV energy electrons in the inner magnetosphere might be adiabatically accelerated through a drift-resonant interaction with Pc 5 ULF waves rather than drift-bounce resonant interaction.

As discussed in section 2.7.2, poloidal mode waves can accelerate electrons via drift-resonant interaction in a dipole field and the resonance condition is given by

$$\omega = m\omega_d. \tag{6.16}$$

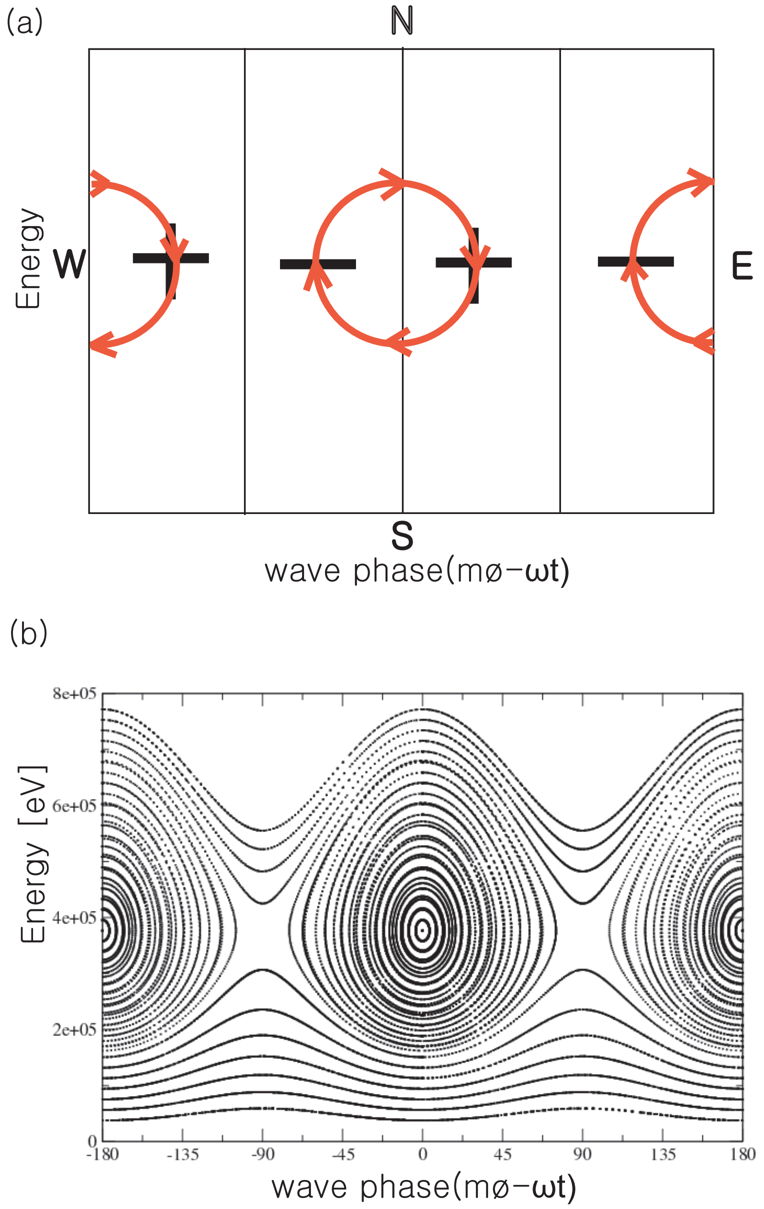

Figure 6.4: (a) Schematics showing the relation of Energy and wave phase. (b) Poincaré map showing the phase plane dynamics of electron with uniform first adiabatic invariant moving in the poloidal mode field for a 1.5 mHz frequency, 3 mV/m electric field, m=2 mode with zero convection and corotation electric fields.

Here, ω is the wave frequency and ω_d is the drift frequency of the particle. Figure 6.4 (a) shows a cartoon depicting an electron bouncing in the wave frame of

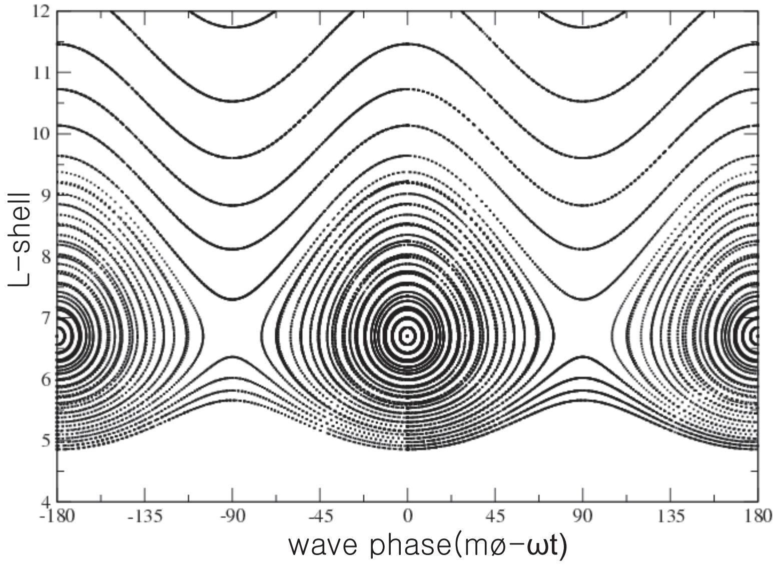

Figure 6.5: Poincaré map showing the L-shell and wave phase relation of electron with uniform first adiabatic invariant moving in the poloidal mode field for a 1.5 mHz frequency, 3 mV/m electric field, m=2 mode with no convection electric field.

reference for m=2 poloidal wave mode. In this case we used 'box model of magnetosphere' where field lines are straightend along one L-shell. For this particular wave mode, particle energy shares the y-axis with the north-south direction and the positive and negative signs represent eastward and westward azimuthal electric fields, respectively.

The red circles represent the drift-bounce motion of electrons in the frame moving with the azimuthal phase speed of this ULF wave. At the bottom of the circles the electrons have energies slightly below the resonant energy so that $\dot{\phi} < \omega/m$ and the electrons move westward in the negative electric field region. Thus energies increase since $\dot{W} = q\mathbf{E} \cdot \mathbf{v}_d > 0$. When electron passes the middle of the circle the energies pass the resonant energy so that $\dot{\phi} > \omega/m$ and the electrons move eastward. At the top of the circles the electrons have energies slightly above the resonant energy so that still $\dot{\phi} > \omega/m$ and the electrons move eastward. But electrons enter the region of negative electric field so that energies decrease ($\dot{W} = q\mathbf{E} \cdot \mathbf{v}_d < 0$) and reach the resonant energy in the middle of circle. Below the middle of circle $\dot{\phi} < \omega/m$ and electrons move westward until they reach the bottom of the circles.

Figure 6.4 (b) is the Poincaré map showing the phase space plot of particles with the same first adiabatic invariant, $M = P_{\perp}/2m_oB$, moving in the poloidal mode field in an m=2 mode, with convection and co-rotational electric field neglected. The amplitude of the electric field varies with L-shell as defined in equation 6.13 and has a frequency of 1.5 mHz. The plot shows the resonant island centered at $W \sim 370$keV. Figure 6.5 also shows the phase plane dynamics of the particles, but here L-shell is plotted as a function of wave phase instead of energy W. The phase space plot of electron motion provides a method for verifying the nature of acceleration.

The resonant electrons illustrated in Figures 6.4 and 6.5 will experience equal acceleration and deceleration by the ULF wave. There will be no change in their average energy over one complete circle around the resonance island. However, if the wave amplitude decays on a time scale equal to half the time it takes the electron to circle the resonance island, then it is possible for the electrons to remain permanently energized. For example, particles started at lower energy can stay at higher energy if wave activity has stopped by the time they reach higher energy. As shown in Figure 6.2, more charged particles exist at lower L-shells and lower energies. Thus, more low energy particles will gain energy while less high energy particles will lose energy, resulting in a bulk acceleration and energization of the particle flux.

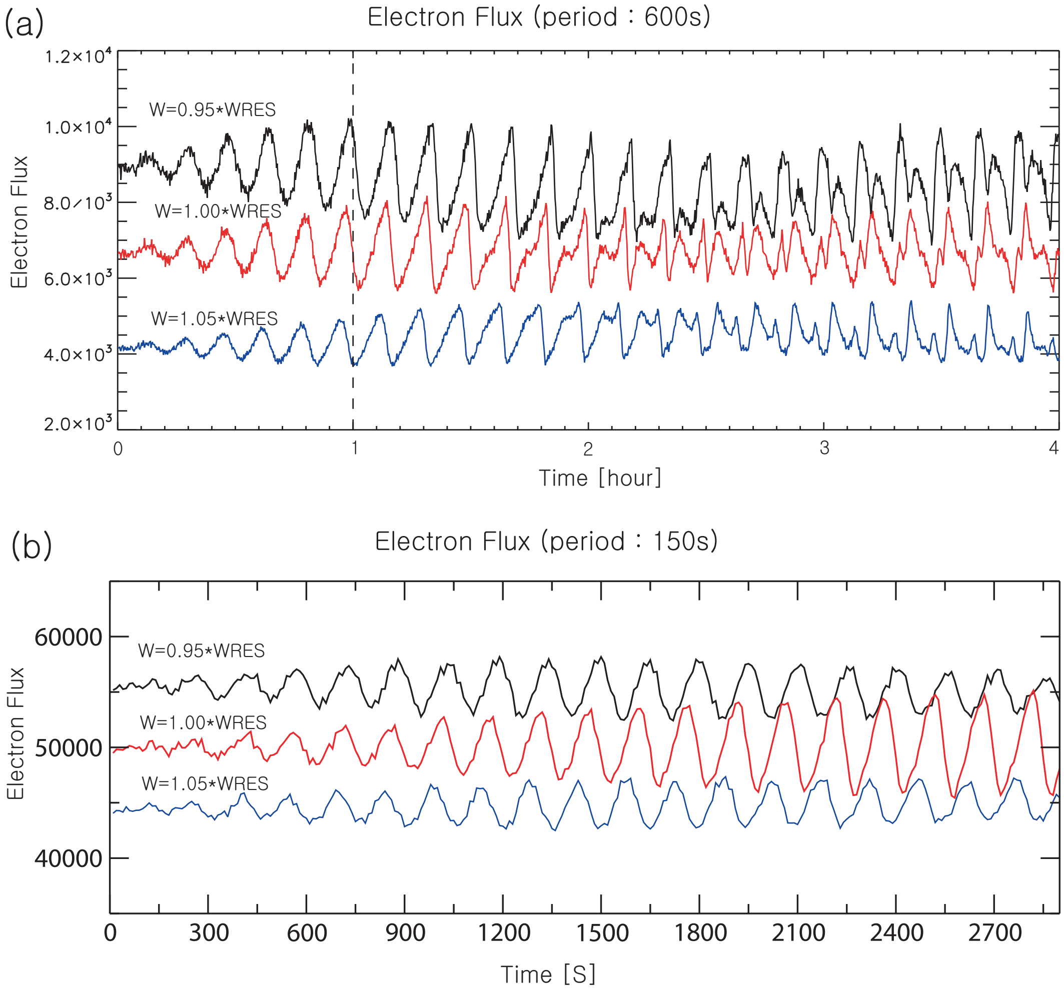

Figure 6.6: Electron flux oscillation in time under the influence of (a) 600s period poloidal waves and (b) 150s period poloidal waves.

Figure 6.6 (a) illustrates the result from our simulation showing the resonance behavior of charged particles with a resonant energy of Wres ∼ 420keV. This plot shows the flux variation in response to the ULF wave electric field. We used a magnetic pulsation with a period of 600s. Initially 2×10^7 electrons were uniformly distributed in space from L = 4.5 to L = 9.5. The number of electrons is counted when they pass through the morning sector, $89^\circ < \Phi < 91^\circ$, where Φ is azimuthal angle, and a L-shell between L = 6.6 and L=6.8. Three different

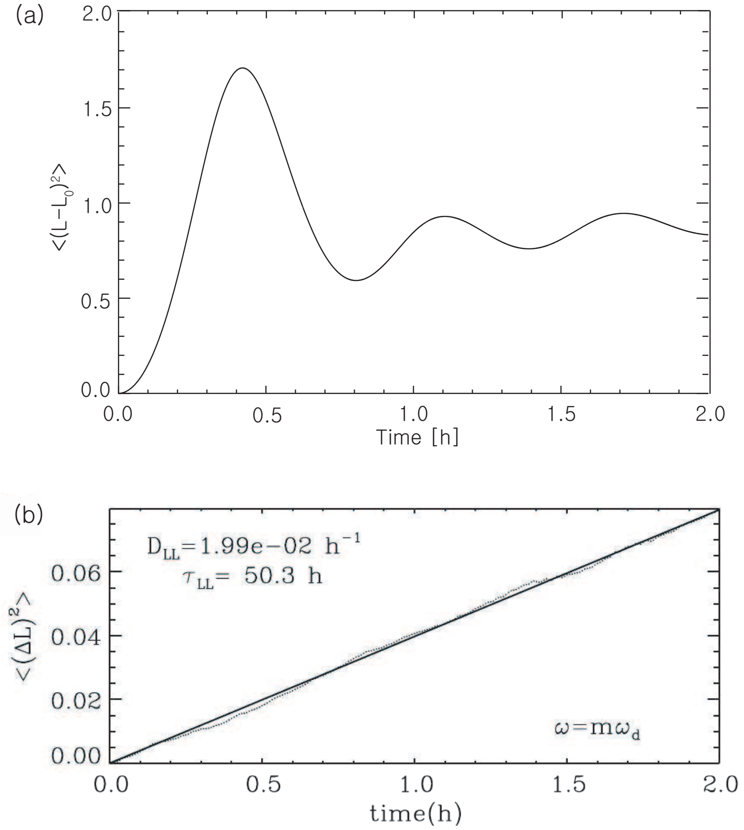

Figure 6.7: (a) Mean squared spread in time at L = 6.7 and W = 376 keV under the influence of $m = 2$ poloidal waves at the frequency 1.7 mHz (b) Mean squared spread in time at L = 6.6 and W = 1 MeV under the influence of $m = 2$ waves in the frequency range 2.5 - 4.5 mHz by *Elkington et al.* [2003]

electron initial energies, 0.95 times resonance energy, the resonance energy, and 1.05 times resonance energy, were chosen to study the behavior of particles near resonance energy.

Compared to the non-resonant case, the electron flux shows a clear phase change across the resonance energy. The vertical dotted line illustrates that higher energy is leading lower energy particle flux. Figure 6.6 (b) also shows energy flux as a function of time, but with a different ULF wave electric field (150s period wave). It is very clearly shown that particle flux oscillates at the same period (150s) as the background wave period and that the largest amplitude from modulation appears at the resonant energy, and there is a clear phase change across the resonant energy. In summary, our simulation results for the case of drift-resonance show that a flux modulation amplitude peak appears at the resonant energy with a phase change across the peak. This result is consistent with the observation shown in Chapter 5 for the case of a drift-resonance interaction.

Finally, Figure 6.7 (a) shows the mean squared deviation $< (L - L_0)^2 >$ as a function of time. 360 particles are uniformly distributed azimuth at constant $L_0 = 6.7$ with the initial energy of $W_0 = 376$keV. The particles move under the influence of m=2 waves with a frequency of 1.7 mHz. Figure 6.7 (b) shows the diffusion of particles under the influence of a azimuthal electric field in the frequency range 2.5-4.5 mHz in a compressed dipole by *Elkington et al.* [2003]. Their result shows that the mean squared deviation $< (L - L_0)^2 >$ increases linearly with time, as expected for a purely diffusive process. However, our result shows the impact of resonant behavior. Also, this mechanism is much faster than the diffusion but can only affect a limited range of particles close to the resonant energy.

6.3 Summary

We have shown particle simulations where flux modulation occur as a result of both advection of a flux gradient by a ULF poloidal wave and by drift resonant acceleration. In the case of advection, we find that if the initial energy is far from the theoretical resonance energy then the electron flux oscillates in phase with the wave at all energies, and both protons and electrons oscillate in phase. In the resonance case, we find out the drift-resonance interaction is a possible mechanism for flux modulation and that wave propagation direction and particle species are important. Our simulations clearly show that the flux oscillations vary with energy, and that the largest amplitude flux oscillations occur near the resonant energy. Both results for the advection and resonance cases show consistency with our hypothesis discussed in Chapter 5, and verify our interpretation of the observational data presented in that Chapter.

Chapter 7

Conclusions and Future Work

7.1 Concluding Remarks

In this thesis we examined the generation mechanisms of Pc 5 ULF waves during geomagnetic storms and the interaction between Pc 5 ULF waves and energetic particles in the radiation belts.

Chapter 4 presented observational studies of Pc 5 pulsations using ground-based magnetometer and satellite data during geomagnetic storm times. Three storm time events, (A) March 24, 1991, (B) March 28, 2001 , and (C) July 28, 1990 were selected for detailed analysis. Each showed a brief increase in Dst in the main phase of the storm due to the compression of the magnetosphere during the development of the ring current in the main phase.

During the great magnetic storm time of March 24, 1991, we observed intense Pc5 pulsations at unusually low sub-auroral latitudes. These pulsations showed multiple wave packets having power which peaked at different dayside local times. We suggested that these pulsations might have been driven by different solar wind Pc 5 wave sources at different times, such as magnetopause shear-flow instabilities and solar wind pressure pulses.

During the geomagnetic storm of March 27 - 28, 2001, we showed that geomagnetic pulsations were observed by both ground-based magnetometers and geosynchronous satellites. These geomagnetic pulsations appeared simultaneously with solar wind dynamic pressure perturbations. The correlation of solar wind dynamic pressure oscillations and geomagnetic pulsations was much stronger than with solar wind speed, suggesting that solar wind dynamic pressure variations can be a direct source of geomagnetic pulsations.

During the geomagnetic storm of July 28, 1990, we observed very large amplitude compressional Pc 5 pulsations near local noon. GOES 6 and GOES 7 observed magnetopause boundary crossings in the same time interval that we observed large geomagnetic perturbations at ground level. We suggest that the periodic variation in solar wind dynamic pressure drove the compressional Pc 5 pulsations at local noon.

In Chapter 5 we presented results showing the interaction between Pc 5 ULF waves and energetic particles in the outer radiation belt for three storm time events.

Firstly, during the great storm of March 24, 1991, we observed very strong Pc 5 oscillations of 1.7 mHz frequency between 1200 and 1340 UT and electron flux modulation with same frequencies simultaneously. The observed electron flux showed resonant behavior such as phase and amplitude changes with energy across the peak amplitude modulations at energy $\sim$ 400 keV. We suggest that during this storm time, in a compressed dipole, toroidal mode Pc 5 ULF waves accelerated electrons via a drift-resonance interaction [*Elkington et al.*, 1999, 2003].

Secondly, during the Bastille day storm of July 16, 2000, we also observed geomagnetic Pc 5 pulsations and energetic particle flux oscillations simultaneously. Based on our observations, two explanations for a variety of observed flux modulations are suggested: (1) Advection of an energetic particle density gradient (proton and electron show no change in phase with energy and similar amplitudes); (2) Energetic electron drift resonance (clear flux oscillation amplitude and phase change across different energy channels). The frequent absence of proton flux modulations is likely due to the open drift paths of protons or wave propagation directions, perhaps related to this modulations being observed only on the drift paths of one ion or electron species at any given location.

Finally, we observed energetic particle flux oscillations at local noon during the storm of June 09, 2000. Compared to the previous two storms, the size of this storm is much smaller; particle modulation occurs only at local noon; and proton flux modulation was larger than electron flux modulation. The mechanism responsible is likely the advection of a spatial density gradient.

In summary, we have observed clear association between energetic particle flux oscillations and Pc 5 ULF waves during geomagnetic storm events. Based on the observations, we concluded that the modulation of energetic particle flux might be associated with either drift-resonance interaction or the advection of an energetic particle density gradient.

Finally, in Chapter 6 we showed particle simulations solving the guiding center equation of motion of a relativistic charged particle. We showed the differences between advection and drift-resonance mechanisms using a simulation of the ULF wave-particle interaction. In the case of advection, both electron and proton fluxes oscillate in phase with the wave at all energies. In the drift resonance case, flux oscillations show a phase change with energy and have the largest amplitude modulation near the resonant energy. The numerical simulations of the particle flux modulations are in perfect agreement with the flux modulations measured in situ by LANL satellites and CURREY'S satellite. Overall, we suggest that the Pc 5 waves may play an important role in energetic particle dynamics in the radiation belt and ring current.

7.2 Future Work

In this thesis we have focused on identifying the excitation mechanisms of Pc 5 magnetic pulsations and the relationship between Pc 5 ALF waves and energetic particle flux modulations in the radiation belt. Each of these subjects could be extended with future work to support our suggested interpretations and to gain a greater understanding of related aspects of these dynamics.

We have examined the excitation mechanisms during three geomagnetic storms in Chapter 4. A better understanding of Pc 5 excitation mechanisms may be achieved by examining additional similar events. Especially, the absence of solar wind data for March 24 1991 events has limited our interpretation. Thus, by examining similar events with upstream solar wind information will enable a clearer interpretation of the excitation mechanisms. Also, further observations of the MLT dependence may be investigated statistically, so that the dependence of excitation mechanisms with local time and any dawn/dusk asymmetry may be better understood. All three events were observed during the main phase of geomagnetic storms. Comparing with Pc 5 pulsations observed in the recovery phase of storms, or during non-storm times, would allow a full characterization of the Pc 5 pulsations.

We also observed an eigenfrequency reduction during the main phase of the storms on March 24, 1991 and March 28, 2001. Further observations examining the reduction of the local Alfvén eigenfrequency continuum as compared to non-storm times may add support to the current suggestion that heavy ions play a role in the radiation belt electron dynamics via the intermediary of ULF waves. In addition, more examples showing MeV electron flux enhancements during the penetration of Pc 5 pulsations to low latitude may be also very useful.

In Chapter 5, we showed evidence for a relationship between Pc 5 pulsations and particle flux oscillations. How this is related to the enhancement of MeV electron flux should be included in future work. Statistically diagnosing the relationship between occurrences of particle flux modulation and MeV electron enhancements may also be valuable. This may be achieved by examining various different satellite data sets which show MeV electron enhancement, and investigating the relationship to particle flux modulations.

Bibliography

Allan, W., and F. B. Knox (1979), The effect of finite ionosphere conductivities on axisymmetric toroidal Alfvén wave resonances, *Planet. Space Sci*, *27*, 939–950.

Allan, W., and E. M. Poulter (1992), ULF waves-their relationship to the structure of the Earth's magnetosphere, *Rep. Prog. Phys.*., *55*, 533.

Allan, W., S. White, and E. M. Poulter (1986), Impulse-excited hydromagnetic cavity and field line resonances in the magnetosphere, *Planet. Space Sci.*, *34*, 371.

Araki, T., S. Fujitani, K. Yumoto, and K. Shiokawa (1997), Anomalous sudden commencement on March 24, 1991, *J. Geophys. Res.*, *102*, 14,075.

Baker, D. N., G. M. Mason, O. Figueroa, G. Colon, J. G. Watzin, and R. M. Aleman (1993), An Overview of the Solar, Anomalous, and Magnetospheric Particle Explorer SAMPEX Mission, *IEEE Transactions on Geoscience and Remote Sensing*, *31*(3), 531–541.

Baker, D. N., S. Kanekal, J. B. Blake, B. Klecker, and G. Rostoker (1994), Satellite anomalies linked to electron increase in the magnetosphere, *EOS Trans. AGU*, *75*, 410.

Baker, D. N., S. G. Kanekal, X. Li, S. P. Monk, J. Goldstein, and J. L. Burch (2004), An extreme distortion of the Van Allen belt arising from the Hallowe'en solar storm in 2003, *Nature*, *432*(7019), 878–881.

Banks, R. (1975), Complex demodulation of geomagnetic data and the estimation of transfer functions, *Geophysical Journal International*, *43*(1), 87–101.

Baumjohann, W., and R. A. Treumann (1997), Basic space plasma physics, *Imperical College Press*.

Beamish, D., H. W. Hanson, and D. C. Webb (1979), Complex demodulation applied to Pi2 geomagnetic pulsations, *Geophys. J. R. Astron. Soc.*, *58*, 471.

Belian, R. D., G. R. Gisler, T. E. Cayton, and R. A. Christensen (1992), High-z energetic particles at geosynchronous orbits during the great solar proton event series of october, *J. Geophys. Res.*, *97*, 897.

Bingham, G., M. D. Godfrey, and J. W. Tuckey (1967), Modern techniques of power spectrum estimation, *IEEE Transactions on audio and electroacoustics*, *AU-15, Number 2*.

Blake, J. B., W. A. Kolasinski, R. W. Fillius, and E. G. Mullen (1992), Injection of electrons and protons with energies of tens of MeV into l 3 on March 24, 1991, *Geophys. Res. Lett.*, *19*, 821.

Cahill, L. J., and J. R. Winckler (1974), Magnetopause crossings observed at 6.6 *r_e*, *J. Geophys. Res.*, *79*, 1024.

Chen, L., and A. Hasegawa (1974), A theory of long-period magnetic pulsations, 1. Steady state excitation of field line resonance, *J. Geophys. Res.*, *79*, 1024.

Chisham, G. (1996), Giant pulsations: An explanation for their rarity and occurrence during geomagnetically quiet times, *J. Geophys. Res.*, *101*(11), 24,755–24,764.

Chisham, G., and D. Orr (1997), A statistical study of the local time asymmetry of Pc 5 ULF wave characteristics observed at midlatitudes by SAMNET, *J. Geophys. Res.*, *102*, 24,339.

Cumming, W. D., and P. J. Coleman (1968), Magnetic fields in the magnetopause and vicinity at synchronous altitude, *J. Geophys. Res.*, *73*, 5699.

Daglis, I. A., and R. M. Thorne (1999), The terrestrial ring current: origin, formation, and decay, *Rev. Geophys.*, *37*, 407.

Dungey, J. W. (1954), Electrodynamics of the outer atmosphere, *University Park.*

Elkington, S. R., M. K. Hudson, and A. A. Chan (1999), Acceleration of relativistic electrons via resonant interaction with toroidal-mode Pc-5 ULF oscillations, *Geophys. Res. Lett.*, *26*, 187.

Elkington, S. R., M. K. Hudson, and A. A. Chan (2003), Resonant acceleration and diffusion of outer zone electrons in an asymmetric geomagnetic field, *J. Geophys. Res.*, *108*(A3), 111, doi:10.1029/2001JA009202.

Feng, Q., B. J. Fraser, F. W. Menk, C. W. S. Ziesolleck, O. Saka, and T. Kitamura (1995), Pc 3-4 geomagnetic pulsations observed at very low latitude conjugate stations, *J. Geophys. Res.*, *100*, 19,287.

Francia, P., S. Lepidi, and U. Villante (2001), Low latitude geomagnetic field fluctuations at discrete frequencies as possible indicators for global magnetospheric oscillations, *Mem. S.A.It.*, *72*, 606.

Fraser, B. J., J. L. Horwitz, J. A. Slavin, Z. C. Dent, and I. R. Mann (2005), Heavy ion mass loading of the geomagnetic field near the plasmapause and ULF wave implications, *Geophys. Res. Lett.*, *32*(4), L04102, doi: 10.1029/2004GL021315.

Fujitani, S. T., T. Araki, K. Yumoto, K. Shiokawa, S. Tsunomura, and Y. Yamada (1993), Global Pc5 on March 24, 1991, *STEP-GBRSC-NEWS, Special Issue SOLTIP Data Analysis Activity*, *3*, 15.

Glassmeier, K. H. (1984), On the influence of ionospheres with non-uniform conductivity distribution on hydromagnetic waves, *J. Geophys.*, *54*, 125–137.

Gonzalez, W. D., J. A. Joselyn, Y. Kamide, H. W. Kroehl, G. Rostoker, B. T. Tsurutani, and V. M. Vasyliunas (1994), What is a geomagnetic storm?, *Journal of Geophysical Research-Space Physics*, *99*(A4).

Hamlin, D. A., R. Karplus, R. C. Vik, and K. M. Watson (1961), Mirror and azimuthal drift frequencies for geomagnetically trapped particles, *J. Geophys. Res.*, *66*(1), 1–4.

Harrold, B. G., and J. C. Samson (1992), Standing ULF modes of the magnetosphere: A theory, *Geophys. Res. Lett.*, *19*, 1811.

Hasegawa, H., M. Fujimoto, T.-D. Phan, H. Rême, A. Balogh, M. Dunlop, C. Hashimoto, and R. TanDokoro (2004), Transport of solar wind into earth's magnetosphere through rolled-up kelvin-helmholtz vortices, *Nature*, p. 755.

Higbie, P. R., D. N. Baker, R. D. Zwickl, R. D. Belian, J. R. Asbridge, J. F. Fennell, B. Wilken, and C. W. Arthur (1982), The global Pc 5 event of November 14-15, 1979, *J. Geophys. Res.*, *87*, 2337.

Horne, R. B., et al. (2005), Wave acceleration of electrons in the Van Allen radiation belts, *Nature*, *437*, doi:10.1038/nature03939.

Hudson, M. K., A. D. Kotelnikov, X. Li, I. Roth, M. Temerin, J. Wygant, J. B. Blake, and M. S. Gussenhoven (1995), Simulation of proton radiation belt formation during the March 24, 1991 SSC, *Geophysical Research Letters*, *22*(3), 291–294.

Hudson, M. K., R. E. Denton, M. R. Lessard, E. G. Miftakhova, and R. R. Anderson (2004), A study of Pc-5 ULF oscillations, *Ann. Geophy.*, *22*, 289.

Hughes, W. J. (1994), Magnetospheric ULF waves: A tutorial with a historical perspective, in *Solar Wind Sources of Magnetospheric Ultra-Low-Frequency Waves*, *Geophys. Monogr. Ser.*, vol. 81, edited by M. J. Engebreston, K. Takahashi, and M. Scholer, p. 1, AGU, Washington, D.C.

Hughes, W. J., and D. J. Southwood (1976), The screening of micropulsation signals by the atmosphere and ionosphere, *J. Geophys. Res.*, *81*(19).

Hughes, W. J., and D. J. Southwood (1978), Alfven waves generated by an inverted plasma energy distribution, *Nature*, *275*(7), 43.

Jacobs, J. A., Y. Kato, S. Matsushta, and V. A. Troitskaya (1964), Classification of geomagnetic micropulsations, *J. Geophys. Res..*, *69*, 180.

Kepko, L., and H. E. Spence (2002), Ulf waves in the solar wind as direct drivers of magnetospheric pulsations, *Geophys. Res. Lett.*, doi:10.1029/2001GL014405.

Kessel, R. L. (2008), Solar wind excitation of Pc5 fluctuations in the magnetosphere and on the ground, *J. Geophys. Res.*, *113*, doi:10.1029/2007JA012255.

Kivelson, M., and C. Russell (1995), *Introduction to space physics*, Cambridge university press.

Kivelson, M. G. (2005), Ulf waves from the ionosphere to the outer planets, *UCLA Institute of Geophysics and Planetary Physics Publication*, *6264*.

Kivelson, M. G., and D. J. Southwood (1985a), Resonant ULF waves - a new interpretation, *Geophys. Res. Lett.*, *12*, 49.

Kivelson, M. G., and D. J. Southwood (1985b), Charged particle behavior in low-frequency geomagnetic pulsations, 4, Compressional waves, *J. Geophys. Res*, *90*(A2), 1486–1498.

Kivelson, M. G., and D. J. Southwood (1986), Coupling of global magnetospheric MHD eigenmodes to field line resonances, *J. Geophys. Res.*, *91*, 4345.

Kivelson, M. G., and D. J. Southwood (1988), Hycromagnetic waves and the ionosphere, *Geophys. Res. Lett.*, *15*, 1271.

Kivelson, M. G., J. Etcheto, and J. G. Trotignon (1984), Global compressional oscillations of the terrestrial magnetosphere - the evidence and a model, *J. Geophys. Res..*, *89*, 9851.

Kokubun, S., M. G. Kivelson, R. L. McPherron, C. T. Russell, and H. I. West (1977), OGO 5 observations of Pc 5 waves- Particle flux modulations, *Journal of Geophysical Research*, *82*, 2774–2786.

Le, G. M., Z. H. Ye, J. H. Gong, Y. H. Tan, H. Lu, and Y. Q. Tang (2003), Time determination of March 1991's CME hitting magnetosphere, *in Proceeding of 28th International Cosmic Ray Conference*, p. 3601.

Lee, D. H., and R. L. Lysak (1991), Impulsive excitation of ULF waves in the three-dimensional dipole model: The initial results, *J. Geophys. Res.*, *96*, 3479–3486.

Lee, E. A., I. R. Mann, T. M. Loto'aniu, and Z. C. Dent (2007), Global Pc5 pulsations observed at unusually low L during the great magnetic storm of 24 March 1991, *J. Geophys. Res.*, *112*, A05208, doi:10.1029/2006JA011872.

Lee, L. C., R. K. Albano, and J. R. Kan (1981), Kelvin-helmholtz instability in the magnetopause-boundary layer region, *J. Geophys. Res.*, *86*, 54.

Lenz, J., H. Inc, and M. Minneapolis (1990), A review of magnetic sensors, *Proceedings of the IEEE*, *78*(6), 973–989.

Lepidi, S., P. Francia, U. Villante, A. Meloni, A. J. Lazarus, and R. P. Lepping (1999), The Earth's passage of the April 11, 1997 coronal ejecta: geomagnetic field fluctuations at high and low latitude during north interplanetary magnetic field conditions, *Ann. Geophys.*, *17*, 1245.

Li, X., and A. Temerin (2001), The Electron Radiation Belt, *Space Sci. Rev.*, *95*, 569–580.

Li, X., I. Roth, M. Temerin, J. R. Wygant, M. K. Hudson, and J. B. Blake (1993), Simulation of the prompt energization and transport of radiation belt particles during the March 24, 1991 SSC, *Geophysical Research Letters*, *20*, 2423–2423.

Lin, N., M. J. Engebretson, R. L. McPherron, M. G. Kivelson, W. Baumjohann, H. Luehr, T. A. Potemra, B. J. Anderson, and L. J. Zanetti (1991), A comparison of ULF fluctuations in the solar wind, magnetosheath, and dayside magnetosphere. 2. Field and plasma conditions in the magnetosheath, *J. Geophys. Res.*, *96*, 3455.

Loto'aniu, T. M., I. R. Mann, L. G. Ozeke, A. A. Chan, Z. C. Dent, and D. K. Milling (2006), Radial diffusion of relativistic electrons into the radiation belt slot region during the 2003 Halloween geomagnetic storms, *J. Geophys. Res.*, *111* (A4), A04218, doi:10.1029/2005JA011355.

Mann, I., et al. (2008), The Upgraded CARISMA Magnetometer Array in the THEMIS Era, *Space Science Reviews*, *141* (1), 413–451.

Mann, I. R., A. N. Wright, K. J. Mills, and V. M. Nakariakov (1999), Excitation of magnetospheric waveguide modes by magnetosheath flows, *J. Geophys. Res.*, *104*, 333.

Mathie, R. A., and I. R. Mann (2000a), Observations of Pc5 field line resonance azimuthal phase speeds: A diagnostic of their excitation mechanism, *J. Geophys. Res.*, *105*, 10,713.

Mathie, R. A., and I. R. Mann (2000b), A correlation between extended intervals of ULF wave power and storm-time geosynchoronous relativistic electron flux enhancements, *Geophys. Res. Lett.*, *27*, 3261.

Mathie, R. A., I. R. Mann, F. W. Menk, and D. Orr (1999a), Pc5 ULF pulsations associated with waveguide modes observed with the IMAGE magnetometer array, *J. Geophys. Res.*, *104*, 7025.

Mathie, R. A., F. W. Menk, I. R. Mann, and D. Orr (1999b), Discrete field line resonances and the Alfvén continuum in the outer magnetosphere, *Geophys. Res. Lett.*, *26*, 659.

McComas, D. J., S. J. Bame, P. Barker, W. C. Feldman, J. L. Phillips, P. Riley, and J. W. Griffee (1998), Solar wind electron proton alpha monitor (SWEPAM) for the Advanced Composition Explorer, *Space Science Reviews*, *86*(1), 563–612.

Menk, F. W., B. J. Fraser, C. L. Waters, C. W. S. Ziesolleck, Q. Feng, S. H. Lee, and P. W. McNabb (1994), Ground measurements of low latitude magnetospheric field line resonances, in *Solar Wind Source of Magnetospheric Ultra-Low-Frequency Waves*, *Geophys. Monogr. Ser.*, vol. 81, edited by M. Egebretson, K. Takahashi, and M. Scholer, p. 299, AGU, Washington, D.C.

Menk, F. W., D. Orr, M. A. Cliverd, A. J. Smith, C. L. Waters, D. K. Milling, and B. J. Fraser (1999), Monitoring spatial and temporal variations in the dayside plasmashpere using geomagnetic field line resonances?, *J. Geophys. Res.*, *104*, 19,955.

Mewaldt, R. A., A. C. Cummings, and E. C. Stone (1994), Anomalous cosmic rays: Interstellar interlopers in the heliosphere and magnetosphere, *Eos Trans. AGU*, *75*(16), 185.

Myers, A. P., and D. Orr (1995), Ulf wave analysis and complex demodulation, *special publication ESA*, *371*, 24.

Northrop, T. (1963), Adiabatic charged-particle motion, *Rev. Geophys*, *1*(3), 283–304.

Nosé, M., T. Iyemori, M. Sugiura, and J. A. Slavin (1995), A strong dawn/dusk asymmetry in pc5 pulsation occurrence observed by the de-1 satellite, *Geophys. Res. Lett.*, *22*, 2053.

Ogilvie, K. W., et al. (1995), SWE, a comprehensive plasma instrument for the Wind spacecraft, *Space Science Reviews*, *71*(1), 55–77.

Ozeke, L. G., and I. R. Mann (2001), Modeling the properties of high-m Alfvén waves driven by the drift-bounce resonance mechanism, *Journal of Geophysical Research*, *106*(A8), doi:10.1029/2000JA000393.

Ozeke, L. G., and I. R. Mann (2008), Energization of radiation belt electrons by ring current ion driven ULF waves, *J. Geophys. Res.*, *113*(A2), A02,201, doi:10.1029/2007JA012468.

Parker, E. N. (1958), Dynamics of the Interplanetary Gas and Magnetic Fields., *The Astrophysical Journal*, *128*, 664.

Pathan, B. M., N. G. Kleimenova, O. V. Kozyreva, D. R. K. Rao, and R. L. Asinkar (1999), Equatorial enhancement of Pc5-6 magnetic storm time geomagnetic pulsations, *Earth Planets Space*, *51*, 959.

Press, W., B. Flannery, S. Teukolsky, and W. Vetterling (1992), Numerical recipes in C: the art of scientific programming, *Cambridge U. Press, Cambridge, England*, *5*.

Radoski, H. R. (1967), A note on oscillating field lines, *J. Geophys. Res.*, *72*(1).

Reddy, C. A., S. Ravindran, K. S. Viswanathan, B. V. K. Murthy, D. R. K. Rao, and T. Araki (1994), Observations of Pc5 micropulsation-related electric field oscillations in equatorial ionosphere, *Ann. Geophy.*, *12*, 565.

Rickard, G. J., and A. N. Wright (1994), Alfven resonance excitation and fast wave propagation in magnetospheric waveguides, *J. Geophys. Res.*, *99*, 13,455.

Roberts, W. T. J., R. H. Horwitz, C. R. Chappell, J. J. H. Waite, and J. L. Green (1987), Heavy ion density enhencements in the outer plasmasphere, *J. Geophys. Res.*, *92*, 13,499.

Rostoker, G., and B. T. Sullivan (1969), Polarization characteristics of Pc5 magnetic pulsations in the dusk hemisphere, *Planet. Space Sci.*, *17*, 349.

Rostoker, G., S. Skone, and D. N. Baker (1998), On the origin of relativistic electrons in the magnetosphere associated with some geomagnetic storms, *Geophys. Res. Lett.*, *19*, 3701.

Ruohoniemi, J. M., R. A. Greenwald, K. B. Baker, and J. C. Samson (1991), HF radar observations of Pc 5 field line resonances in the midnight/early morning MLT sector, *Geophys. Res. Lett.*, *96*, 15,697.

Russell, C. T. (1976), On the occurence of magnetopause crossing at 6.6 re, *Geophys. Res. Lett.*, *3(10)*, 593.

Samson, J. C., J. A. Jacobs, and G. Rostoker (1971), Latitude-dependent characteristics of long-period geomagnetic micropulsations, *J. Geophys. Res.*, *76*(16).

Samson, J. C., R. A. Greenwald, J. M. Ruohoniemi, T. J. Hughes, and D. D. Wallis (1991), Magnetometer and radar observations of magnetohydrodynamic cavity modes in the Earth's magnetosphere, *Can. J. Phys.*, *69*.

Samson, J. C., B. B. Harrold, J. M. Ruohoniemi, R. A. Greenwald, and A. D. M. Walker (1992), Field line resonances associated with MHD waveguides in the magnetosphere, *Geophys. Res. Lett.*, *19*, 441.

Schott, J. J., N. G. Kleimenova, J. Bitterly, and V. Kozyreva (1998), The strong Pc5 geomagnetic pulsations in the initial phase of the great magnetic storm of March 24, 1991, *Earth Planets Space*, *50*, 101.

Schulz, M., and L. Lanzerotti (1974), *Particle diffusion in the radiation belts*, Springer-Verlag.

Shea, M. A., and D. F. Smart (1993), March 1991 solar-terrestrial phenomena and related technological consequences, *in Proceeding of 23rd International Cosmic Ray Conference, Calgary, Canada*, *3*, 739.

Sibeck, D. G. (1989), The magnetospheric response to 8 min-period strong amplitude upstream pressure variations, *J. Geophys. Res.*, *94*, 2505.

Smith, C. W., J. L'Heureux, N. F. Ness, M. H. Acuna, L. F. Burlaga, and J. Scheifele (1998), The ACE magnetic fields experiment, *Space Science Reviews*, *86*(1), 613–632.

Smith, C. W., et al. (2001), ACE observations of the Bastille Day 2000 interplanetary disturbances, *Solar Physics*, *204*(1), 227–252.

Southwood, D. J. (1973), The behaviour of ULF waves and particles in the magnetosphere, *Planetary and Space Science*, *21*, 53–65.

Southwood, D. J. (1974), Some features of field line resonances in the magnetosphere, *Planet. Space Sci.*, *22*, 483.

Southwood, D. J., and W. J. Hughes (1983), Theory of hydromagnetic waves in the magnetosphere, *Space Sci. Rev.*, *35*, 301.

Southwood, D. J., and M. G. Kivelson (1981), Charged particle behaviour in low frequency geomagnetic pulsations I: Transverse waves, *J. Geophy. Res.*, *86*, 5643.

Southwood, D. J., J. W. Dungey, and R. J. Etherington (1969), Bounce resonant interaction between pulsations and trapped particles, *Planet. Space Sci.*, *22*, 483.

Stephenson, J. A. E., and A. D. M. Walker (2002), Hf radar observations of pc5 ulf pulsations driven by the solar wind, *Geophys. Res. Lett.*, *29*, 1297.

Takahashi, K., and A. Y. Ukhorskiy (2007), Solar wind control of Pc5 pulsation power at geosynchronous orbit (DOI 10.1029/2007JA012483), *J. Geophys. Res.*, *112*(A11205), doi:10.1029/2007JA012483.

Takahashi, K., P. R. Higbie, and D. N. Baker (1985), Energetic electron flux pulsations observed at geostationary orbit: Relation to magnetic pulsations, *J. Geophys. Res.*, *24*, 1683.

Thorne, R. M. (1973), Plasmaspheric hiss, *J. Geophys. Res*, *78*, 1581.

Trivedi, N. B., B. R. Arora, A. L. Padilha, J. M. D. Costa, S. L. G. Dutra, F. H. Chamalaun, and A. Rigoti (1997), Global Pc5 geomagnetic pulsations of March 24, 1991, as observed along the American sector, *Geophys. Res. Lett.*, *24*, 1683.

Tsyganenko, N. A., and M. I. Sitnov (2005), Modeling the dynamics of the inner magnetosphere during strong geomagnetic storms, *J. Geophys. Res.*, *110*, doi:10.1029/2004JA010798.

Viljanen, A., and L. Hakkinen (1997), Image magnetometer network satellite-ground-based coordination sourcebook, *ESA Publications, Edited by M. Lockwood, M. N. Wild, and H. J. Opgenoorth*, p. 111.

Walker, A. D. M., R. A. Greenwald, W. F. Stuart, and C. A. Green (1979), Stare auroral radar observations of Pc 5 geomagnetic pulsations, *J. Geophys. Res.*, *84*, 3373.

Walker, A. D. M., J. M. Ruohoniemi, K. B. Baker, R. A. Greenwald, and J. C. Samson (1992), Spatial and temporal behavior of ULF pulsations observed by the Goose Bay HF radar, *J. Geophys. Res.*, *97*, 12,187.

Walt, M. (1971), The radial diffusion of trapped particles induced by fluctuating magnetospheric fields, *Space Science Reviews*, *12*(4), 446–485.

Walt, M. (2005), Introduction to geomagnetically trapped radiation, *Introduction to Geomagnetically Trapped Radiation, by Martin Walt, pp.. ISBN 0521616115. Cambridge, UK: Cambridge University Press, 2005.*

Waters, C. L., J. C. Samson, and E. F. Donovan (1995), The temporal variation of the frequency of high latitude field line resonances, *J. Geophys. Res.*, *100*, 7987.

Wright, A. N. (1994), Dispersion and wave coupling in inhomogeneous MHD waveguides, *J. Geophys. Res.*, *99*, 159.

Wright, A. N., K. J. Mills, and M. S. Ruderman (2002), The nature of convectively unstable waveguide mode disturbances on the magnetospheric flanks, *J. Geophys. Res.*, *107*(A9), 1242, doi:10.1029/2001JA005091.

Yumoto, K., et al. (1992), coordinated magnetic observations along 210^o magnetic meridian during STEP period: 1. Preliminary results of low latitude Pc 3ś, *J. Geomag. Geoelctr.*, *44*, 261–276.

Yumoto, K. H., and 210^o MM Magnetic Observation Group (1996), The STEP 210^0 magnetic meridian network project, *J. Geomag. Geoelctr.*, *48*, 1297.

Ziesolleck, C. W. S., and D. R. McDiarmid (1994), Auroral latitude Pc 5 field line resonances: Quantized frequencies, spatial characteristics, *J. Geophys. Res.*, *99*, 5817.

Ziesolleck, C. W. S., and D. R. McDiarmid (1995), Statistical survey of auroral latitude Pc 5 spectral and polarization characteristics, *J. Geophys. Res.*, *100*, 19,299.

Appendix A

Ground-based Magnetometer Station Locations

Station Name	Station Code	Geographic lat.	Geographic lon.	CGM° lat.	CGM° lon.	L-shell
IMAGE stations						
Ny Ålesund	NAL	78.92	11.96	75.97	113.20	NA
Longyearbyen	LYR	78.20	15.82	75.01	113.86	15.24
Hornsund	HOR	77.00	15.60	73.92	111.26	13.29
Hopen Island	HOP	76.51	25.01	72.79	116.55	11.64
Bear Island	BJN	74.50	19.20	71.25	109.48	9.86
Nordkapp	NOR	71.09	25.79	67.50	110.47	6.96
Sørøya	SOR	70.54	22.22	67.16	107.26	6.76
Kevo	KEV	69.76	27.01	66.11	110.22	6.21
Tromsø	TRO	69.66	18.94	66.49	103.98	6.40
Masi	MAS	69.46	23.70	65.99	107.42	6.16
Andenes	AND	69.30	16.03	66.33	101.46	6.32
Ivalo	IVA	68.56	27.29	64.89	109.48	5.66
Abisko	ABK	68.35	18.82	65.17	102.76	5.78
Leknes	LEK	68.13	13.54	65.31	98.55	5.84
Muonio	MUO	68.02	23.53	64.55	106.15	5.52
Lovozero	LOZ	67.97	35.08	63.96	115.27	5.29
Kiruna	KIR	67.84	20.42	64.55	103.60	5.52
Sodankylä	SOD	67.37	26.63	63.73	108.12	5.20
Pello	PEL	66.90	24.08	63.38	105.79	5.08
Dønna	DON	66.11	12.50	63.31	96.21	5.05
Rrvik	RVK	64.94	10.98	62.20	94.23	4.68
Lycksele	LYC	64.61	18.75	61.33	100.11	4.43
Mekrijärvi	MEK	62.77	30.97	58.87	109.07	3.81
Dombås	DOB	62.07	9.11	59.30	91.01	3.91
Solund	SOL	61.08	4.84	58.58	87.11	3.75
Uppsala	UPS	59.90	17.35	56.44	96.50	3.33
Karmøy	KAR	59.21	5.24	56.50	86.45	3.34
Tartu	TAR	58.26	26.46	54.32	103.40	2.99
IMAGE stations, 1-second data available from SAMNET						
Kilpisjärvi	KIL	69.06	20.77	65.76	104.84	6.05
Oulujärvi	OUJ	64.52	27.23	60.80	106.87	4.28
Hankasalmi	HAN	62.25	26.60	58.49	105.19	3.73
Nurmijärvi	NUR	60.50	24.65	56.74	102.78	3.39
SAMNET stations						
Oulu	OUL	65.10	25.85	61.46	106.08	4.46
Nordli	NOR	64.37	13.36	61.43	95.72	4.45
Hella	HLL	63.77	339.44	64.71	68.74	5.58
Faroes	FAR	62.05	352.98	60.90	78.40	4.31
Kvistaberg	KVI	59.50	17.63	56.00	96.55	3.26
Thurso	THU	58.36	356.31	56.42	79.00	3.33
Borok	BOR	58.03	38.33	53.81	113.63	2.92
Glenmore Lodge	GML	57.16	356.32	55.06	78.43	3.11
York	YOR	53.95	358.95	51.09	79.17	2.58
BGS stations, data available from SAMNET						
Lerwick	LER	60.13	358.82	58.12	81.87	3.65
Eskdalemuir	ESK	55.32	356.80	52.90	78.01	2.80
Hartland	HAD	50.99	355.52	47.90	75.37	2.27

Table A.1: IMAGE and SAMNET magnetometer station locations. Corrected GeoMagnetic (CGM) coordinates for 1991 at 120 km were calculated from SPDF/Modelweb.

Station	Station	Geographic	Geographic	CGM°	CGM°	
Name	Code	lat.	lon.	lat.	lon.	L-shell
GREENLAND West Coast stations						
Qaanaaq	THL	77.47	290.77	85.8	34.3	NA
Savissivik	SVS	76.02	294.90	84.01	36.59	NA
Upernavik	UPN	72.78	303.85	79.9	42.5	NA
Uummannaq	UMQ	70.68	307.87	77.3	44.3	NA
Qeqertarsuaq	GDH	69.25	306.47	76.2	40.6	NA
Attu	ATU	67.93	306.43	75.0	38.8	NA
Kangerlussuaq	STF	67.02	309.28	73.6	41.8	12.8
Maniitsoq	SKT	65.42	307.10	73.5	37.9	11.2
Nuuk	GHB	64.17	308.27	71.0	38.5	9.6
Paamiut	FHB	62.00	310.32	68.5	39.5	7.6
Narsarsuaq	NAQ	61.16	314.56	66.8	43.86	6.8
CARISMA CGSM sations						
Contwoyt	CONT	65.75	248.75	73.39	300.74	12.47
Dawson	DAWS	64.05	220.89	65.93	270.78	6.12
Eskimo Point	ESKI	61.11	265.95	71.53	330.34	10.15
Fort Churchill	FCHU	58.76	265.91	69.31	330.91	8.16
Fort Simpson	FSIM	61.76	238.77	67.60	291.01	7.01
Fort Smith	FSMI	60.03	248.07	67.86	303.77	7.18
Gillam	GILL	56.38	265.36	66.99	330.56	6.67
Island Lake	ISLL	53.86	265.34	64.56	331.00	5.52
Fort Mcmurray	MCMU	56.66	248.79	64.74	306.42	5.60
Pinawa	PINA	50.20	263.96	60.82	329.52	4.29
Rabbit Lake	RABB	58.22	256.32	67.60	316.22	7.01
Rankin Inlet	RANK	62.82	267.89	73.26	333.17	12.28
Taloyoak	TALO	69.54	266.45	79.29	326.75	NA
Selected 210 MM stations						
Adelaide	ADL	-34.67	138.65	-46.18	213.60	2.13
Moshiri	MSR	44.37	142.27	37.24	213.10	1.61
Birdsville	BSV	-25.54	139.21	-36.07	212.89	1.56
Kagoshima	KAG	31.48	130.72	24.35	202.14	1.23
Chichijima	CBI	27.15	142.30	19.53	212.92	1.15
Chokurdakh	CHD	70.62	147.89	64.56	211.83	5.52
Zyryanka	ZYK	65.75	150.78	59.52	216.47	3.96
Magadan	MGD	59.97	150.86	53.42	218.47	2.87
Selected WDC stations						
Chambon-La-Foret	CLF	48.02	2.27	43.65	79.84	1.95
Furstenfeldbruck	FUR	48.17	11.28	43.42	87.30	1.93
Hermanus	HER	-34.42	19.23	-41.99	81.94	1.84
Hartebeesthoek	HBK	-25.88	27.71	-35.83	94.46	1.55
Sodankyla	SOD	67.37	26.36	63.74	107.91	5.21
Abisko	ABK	68.36	18.82	65.18	102.76	5.78
St. Johns	STJ	47.60	307.32	54.55	31.09	3.03
Tihany	THY	46.90	17.89	41.82	92.62	1.83
Selected Intermagnet stations						
Barrow	BRW	71.30	203.25	69.83	249.51	8.57
College	CMO	64.90	212.20	65.02	262.56	5.71
Poste-de-la-Baleine	PBQ	55.30	282.20	66.31	357.69	6.31
Iqaluit	IQA	63.80	291.50	73.43	14.36	12.53
Irkutsk	IRT	52.17	104.45	46.87	176.90	2.18
Port Alfred	CZT	-46.43	51.85	-53.12	106.06	2.83
Belsk	BEL	51.84	20.79	47.47	96.43	2.23
Martin de Vivies-Amsterdam Island	AMS	-37.79	77.57	-48.97	138.33	2.36
Beijing Ming Tombs	BMT	40.30	116.20	34.13	188.31	1.49
Memambetsu	MMB	43.90	144.20	36.71	214.81	1.59

Table A.2: GREENLAND West Coast, CARISMA CGSM and selected 210 MM, WDC and Intermagnet station locations. Corrected GeoMagnetic (CGM) coordinates for 1991 at 120 km were calculated from SPDF/Modelweb.

Station Name	Station Code	Geographic lat.	Geographic lon.	CGM° lat.	CGM° lon.	L-shell
IMAGE stations						
Ny Ålesund	NAL	78.92	11.96	76.19	111.58	NA
Longyearbyen	LYR	78.20	15.82	75.25	112.41	15.71
Hornsund	HOR	77.00	15.60	74.13	109.89	13.63
Hopen Island	HOP	76.51	25.01	73.05	115.44	11.98
Bear Island	BJN	74.50	19.20	71.45	108.34	10.06
Nordkapp	NOR	71.09	25.79	67.71	109.65	7.08
Sørøya	SOR	70.54	22.22	67.34	106.41	6.87
Kevo	KEV	69.76	27.01	66.32	109.49	6.31
Tromsø	TRO	69.66	18.94	66.65	103.12	6.48
Masi	MAS	69.46	23.70	66.18	106.65	6.24
Andenes	AND	69.30	16.03	66.46	100.57	6.39
Ivalo	IVA	68.56	27.29	65.09	108.81	5.74
Abisko	ABK	68.35	18.82	65.31	101.96	5.84
Leknes	LEK	68.13	13.54	65.41	97.68	5.88
Muonio	MUO	68.02	23.53	64.25	114.77	5.40
Lovozero	LOZ	67.97	35.08	64.20	114.74	5.38
Kiruna	KIR	67.84	20.42	64.70	102.85	5.58
Sodankylä	SOD	67.37	26.63	63.92	107.49	5.27
Pello	PEL	66.90	24.08	63.55	105.13	5.14
Dønna	DON	66.11	12.50	63.38	95.41	5.08
Rrvik	RVK	64.94	10.98	62.26	93.46	4.70
Lycksele	LYC	64.61	18.75	61.45	99.47	4.46
Mekrijärvi	MEK	62.77	30.97	59.07	108.66	3.86
Dombås	DOB	62.07	9.11	59.32	90.33	3.91
Solund	SOL	61.08	4.84	58.55	86.40	3.74
Uppsala	UPS	59.90	17.35	56.53	95.99	3.35
Karmøy	KAR	59.21	5.24	56.46	85.81	3.34
Tartu	TAR	58.26	26.46	54.48	103.06	3.02
IMAGE stations, 1-second data available from SAMNET						
Kilpisjärvi	KIL	69.06	20.77	65.93	104.05	6.12
Oulujärvi	OUJ	64.52	27.23	60.99	106.35	4.33
Hankasalmi	HAN	62.25	26.60	58.66	104.74	3.77
Nurmijärvi	NUR	60.50	24.65	56.90	102.36	3.42
SAMNET stations						
Oulu	OUL	65.10	25.85	61.63	105.51	4.51
Nordli	NOR	64.37	13.36	65.05	68.10	5.73
Hella	HLL	63.77	339.44	64.41	67.70	5.46
Faroes	FAR	62.05	352.98	60.74	77.53	4.26
Kvistaberg	KVI	59.50	17.63	56.09	96.05	3.27
Thurso	THU	58.36	356.31	56.26	78.27	3.30
Borok	BOR	58.03	38.33	54.05	113.45	2.96
Glenmore Lodge	GML	57.16	356.32	54.89	77.75	3.08
York	YOR	53.95	358.95	50.92	78.59	2.56
BGS stations, data available from SAMNET						
Lerwick	LER	60.13	358.82	58.01	81.12	3.63
Eskdalemuir	ESK	55.32	356.80	52.72	77.38	2.78
Hartland	HAD	50.99	355.52	47.65	74.82	2.25

Table A.3: IMAGE and SAMNET magnetometer station locations. Corrected GeoMagnetic (CGM) coordinates for 2001 at 120 km were calculated from SPDF/Modelweb.

Station Name	Station Code	Geographic lat.	Geographic lon.	CGM° lat.	CGM° lon.	L-shell
GREENLAND West Coast stations						
Qaanaaq	THL	77.47	290.77	85.23	30.63	NA
Savissivik	SVS	76.02	294.90	83.49	33.81	NA
Upernavik	UPN	72.78	303.85	79.36	40.58	NA
Uummannaq	UMQ	70.68	307.87	76.79	42.73	NA
Qeqertarsuaq	GDH	69.25	306.47	75.67	39.22	NA
Attu	ATU	67.93	306.43	74.41	37.97	14.10
Kangerlussuaq	STF	67.02	309.28	73.02	40.76	11.95
Maniitsoq	SKT	65.42	307.10	71.83	37.06	10.48
Nuuk	GHB	64.17	308.27	70.40	37.67	9.06
Paamiut	FHB	62.00	310.32	67.86	38.87	7.18
Narsarsuaq	NAQ	61.16	314.56	66.17	43.14	6.24
CARISMA CGSM sations						
Contwoyt	CONT	65.75	248.75	73.10	302.98	12.06
Dawson	DAWS	64.05	220.89	65.93	272.50	6.12
Eskimo Point	ESKI	61.11	265.95	71.01	331.91	9.62
Fort Churchill	FCHU	58.76	265.91	68.80	332.36	7.79
Fort Simpson	FSIM	61.76	238.77	67.41	292.79	6.90
Fort Smith	FSMI	60.03	248.07	67.57	305.48	7.00
Gillam	GILL	56.38	265.36	66.50	331.93	6.41
Island Lake	ISLL	53.86	265.34	64.08	332.30	5.33
Fort Mcmurray	MCMU	56.66	248.79	64.45	307.92	5.48
Pinawa	PINA	50.20	263.96	60.39	330.73	4.17
Rabbit Lake	RABB	58.22	256.32	67.21	317.79	6.79
Rankin Inlet	RANK	62.82	267.89	72.71	334.75	11.54
Taloyoak	TALO	69.54	266.45	78.77	329.12	NA
Selected 210 MM stations						
Adelaide	ADL	-34.67	138.65	-45.91	213.98	2.10
Moshiri	MSR	44.37	142.27	37.60	213.69	1.62
Birdsville	BSV	-25.54	139.21	-35.76	213.27	1.55
Kagoshima	KAG	31.48	130.72	24.70	202.64	1.23
Chichijima	CBI	27.15	142.30	19.88	213.43	1.15
Chokurdakh	CHD	70.62	147.89	64.96	212.71	5.69
Zyryanka	ZYK	65.75	150.78	59.89	217.30	4.05
Magadan	MGD	59.97	150.86	53.42	219.47	2.87
Selected WDC stations						
Chambon-La-Foret	CLF	48.02	2.27	43.50	79.41	1.94
Furstenfeldbruck	FUR	48.17	11.28	43.41	86.98	1.93
Hermanus	HER	-34.42	19.23	-42.08	82.69	1.85
Hartebeesthoek	HBK	-25.88	27.71	-35.74	95.08	1.55
Sodankyla	SOD	67.36	26.36	63.93	107.27	5.28
Abisko	ABK	68.36	18.82	65.32	101.93	5.83
St. Johns	STJ	47.60	307.32	53.61	31.11	2.90
Tihany	THY	46.90	17.89	41.90	92.41	1.84
Selected Intermagnet stations						
Barrow	BRW	71.30	203.25	70.04	251.32	8.74
College	CMO	64.90	212.20	65.09	264.19	5.74
Poste-de-la-Baleine	PBQ	55.30	282.20	65.61	358.52	5.97
Iqaluit	IQA	63.80	291.50	72.73	14.49	11.55
Irkutsk	IRT	52.17	104.45	47.23	177.30	2.21
Port Alfred	CZT	-46.43	51.85	-53.19	106.34	2.84
Belsk	BEL	51.84	20.79	47.58	96.16	2.24
Martin de Vivies-Amsterdam Island	AMS	-37.79	77.57	-49.05	138.88	2.37
Beijing Ming Tombs	BMT	40.30	116.20	34.51	188.59	1.50
Memambetsu	MMB	43.90	144.20	37.06	215.41	1.60

Table A.4: GREENLAND West Coast, CARISMA CGSM and selected 210 MM, WDC and Intermagnet station locations. Corrected GeoMagnetic (CGM) coordinates for 2001 at 120 km were calculated from SPDF/Modelweb.